

**Development of a Direct Density Measurement Technique for Aero-Optic
Analysis of a High-Velocity, Compressible Flow Field**

by

John Zachary Reid

A thesis submitted to the Graduate Faculty of
Auburn University
in partial fulfillment of the
requirements for the Degree of Master of Science

Auburn, Alabama
August 6, 2011

Keywords: Acetone PLIF, Aero-Optics, Compressible, Density, Shear Layer,
Turbulent Wake

Copyright 2010 by John Zachary Reid

Approved by

Brian S. Thurow, Chair, Associate Professor of Aerospace Engineering
Anwar Ahmed, Professor of Aerospace Engineering
Roy J. Hartfield, Professor of Aerospace Engineering

Abstract

A direct density measurement technique was developed for high-velocity, compressible flow fields using acetone planar laser induced fluorescence (PLIF). Motivation for this work was mainly aero-optics. A 4" x 4" transonic wind tunnel ($M_\infty \approx 0.78$) was designed/fabricated to investigate the shear layer and wake region of a small-scale hemisphere. The flow was seeded with acetone vapor and the acetone vapor was excited by a 266 nm laser sheet. Resulting fluorescence was converted to density field data. The centerline was the main area of interest, however other parallel planes of the flow were also investigated. Large density drops and distinct vortex cores were seen in the shear layer and wake region, along with shocks at the point of separation. Schlieren and shadowgraph imaging and PIV experiments were also performed. Aero-optic distortion was calculated for the density field data and connections were made between flow structures, velocity, vorticity, density, and aero-optic distortion.

Acknowledgements

The author would like to thank God for His saving grace through Jesus Christ and for giving him the opportunity to further his education at Auburn University. The author would also like to thank his family and friends for all of their support over the past three years. The author would like to thank the Air Force Office of Scientific Research (AFOSR) for providing the funding for this work through an AFOSR Young Investigator Program Grant (FA9550-08-1-0150). The author would also like to thank his advisor, Dr. Brian S. Thurow, for his patience, guidance, support, and knowledge/expertise while this research was being conducted. Additionally, the author would like to thank his other committee members, Dr. Anwar Ahmed and Dr. Roy Hartfield, for their guidance, assistance, and input during the research process. The author would like to give a huge thank you to Kyle Lynch (GRA) for his knowledge and support, for helping set up and run experiments, for operating the pulse burst laser, for upgrading the wind tunnel so it is operated by a computer, and for help with image processing and some coding. The author also would like to thank David Wall (current GRA/undergraduate at the time) for conceptually designing the transonic wind tunnel/creating the CAD drawings and for helping the author construct the wind tunnel after the machining of the parts of the wind tunnel was complete. Also, the author would like to thank Andy Weldon for performing almost all of the machining for this research and Kevin Albarado (current GRA/undergraduate at the time) for assisting in some of the assembly of the wind tunnel and providing some coding help. Finally, the author would like to

thank Abhishek Bichal (GRA), Nathan Kearns (undergraduate student), Tim Fahringer (undergraduate student), and Rex Newman (undergraduate student) for assistance with experiments/experimental set-up and knowledge/input on the research.

Table of Contents

Abstract.....	ii
Acknowledgements	iii
List of Tables	xii
List of Figures	xiii
List of Abbreviations and Symbols	xx
I. Introduction and Motivation	1
A. Importance of Direct Density Measurement Technique.....	3
B. Shear Layer/Turbulent Wake of a Hemisphere – Why a Hemisphere?	4
C. Goals and Objectives.....	7
II. Background of Aero-Optics	8
A. Quantifying Aero-Optic Distortion	8
B. Severity of Aero-Optic Distortion	9
C. Wavefront Distortion: Aero-Optic Distortion and Atmospheric Propagation	10
D. Recent Aero-Optic Work and Research	11

III. Background of Acetone Planar Laser Induced Fluorescence	17
A. Description of Acetone PLIF Technique	17
B. Photophysics/Characteristics of Acetone	17
C. Fluorescence of Acetone	18
D. Advantages and Disadvantages of Acetone	19
E. Comparison of Acetone to Other Flow Tracers	21
F. Recent Acetone Photophysics and Acetone PLIF Work	22
a. Acetone Photophysics Work	22
b. Temperature, Concentration/Mixing, and Convective Velocity Measurements with Acetone PLIF	26
c. Aero-Optic Measurements with Acetone PLIF	30
IV. Acetone PLIF for Direct Density Measurements	33
A. Acetone Fluorescence Signal Equation	33
B. Image Processing and In-Situ Calibration	35
a. Dark Image Subtraction, COS^4 Vignetting Correction, and Filtering of High Intensity Particles	36
b. Laser Sheet Non-Uniformity Correction	41
c. Normalization to Freestream Conditions	47
C. Behavior of σ and ϕ for ρ , T , and P	50

D.	Sensitivity of σ and ϕ	52
E.	Curves of $S_f/S_{f\infty}$ vs. ρ/ρ_∞ and Conversion to Density.....	53
F.	Random Error in Density Measurement Due to Uncertainty in Local Pressure P	55
V.	Test Facility Part I: Transonic Wind Tunnel and Hemisphere Model.....	57
A.	Characterization of Transonic Wind Tunnel.....	57
B.	Transonic Wind Tunnel Design Constraints	58
C.	Transonic Wind Tunnel Design Description: Inlet and Test Section.....	60
D.	Transonic Wind Tunnel Design Description: Choke Block and Diffuser	65
E.	Transonic Wind Tunnel Operation.....	67
F.	Hemisphere Model.....	68
VI.	Tunnel/Flow Field Validation and Characteristics.....	70
A.	Pressure Measurements With and Without Hemisphere Mounted.....	70
B.	Pressure Measurements During Acetone PLIF Experiments.....	79
C.	Experimental Conditions in Test Section.....	82
D.	Schlieren and Shadowgraph Imaging	89
VII.	Test Facility Part II: Liquid Acetone/Alumina Particle Seeding.....	93

A.	Seeding System Design and Operation.....	93
B.	Acetone Mole Fraction.....	95
C.	Spray Nozzle Selection.....	98
D.	Acetone Vapor Pressure Curve.....	99
E.	Acetone Condensation Tests.....	102
F.	PIV Seeding.....	105
VIII.	Particle Image Velocimetry Experiments.....	107
A.	Background of PIV.....	107
B.	Details of Experimental Arrangement.....	108
a.	Illumination and Optical Arrangement.....	108
b.	Seeding for PIV Experiments.....	109
c.	Camera, Image Acquisition, and PIV Processing.....	111
C.	Expectations for PIV Experiments.....	113
D.	Results of PIV Experiments.....	114
IX.	Single-Plane, Single-Shot Acetone PLIF Experiments.....	117
A.	Details of Experimental Arrangement.....	117
a.	Laser Excitation and Optical Arrangement.....	118
b.	Seeding for Single-Shot Acetone PLIF Experiments.....	123
c.	Camera and Image Acquisition.....	124

B.	Expectations for Single-Shot Acetone PLIF Experiments.....	127
C.	Analysis of Density Images.....	128
a.	Centerline Wake Region Images	130
b.	Parallel Plane Wake Region Images	138
c.	Centerline Separation Region Images	142
d.	What Causes Flow Separation on the Hemisphere?	144
D.	Overall Error in Density Measurement.....	147
X.	Calculating Aero-Optic Distortion from Density Values	151
A.	Overview of Aero-Optic Distortion Calculations and Characteristics of Wavefront	151
B.	Calculation of <i>OPL</i> and <i>OPD</i>	154
C.	Calculation of Steady and Unsteady Wavefront Distortion	158
XI.	Time-Resolved Acetone PLIF Experiments	162
A.	Details of Experimental Arrangement	162
a.	Laser Excitation and Optical Arrangement.....	162
b.	Seeding for Time-Resolved Acetone PLIF Experiments	163
c.	Camera and Image Acquisition.....	164

B.	Expectations for Time-Resolved Acetone PLIF Experiments.....	165
C.	Results of Time-Resolved Acetone PLIF Experiments.....	166
XII.	Conclusions and Future Work.....	171
A.	Conclusions	171
B.	Future Work.....	173
a.	Improvements to the Wind Tunnel	173
b.	Improvements to Optical Setup, Image Processing, and Camera/Excitation Laser	178
c.	Improvements to Fluorescence Quantum Yield Model and Absorption Cross-Section Data.....	179
d.	Improvements to Particle Image Velocimetry Experiments	182
e.	Validation of Density Measurement Technique and Wavefront Distortion Calculations.....	183
	Works Cited	184
	Appendix A: Single-Shot Acetone PLIF Density Images (values normalized to freestream) - Centerline – Wake Region.....	196
	Appendix B: Off-Centerline Plane, Single-Shot Acetone PLIF Density Images (values normalized to freestream) – Wake Region	206
	Appendix C: Single-Shot Acetone PLIF Density Images (values normalized to freestream) – Centerline – Separation Region.....	216

Appendix D: Example Wavefronts218

List of Tables

Table 1: Location of Static Pressure Ports Inside of Test Section (Flow is Left to Right).....	71
Table 2: Laser Settings for PIV Experiment.....	112
Table 3: Spatial Resolution and Field of View for Planes Investigated	126
Table 4: Laser and Camera Settings for Acetone PLIF Experiments	127

List of Figures

Figure 1: Hemispherical Turret Flow Field at Subsonic Conditions [Gordeyev and Jumper (2010) ¹⁷]	6
Figure 2: Transonic Flow Over Hemispherical Turret [Gordeyev and Jumper (2010) ¹⁷]	6
Figure 3: Calculated Pressure Field (a) CFD – COBALT (b) WCM [Rennie et al. (2008) ¹¹]	13
Figure 4: Calculated Static Temperature Field (a) CFD – COBALT (c) WCM	14
Figure 5: Excitation and De-Excitation of Acetone [Thurber (1999) ⁴⁸]	19
Figure 6: Temperature Field for Flow Over Heated Cylinder [Thurber (1999) ⁴⁸]	27
Figure 7: Temperature Field of Heated Jet in Cross-Flow (a) Re=20 (b) Re=100 [Thurber (1999) ⁴⁸]	27
Figure 8: Acetone PLIF Image of Vortex Ring Mixing of Fuel/Air [Choi et al. (2002) ⁶⁶]	28
Figure 9: Temporal Acetone PLIF Images of Vortex Ring Mixing [Choi et al. (2002) ⁶⁶]	29
Figure 10: Vortex Ring Flame Propagation (a) Acetone PLIF Image of Vortex Ring Mixing Structure (b) Direct Image of Intensity of Propagating Flame [Choi et al. (2002) ⁶⁶]	29

Figure 11: Image of Compressible Shear Layer (a) Index of Refraction Field (b) Interfacial Fluid Thickness Field [Catrakis et al. (2006) ⁴⁴]	31
Figure 12: Flow Chart of Image Processing and In-Situ Calibration Procedure	35
Figure 13: Example Acetone PLIF Raw Image (i.e. Example Image Z)	36
Figure 14: Example Image Z After Average Dark Image Subtraction	37
Figure 15: Example Image Z After Vignetting Correction	38
Figure 16: Example Image Z After Filtering Out High-Intensity Particles	40
Figure 17: Angle θ_{ij} and Radial Distance R_{ij}	42
Figure 18: Example Image Z After Correction for Drops in Laser Intensity Along Lines of Constant θ_{ij}	43
Figure 19: 2-D Interpolated Fluorescence Intensity Values in Freestream Region for Example Image Z (sample values on x-axis and y-axis represent increasing θ_{ij} and R_{ij} , respectively)	44
Figure 20: Plot of Conversion Factor vs. θ_{ij} for Example Image Z	45
Figure 21: Example Image Z After Laser Sheet Non-Uniformity Correction	47
Figure 22: Example Image Z Normalized to Average Freestream Intensity $I_f/I_{f\infty}=S_f/S_{f\infty}$ (Example Image Z Inlayed)	49
Figure 23: Curves of $S_f/S_{f\infty}$ vs. ρ/ρ_∞ for a Single Image	55

Figure 24: Compressed Air Supply Line Pipe and Stagnation/Settling Chamber	58
Figure 25: Supersonic Wind Tunnel Mobile Unit.....	59
Figure 26: Schematic of Transonic Wind Tunnel (not drawn to scale).....	60
Figure 27: Transonic Wind Tunnel	61
Figure 28: Stagnation/Settling Chamber, Flange, Contoured Inlet Nozzle, and Test Section	62
Figure 29: Test Section Optical Access	62
Figure 30: Bottom Stepped Window	63
Figure 31: Choke Block and Throat Section	66
Figure 32: 90° PVC/Plastic Elbow Section.....	67
Figure 33: Location of Pressure Ports for Pressure Experiments.....	71
Figure 34: One Rectangular Side Window Installed During Pressure Experiments	72
Figure 35: Plot of Freestream Static Pressure vs. x/D (Without Hemisphere).....	75
Figure 36: Plot of Freestream Mach Number vs. x/D (Without Hemisphere).....	76
Figure 37: Plot of Freestream Static Pressure vs. x/D (With Hemisphere).....	78
Figure 38: Plot of Freestream Mach Number vs. x/D (With Hemisphere).....	79

Figure 39: Plot of $P_{storage}$ for Wind Tunnel Test Run (hemisphere mounted)	83
Figure 40: Plot of $T_{storage}=T_0$ for Wind Tunnel Test Run (hemisphere mounted)	84
Figure 41: Plot of P_0 for Wind Tunnel Test Run (hemisphere mounted).....	85
Figure 42: Plot of T_∞ for a Wind Tunnel Test Run (hemisphere mounted)	86
Figure 43: Plot of P_∞ and P_{wake} for Wind Tunnel Test Run (hemisphere mounted)	87
Figure 44: Plot of ρ_∞ for Wind Tunnel Test Run (hemisphere mounted).....	88
Figure 45: Plot of V_∞ for Wind Tunnel Test Run (hemisphere mounted).....	89
Figure 46: Schlieren Images of Hemisphere ($P_\infty \approx 1.33 \text{ atm} \approx$ 19.5 psia) – Knife Edge Horizontal	91
Figure 47: Schematic of Seeder.....	94
Figure 48: Plot of Acetone Vapor Pressure Curve (partial pressure curves created using freestream pressure and temperature values for valid data region)	101
Figure 49: Instantaneous Velocity Magnitude Field (m/s) - Centerline [Reid et al. (2010) ¹⁰³]	115
Figure 50: Instantaneous Vorticity Field (rad/s) – Centerline [Reid et al. (2010) ¹⁰³].....	115
Figure 51: Schematic of Acetone PLIF Experimental Setup.....	120
Figure 52: Cardboard Boxes to Block Ambient 532 nm Light	120

Figure 53: Optical Setup Below Wind Tunnel Test Section	121
Figure 54: Camera Setup	125
Figure 55: Example Single-Shot Acetone PLIF Density Image (values normalized to freestream) – Centerline – Wake Region	129
Figure 56: Wake Thickness of Single-Shot Acetone PLIF Density Image (values normalized to freestream) – Centerline – Wake Region	130
Figure 57: Flapping Motion in Single-Shot Acetone PLIF Density Image (values normalized to freestream) – Centerline – Wake Region	131
Figure 58: Abrupt Drop in Wake Thickness in Single-Shot Acetone PLIF Density Image (values normalized to freestream) – Centerline – Wake Region.....	132
Figure 59: Vortex Cores in Single-Shot Acetone PLIF Density Image (values normalized to freestream) – Centerline – Wake Region	133
Figure 60: Swirling/Folding Near Vortex Cores in Single- Shot Acetone PLIF Density Image (values normalized to freestream) – Centerline – Wake Region.....	134
Figure 61: Large Protruding Structures in Single-Shot Acetone PLIF Density Image (values normalized to freestream) – Centerline – Wake Region.....	135
Figure 62: Fairly Calm Shear Layer and Wake in Single-Shot Acetone PLIF Density Image (values normalized to freestream) – Centerline – Wake Region.....	135
Figure 63: Ensemble Average of Single-Shot Acetone PLIF Normalized Density Images – Centerline – Wake Region.....	136

Figure 64: Standard Deviation of Single-Shot Acetone PLIF Normalized Density Images – Centerline – Wake Region.....	137
Figure 65: D/8 Plane Single-Shot Acetone PLIF Density Image (values normalized to freestream)	138
Figure 66: D/4 Plane Single-Shot Acetone PLIF Density Image (values normalized to freestream)	139
Figure 67: 3D/8 Plane Single-Shot Acetone PLIF Density Image (values normalized to freestream)	140
Figure 68: D/2 Plane Single-Shot Acetone PLIF Density Image (values normalized to freestream)	141
Figure 69: 5D/8 Plane Single-Shot Acetone PLIF Density Image (values normalized to freestream)	142
Figure 70: Weak Shocks for Single-Shot Acetone PLIF Density Image (values normalized to freestream) – Centerline – Separation Region.....	143
Figure 71: Lambda Shocks for Single-Shot Acetone PLIF Density Image (values normalized to freestream) – Centerline – Separation Region.....	144
Figure 72: Plot of Drag Coefficient (C_D) vs. Reynolds Number (Re) and Mach Number (Ma) for a Sphere [Munson et al. (2002) ¹⁰⁴]	146
Figure 73: Lambda Shock and Laminar Boundary Layer Separation [Houghton and Carpenter (1993) ⁹⁰]	147
Figure 74: No Hemisphere Single-Shot Acetone PLIF Density Image (values normalized to freestream)	150
Figure 75: Example Index of Refraction Image with Wavefront Geometry Drawn.....	153

Figure 76: Example Index of Refraction Image with Outline of Wavefront Geometry Drawn.....	154
Figure 77: Plot of OPD vs. x'/D for Example Index of Refraction Image.....	156
Figure 78: Scatter Plot of Spatial OPD_{rms} Values for Images	157
Figure 79: Histogram of OPD_{rms} Values for Images (15 bins)	158
Figure 80: Plot of $\langle OPD \rangle$ vs. x'/D	159
Figure 81: Plot of OPD' vs. x'/D for Example Index of Refraction Image.....	160
Figure 82: Plot of Temporal OPD'_{rms} vs. x'/D	161
Figure 83: Design for Top Wall Stepped-Window (not drawn exactly to scale)	175
Figure 84: Easy Access to Supersonic Wind Tunnel Test Section	177

List of Abbreviations and Symbols

σ = absorption cross-section

S_f = acetone fluorescence signal

$\chi_{acetone}$ = acetone mole fraction

AR = anti-reflective

A = cross-sectional area of test-section

A^* = area of throat

BBO = beta barium borate

k = Boltzmann's constant

CCD = charge-coupled device

dV_c = collection volume

$\langle OPD \rangle$ = ensemble average of OPD (steady component of wavefront distortion)

OPD'_{rms} = temporal rms of OPD' (temporal standard deviation of OPD)

FOV = field of view

I_f = fluorescence intensity

ϕ = fluorescence quantum yield

$S_{f\infty}$ = freestream acetone fluorescence signal

ρ_∞ = freestream density

I_{∞} = freestream fluorescence intensity

M_{∞} = freestream Mach number

P_{∞} = freestream pressure

T_{∞} = freestream temperature

V_{∞} = freestream velocity

$K(\lambda_{\text{LIF}})$ = Gladstone-Dale constant

n = index of refraction

LIF = laser induced fluorescence

$I_{\text{Laser},ij}$ = laser sheet intensity

ρ = local density

I_f = local fluorescence/pixel intensity

E = local laser fluence

P = local pressure

T = local temperature

\overline{OPL} = mean spatial optical path length

Nd:YAG = neodymium-doped yttrium aluminum garnet

η_{opt} = optical collection efficiency

OPD = optical path difference

OPL = optical path length

PIV = particle image velocimetry

PLIF = planar laser induced fluorescence

h = Planck's constant

KDP = potassium dihydrogen phosphate

SNR = signal to noise ratio

OPD_{rms} = spatial rms of OPD

ρ_0 = stagnation density

P_0 = stagnation pressure

T_0 = stagnation temperature

$P_{storage}$ = storage pressure

$T_{storage}$ = storage temperature

R = universal gas constant

OPD' = unsteady component of wavefront distortion

P_{wake} = wake static pressure

λ = wavelength of excitation

λ_{wf} = wavelength of wavefront

I. Introduction and Motivation

New environments and applications for particular technologies arise as human innovation pushes and strives to achieve the unthinkable. The field of aero-optics has grown recently as directed energy sources, optical communications, and imaging systems have come to be used in new environments and on new platforms. These technologies are important because of the benefits they can provide under ideal conditions. However, in these new environments the performance of these technologies can be affected by a problem known as aero-optic distortion (or wavefront distortion). As a result, the causes and effects of wavefront distortion have been studied extensively.

Aero-optic distortion is a problem that negatively affects a wavefront in a multitude of ways. In the case of a directed energy source, such as a high-powered laser mounted to an aircraft, aero-optic distortion can cause problems such as defocus and jitter in the beam.^{1,2} This can cause the laser beam to be less effective once it reaches its final target.

Aero-optic distortion occurs when a wavefront passes through a flow field region containing index of refraction fluctuations, mainly caused by density fluctuations (index of refraction also slightly depends on the wavelength of light). The index of refraction of a material or medium is a function of density $\rho(x, y, z, t)$ and the Gladstone-Dale constant, $K(\lambda_{wf})$, as seen in Equation 1.

$$n(x, y, z, t) = 1 + K(\lambda_{wf})\rho(x, y, z, t) \quad \mathbf{1}$$

The index of refraction of a material or medium is the speed at which light travels through free space divided by the speed at which light travels through that specific material or medium.³ This means that as the index of refraction of a material or medium increases, the speed at which light travels through that

specific material or medium decreases. Therefore, if a wavefront passes through a region containing differences in index of refraction, portions of the wavefront speed up or slow down depending on the local index of refraction. This causes the wavefront to become distorted as it propagates away from the origin as certain portions of the wavefront travel faster or slower than other parts of the wavefront.

An example of a distorted wavefront is the road or the hood of a car appearing blurry near its surface on a hot day. This blurriness is heat haze/shimmer/mirage^{4,5} and is caused by differences in index of refraction in this region near the surface of the road or hood of the car, which are caused by density fluctuations (temperature fluctuations lead to density fluctuations through the ideal gas law). The light waves (wavefront) traveling from the street or hood of the car to one's eyes become distorted when they pass through this region of fluctuating index of refraction, so they appear blurry and out of focus when they reach one's eyes.

Aero-optic distortion is typically encountered in turbulent flow fields because turbulent flow fields exhibit many characteristics and flow features that cause density fluctuations. These flow features vary in a spatial and temporal manner and therefore cause the flow density to vary in a similar manner. In order to further investigate the aero-optic distortion problem in turbulent flow fields, a direct density measurement technique is needed that can resolve the spatial and temporal fluctuations in density. Acetone planar laser induced fluorescence (PLIF) was chosen as the measurement technique for this work because density values can be directly obtained from fluorescence images of a flow field.

A. Importance of Direct Density Measurement Technique

The ability to directly measure density in a high-velocity, compressible flow field is very important. As explained previously, turbulent flow fields cause the density field to fluctuate temporally and spatially, directly leading to aero-optic distortion if a wavefront is propagated through the flow field. A direct density measurement technique is necessary which can determine point by point values of density, so the aero-optic distortion for any wavefront type, size, wavelength, and orientation/path through the density field (and thus index of refraction field) can be calculated. Traditional wavefront measurement techniques using a Malley probe⁶⁻⁸ or a Shack-Hartmann wavefront sensor⁶⁻⁸ make aero-optic distortion measurements under specific wavefront experimental conditions (such as beam diameter, beam wavelength, and orientation/path through the flow field) where a separate experiment has to be conducted whenever these conditions are modified. This is less economical and more labor intensive than a direct density measurement technique (which instead offers a limitless number of wavefront possibilities). In addition, traditional techniques do not provide density information, so no comparison between distortion and density fluctuations can be made. [For more information on the Shack-Hartmann wavefront sensor see Platt and Shack (2001)⁹ and Schwiegerling and Neal¹⁰]

Density field data is also important because it can be coupled with velocity field data to better understand flow characteristics and features causing aero-optic distortion. Attempts have been made to use the velocity field of a separated shear layer flow in conjunction with the Weakly Compressible Model (WCM)^{6,11-14} and in conjunction with CFD (COBALT)^{11,14} to estimate density, temperature, and pressure fields. Then, the calculated density field from both models can be used to estimate the aero-optic distortion. Weakly compressible

shear layer results of temperature and density from CFD (COBALT) and the WCM are different and there is an ongoing debate between the two camps.^{11,14} The pressure results between CFD (COBALT) and the WCM are similar however.^{11,14} By developing a technique to directly measure density, some light can be shed on this debate. The WCM is explained in more detail in Section II.D.

Finally, it was thought that if a 2-D direct density measurement technique could be developed successfully, then a 3-D density measurement technique through laser sheet scanning acetone PLIF could ultimately be developed in the future. This is because previous work at Auburn University successfully established a 3-D flow visualization technique (532 nm) using a pulse burst laser system, a galvanometric scanning mirror, and a high-speed camera for low-speed, incompressible flow fields.^{15,16} However, a 3-D density measurement technique is a long term goal of this work and is beyond the purpose, scope, and focus of this thesis.

B. Shear Layer/Turbulent Wake of a Hemisphere – Why a Hemisphere?

The first step in the development of the direct density measurement technique was establishing a relevant flow field to investigate with the technique. A wall-mounted hemisphere at transonic conditions was chosen as the flow field of investigation for this work for three main reasons: the flow field exhibits large spatial and temporal density fluctuations in the shear layer and wake region, it is a highly three-dimensional, high-velocity, compressible flow field, and it is a relevant flow field because it is similar to the flow over a laser turret mounted to the fuselage of an aircraft. In the real world application of a laser turret mounted to the fuselage of an aircraft, aero-optic distortion is a problem when the high-powered laser beam passes through the shear layer and the turbulent wake

region. The laser needs to have full 180° firing capability and not be limited to the region upstream of the separated shear layer. Thus, being able to quantify the extent of the density fluctuations in the shear layer and turbulent wake region causing aero-optic distortion is very valuable. These two specific regions of the flow field are the focus of this work.

The general flow features/characteristics of a wall-attached hemisphere, and other bluff bodies, in a freestream flow are well-established in literature.^{8,17-38} This flow field consists of a flat-plate boundary layer upstream of the hemisphere, followed by a horseshoe/necklace vortex that forms just slightly upstream of the hemisphere near the junction of the hemisphere and the wall. The horseshoe/necklace vortex wraps around the bottom of the hemisphere and moves backward to the wake region. A separated shear layer forms on the top of the hemisphere as well as shedding vortices. These shedding vortices evolve into the turbulent wake downstream of the hemisphere. Shocks also can potentially form on top of the hemisphere at approximately 90° from the horizontal and are typically non-stationary. Images of the hemispherical turret flow field features at subsonic and transonic conditions are shown in Figure 1 and Figure 2, respectively. Additional information on flow separation over a hemisphere/sphere/cylinder is provided in Section IX.C.

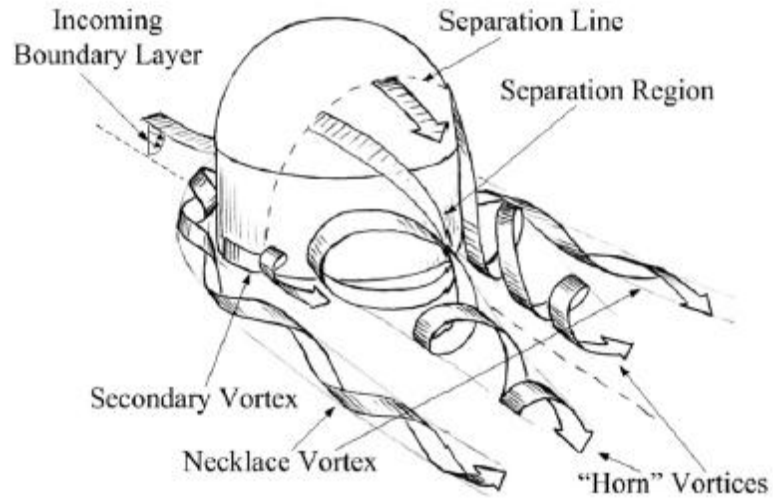


Figure 1: Hemispherical Turret Flow Field at Subsonic Conditions [Gordeyev and Jumper (2010)¹⁷]

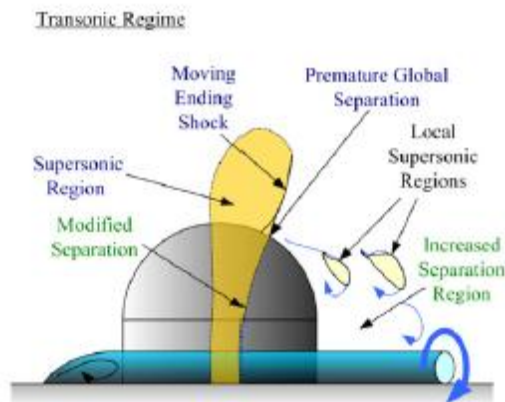


Figure 2: Transonic Flow Over Hemispherical Turret [Gordeyev and Jumper (2010)¹⁷]

C. Goals and Objectives

The main goal of this work was to demonstrate the viability of acetone PLIF to directly measure local density in a high-velocity, compressible flow field that experiences spatial and temporal density fluctuations. Motivation was primarily aero-optics and therefore an additional goal was to make aero-optic distortion calculations for the measured density fields. A long term goal of this work, which is beyond the scope of this thesis, is extension to 3-D density measurements through laser sheet scanning acetone PLIF.

This paper presents the development of the direct density measurement technique. Construction and flow validation of a test facility which creates the conditions of a wall-mounted hemisphere at approximately $M_\infty \approx 0.78$ is also presented. The acetone PLIF experimental setup in this flow facility is explained, as well as extraction of density data from acetone PLIF images and calculations of aero-optic distortion for these density fields. Analysis of the density fields is provided, as well as analysis of the calculated aero-optic distortion.

II. Background of Aero-Optics

A. Quantifying Aero-Optic Distortion

Traditionally, aero-optic distortion is quantified through the optical path difference (OPD), which has a direct correlation to the flow field density. The optical path difference is the difference between optical path length (OPL) and mean spatial optical path length (\overline{OPL}), as seen in Equation 2.

$$OPD(x, y, t) = OPL(x, y, t) - \overline{OPL(x, y, t)} \quad 2$$

OPL is quantified by integrating, in the direction of light propagation, z , the three-dimensional index of refraction, as seen in Equation 3. Physically speaking, OPL is the distance light travels in freespace (or a vacuum, $n=1$) in the same amount of time it takes the same light to travel through a specific material or medium with a particular index of refraction value (or through a region with varying index of refraction values). Thus, it makes physical sense that OPL increases as the index of refraction increases because light travels slower through higher index of refraction regions. As shown in Equation 1, the index of refraction is a function of density.

$$OPL(x, y, t) = \int n(x, y, z, t) dz \quad 3$$

If a theoretical wavefront is propagated through an index of refraction field (calculated from the measured density field), then the expected aero-optic distortion can be quantified. For example, assume a theoretical wavefront consists of 100 rays physically/geometrically equal in length and parallel to each other. If OPL for each ray is calculated, then \overline{OPL} is simply the average of all 100 OPL values. The OPD value for each ray is calculated by subtracting \overline{OPL} from

the *OPL* value for each ray to yield 100 different *OPD* values. For a planar wavefront with little to no distortion, these *OPD* values would all be approximately the same and be close to zero and the wavefront would maintain the same basic planar shape. For a wavefront that suffers from distortion, these *OPD* values would be on the order of fractions of microns (positive and negative).

B. Severity of Aero-Optic Distortion

The severity of the aero-optic distortion is not only dependent on the density fluctuations, but is also dependent on the wavelength of the wavefront passing through the flow field and the Mach number of the flow. The Gladstone-Dale constant, $K(\lambda_{wf})$ in Equation 1, is dependent on the wavelength of the light wavefront^{39,40}, directly (although slightly) affecting the index of refraction. For example, air at 288 K has a Gladstone-Dale constant that drops from 2.33 m³/kg to 2.239 m³/kg as the wavelength increases from 356.2 nm to 912.5 nm.^{39,40} Therefore, *OPL* and *OPD* decrease as the wavelength of the wavefront increases.

Strehl ratio is a value that can explain whether or not a wavefront will be significantly distorted for a particular wavefront wavelength.⁶ The equation for Strehl ratio is shown in Equation 4 and $I(t)$ and I_0 are the maximum irradiance values with distortion (far-field) and without distortion, respectively.⁶

$$SR(t) = \frac{I(t)}{I_0} \quad 4$$

If the large-aperture approximation is used, then Equation 5 results ($OPD_{rms}(t)$ means spatial $OPD_{rms}(t)$).^{6,17} Ideal $SR(t)$ values are close to 1 and decrease as the wavefront wavelength decreases.

$$SR(t) = \exp\left(-\left(2\pi OPD_{rms}(t) / \lambda\right)^2\right) \quad 5$$

The directed energy source for the airborne laser project, for example, is a chemical oxygen-iodine laser (COIL), which has a wavelength of approximately 1315 nm⁶ (the Advanced Tactical Laser⁴¹⁻⁴³ is also a chemical oxygen-iodine laser). This wavelength is relatively short when compared with other lasers, such as a CO₂ laser which has a wavelength of approximately 10600 nm.⁶ Because the wavelength is shorter, Strehl ratio decreases and thus aero-optic distortion is not negligible for COIL lasers.⁶ This begs the question, why use a lower wavelength laser if a higher wavelength laser yields a Strehl ratio closer to 1 and therefore suffers from less distortion? The answer to this question is simple. The value of I_0 decreases as the wavelength increases, thus a happy medium must be reached where I_0 and $SR(t)$ are both maximized. Unfortunately, this means that wavefront wavelengths have to be used where aero-optic distortion is not negligible.

C. Wavefront Distortion: Aero-Optic Distortion and Atmospheric Propagation

Aero-optic distortion, in particular, applies to aberration/distortion that occurs close to the aperture which the wavefront passes through.⁶ For example, the aperture for a hemisphere is located on the surface of the hemisphere where density fluctuations, and thus distortions, begin. The planar beam/wavefront originates at a plane that passes through the centerpoint of the hemisphere (perpendicular to the beam propagation direction). Calculations of OPL begin at this plane as well, but distortions (resulting in differences in OPL , and thus OPD , from ray to ray) do not begin until one of the rays in the wavefront reaches the surface of the hemisphere. This is because the optical environment (i.e. index of refraction) inside the hemisphere is constant. Also, a hemisphere has a curved surface and the central portions of the wavefront travel longer physical distances

through the constant index region inside of the hemisphere before reaching the hemisphere surface than the outer edge portions of the wavefront. This naturally causes a decrease in *OPD* values at the central portion of the wavefront. Short geometric/physical path lengths for which *OPL* and *OPD* values are calculated denote the aero-optic distortion region.⁶ Longer geometric/physical path lengths for which *OPL* and *OPD* values are calculated denote atmospheric propagation regions.⁶ In principle, the longer geometric/physical paths are much larger than the aperture size and the shorter geometric/physical paths are on the order of the aperture size.⁶

D. Recent Aero-Optic Work and Research

Extensive aero-optic research has been performed recently. This work has included traditional aero-optic distortion measurement techniques, flow control attempts, flow visualization experiments, modeling efforts, and a non-traditional aero-optic distortion measurement technique using acetone PLIF.

Aero-optic distortion measurements have been obtained experimentally for turret flows. Gordeyev et al. (2007)^{7,8} investigated the aero-optic distortion of a hemisphere mounted on top of a cylinder/pedestal with a flat and conformal aperture/window. Time-resolved point measurements of distortion were made with a Malley probe and spatial distortion measurements were made with a Shack-Hartmann wavefront sensor. Additionally for the conformal window turret, flow visualization experiments were conducted, as well as high-bandwidth wavefront measurements. Distortion measurements were made for both turret designs. The azimuth angle was varied for both turrets (the same angles were not measured for both types of turrets). The elevation angle was varied for the conformal window turret, while the elevation angle was held

constant for the flat window turret. Mach numbers tested were different for the two types of turrets. The flat aperture/window aero-optic distortion data showed that for the conditions tested, the distortions increase with Mach number, freestream density, and azimuth angle. Conformal aperture/window data revealed that separation occurs later than for the flat window turret, but is not steady. The conformal aperture/window aero-optic distortion data is more random than the aero-optic distortion data for the flat window turret.

To go along with traditional wavefront measurements of turret flow fields, several flow control techniques have been investigated to mitigate the aero-optic distortion. Gordeyev et al. (2009)¹ and Vukasinovic et al. (2009)²⁷ investigated the use of suction/blowing jet actuators on turrets. The purpose of these actuators is to delay flow separation over the surface of the turret, which will enable larger backward facing angles for a laser beam to exit the turret with less aero-optic distortion. In addition, the purpose of these actuators is to dissipate and decrease downstream turbulence. These actuators decrease the near wake turbulent kinetic energy. Several backward facing angles and Mach numbers (0.3, 0.4, and 0.5) were investigated with different combinations of jet actuators and jet velocities. The OPD_{rms} was found through the use of a Malley probe and for the most part there was an improvement in the OPD_{rms} with the jet actuators as opposed to the same cases with no jet actuators. Other flow control techniques have been studied/attempted as well, such as work by Cain et al. (2008)²¹ that looked into fairing designs for turrets, coupled with aero-acoustics. For information on additional flow control techniques see Gordeyev and Jumper (2010).¹⁷

Modeling efforts have also been made in order to better characterize weakly compressible flows, in particular separated shear layer flows. The work of Jumper and Fitzgerald (2001)⁶, Fitzgerald and Jumper (2004)¹², and Jumper

(2006)¹³ established the Weakly Compressible Model that uses the unsteady Euler equations, least-squares fitting, the isentropic relationship between temperature and pressure, and the ideal gas law in an iterative process in order to find pressure, temperature, and density at all points in the flow from velocity field data. If the flow field is weakly compressible and time-resolved velocity data is known, then this model can be implemented. Rennie et al. (2008)¹¹ used the WCM and CFD (COBALT) to find the temperature, pressure, and density fields of the same velocity field (compressible, separated shear layer flow). As explained in Section I.A., it was found that there is agreement between the pressure fields, as seen in Figure 3, but the temperature and density fields differ, as seen in Figure 4.

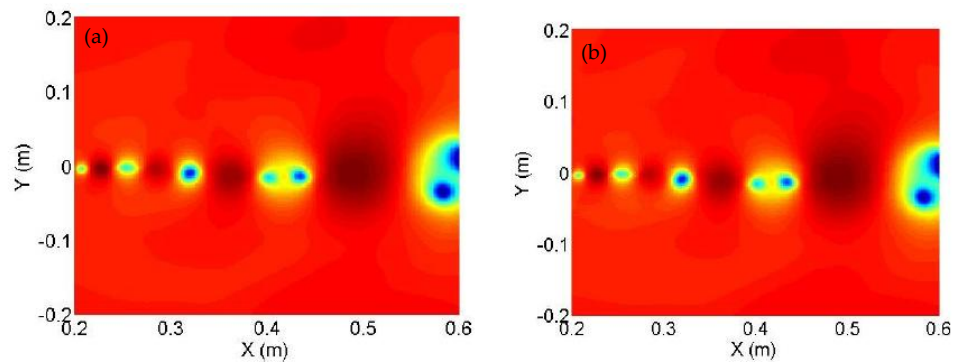
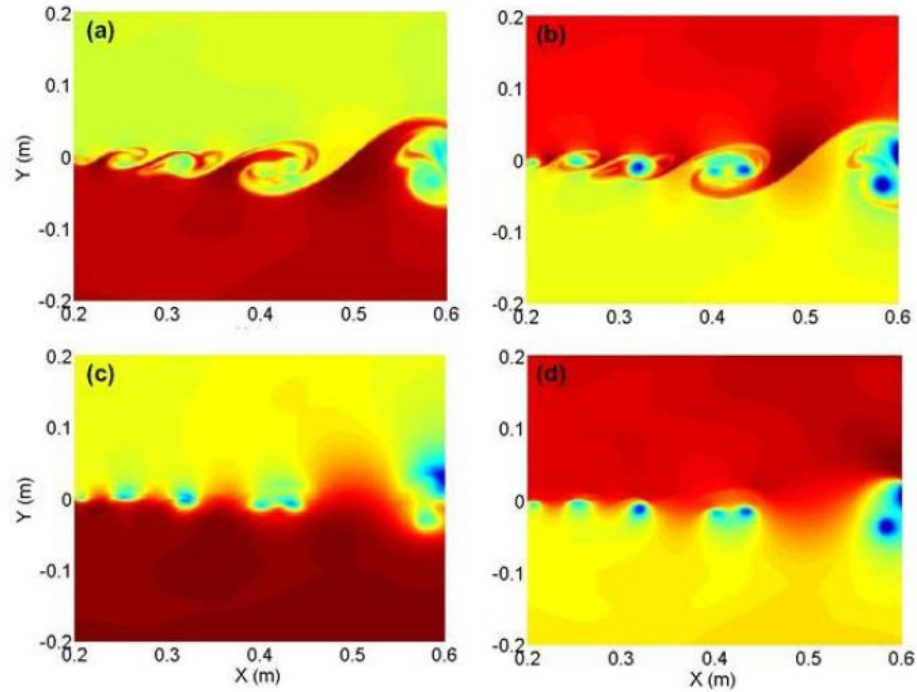


Figure 3: Calculated Pressure Field (a) CFD – COBALT (b) WCM [Rennie et al. (2008)¹¹]



**Figure 4: Calculated Static Temperature Field (a) CFD – COBALT (c) WCM
Calculated Density Field (b) CFD – COBALT (d) WCM [Rennie et al. (2008)¹¹]**

Also, as explained in Section I.A., aero-optic distortion calculations were made by Ponder et al. (2010)¹⁴ for WCM calculated density fields and CFD (COBALT) calculated density fields and compared to experimental aero-optic distortion measurements (*OPD*) of a similar flow field. It was found that the aero-optic distortion results from the CFD density fields did not agree very well with the aero-optic distortion results obtained experimentally and those calculated from the WCM density fields. However, the aero-optic distortion results obtained experimentally and those calculated from the WCM density fields were fairly similar.

In addition, during the process of developing the weakly compressible model, researchers developed new explanations for weakly compressible shear layer aero-optic behavior. For weakly compressible shear layers, researchers

propose that pressure changes are actually the main factor in creating density fluctuations (and thus distortions) as opposed to the traditional school of thought where differences in temperature are thought to be the main cause.^{6,12-13} The shear layer flow region possesses well-defined, rolling-up structures that have low pressure and thus low density cores. There are also regions of high density and high pressure that join these well-defined structures together. There is a great amount of curvature of the flow inside of these rolling-up structures and along with this curvature is a gradient in pressure. This gradient in pressure creates low pressure (and thus low density) cores.¹³ The density values (and thus indices of refraction) created by the WCM that are very low in value are seen to slowly and gradually transition to higher values as the distance from the center of these low density/low index value regions increases. There is not an abrupt change in density/index values in the WCM density results, as there is in the density results from CFD (COBALT).^{11,14} The density results of the work in this thesis enable the reader to develop their own conclusions on this debate or simply shed more light on this debate.

Aero-optic distortion of a compressible shear layer was investigated using acetone PLIF in the work of Catrakis et al. (2006)⁴⁴, Catrakis (2006)⁴⁵, and Catrakis (2004)⁴⁶. The index of refraction values for a compressible shear layer flow field (created from a freestream flow of acetone vapor/air interacting with stagnant air) were estimated with acetone PLIF and then calculation of interfacial fluid thickness values was straightforward. These two parameters, index of refraction and interfacial fluid thickness, were used to calculate the resulting aero-optic distortion (OPD and OPD_{rms}). A Shack-Hartmann wavefront sensor was also used to measure aero-optic distortion. Note that this technique to find index of refraction is flawed however. The acetone fluorescence is used to calculate the index of refraction. Acetone seeding is not uniform and thus there is no way to

decipher whether acetone fluorescence differences in each image are due to differences in local acetone mole fraction, differences in local values of pressure, temperature, and density, or both. This work and its flaws are explained in more detail in Section III.F.c.

The field of aero-optics has not only been investigated for hemisphere/turret flow fields and shear layers, but other flow fields as well. For example, in the work of Wyckam et al. (2003)⁴⁷, Shack-Hartmann wavefront measurements were used to study the aero-optic distortion of a Mach 2.4 flow past a wedge, a Mach 1 nitrogen jet, and a hypersonic (Mach 8) boundary layer.

III. Background of Acetone Planar Laser Induced Fluorescence

A. Description of Acetone PLIF Technique

Acetone PLIF is a non-intrusive flow diagnostic technique that can be used to obtain quantitative values of flow properties. Acetone molecules are seeded into the flow field and absorb ultraviolet light (UV laser sheet) that is passed through the flow field. A fraction of the acetone molecules fluoresce and the fluorescence is captured on a CCD. In general, and depending on application, this fluorescence can be used to find flow properties such as concentration/mixing, temperature, pressure, or convective velocity. In this work, however, the fluorescence at each point/pixel in the image was used to quantify the local density, enabling the entire density field of a high-velocity, compressible flow (the shear layer and turbulent wake of a hemisphere) to be quantified.

B. Photophysics/Characteristics of Acetone

Acetone is a chemical that was used as the tracer molecule in this work. It is made up of carbon, hydrogen, and oxygen in the form CH_3COCH_3 .⁴⁸ It has a high vapor pressure, so it can be seeded into air and evaporate quickly. Acetone has broadband absorption and fluorescence spectrums of 225-320 nm and 350-550 nm, respectively.^{48,49} The absorption peaks at 260-290 nm and the fluorescence peaks at 435 nm and 480 nm.^{48,49} The absorption is ultraviolet and the fluorescence is low-wavelength visible light that can be detected by a CCD. Acetone has short fluorescence and phosphorescence lifetimes of 5 ns and 200 μs ,

respectively.⁴⁹ Acetone phosphorescence is fully quenched in flow fields with relatively small partial pressures of oxygen⁴⁸⁻⁵⁴, eliminating the need for a gated camera when investigating these types of flow fields. Also, it has been shown that oxygen slightly quenches acetone fluorescence.^{48,50-51}

C. Fluorescence of Acetone

Acetone molecules are energized to a level of the S_1 first excited singlet state from the S_0 ground electronic state when they are excited by an absorption spectrum wavelength^{48,50,54}, as seen in Figure 5. In order to return to the ground electronic state, there are five possible events that the acetone molecules can experience (a combination of several of these is also possible). These events are fluorescence, relaxation through vibration, internal conversion, intersystem crossing to the triplet state, and collisional quenching.^{48,50,54} For more in-depth information on these five events, see Hartwig (2010)⁵¹. Relaxation through vibration takes the energy of the acetone molecules to a lower energy level within S_1 where any of the five de-excitation events can still occur. Internal conversion, collisional quenching, and fluorescence take the energy of the acetone molecules to the S_0 ground electronic state.⁵⁴ Acetone molecules that have intersystem crossing to the triplet state experience de-excitation events closely related to those in the singlet state.⁵⁴ However, instead of fluorescence, longer time-elapsd phosphorescence is experienced.⁵⁴

By having different events that can de-excite the acetone molecules in terms of their energy at multiple energy levels, the fluorescence of acetone molecules is broadband. If the excited acetone molecules move to a lower energy level within S_1 due to vibrational relaxation, for example, any of the five de-excitation events can occur to continue the de-excitation of the acetone

molecules. Fluorescence can occur at any moment and from any S_1 energy level while the acetone molecules are moving to lower and lower energy levels due to vibrational relaxation.

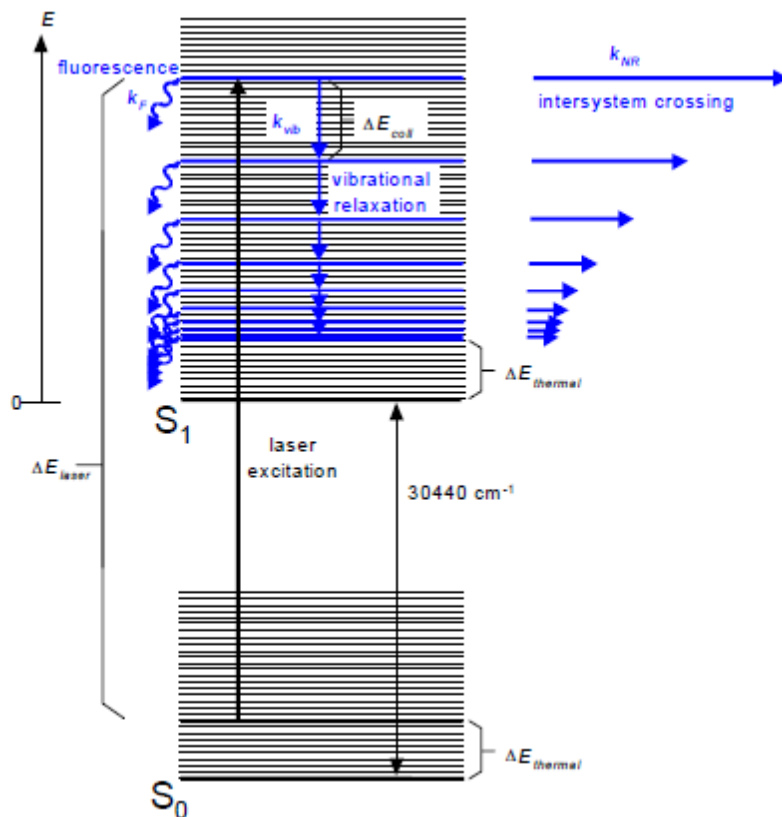


Figure 5: Excitation and De-Excitation of Acetone [Thurber (1999)⁴⁸]

D. Advantages and Disadvantages of Acetone

Acetone was chosen as the seeding particle for this work because it is relatively inexpensive, it is safe to humans, it has a high vapor pressure at standard atmospheric conditions, and it has a broadband absorption spectrum. Being inexpensive and safe to humans enables acetone PLIF to be used for high flow rate applications. The fact that acetone has a high vapor pressure at

atmospheric conditions is important because in this work the acetone was seeded in liquid form far upstream of the test section and had to evaporate before entering the test section. Having a broadband absorption spectrum in the ultraviolet is important because 266 nm light, the fourth harmonic of Nd:YAG, is rather easily obtained using a KDP or BBO crystal. Finally, acetone is well established in literature as a molecular tracer for PLIF and its photophysical behavior is well-characterized.⁴⁸⁻⁵⁴

Acetone for all of its advantages still has two main disadvantages. The first disadvantage is acetone is very corrosive to specific types of rubber and specific types of plastic. It corrodes rubber seals for example. Before using acetone in an experimental manner it is highly advised to consult a chemical properties sheet⁵⁵ which outlines materials that acetone corrodes and materials that acetone does not corrode. In this work, liquid acetone was injected in short bursts, so the wetted parts that the liquid acetone came into contact with were only exposed momentarily and then the acetone evaporated (i.e. these parts that were not compatible with acetone were not left to soak in liquid acetone for extended periods of time). In addition, most (but not all) of the wetted materials were either metal or were compatible with acetone. The second disadvantage is there is a limit to the acetone mole fraction. If too much acetone is injected into the flow field for a particular temperature (i.e. the acetone partial pressure is too high for a particular temperature), the acetone cannot fully evaporate or the acetone vapor cannot fully remain in the vapor state and will condense. At standard atmospheric conditions, the acetone vapor pressure is high, but as the temperature drops, so does the acetone vapor pressure. Thus, for very cold flow fields, care must be taken to determine an adequate acetone mole fraction that prevents condensation, while also reaching a maximum in fluorescence signal. In

this work, fully evaporated acetone in the flow field was a necessity in order to quantify density. Condensation is discussed in detail in Section VII.D.-E.

E. Comparison of Acetone to Other Flow Tracers

There are other flow tracers that have been used for PLIF experiments besides acetone. These tracers are either seeded into the flow field or they naturally exist in the flow field.⁴⁹ Lozano (1992)⁴⁹ performed extensive research into different flow tracers used for PLIF and although this work eventually centered upon biacetyl and acetone, discussion of other tracers is also provided. NO PLIF has been performed in the past by researchers, such as Danehy et al. (2006)⁵⁶. This tracer was determined to not be a possible tracer candidate for the work in this thesis for multiple reasons. First and foremost, NO is hazardous⁴⁹ and the work presented in this thesis involves high-flow rates, so large amounts of NO would have been too dangerous. In addition, the harmonics of Nd:YAG lasers were used in this work for excitation purposes (specifically 266 nm, the 4th harmonic). The harmonics of these lasers could not be used to excite NO as NO is excited by approximate wavelengths of 193 nm, 214 nm, 226 nm, 236 nm, and 248 nm.^{49,53} Finally, oxygen causes quenching of the fluorescence of NO.⁴⁹ The flow field in this work is mainly air and thus oxygen quenching of fluorescence would certainly exist.

Biacetyl was also determined to not be a possible tracer candidate for this work. Lozano explained that biacetyl is only a viable tracer for obtaining green phosphorescence data.⁴⁹ In addition, biacetyl has a phosphorescence lifetime that is long and it cannot be used as a tracer in flows that contain oxygen and flows that are not isothermal.⁴⁹ This work involves a flow field that is almost entirely dry air and is not isothermal. Based upon the characteristics of acetone explained

in Section III.B.,D., and E. and comparison to other PLIF flow tracers established in literature^{49,53}, acetone was chosen as the ideal flow tracer for this work.

F. Recent Acetone Photophysics and Acetone PLIF Work

The photophysics of acetone have been studied extensively in order to better understand and gauge the viability of acetone as a flow tracer in flow diagnostic experiments. In addition to this research into photophysical behavior, acetone PLIF experiments have been performed in multiple flow fields to investigate temperature, concentration/mixing, convective velocity, and index of refraction fields. The information presented here is meant to show the reader that acetone PLIF is a widely used flow diagnostic technique and to provide the reader with a frame of reference, so they can truly appreciate the work presented in this thesis with acetone PLIF and its contribution to previous work.

a. Acetone Photophysics Work

A large portion of acetone PLIF research has been performed at Stanford University, such as modeling work and experimental work with the PLIF of acetone and other flow tracers. Thurber (1999)⁴⁸ developed a fluorescence quantum yield (ϕ) model for acetone based upon personal research and past research of others that takes into account excitation wavelength, temperature, pressure, and type of bath gas. Thurber performed flow cell measurements where fluorescence signal and absorption cross-section data for acetone in a nitrogen bath gas were obtained for different excitation wavelengths and temperatures at a constant pressure of 1 atm. Fluorescence quantum yield data was calculated from the fluorescence signal and absorption cross-section data.

Thurber also performed static gas cell measurements where absorption cross-section and fluorescence signal data were obtained for acetone in multiple bath gases while the temperature was held constant (297 K, room temperature) and the pressure and excitation wavelength were varied.⁴⁸ The fluorescence quantum yield model was optimized to fit the data from literature and the data from the static and flow cell experiments.⁴⁸ Note that Thurber's absorption cross-section versus temperature data for 266 nm was extrapolated/interpolated for specific temperature values in the work presented in this thesis.

Thurber's final fluorescence quantum yield model is based upon the fluorescence quantum yield equation, seen in Equation 6⁴⁸. The terms in this equation are the de-excitation rates of k_{NR} (rate of non-radiative relaxation/rate of intersystem crossing), k_f (rate of fluorescence), k_{coll} (rate of collision), and k_{O_2} (rate of oxygen quenching). This model is a multi-step decay model that uses probability to determine the fluorescence quantum yield. Thurber (1999)⁴⁸ provides a source code (C++) for a simpler version of the final fluorescence quantum yield model where pressure, temperature, and excitation wavelength are inputs and the fluorescence quantum yield is the output. In this original source code, k_{coll} is only calculated for acetone in a nitrogen bath gas and the k_{O_2} term is not included. However, Thurber outlines steps to modify the bath gas, including the addition of the de-excitation term k_{O_2} if the bath gas contains oxygen.

$$\phi = \frac{k_f}{k_f + k_{coll} + k_{NR,1} + k_{O_2}} + \sum_{i=2}^{N-1} \left(\frac{k_f}{k_f + k_{coll} + k_{NR,i} + k_{O_2}} \prod_{j=1}^{i-1} \left[\frac{k_{coll}}{k_f + k_{coll} + k_{NR,j} + k_{O_2}} \right] \right) + \frac{k_f}{k_f + k_{NR,N} + k_{O_2}} \prod_{j=1}^{N-1} \left[\frac{k_{coll}}{k_f + k_{coll} + k_{NR,j} + k_{O_2}} \right] \quad 6$$

In Thurber's work, the acetone mole fraction was very small and the bath gas mole fraction was approximately 1.^{48,50} Thus, the fluorescence quantum yield model assumes that the bath gas mole fraction is also approximately 1.^{48,50} This

enabled Thurber to model collision frequency, a component of k_{coll} , in the fluorescence quantum yield model with a Lennard-Jones potential. The Lennard-Jones potential is typically used to calculate collision frequency between non-polar molecules. Acetone is a polar molecule and thus the Stockmayer potential should technically be implemented in the current model instead of the Lennard-Jones potential when modeling collisions between acetone molecules in order to include the dipole moment⁴⁸ (Stockmayer potential is similar to the Lennard-Jones potential, except dipole interactions are not included in the Lennard-Jones potential as they are in the Stockmayer potential^{48,57}). However, for low acetone mole fraction applications, such as in Thurber's work, the Lennard-Jones potential and Stockmayer potential yield similar results, in terms of collision frequency, within a few percent.⁴⁸ Thurber explains the reasoning for using Lennard-Jones in this model instead of Stockmayer potential in much greater detail in Thurber (1999)⁴⁸. Also, for collisions of the bath gas molecules (non-polar) with acetone molecules (polar), the calculated terms for molecule collision diameter and collision potential energy in the current model should be updated to include the dipole moment⁴⁸ (these parameters do not need to be modified for collisions between polar acetone molecules). The equations and variables for updating these terms are clearly presented in Hirschfelder et al. (1954)⁵⁷. Note that additional information on Lennard-Jones potential and Stockmayer potential can be found in Reid et al. (1977)⁵⁸, Brokaw (1969)⁵⁹, Mourits and Rummens (1977)⁶⁰, and Troe (1977)⁶¹.

The work presented in this thesis conveniently used a small acetone mole fraction, approximately 3%, and thus Thurber's current model was assumed to be valid in this regard and the above changes listed in the previous paragraph were not necessary. If the acetone mole fraction was higher, then the changes to the current model (explained in the previous paragraph) would have been much

more necessary. Note that the accuracy of the acetone mole fraction that is physically input into the current model is not extremely important, as long as it is small. This is because under the current model, the normalized fluorescence quantum yield (i.e. normalized by fluorescence quantum yield at freestream conditions) does not significantly change as the acetone mole fraction is changed. This is most likely due to the limitations of the current model that are explained in the previous paragraph.

Photophysical work with acetone has also been conducted at other universities/research facilities to test Thurber's model under different conditions and to offer improvements to the model. Hartwig (2010)⁵¹ performed laboratory experiments to test Thurber's fluorescence quantum yield model at high pressure and temperature conditions. Based upon these experiments and results, which were performed for an excitation wavelength of 282 nm, Hartwig modified Thurber's model, so it better fit his data and other data established in literature (for excitation wavelengths in addition to 282 nm), including Thurber's original data. Tran (2008)⁵⁰ investigated the photophysics of acetone vapor, as well as the photophysics of liquid acetone. Tran tested the validity of the fluorescence quantum yield models of Thurber (1999)⁴⁸ and Braeuer et al. (2006)⁶² at high pressure and temperature values. Bryant et al. (2000)⁵² performed static gas cell measurements to test the behavior and sensitivity of the acetone fluorescence signal at low temperature and low pressure values. The pressure and temperature values tested were from 0.1-1atm and 240-295 K, respectively.

Researchers have updated variable values in Thurber's model and suggestions have been made in order to improve Thurber's original model or in order to modify it to fit specific experimental data.^{51,62-63} The reader should keep in mind that Thurber's model is not perfect and it can be improved (as explained previously in this subsection). With that being said, the work presented in this

thesis was not specifically about the photophysics of acetone or other flow tracers for PLIF, as an entire dissertation can comprise that sort of work (see Lozano (1992)⁴⁹). Instead this work was about testing the validity of using acetone as a flow tracer for a flow diagnostic technique (PLIF) that would enable density field calculations in a high-velocity, compressible flow field. Therefore, Thurber's fluorescence quantum yield model in its original form in Thurber (1999)⁴⁸ was used, with the only modifications being bath gas type (dry air as opposed to nitrogen and addition of an oxygen quenching term k_{O_2}) and acetone mole fraction. The C++ code was also modified, so it would execute in MATLAB. More information on Thurber's model and application to this work is presented in Section IV.C.

b. Temperature, Concentration/Mixing, and Convective Velocity Measurements with Acetone PLIF

As photophysical work with acetone has progressed, so have the acetone PLIF experiments and their use as flow diagnostic tools. Thurber (1999)⁴⁸ showed the viability of acetone PLIF to obtain temperature field data for the flow over a heated cylinder and the flow of a heated jet subject to a cross-flow. The cylinder was very small in scale ($D = 3$ mm) and the flow was very slow ($Re=6$). At 248 nm excitation, quality fluorescence images were obtained and converted to temperature data, as seen in Figure 6. For the heated jet in cross-flow experiments, the jet and cross-flow had the same uniform acetone mole fraction and pressure and only the temperature varied. Fluorescence images of this flow field were obtained with initial excitation of 266 nm and were converted to temperature data, as seen in Figure 7.

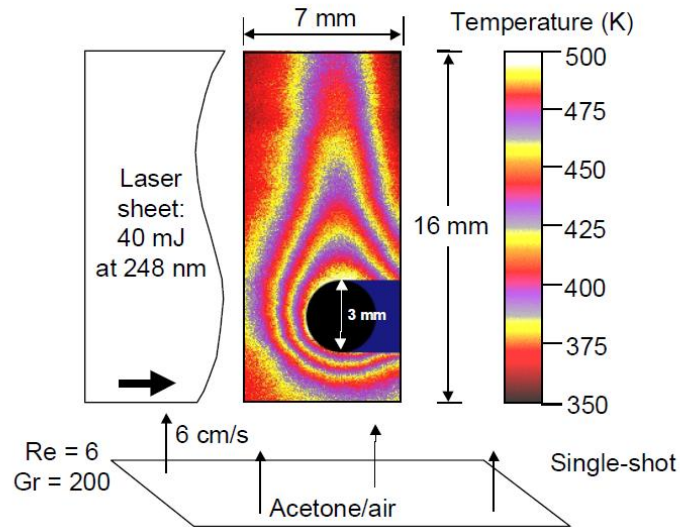


Figure 6: Temperature Field for Flow Over Heated Cylinder [Thurber (1999)⁴⁸]

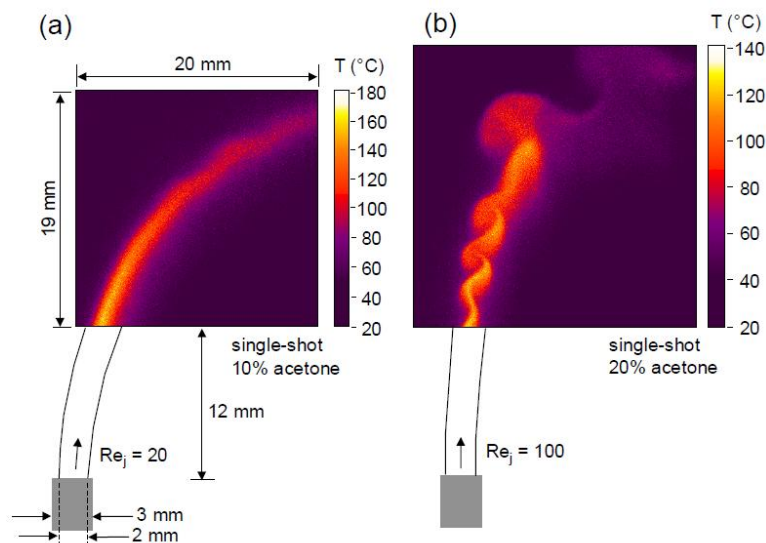


Figure 7: Temperature Field of Heated Jet in Cross-Flow (a) $Re=20$ (b) $Re=100$ [Thurber (1999)⁴⁸]

Thurber also introduced a technique of using two excitation wavelengths (248 nm and 308 nm, although 266 nm and 308 nm could also be used) and using the resulting fluorescence images at each excitation wavelength to yield final results

of temperature and pressure data (if acetone mole fraction is uniform) or temperature and acetone mole fraction data (if pressure is uniform).⁴⁸ Additional work of note is the work of Kearney and Reyes (2003)⁶⁴ who used acetone PLIF to investigate the temperature fields created by Rayleigh-Bénard convection between a hot and cold plate.

In addition to temperature measurements with acetone PLIF, concentration/mixing experiments have also been performed. Nygren et al. (2002)⁶⁵ successfully performed 3-D acetone LIF (acetone mixed with ethanol) to study fuel location and concentration in an HCCI (homogenous charge combustion ignition) engine. Information about the combustion can be drawn from this data. Choi et al. (2002)⁶⁶ used acetone PLIF (excitation $\lambda=280\text{nm}$) to study fuel/air mixing in a non-premixed vortex ring, as seen in Figure 8. Acetone vapor and propane were mixed in a reservoir and then a speaker created the vortex ring.

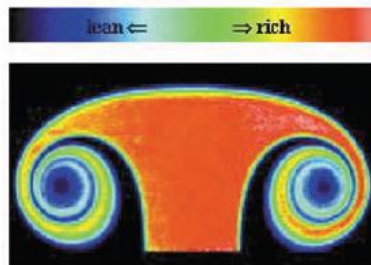


Figure 8: Acetone PLIF Image of Vortex Ring Mixing of Fuel/Air [Choi et al. (2002)⁶⁶]

The amplitude of the speaker was varied and the mixing of fuel and air in the inner ring of the vortex ring was affected. It was found that lower amplitude values resulted in greater mixing of fuel and air in the inner ring of the overall vortex ring. The temporal characteristics of the vortex ring were also investigated

(Schlieren and acetone PLIF) and diameter of the inner ring of the overall vortex ring was found to grow over time, as seen in Figure 9. Also, mixing increased throughout time.

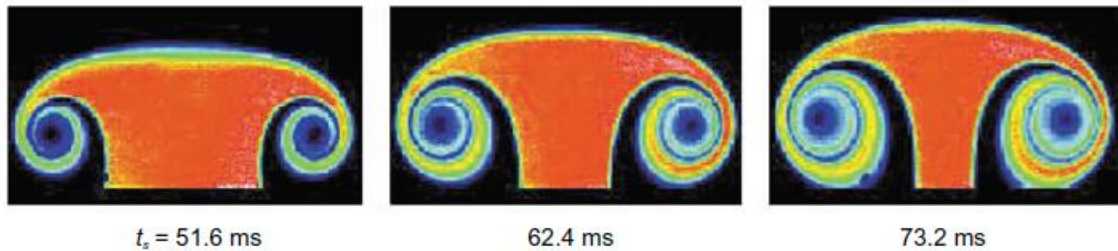


Figure 9: Temporal Acetone PLIF Images of Vortex Ring Mixing [Choi et al. (2002)⁶⁶]

Propagation of a flame through the vortex ring was also investigated and it was concluded that the stoichiometric region, the low intensity core region of Figure 10(a), of the inner ring of the overall vortex ring is where the flame passed through. The flame intensity structure is seen in Figure 10(b).

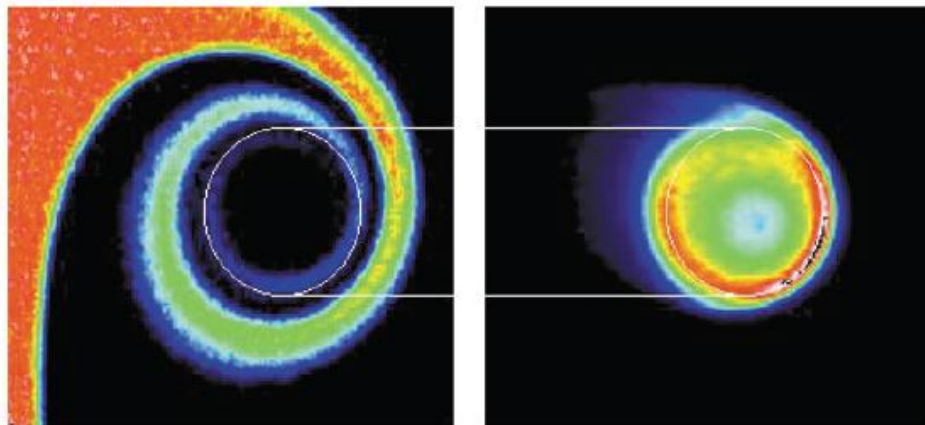


Figure 10: Vortex Ring Flame Propagation (a) Acetone PLIF Image of Vortex Ring Mixing Structure (b) Direct Image of Intensity of Propagating Flame [Choi et al. (2002)⁶⁶]

Convective velocity measurements of eddies of a Mach 1.5 jet have also been performed by Murakami and Papamoschou (2000)⁶⁷ using acetone PLIF and a 2-D cross-correlation technique.

c. Aero-Optic Measurements with Acetone PLIF

Acetone PLIF has also been used in aero-optics research by Catrakis et al. (2006)⁴⁴, Catrakis (2006)⁴⁵, and Catrakis (2004)⁴⁶, introduced in Section II.D. In this particular research, acetone PLIF was used to investigate compressible shear layers and resulting aero-optic distortion. The shear layer is created by an inlet line which blows air/acetone vapor (acetone that has been evaporated in air) through a test section that is full of stagnant air (with no acetone vapor present). An abrupt, vertical drop in the inlet wall creates a sharp 90° edge on which shear layer formation can begin and where the two fluids first start mixing together. When the two fluids mix together in the shear layer, portions of fluid A (air/acetone vapor) are folded into fluid B (stagnant air) and vice versa, but full mixing and uniform seeding is not achieved. In the regions where fluid A (air/acetone vapor) and fluid B (stagnant air) have no mixing, constant/uniform index of refraction values (n_A and n_B , respectively) are present. A 266 nm laser sheet is passed through this shear layer region and the resulting fluorescence is captured.

Catrakis' work assumed that the resulting local fluorescence in the mixing regions can be directly related to local index of refraction by scaling the resulting local fluorescence relative to the constant fluorescence values of fluid A and fluid B, for which the index of refraction values n_A and n_B are known. Fluorescence of the constant index of refraction sections of the flow field can be seen in the solid blue and white sections in Figure 11(a). From the index of refraction values, the

interfacial fluid thickness values are calculated, as seen in Figure 11(b), and together with the index of refraction values are used to calculate aero-optic distortion (OPD and OPD_{rms}). Aero-optic distortion is also measured with a Shack-Hartmann wavefront sensor.^{44,45} For additional work by Catrakis see Catrakis et al. (2002)⁶⁸ and Dimotakis et al. (2001)⁶⁹.

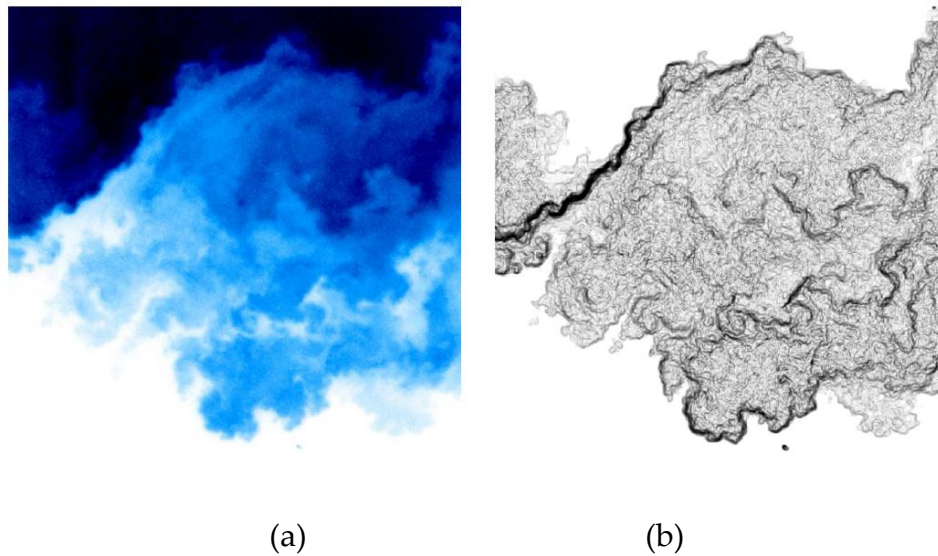


Figure 11: Image of Compressible Shear Layer (a) Index of Refraction Field (b) Interfacial Fluid Thickness Field [Catrakis et al. (2006)⁴⁴]

While this acetone PLIF technique is fundamentally similar to the work in this thesis, its implementation in order to find the index of refraction field is flawed. This is because the estimation of index of refraction values in the shear layer relies upon the fluorescence of acetone in this region. In general, the acetone fluorescence signal, thoroughly explained in Section IV.A., is directly affected by acetone mole fraction and the local values of pressure, temperature, and density. In the mixing regions, the mole fraction is not necessarily constant and unless some sort of simplifying assumptions were made by Catrakis, there is

no way to decipher whether fluorescence is spatially and temporally changing due to acetone mole fraction, or local values of pressure, temperature, and density, or both. Because Catrakis still extracts index of refraction data from the fluorescence images, it can reasonably be assumed that local pressure and local temperature (and thus local density) effects on acetone fluorescence are being neglected, at least in the instantaneous sense. This would mean that Catrakis is assuming differences in fluorescence are due to mixing only.

Statistically speaking, pressure in the shear layer is relatively constant. However, in the instantaneous sense, deep pressure cores can occur due to strong vortices in the shear layer. As explained in Section II.D., pressure has been suggested to be the main cause of density changes and thus aero-optic distortion in compressible, separated shear layers.^{6,12-13} Catrakis is attempting to use this technique to calculate aero-optic distortion. The true measure of aero-optic distortion is not the steady, average distortion, but the unsteady, instantaneous distortion resulting from instantaneous local density changes (local pressure, local temperature, or both) and thus instantaneous local index of refraction changes. Instantaneous pressure and temperature (and thus density) must be taken into account and in doing so the argument that fluorescence in the shear layer (mixing region) is purely due to mixing loses its validity.

The work in this thesis solved this problem by achieving uniform acetone seeding through liquid injection of acetone far upstream of the imaging region. This allowed the liquid acetone ample time to mix with dry air and evaporate before entering the imaging region. Fluorescence changes throughout the imaging region, after image processing and in-situ calibration explained in Section IV.B., could then be purely attributed to changes in the local values of pressure and temperature (and thus density).

IV. Acetone PLIF for Direct Density Measurements

As shown in the previous section, acetone PLIF has been used for multiple flow diagnostic purposes, but the work presented in this thesis extended this work to allow for direct density measurements of a high-velocity, compressible flow field.

A. Acetone Fluorescence Signal Equation

Acetone fluorescence signal, S_f , in collected photons is quantified by the acetone fluorescence signal equation, seen in Equation 7⁴⁸. Most of the terms in this equation are constants for this work, including h (Planck's constant), c (speed of light), λ (wavelength of excitation), dV_c (collection volume), $\chi_{acetone}$ (acetone mole fraction), and k (Boltzmann's constant). The acetone mole fraction is constant because acetone is injected in liquid form far upstream of the test section and has ample time to fully mix with the dry air it is being injected into before entering the test section. This is different from acetone PLIF experiments used for mixing studies⁶⁶, for example, where acetone mole fraction is not constant. By having a constant acetone mole fraction, changes in fluorescence signal can be directly attributed to changes in physical density (i.e. temperature and pressure) as opposed to number density/concentration.

$$S_f = \frac{E}{hc/\lambda} \eta_{opt} dV_c \left[\frac{\chi_{acetone} P}{kT} \right] \sigma(\lambda, T) \phi(\lambda, T, P, \sum \chi_i) = CE \eta_{opt} \rho \sigma(T) \phi(T, P) \quad 7$$

The non-constant terms in Equation 7 are E (local laser fluence), η_{opt} (optical collection efficiency), P (local pressure – total of acetone and air partial pressures), T (local temperature), σ (absorption cross-section), and ϕ (fluorescence quantum yield). Optical collection efficiency is temporally, but not

spatially constant because the solid collection angle, which along with transmission efficiency makes up the optical collection efficiency, varies throughout an image. Local laser fluence is not constant throughout the imaging region because the ultraviolet laser sheet (used for excitation purposes) spreads outwardly as it propagates through the imaging region, resulting in drops in laser sheet intensity along lines of constant angle (relative to a virtual origin). Also, the laser sheet intensity profile is roughly Gaussian and thus the greatest energy is located at the center of the laser sheet.

Laser sheet non-uniformity, due to non-constant laser fluence throughout the imaging region, causes differing 266 nm energy values to excite the acetone molecules throughout the imaging region. This results in changes in fluorescence signal values throughout the imaging region purely due to excitation energy differences and not necessarily due to differences in local values of density, temperature, or pressure. This is compounded by non-constant optical collection efficiency throughout the imaging region (a type of vignetting characterized by COS^4 drops in intensity, as distance from the center of the image is increased, results when this fluorescence signal is collected by a CCD). The image intensity in regions where it should be approximately constant, such as the freestream where conditions of ρ_∞ , T_∞ , and P_∞ are approximately constant, is not constant as a result. As locations away from the freestream region are investigated, such as the wake region, conditions of ρ , T , and P are not constant, causing additional changes in fluorescence signal values. The effects from COS^4 vignetting and laser sheet non-uniformity must be corrected throughout the image. Otherwise there is no way to decipher whether the drops in fluorescence signal throughout the image are due to changes in density, temperature, and pressure, COS^4 vignetting effects, laser sheet non-uniformity, or a combination of these factors.

B. Image Processing and In-Situ Calibration

In order to deduce the fluorescence signal at each point/pixel in an acetone PLIF image down to a density value, an image processing procedure must be performed which involves an in-situ calibration. This procedure is designed to correct for background noise, COS^4 vignetting, high intensity particles, and laser sheet non-uniformity, as well as normalize the intensity at each point/pixel in the image to the average freestream intensity of the image, as seen in Figure 12.

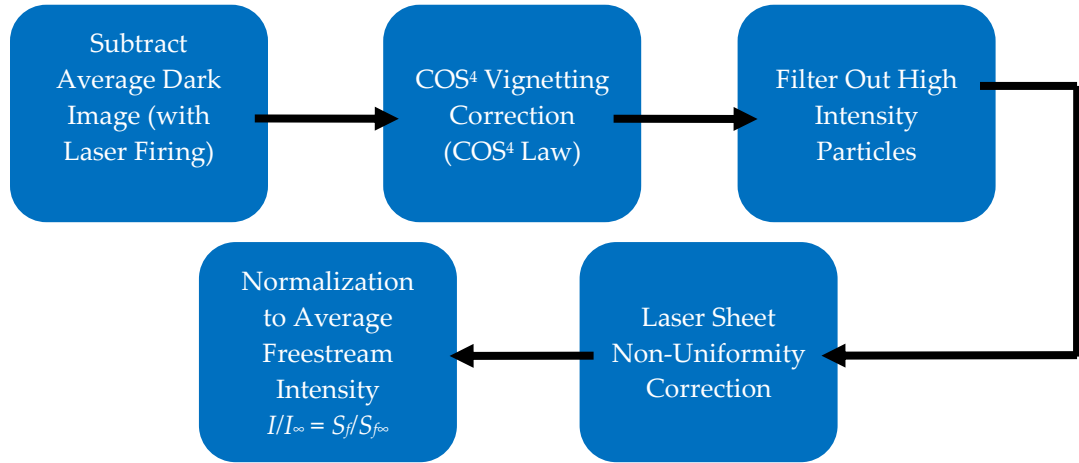


Figure 12: Flow Chart of Image Processing and In-Situ Calibration Procedure

Images in the form of $I_f/I_{f_\infty}=S_f/S_{f_\infty}$ are the result of this procedure. When Equation 7 is normalized by a value representing freestream conditions, Equation 8 results and is a mathematical relationship for S_f/S_{f_∞} that can be applied to images that are in the form S_f/S_{f_∞} .

$$\frac{S_f}{S_{f_\infty}} = \frac{\rho \sigma(T) \phi(T, P)}{\rho_\infty \sigma(T_\infty) \phi(T_\infty, P_\infty)} = \frac{\rho \sigma(T) \phi(T, \rho R T)}{\rho_\infty \sigma(T_\infty) \phi(T_\infty, \rho_\infty R T_\infty)} = \frac{\rho \sigma\left(\frac{P}{\rho R}\right) \phi\left(\frac{P}{\rho R}, P\right)}{\rho_\infty \sigma\left(\frac{P_\infty}{\rho_\infty R}\right) \phi\left(\frac{P_\infty}{\rho_\infty R}, P_\infty\right)} \quad 8$$

a. Dark Image Subtraction, COS^4 Vignetting Correction, and Filtering of High Intensity Particles

The image processing and in-situ calibration procedure begins with average dark image subtraction, COS^4 vignetting correction, and filtering out high intensity particles. An example acetone PLIF raw image is shown in Figure 13. For clarification purposes, as the steps of the image processing and in-situ calibration procedure are explained throughout this subsection, this example acetone PLIF raw image will be referred to as Example Image Z. Note that Example Image Z is flipped in Figure 13 to be in a traditional left to right flow convention (although raw images were actually obtained in a right to left flow convention), so the reader can easily compare this raw image to the final processed/calibrated image in the form $I_f/I_{f\infty}=S_f/S_{f\infty}$.

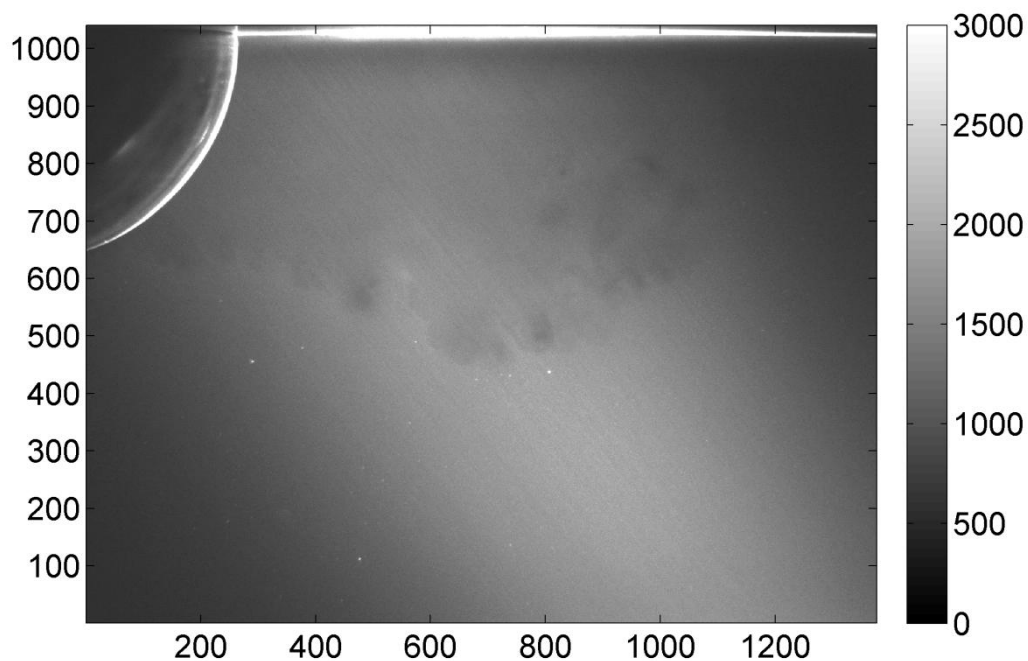


Figure 13: Example Acetone PLIF Raw Image (i.e. Example Image Z)

An average dark image is subtracted from each acetone PLIF raw image to eliminate background noise in the signal, as seen in Figure 14. The average dark image is calculated from a set of dark images obtained with the 266 nm laser sheet firing into the test section (no acetone injection and no flow).

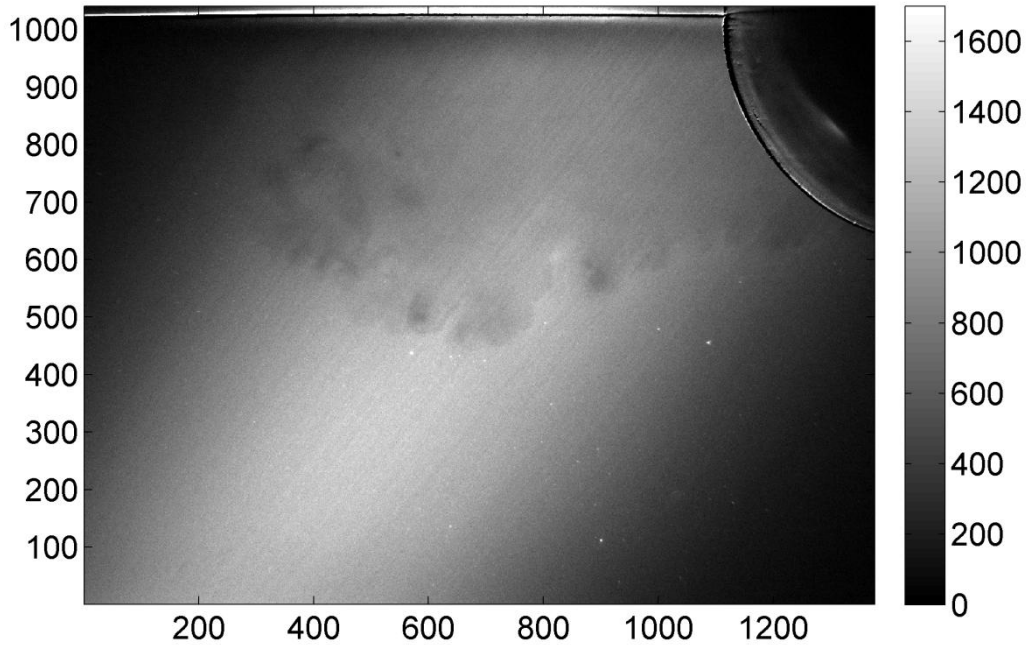


Figure 14: Example Image Z After Average Dark Image Subtraction

Next, a COS^4 vignetting correction is applied to each image. Light intensity in an image decreases as the distance from the center of the image is increased. This decrease in light intensity follows the COS^4 Law⁷⁰⁻⁷⁵ and based upon this law, correction coefficients are created for and applied to each point/pixel in an image to correct for this vignetting effect, as seen in Figure 15. An average flat field correction image (i.e. an average PLIF image with no hemisphere mounted) is the best means to correct for COS^4 vignetting (and laser sheet non-uniformity), however flat field images were not obtained in this work immediately before or

after these acetone PLIF images (with the hemisphere mounted) were obtained. Thus, the COS^4 Law correction coefficient method had to be implemented. Note that other forms of vignetting may also occur in the images during image acquisition.^{70,72} For example, rays of light near the edges of the object may be physically prevented from reaching the CCD^{70,72}, resulting in corresponding dark regions near the edges of the images. However, there is no post-processing correction to account for this. Conveniently, the most pertinent information in the acetone PLIF images is located near the center of the images where this type of vignetting is not a problem (COS^4 vignetting is also minimal near the center of the images).

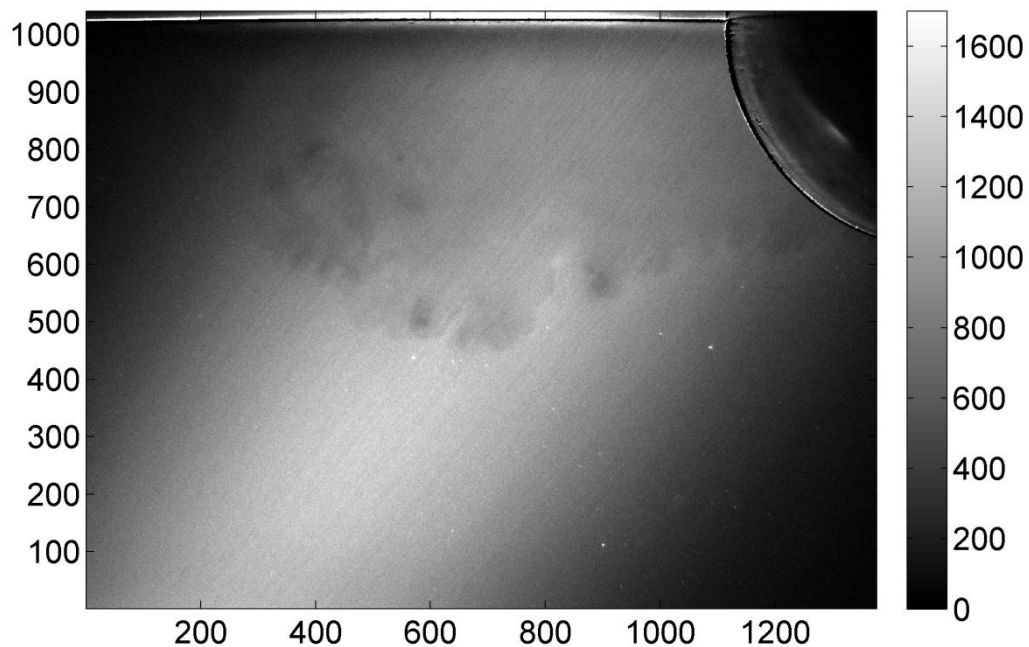


Figure 15: Example Image Z After Vignetting Correction

Also, note that the camera was slightly tilted downward at a small angle during image acquisition, as explained in Section IX.A.c., in order to decrease

noise from the top wall of the wind tunnel test section. This tilt was not accounted for or corrected for with the COS^4 vignetting correction or with any other form/correction during image processing. The ruler image was obtained in a vertical orientation, similar to the orientation of the laser sheet, so the tilted camera technically caused slight magnification changes in the image. However, these effects were assumed to be minimal.

After the COS^4 vignetting correction, high-intensity particles, if any, are filtered out of the images. These particles are infrequent (most likely dust or rust), but when they pass through the flow field they fluoresce and/or scatter fluorescing light. This creates infrequent bright dots/spots in some of the images, which if not eliminated or mostly eliminated can affect the laser sheet non-uniformity correction (explained in the next paragraph). The filtering procedure eliminates some or all of these particles by setting the intensity value of the pixel where the particle is located (and close proximity neighboring pixels) to the average intensity of a group of neighboring pixels, as seen in Figure 16. However, a large number of particles remained in some images after the filtering procedure.

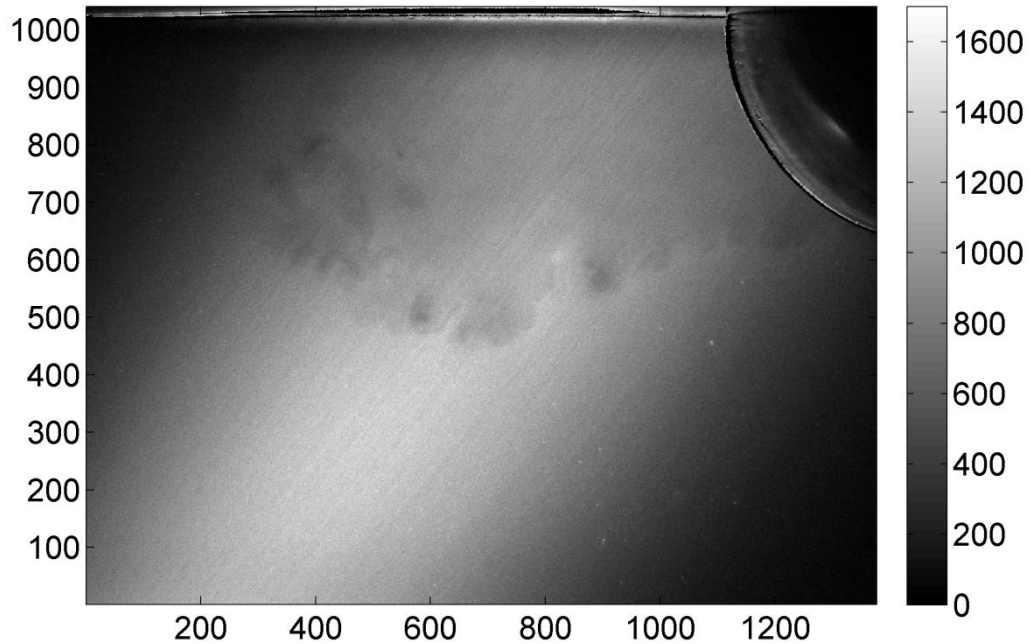


Figure 16: Example Image Z After Filtering Out High-Intensity Particles

The inability to filter all of the particles from an image can most likely be attributed to the fact that the laser sheet profile is roughly Gaussian. Some particles located on the edges of the laser sheet scatter light with only as much intensity as the fluorescing acetone molecules at the center of the laser sheet. Thus, in order to filter out these particles on the edges of the laser sheet, the threshold intensity value (above which a pixel's intensity value is set to an average intensity value of nearest neighboring pixels) has to be set to a value close to the fluorescence intensity of the molecules in the center of the laser sheet. This causes a large number of pixels in the center of the laser sheet to be set to an average intensity value of nearest neighboring pixels, creating an image that looks somewhat smeared in the center. Therefore, this method is not implemented and instead the threshold intensity value is set as low as possible while still being greater than the fluorescence intensity of the molecules in the

center of the laser sheet. Some particles are also very large and the filtering technique does not filter all traces of the particle.

b. Laser Sheet Non-Uniformity Correction

Laser sheet non-uniformity correction is the next step in the in-situ calibration. This correction accounts for laser intensity drops along lines of constant angle relative to the virtual origin, as will be explained below, and the fact that the laser sheet intensity profile is roughly Gaussian. The laser sheet appears trapezoidal in the imaging region because it propagates and spreads from a virtual origin outside of the imaging region. Every point/pixel in each image (x_{ij} and y_{ij}) has a radial distance (R_{ij}) and angle (θ_{ij}) value relative to this virtual origin. Equation 9 is used to calculate R_{ij} and Equation 10 is used to

10

calculate θ_{ij} . Note that x_o and y_o are the distances from the virtual origin to the bottom left corner of the imaging region, as seen in Figure 17.

$$R_{ij} = \sqrt{(x_o + x_{ij})^2 + (y_o + y_{ij})^2} = \sqrt{X_{ij}^2 + Y_{ij}^2} \quad 9$$

$$\theta_{ij} = \text{Tan}^{-1}\left(\frac{y_o + y_{ij}}{x_o + x_{ij}}\right) = \text{Tan}^{-1}\left(\frac{Y_{ij}}{X_{ij}}\right) \quad 10$$

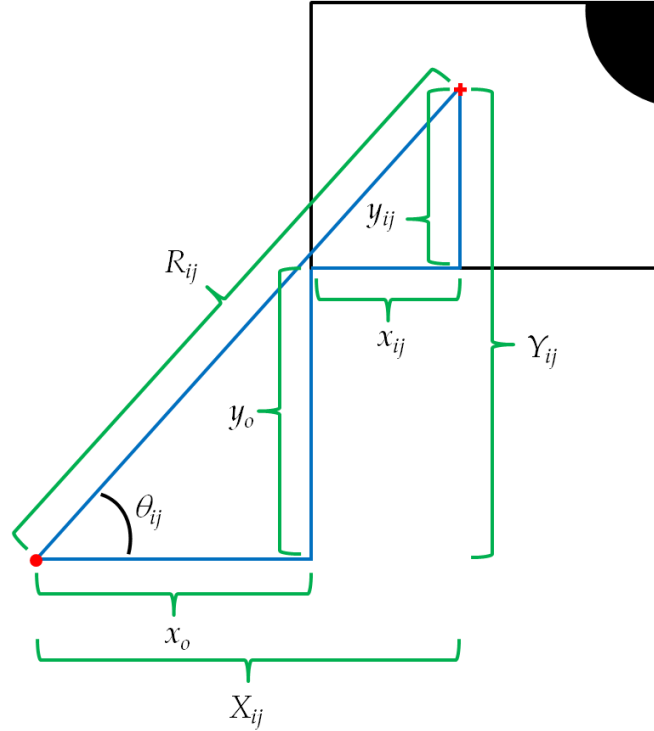


Figure 17: Angle θ_{ij} and Radial Distance R_{ij}

As the laser sheet propagates and spreads from the virtual origin, it is assumed that any drops in laser sheet intensity ($I_{Laser,ij}$) along lines of constant θ_{ij} (relative to the virtual origin), which subsequently result in drops in fluorescence signal and thus fluorescence intensity (I_f), are proportional to R_{ij} ($I_{Laser,ij} \propto \frac{1}{R_{ij}}$).

Drops in laser intensity due to absorption by acetone molecules throughout the test section are assumed to be negligible in this work because the acetone mole fraction is low ($\approx 3\%$). To correct for these drops in laser intensity along lines of constant θ_{ij} , the pixel intensity (i.e. fluorescence intensity I_f) of each point/pixel in the image is multiplied by its corresponding radial distance R_{ij} from the virtual origin. This makes the laser sheet intensity constant along lines of constant θ_{ij} , as seen in Figure 18. However, before the laser sheet non-uniformity correction is

complete, corrections have to be made to account for the laser sheet intensity profile being roughly Gaussian.

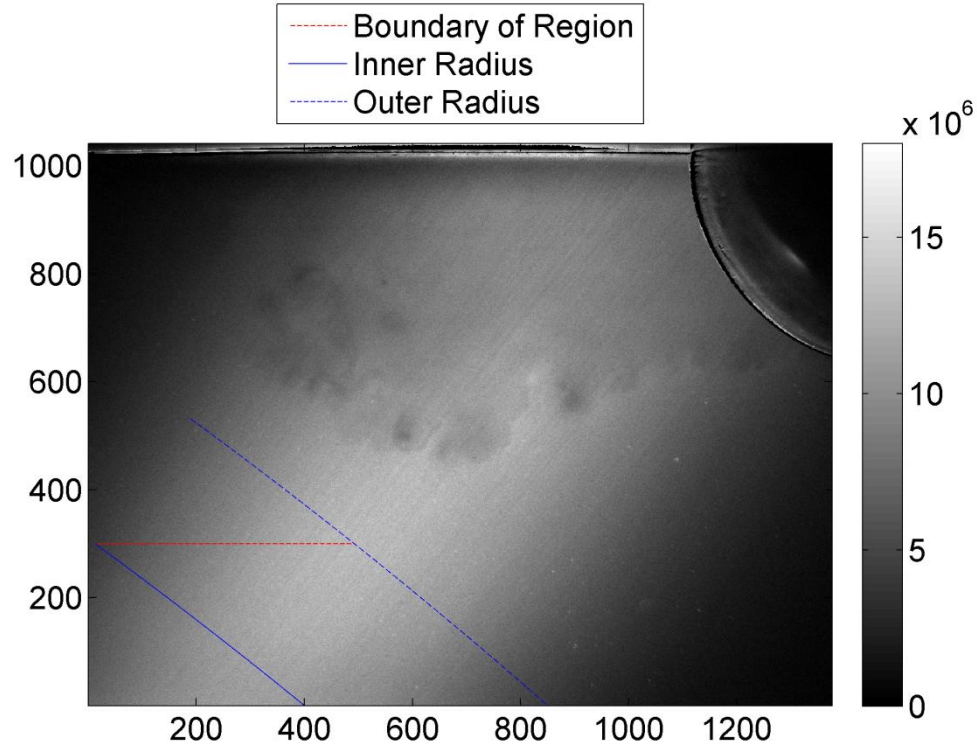


Figure 18: Example Image Z After Correction for Drops in Laser Intensity Along Lines of Constant θ_j

Fluorescence intensity values in the freestream region were used to establish conversion factors versus θ_j that could be used to make the intensity profile of the laser sheet roughly constant as opposed to roughly Gaussian. As stated previously, conditions of ρ_∞ , T_∞ , and P_∞ are assumed constant in the freestream and thus fluorescence signal should be constant as well in this region. However, this is not the case, as clearly seen in Figure 18, and the only reason is because the laser sheet intensity profile is roughly Gaussian. After the previous steps in the in-situ calibration were completed, fluorescence intensity values in

the freestream region were 2-D interpolated along arcs of constant radius R_{ij} for a constant set of θ_{ij} values. The boundaries of these arcs and angles can be seen in Figure 18, where the area enclosed by the red and blue lines is the region of these intensity values. The interpolated intensity values for Example Image Z can be seen in Figure 19, where the sample value on the y-axis corresponds to increasing R_{ij} and the sample value on the x-axis corresponds to increasing θ_{ij} .

The interpolated intensity values were averaged (excluding zero values) for each constant θ_{ij} value, resulting in a single set of average intensity values versus θ_{ij} . Essentially, Figure 19 was column averaged (excluding zero values). The maximum average intensity value was divided by the average intensity value for each θ_{ij} value, resulting in a set of conversion factors versus θ_{ij} . Conversion factors for Example Image Z are plotted in Figure 20. If this set of conversion factors was multiplied element-by-element by the set of average intensity values versus θ_{ij} , then a set of constant values versus θ_{ij} would result (that constant value being the maximum fluorescence intensity).

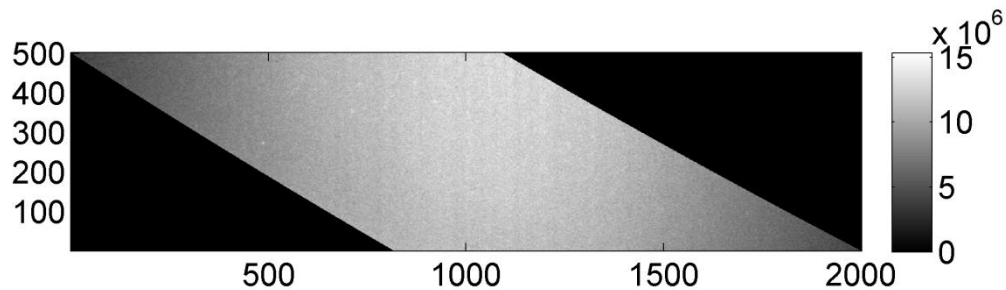


Figure 19: 2-D Interpolated Fluorescence Intensity Values in Freestream Region for Example Image Z (sample values on x-axis and y-axis represent increasing θ_{ij} and R_{ij} , respectively)

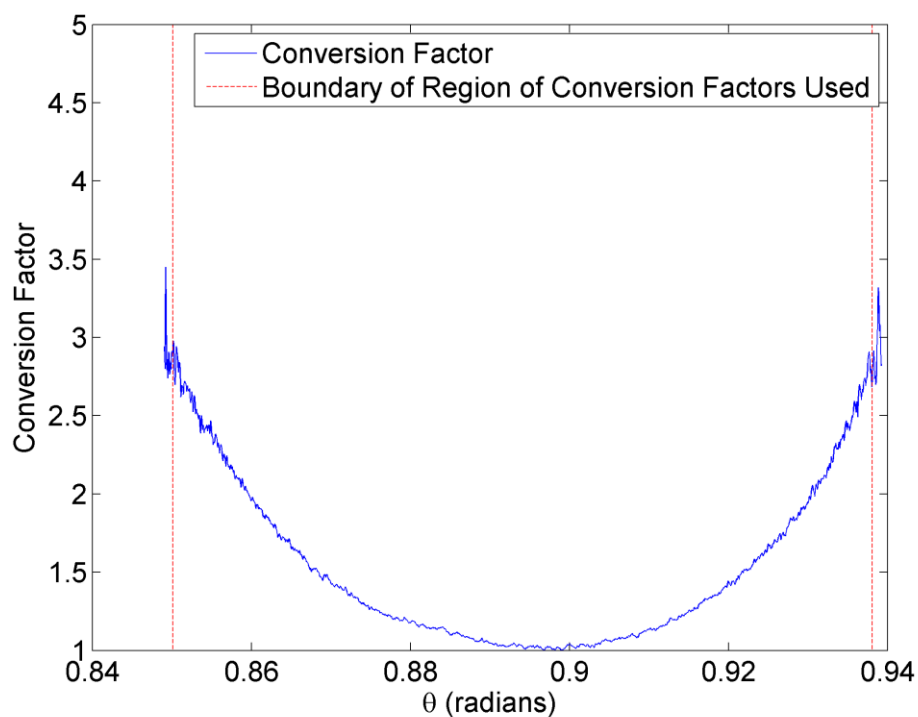


Figure 20: Plot of Conversion Factor vs. θ_j for Example Image Z

Note that the conversion factors at or near maximum and minimum θ_j are not as accurate as the conversion factors at the middle θ_j values. This is because there are far fewer fluorescence intensity values to average over at these values of θ_j because the interpolated intensity region is a rhombus, as seen in Figure 19. Therefore, boundaries were set on the range of θ_j values for which conversion factors were deemed valid, as seen in Figure 20. Conversion factors were only deemed valid for the range of θ_j values that had an adequate number of fluorescence intensity values to average over. The conversion factors outside of this range of θ_j values were set to zero, causing the intensity values of the corresponding pixels (i.e. pixels whose θ_j value is outside of the range of θ_j values for which conversion factors were deemed valid) to also be set to zero when these conversion factors were applied to each image.

Also, note that the boundaries for the fluorescence intensity values in the freestream were specifically chosen in order to neglect the darker regions in the freestream (bottom left corner of Figure 18) and to ensure that flow features sporadically extending from the shear layer and wake were not entering into or interfering with this region of freestream intensity values. This was vital in making sure that the set of conversion factors versus θ_{ij} were as representative as possible of the inverse of the roughly Gaussian laser sheet intensity profile. The COS^4 vignetting correction could not adequately correct for the darker regions in the freestream near the image edges, particularly the corners (flat field images, if they had been obtained, would have improved this). If the darker regions in the freestream had been included, the set of average intensity values versus θ_{ij} would have been affected for the θ_{ij} values specific to these darker regions in the freestream. This would have created conversion factors for these θ_{ij} values that overcompensated/overcorrected for the roughly Gaussian laser sheet intensity profile. In turn this would have caused excessive brightness for all pixels in the image that fell along these values of θ_{ij} .

The conversion factors were applied to all pixels in the image. A conversion factor could be interpolated for each pixel in the image, as θ_{ij} was known for each pixel, and be multiplied by the fluorescence intensity value of that pixel. Once this was complete, the local laser fluence was approximately constant throughout the entire image. Example Image Z after the laser sheet non-uniformity correction is shown in Figure 21.

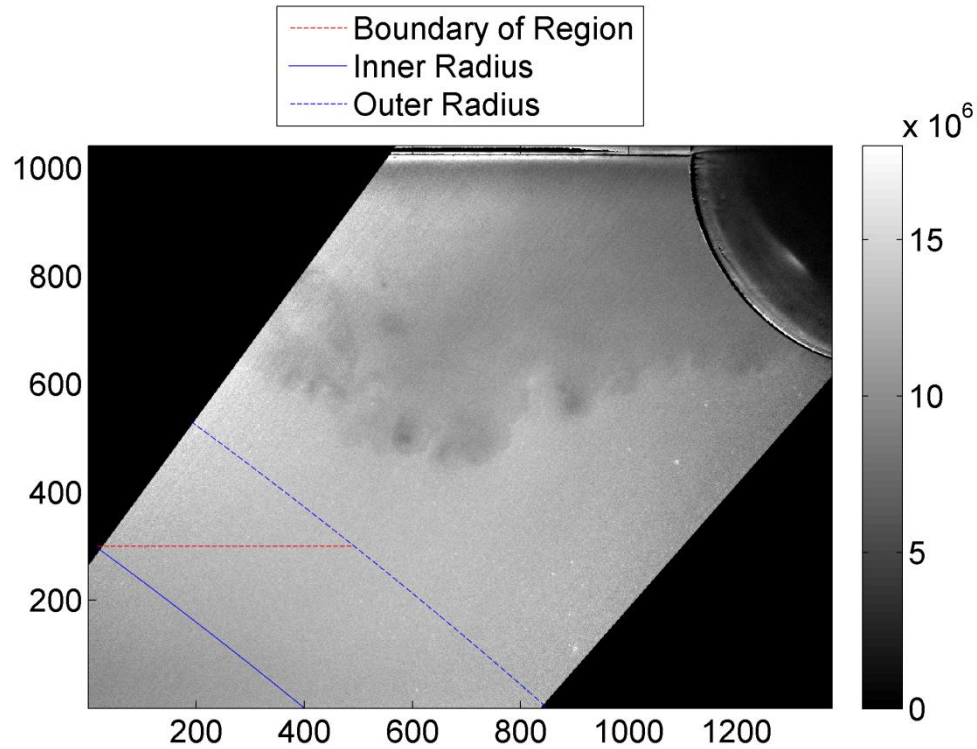


Figure 21: Example Image Z After Laser Sheet Non-Uniformity Correction

c. Normalization to Freestream Conditions

Once the laser sheet non-uniformity correction was completed, the intensity value of every pixel in an image was divided by the average freestream intensity value to yield an image of $I_j/I_{j\infty}=S_j/S_{j\infty}$ values, as seen in Figure 22 (the image is flipped to appear in a left to right flow convention, although raw images were obtained in a right to left flow convention; the original acetone PLIF raw image is inlayed for comparison). To obtain the average freestream intensity value for a single image, intensity values in Figure 21 were 2-D interpolated for the same values of R_{ij} and θ_{ij} (i.e. over the same region location) for which fluorescence intensity values were 2-D interpolated in Figure 18. This region of interpolated intensity values was then averaged (excluding zero values),

resulting in one average freestream intensity value. To reiterate, some zero values are present in this interpolation region because boundaries are set on the range of θ_{ij} values for which conversion factors are deemed valid, as seen in Figure 20. The conversion factors outside of the θ_{ij} range are set to zero. This causes the intensity values of the pixels outside of the θ_{ij} range to also be set to zero when the conversion factors are applied to the images. Some of the 2-D interpolated intensity values in this interpolation region are zero as a result.

Note that during image acquisition, the CCD converts the collected signal S_f in photons to photoelectrons. These photoelectrons are converted to a specific count, which is the intensity I_f in the digital image (this value is proportional to the collected signal in photons). The normalized signal, $S_f/S_{f\infty}$, and the normalized intensity, $I_f/I_{f\infty}$, are both ratios and are thus equal to each other. For more information on how a CCD operates, see Reference 76.

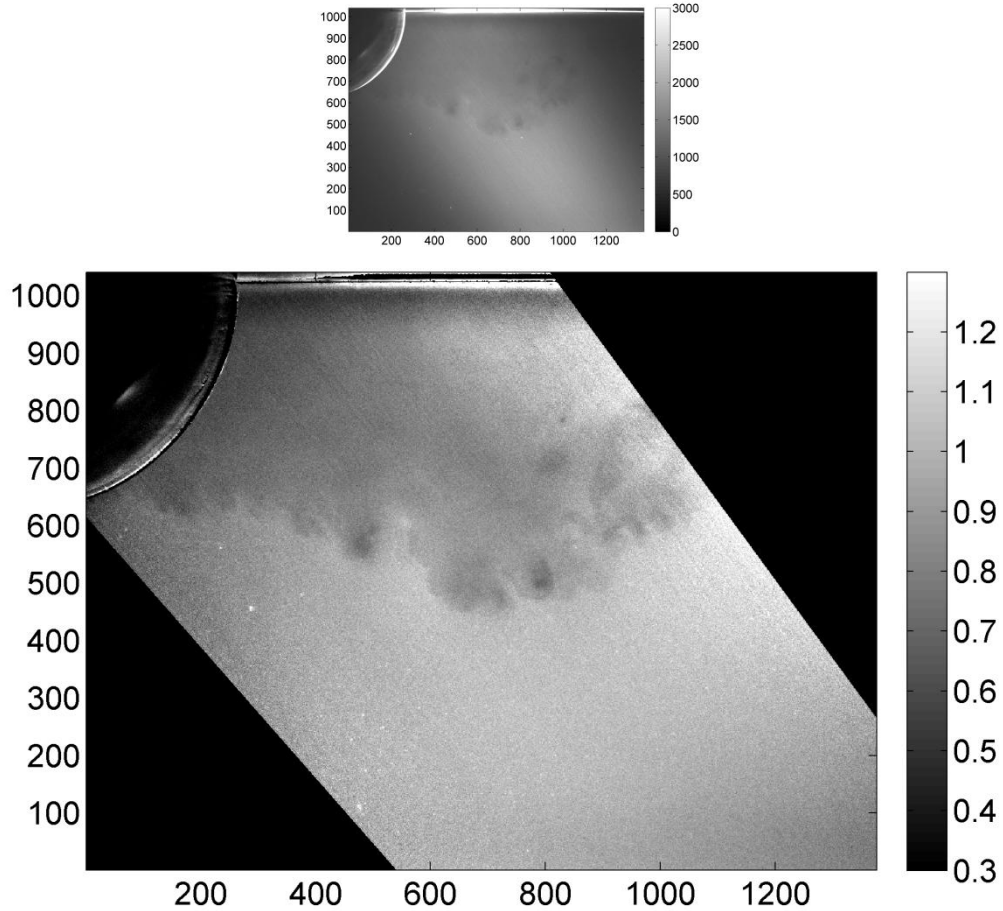


Figure 22: Example Image Z Normalized to Average Freestream Intensity
 $I_f/I_{f\infty}=S_f/S_{f\infty}$ (Example Image Z Inlayed)

Also, note that the virtual origin was moved iteratively to different locations until a “best” final corrected image (normalized to average freestream intensity) was found for several images in the large set of centerline plane (wake region) images. The criteria for “best” was the final corrected image had minimal intense streaks, more visible flow data/features than in the raw image, and approximately constant intensity values in the freestream (with the exception of a few dark regions due to vignetting that could not be corrected). The virtual origin location was not modified for the off-centerline planes that were investigated, explained in Section IX. This is because the changes in spatial

resolution for the off-centerline plane images, relative to the large set of centerline plane (wake region) images, were minimal. Also, it appeared that this virtual origin location still produced quality final corrected images that fit the criteria for “best” for these off-centerline plane images.

It was noticed in the off-centerline plane images that slightly more of the hemisphere was visible than in the large set of centerline plane (wake region) images. These off-centerline plane images were obtained before the large set of centerline plane (wake region) images, so it was assumed that the camera was slightly translated or yawed after these images were acquired and before the large set of centerline plane (wake region) images was acquired. However, this did not warrant a change in the virtual origin location. The virtual origin location was changed for the separation region images because the spatial resolution changed a fair amount and the camera location was translated upstream so a larger portion of the hemisphere could be captured. In all final corrected images in this work, slight darkness near the image edges/corners, a somewhat bright band at the farthest downstream wake locations (along the highest θ_j angles), and slight streakiness suggest that there is still room for improvement in this image processing and in-situ calibration procedure.

C. Behavior of σ and ϕ for ρ , T , and P

The behavior of absorption cross-section and fluorescence quantum yield with changes in density, temperature, and pressure must be understood before Equation 8 can be utilized. As explained in Section III.F.a., Thurber (1999)⁴⁸ created a model for ϕ and also obtained σ vs. T data for acetone (in a nitrogen bath gas) at multiple wavelengths. Thurber provides a C++ source code that calculates the fluorescence quantum yield for acetone in a nitrogen bath gas

when given an input temperature, pressure, and wavelength of excitation.⁴⁸ This source code was taken directly from Thurber (1999)⁴⁸ and was modified to be used in MATLAB, to be applicable with air as the bath gas (as opposed to having nitrogen as the bath gas), and to allow input of acetone mole fraction (which should be a small percentage because the air mole fraction should be close to 1).

Thurber explains how one can modify the code to change the bath gas. For this work, the fluorescence quantum yield model (which already includes nitrogen) was modified to also include oxygen and argon as dry air (the bath gas in this work) is made up primarily of nitrogen, oxygen, and argon (carbon dioxide, hydrogen, neon, helium, krypton, and xenon are negligible components^{77,78}). In addition, a k_{O_2} term was added to the original model, as recommended Thurber, to account for slight oxygen quenching of fluorescence (as explained in Section III.B., oxygen at high enough partial pressure fully quenches phosphorescence). The acetone mole fraction was small, approximately 3%, so adding a term for collisions between acetone molecules did not significantly change the overall value of the k_{coll} term, although this term was added nonetheless.

As explained in Section III.F.a., the Lennard-Jones potential was used in certain areas in Thurber's fluorescence quantum yield model when the Stockmayer potential actually should have been implemented. Collisional effects from the polarity of acetone were not modeled exactly in the correct manner as a result (i.e. dipole interactions were not included). Also, the equations used to calculate the overall molecule collision diameter and collision potential energy for collisions between polar acetone molecules and non-polar molecules (nitrogen, oxygen, and argon) do not include the dipole moment. However, for

low acetone mole fraction applications, these shortcomings in the model were assumed to not have a significant effect.

Thurber's absorption cross-section versus temperature data for 266 nm was added to the MATLAB code. This enabled the absorption cross-section to be interpolated/extrapolated at the specific input temperature and multiplied by the corresponding fluorescence quantum yield calculated from the input pressure and temperature (and thus density). Thus, when the code executed, it produced values of $\sigma(T)\phi(T, P) = \sigma(T)\phi(T, \rho RT) = \sigma\left(\frac{P}{\rho R}\right)\phi\left(\frac{P}{\rho R}, P\right)$ to be used in Equation 8.

Note that the absorption cross-section versus temperature data was only collected by Thurber down to a temperature of 296 K. For temperatures in this flow field that were below 296 K, a linear extrapolation had to be used. This obviously induces some error in results, but with the proper lab equipment, one could easily obtain their own absorption cross-section versus temperature data and eliminate the error from this assumption. Hanson (2010)⁷⁹ and Gierczak et al. (1998)⁸⁰ have created expressions with coefficients to model absorption cross-section of acetone for different temperatures and wavelengths. These absorption cross-section expressions were not used in conjunction with the fluorescence quantum yield model in order to keep consistency. For more information on Thurber's fluorescence quantum yield model and absorption cross-section, see Thurber (1999)⁴⁸, Tran (2008)⁵⁰, Hartwig (2010)⁵¹, Bryant et al. (2000)⁵², Braeuer et al. (2006)⁶², and Koch et al. (2004)⁶³.

D. Sensitivity of σ and ϕ

Thurber verified the original fluorescence quantum yield model at 266 nm excitation down to experimental conditions of 1 atm and 296 K. In this work, the

maximum freestream conditions of pressure and temperature are approximately 1.503 atm and 257 K, respectively. Therefore, in this work, Thurber's modified model and absorption cross-section data have to be interpolated for higher temperature values and extrapolated for lower temperature values. If the absorption cross-section data and modified fluorescence quantum yield model are used to find σ and ϕ , respectively, for the maximum freestream conditions, then it can be seen that the maximum freestream conditions create an increase in ϕ of approximately 15% of the verified condition ϕ and a decrease in σ of approximately 5% of the verified condition σ . This demonstrates the sensitivity of these variables to changes in pressure and/or temperature.

E. Curves of $S_f/S_{f\infty}$ vs. ρ/ρ_∞ and Conversion to Density

In order to extract density data from normalized signal $S_f/S_{f\infty}$ images, curves of normalized signal $S_f/S_{f\infty}$ versus normalized density ρ/ρ_∞ were created for each image using Equation 8. Equation 8 shows that $S_f/S_{f\infty}$ is a function of ρ and either P or T , as ρ , P , and T are related through the ideal gas law. Unfortunately, P and/or T cannot be measured at every point in the flow field (i.e. uncertainty in local pressure P and local temperature T exists). Therefore, experimental bounds must be established for either P or T for their maximum and minimum possible conditions in the flow field in order to utilize Equation 8. Pressure values were constantly monitored in the test section during each test run (freestream static pressure P_∞ and static pressure behind the hemisphere P_{wake}), so the experimental bounds were established for P in this work. Local pressure P values in the flow field were assumed to fall within the bounds established by P_∞ (maximum pressure) and P_{wake} (minimum pressure). This is because the primary region of interest is the shear layer, which is physically

located in between the freestream region and the wake region. Vortex cores in the shear layer and wake region can potentially produce significant pressure drops from the freestream pressure, but these potentially low pressure values were assumed to be within or close to the experimental bounds established for P . Note that random error in the density measurement technique results from uncertainty in local pressure P . This is explained in Section IV.F.

Constant pressure curves of $S_f/S_{f\infty}$ vs. ρ/ρ_∞ were created for the minimum and maximum pressure bounds (lower bound P_{wake} and upper bound P_∞). Density was increased from zero to the stagnation density for each image. These density values were coupled with each constant pressure bound to find the corresponding temperature values (through the ideal gas law) for each constant pressure bound. Equation 8 was then utilized with these input values of P , T , and ρ (for each constant pressure bound) and freestream input values of P_∞ , T_∞ , and ρ_∞ . This resulted in curves of $S_f/S_{f\infty}$ vs. ρ/ρ_∞ for the lower and upper pressure bounds. An average of the two curves was created and applied to the corresponding image in the form $S_f/S_{f\infty}$. This resulted in images in the form ρ/ρ_∞ . An example set of calibration curves for a single image is shown in Figure 23.

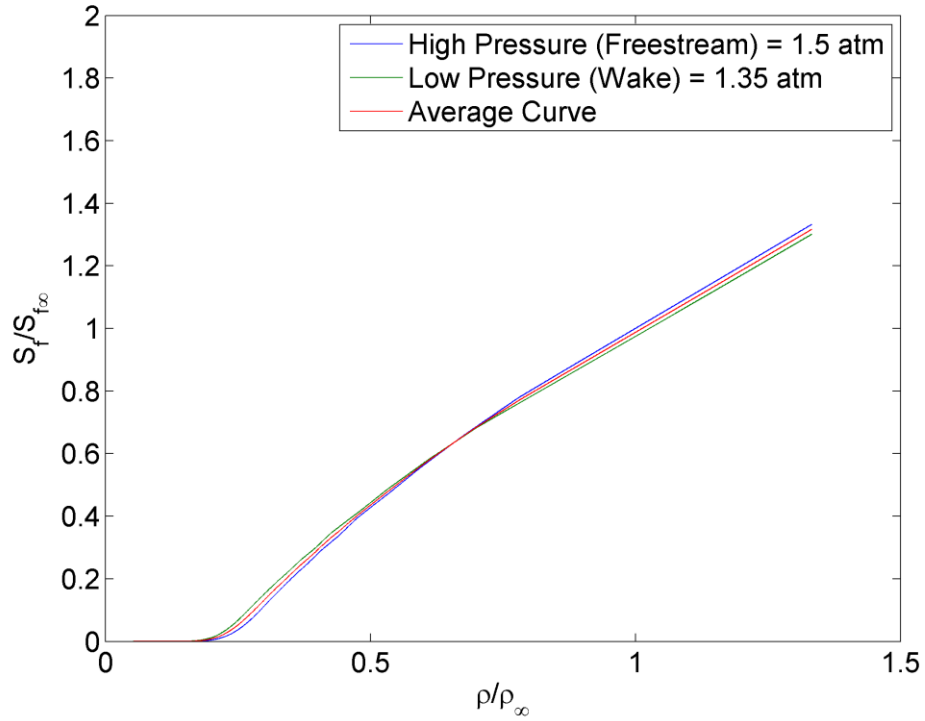


Figure 23: Curves of $S_f/S_{f_{f\infty}}$ vs. ρ/ρ_{∞} for a Single Image

F. Random Error in Density Measurement Due to Uncertainty in Local Pressure P

It was estimated that uncertainty in local pressure P , for the density range expected in this flow field, created random error in the density measurement of $\pm 2.5\%$ at the most. It can be seen in Figure 23 that this form of random error in the density measurement drops to zero as the $S_f/S_{f_{f\infty}}$ vs. ρ/ρ_{∞} curves for constant P_{wake} and P_{∞} intersect at an approximate ρ/ρ_{∞} value of 0.65 (this normalized density intersection point slightly changes during a test run as test section conditions change). The fluorescence quantum yield is a function of temperature and pressure and the absorption cross-section is a function of temperature. At

this intersection point, the changes in both of these parameters are assumed to be in equilibrium with one another.

It can also be seen in Figure 23 that at low ρ/ρ_∞ values, $S_f/S_{f\infty}$ is close to zero. This is caused by two factors: ρ/ρ_∞ is small and at low density values, the temperature has to be quite high in order to keep the pressure bound constant for each $S_f/S_{f\infty}$ vs. ρ/ρ_∞ curve. Fluorescence quantum yield decreases as the temperature increases and absorption cross-section increases as temperature increases, as shown in Thurber (1999)⁴⁸. However, the decrease in fluorescence quantum yield is continuous with increasing temperature, while the increase in absorption cross-section with increasing temperature eventually slows down (and at high enough temperature plateaus).

V. Test Facility Part I: Transonic Wind Tunnel and Hemisphere Model

A. Characterization of Transonic Wind Tunnel

The transonic wind tunnel (the supersonic wind tunnel as well) is characterized as a blowdown wind tunnel. High-pressure air is pushed through the wind tunnel during use, creating high-subsonic conditions in the test section. An Ingersoll-Rand compressor pressurizes and stores dry air in two large storage tanks. When the wind tunnel is operational, this pressurized air is sent from the storage tanks into a compressed air supply line pipe that directly leads to the stagnation/settling chamber, as seen in Figure 24. The stagnation/settling chamber is outfitted with a control knob/valve that prevents the stagnation pressure, P_0 , from being as high as the storage pressure (during acetone PLIF experimentation, this knob was set to a value of 10; during PIV and Schlieren imaging, this knob was set to a value of 8). This in turn prevents the test section from being pressurized to an extremely high freestream static pressure, P_∞ , that could damage windows. The stagnation/settling chamber also has a feedback controller which ensures that the P_0/P_∞ ratio remains constant, and thus M_∞ remains constant, as storage pressure, stagnation pressure, and static pressure change during a test run. Note that an air dryer dries the air that is stored in the pressurized storage tanks. This prevents condensation of water vapor in air when air passes through the test section of the wind tunnel.



Figure 24: Compressed Air Supply Line Pipe and Stagnation/Settling Chamber

B. Transonic Wind Tunnel Design Constraints

In order to study the separated shear layer and turbulent wake region of a wall-mounted hemisphere in a freestream flow using acetone PLIF and PIV, the inlet, test section, and diffuser sections of a blowdown wind tunnel had to be specifically created for transonic conditions. The stagnation/settling chamber previously housed only a supersonic wind tunnel inlet, test section, and diffuser. The idea was to make the existing supersonic wind tunnel (inlet, test section, and diffuser sections) and designed/fabricated transonic wind tunnel (inlet, test section, and diffuser sections) into mobile units that could be easily connected/disconnected from the stagnation/settling chamber whenever experimentation at supersonic or transonic conditions was necessary. The supersonic wind tunnel mobile unit is shown in Figure 25.



Figure 25: Supersonic Wind Tunnel Mobile Unit

During the design of the transonic wind tunnel mobile unit⁸¹, five design constraints had to be met:

1. The test section had to be large enough to contain a hemisphere model of reasonable size, while also minimizing blockage effects
- 2.) The test section had to have optical access on at least three of the four sides
- 3.) The inlet (i.e. inlet duct/inlet nozzle) had to be compatible/interchangeable with the existing stagnation/settling chamber (previously used only for the supersonic wind tunnel)
- 4.) The wind tunnel had to establish and hold transonic conditions in the test section during test runs
- 5.) Everything had to be economical and relatively easy to build

The supersonic wind tunnel mobile unit has a 4" x 4" test section. It was desired to keep the same size for the test section of the transonic wind tunnel mobile unit. This was partly based upon the physical constraints of the overall facility. The inlet, test section, and diffuser had to mesh well with the existing stagnation/settling chamber and PVC/plastic elbow section (and exit pipe out of

the laboratory). A 4" x 4" test section was also deemed to be an adequate size for necessary run times, based upon the 625 ft³ overall/combined storage tank volume pressurized to 125 psig.⁸¹

A small diameter hemisphere (relative to the cross-sectional area) was desired, so blockage and wall effects were minimal. Also, it was important to be able to obtain data for several diameters of the wake region (this affected the size of the hemisphere and the optical windows). The size of the windows was constrained by the fact that if the windows were too large, then they would be more prone to structural failure. The diameter of the hemisphere was correspondingly selected to be 1 inch based upon these design constraints.

C. Transonic Wind Tunnel Design Description: Inlet and Test Section

Taking all of the above factors into account, the inlet, test section (4" x 4"), and diffuser for the transonic wind tunnel mobile unit were designed and fabricated, yielding a nominal freestream Mach number of approximately 0.78. A schematic representation of the transonic wind tunnel is shown in Figure 26 and two actual images of the wind tunnel are shown in Figure 27.

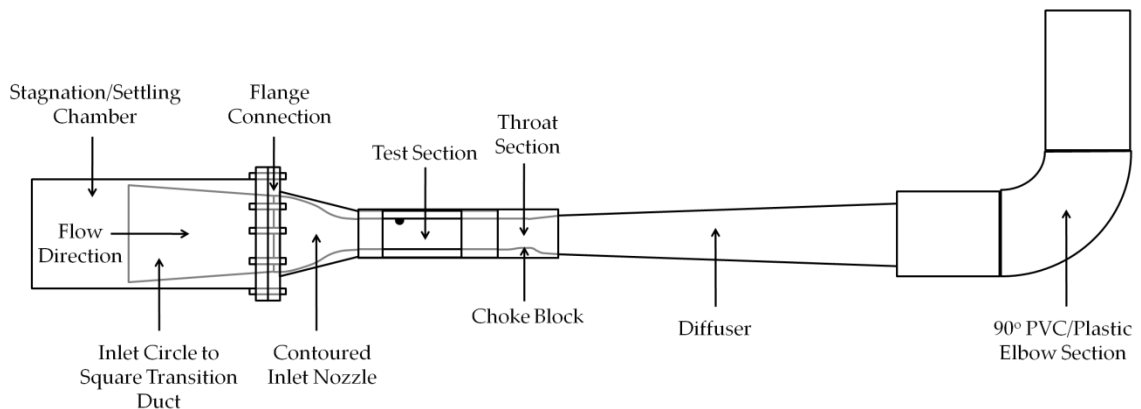


Figure 26: Schematic of Transonic Wind Tunnel (not drawn to scale)



Figure 27: Transonic Wind Tunnel

A steel circular flange and an aluminum contoured inlet nozzle form the backbone of the transonic wind tunnel, as seen in Figure 28. A steel inlet circle to square transition duct is welded to the upstream side of the circular flange (this circular flange has a square section removed from its middle and the square end of the inlet circle to square transition duct fits into this section, as seen in Figure 26). The contoured inlet nozzle is bolted to the downstream side of the circular flange (the lip of the upstream end of the contoured inlet nozzle fits into this square section as well). Laminar flow upon entrance to the test section is achieved by making sure that the contour at the beginning and end of the contoured inlet nozzle has a first and second derivative equal to zero.⁸¹⁻⁸³ Bondo was applied to the sharp corners/edges inside of the contoured inlet nozzle and sanded to increase smoothness.



Figure 28: Stagnation/Settling Chamber, Flange, Contoured Inlet Nozzle, and Test Section

The 4" x 4" test section, constructed almost entirely of aluminum, is attached to and located just downstream of the contoured inlet nozzle, as seen in Figure 28. Three sides of the test section have optical access (the bottom, the left side, and the right side), as seen in Figure 29.



Figure 29: Test Section Optical Access

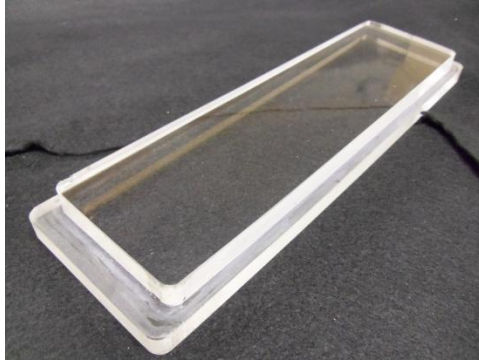


Figure 30: Bottom Stepped Window

The bottom stepped window is 1" thick and is mounted into the bottom wall of the test section. As seen in Figure 30, the bottom 0.5" of the overall 1" thickness has an area of 3.5" x 12" and the top 0.5" of the overall 1" thickness has an area of 3" x 11" (actual viewing area is 3" x 11"). The rectangular side windows are 5" x 6" x 0.5" (actual viewing area is 4" x 6") and the outside edges (non-wetted edges) of these windows are slightly beveled/chamfered to reduce the probability of chipping.

All windows are constructed of UV fused silica, but the bottom window also has an AR coating specifically peaked for 266 nm and 532 nm. UV fused silica (from ESCO Products) was selected because it has an optimum transmission range of 180-2000 nm.⁸⁴ As explained earlier, the excitation wavelength in this work is 266 nm and the general fluorescence spectrum of acetone is 350-550 nm.^{48,49} Standard BK-7 optical glass from ESCO Products was initially tested for the rectangular side windows (the UV fused silica bottom stepped window with an AR coating was the same, however). Unfortunately, standard BK-7 has an optimum transmission range of 350-2000 nm⁸⁵, so it does not perform well in the lower UV. This resulted in the rectangular side windows fluorescing during acetone PLIF experiments, creating a large amount of noise

that would have greatly affected image quality if left unchanged. Thus, UV fused silica was selected instead for the rectangular side windows and was found to perform well in the lower UV.

The side walls of the test section comprised the rectangular side windows and small, black, rectangular delrin insert plates, as seen in Figure 29. Delrin plates upstream of the side windows are 2.5" x 5" x 0.5" and delrin plates downstream of the side windows are 3.5" x 5" x 0.5". Using delrin insert plates gives flexibility to the test section design because these inserts can be machined to any width, enabling the rectangular side windows themselves to be placed at any location in the test section. This is valuable if it is desired to gather data at locations far upstream or downstream of the hemisphere model in the test section. The current delrin insert and rectangular side window configuration (and only configuration used in this work) allows for viewing of 1.5D upstream of the hemisphere and 4.5D downstream of the hemisphere. Note that one set of the delrin plates is outfitted with static pressure ports and their arrangement is explained in Section VI.A.-B.

All windows and delrin inserts are held in place by hollow, aluminum, rectangular brackets that are bolted to the test section, as seen in Figure 29. The brackets provide pressure to the outer edges of each window and delrin insert to hold them in place. These brackets are lined with thin cork sheet for cushioning purposes to protect the windows. The test section is also outfitted with o-ring chord in several locations to cushion the windows and also decrease leaks. However, leaks are inevitable and this wind tunnel is no different as a few places upstream and downstream of the test section, and even the test section itself, suffer from leaks when the wind tunnel is operational. These leaks are small and assumed to not affect the validity of the data collected in this wind tunnel.

D. Transonic Wind Tunnel Design Description: Choke Block and Diffuser

Transonic conditions had to be established and held for a prolonged period of time during a test run. Storage pressure, $P_{storage}$, during a test run is constantly dropping and thus the stagnation pressure, $P_{0,t}$, and freestream static pressure, $P_{\infty,t}$, are constantly changing. A feedback controller in the stagnation/settling chamber regulates the ratio of stagnation pressure to freestream static pressure to ensure that this ratio remains constant, and thus the freestream Mach number remains constant, during a test run. Taking these facts into account, it was determined that the best method to establish and hold transonic conditions in the test section was to use a choke block located just downstream of the test section on the bottom wall of the wind tunnel. This choke block, seen in Figure 31, has a slight bump that creates a throat area A^* , which chokes the flow. This forces the freestream Mach number of approximately 0.78 in the test section based upon A/A^* , the ratio of test section area to throat area. At the top of the slight bump on the choke block, the block plateaus for a couple inches. Then there is a downward dip in the choke block, creating a larger cross-sectional area. At the approximate location where the dip begins, the top wall of the wind tunnel begins to slightly ramp upward, also contributing to a larger cross-sectional area.

Original design of the choke block was not for this particular Mach number ($M_{\infty} \approx 0.78$), but boundary layer growth on the wind tunnel walls (not taken into account during the design process) contributed to this Mach number. The freestream Mach number is slightly less than 0.78 at the beginning of the test section and slightly more than 0.78 at the end of the test section. This increase in Mach number can be attributed to boundary layer constriction created by the boundary layers on the walls of the wind tunnel that grow as downstream

distance increases. There was a slight blockage effect that affected the Mach number near the mounted hemisphere. This is explained in Section IV.A.-B.

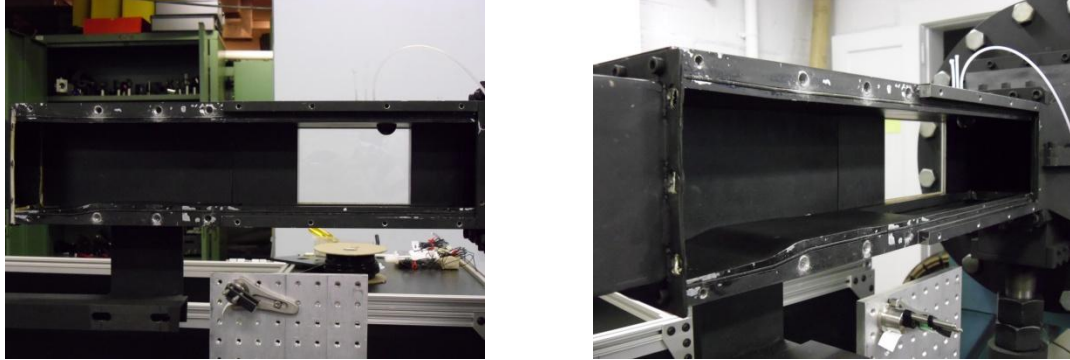


Figure 31: Choke Block and Throat Section

A diffuser constructed of steel sheet is located just downstream of the choke block. The diffuser decreases the velocity of the flow before it enters a 90° PVC/plastic elbow section and then exits the laboratory through a metal pipe. This entire transonic wind tunnel mobile unit (i.e. inlet, test section, and diffuser) is mounted on a steel chassis with wheels, similar to the supersonic wind tunnel, that enable it to be mobile and interchangeable in and out of the stagnation/settling chamber.

The entire wind tunnel mobile unit was painted flat black, including the inside walls of the test section. The inside walls of the test section, as well as the inside walls of the contoured inlet nozzle and choke block section, were also wet sanded to increase smoothness.

E. Transonic Wind Tunnel Operation

When experiments are performed in the transonic wind tunnel, the transonic wind tunnel mobile unit is bolted to the stagnation/settling chamber at the flange connection, shown in Figure 26. In addition, the downstream end of the diffuser is attached to the upstream end of the 90° PVC/plastic elbow section, as seen in Figure 32. The downstream end of this elbow section is attached to the upstream end of a large diameter metal pipe that exits the laboratory through the ceiling. This enables the flow to exit the laboratory after it passes through the transonic wind tunnel. Heavy-duty Saran wrap is wrapped around both ends of the elbow section (where the elbow section connects to the diffuser and connects to the pipe exiting the laboratory), as well as the middle of the elbow section. This greatly decreases noise during experimentation and also helps to prevent large amounts of the flow from entering the laboratory, such as air/acetone vapor during PLIF experiments (Section IX. and XI.) and air/acetone vapor/alumina particles during PIV experiments (Section VIII.).



Figure 32: 90° PVC/Plastic Elbow Section

The transonic wind tunnel is fully operated by a National Instruments DAQ card (NI USB-6259 BNC⁸⁶) and a LabView program created by Kyle Lynch.

The program and DAQ card can additionally simultaneously control/operate other components. In the case of this work, the program and DAQ card controlled a solenoid valve for the seeder (Section VII.A.), pressure transducers (Section VI.A.-B.), and pulse generators (Section VIII.B.c.). Note that the pulse generators control the PIV laser and the camera. By having the ability to operate several components off of one central console, acetone PLIF and PIV experiments can in principle be conducted by one person (however, two people are recommended when removing the test section windows and reinstalling them). A unique feature of this transonic wind tunnel is the ability to be fully automated where the user can specify a starting storage pressure and ending storage pressure for the test run. When the storage tanks are pressurized to the specified storage pressure, the wind tunnel turns on and operates until the storage tanks reach the ending storage pressure. This feature enables consistency between test runs.

F. Hemisphere Model

A 1 inch diameter, aluminum hemisphere model was used in this work. It was fabricated from an aluminum cylinder by using a lathe and a process of filing, sanding, and polishing. It was mounted to the ceiling of the test section, 4 inches downstream from the beginning of the test section. A bolt passed through the top wall of the test section and screwed into the hemisphere in order to hold it in place. The hemisphere was first painted flat black, but there were reflection problems when using 532 nm light and slight fluorescence problems when using 266 nm light. Different techniques were used to mitigate these negative effects.

The hemisphere model was coated, along with the top wall of the test section, with rhodamine 590 dye/polyurethane for PIV experiments (532 nm light

was used for PIV in this work). When rhodamine 590 dye is excited by a wavelength near 530 nm, it fluoresces a different wavelength (approximately 560 nm).⁸⁷ A color filter can then be used in front of the camera lens to only allow the excitation wavelength to pass to the CCD. This eliminates a large amount of noise near surfaces of models and walls during experimentation. The flat black paint and rhodamine 590 dye/polyurethane were stripped from the hemisphere model and wind tunnel walls prior to the acetone PLIF experiments.

For the acetone PLIF experiments, the wind tunnel walls were painted flat black and the hemisphere model was anodized black. This greatly reduced (but did not eliminate) the low visible wavelength fluorescence on the hemisphere surface created by the 266 nm light. Note that for condensation experiments, 532 nm light was used. This caused significant noise on the surface of the black anodized hemisphere. However, imaging during condensation experiments, explained in Section VII.E., did not need to be high-quality near the surface of the hemisphere and even with noise it was obvious when significant condensation occurred during the test run.

VI. Tunnel/Flow Field Validation and Characteristics

Several techniques were used to characterize the flow in the transonic wind tunnel test section with the hemisphere mounted. This included pressure measurements, Schlieren imaging, and shadowgraph imaging. PIV experiments were also performed for this flow field with the hemisphere mounted, but these experiments are explained in Section VIII.

A. Pressure Measurements With and Without Hemisphere Mounted

Static pressure (freestream static pressure and wake static pressure), stagnation pressure, and storage pressure values were measured for the transonic wind tunnel with and without the hemisphere mounted. Pressure values were obtained at approximately 10 Hz using Omega PX209⁸⁸ pressure transducers. Pressure measurements were also taken with no flow to make sure the pressure transducers were operating correctly. The stagnation pressure was measured in the stagnation/settling chamber and the storage pressure was measured in the compressed air supply line pipe.

A 12" x 5" x 0.5" delrin insert plate was outfitted with static pressure ports at multiple locations, as seen in Figure 33, and was mounted in the test section in place of one rectangular side window and two small delrin insert plates. Pressure ports were located along the centerline of this large delrin plate, from the upstream end to the downstream end. This enabled the freestream static pressure values versus downstream location (x/D) to be obtained (freestream Mach number versus x/D can be calculated based upon the ratio of stagnation pressure to freestream static pressure $P_{0,t}/P_{\infty,t}$). Due to the small number of pressure transducers, a separate wind tunnel test run had to be performed for each

pressure port along the centerline of the 12" x 5" x 0.5" delrin plate in order to acquire pressure data at each specific port. Pressure ports were also installed off-centerline on this large 12" x 5" x 0.5" delrin plate, but these pressure ports were not used for measurement purposes in this work.

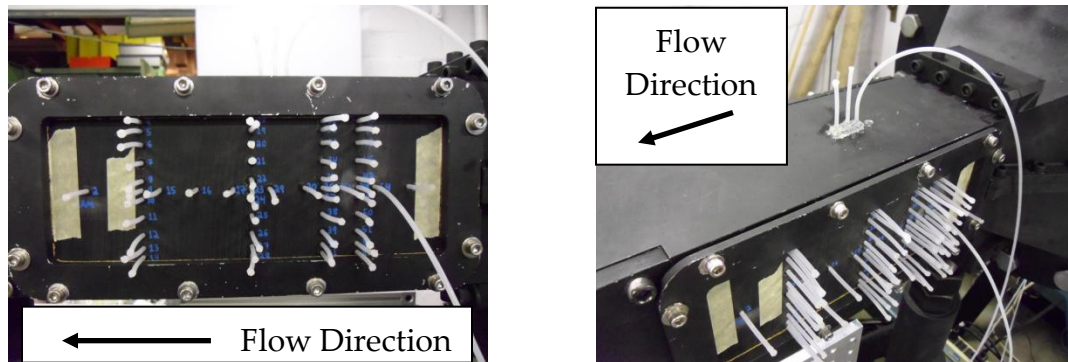


Figure 33: Location of Pressure Ports for Pressure Experiments

In Table 1, pressure port number and location relative to the centerpoint of the hemisphere is given for the centerline pressure ports on the large delrin plate (negative x/D values indicate a port that is upstream from the centerpoint of the hemisphere). This table shows the orientation of the pressure ports when viewed from the inside of the test section with the flow moving from left to right.

Table 1: Location of Static Pressure Ports Inside of Test Section (Flow is Left to Right)

Pressure Port Number	55	54	48	42	36	30	29	23	17	16	15	9	2
Location, x/D	-2.5	-1.5	-1	-0.5	0	0.5	1.5	2	2.5	3.5	4.5	5	6.5

Three static pressure ports were also installed along the centerline of the top wall of the test section, just behind/slightly downstream of the centerpoint of the hemisphere (0.5D, 1D, and 1.5D), as seen in Figure 33. Note that the third pressure port (i.e. the farthest downstream location from the centerpoint of the hemisphere) was slightly off centerline. Static pressure measurements were made for these port locations. These pressure measurements were vital in quantifying the approximate pressure in the wake region (i.e. the wake static pressure).

For the pressure measurement experiments, one of the rectangular side windows was installed, as seen in Figure 34, along with the bottom stepped window and the 12" x 5" x 0.5" delrin plate. The small delrin insert plates, upstream and downstream of the rectangular side window, were each outfitted with three pressure ports (the specifics of these pressure ports on the small delrin insert plates are explained in Section VI.B.). Freestream static pressure values were obtained for the bottom port (2.5D measured vertically from the centerpoint of the hemisphere) on these small delrin insert plates.

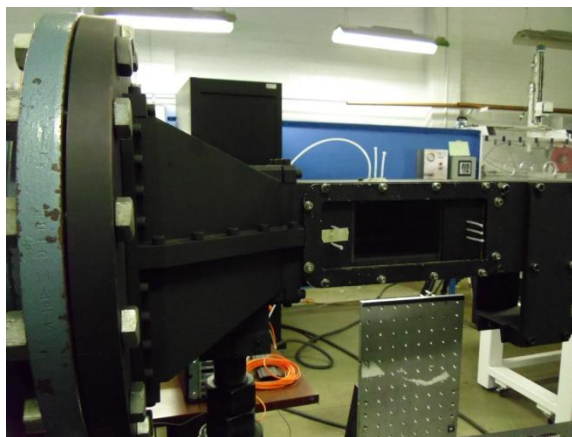


Figure 34: One Rectangular Side Window Installed During Pressure Experiments

Note that when data was not being obtained at a pressure port location, the pressure port was covered with a plastic tubing sleeve/cap to prevent air from leaking through the port hole, as seen in Figure 33. During the single-shot and time-resolved acetone PLIF experiments, explained in Section IX. and XI., the plastic tubing covers were not used. However, only 4 of the 6 pressure port holes on the small delrin insert plates were open (two of the pressure ports were connected to pressure transducers) during the acetone PLIF experiments because both rectangular side windows were installed and the three pressure ports downstream of the hemisphere (on the top wall of the test section) were not yet installed. It was also noticed during these test runs that there were slight leaks in the test section. However, the effects on the flow from these leaks were assumed to be negligible.

Also, note that for the test runs where pressure measurements were taken at 0D (port 36) with the hemisphere mounted and -1.5D (port 54) without the hemisphere mounted, the pressure data (storage pressure, stagnation pressure, freestream static pressure, and wake static pressure) for each test run was saved in two separate data files (the pressure data for each test run should have been saved to a single data file for that particular test run). Conveniently, the first data file only contained pressure data for one point in time (i.e. the true starting pressure conditions). The second data file contained the rest of the pressure data acquired throughout the test run. Pressure data was acquired at approximately 10 Hz and therefore, the first data file for each of these test runs was discarded and only the second data file was used (the beginning pressure data in the second file was assumed to be the starting pressure conditions).

Also, note that for the following plots (in this subsection and in Section VI.C.), the start of the valid data region (approximately 7.35 seconds into the wind tunnel test run) and the end of the valid data region (approximately 11.1

seconds into the wind tunnel test run) define the time window over which acetone PLIF images are deemed valid because condensation is minimal (see Section VII.E. for further discussion of this valid data region).

The pressure measurement experiments revealed that the storage pressure and stagnation pressure behavior throughout a test run are very consistent from run to run for the hemisphere mounted and not mounted case. The drop in storage pressure is a rather consistent linear drop.

Pressure measurements without the hemisphere mounted revealed many important characteristics for this wind tunnel. Once transonic conditions were established in the test section, the freestream Mach number was approximately constant throughout the remainder of the test run and the freestream static pressure only changed slightly throughout the remainder of the test run. As the distance downstream in the test section increased (i.e. x/D increased), the freestream static pressure for the most part gradually decreased, as seen in Figure 35 (the freestream Mach number for the most part gradually increased, as seen in Figure 36). This slight decrease in static pressure and slight increase in freestream Mach number was thought to be due to boundary layer constriction. Note that freestream static pressure was not acquired at some ports along the centerline of the 12" x 5" x 0.5" delrin plate for the case without the hemisphere mounted. This was because some of the pressure ports were damaged during the pressure measurement experiments with the hemisphere mounted (the pressure measurement experiments without the hemisphere mounted were performed after the pressure measurement experiments with the hemisphere mounted).

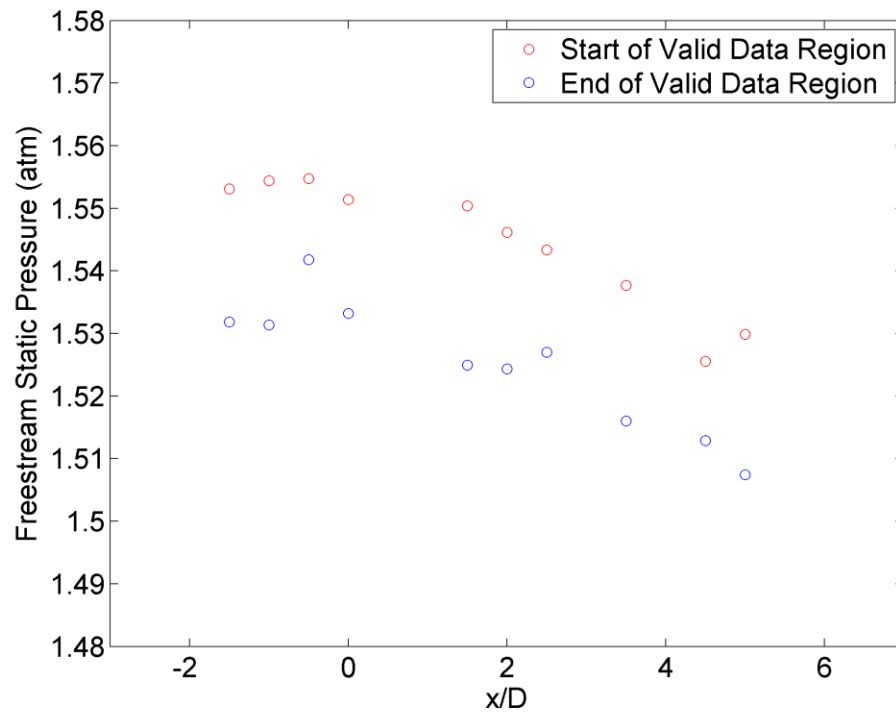


Figure 35: Plot of Freestream Static Pressure vs. x/D (Without Hemisphere)

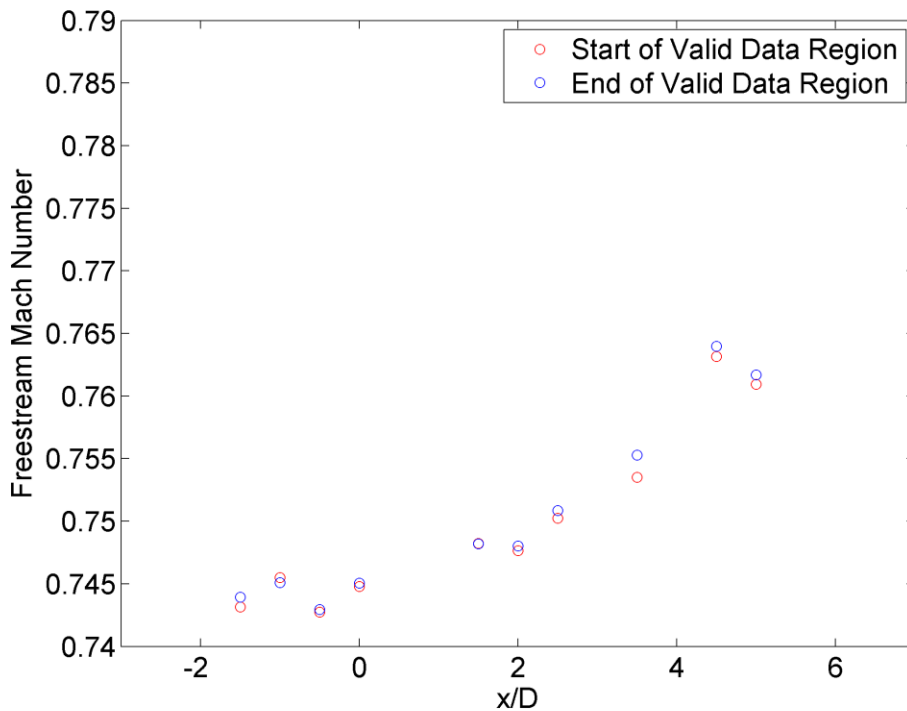


Figure 36: Plot of Freestream Mach Number vs. x/D (Without Hemisphere)

Pressure measurements for the three pressure ports behind/downstream of the hemisphere, when no hemisphere was mounted, yielded interesting results as well. The first port (0.5D) yielded lower static pressure than the other two ports (1D and 1.5D). This was thought to be due to the fact that there was a through hole present where the hemisphere was usually mounted with a bolt. During these tests, a piece of duct tape was used to cover the outer portion of this hole (i.e. outside of the test section) and pressure was applied with a finger to prevent leaks. However, it was thought that the flow was still being disrupted by this hole, creating an area of slightly lower static pressure.

The pressure measurements with the hemisphere mounted also revealed interesting characteristics for this flow field. Once transonic conditions were established in the test section, the freestream Mach number was approximately

constant throughout the remainder of the test run and the freestream static pressure slightly changed throughout the remainder of the test run. As the distance downstream in the test section increased (i.e. x/D increased) from $-2.5D$ to $0.5D$, the freestream static pressure decreased, as seen in Figure 37 (freestream Mach number increased, as seen in Figure 38). At $0.5D$, the freestream static pressure was a minimum and the freestream Mach number was a maximum. It was thought that this was due to a slight blockage effect from the hemisphere. The mass flow rate, \dot{m} , is quantified by $\dot{m} = \rho_{\infty} A V_{\infty}$ and it must remain constant. The cross-sectional area, A , is smaller at the location of the hemisphere, so the freestream velocity, V_{∞} , has to increase in order to keep the mass flow rate constant (assuming the freestream density, ρ_{∞} , is fairly constant with downstream distance). As the downstream distance increased from $0.5D$, the freestream static pressure increased, but eventually began to decrease again (the freestream Mach number decreased, but eventually began to increase again). This behavior at the higher values of x/D (i.e. the freestream static pressure decreasing and the freestream Mach number increasing) was thought to be due to boundary layer constriction.

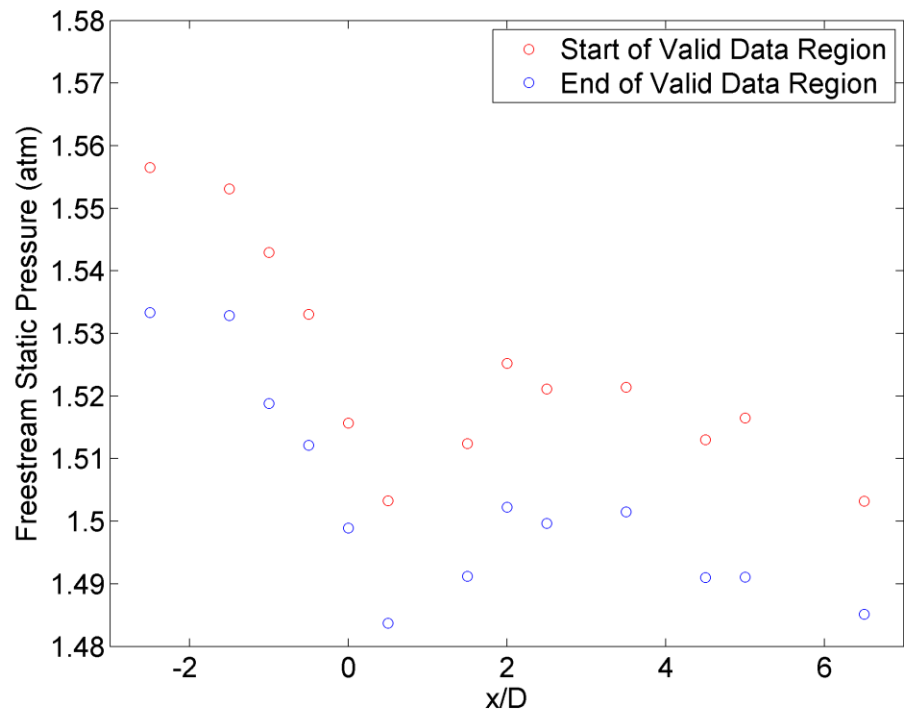


Figure 37: Plot of Freestream Static Pressure vs. x/D (With Hemisphere)

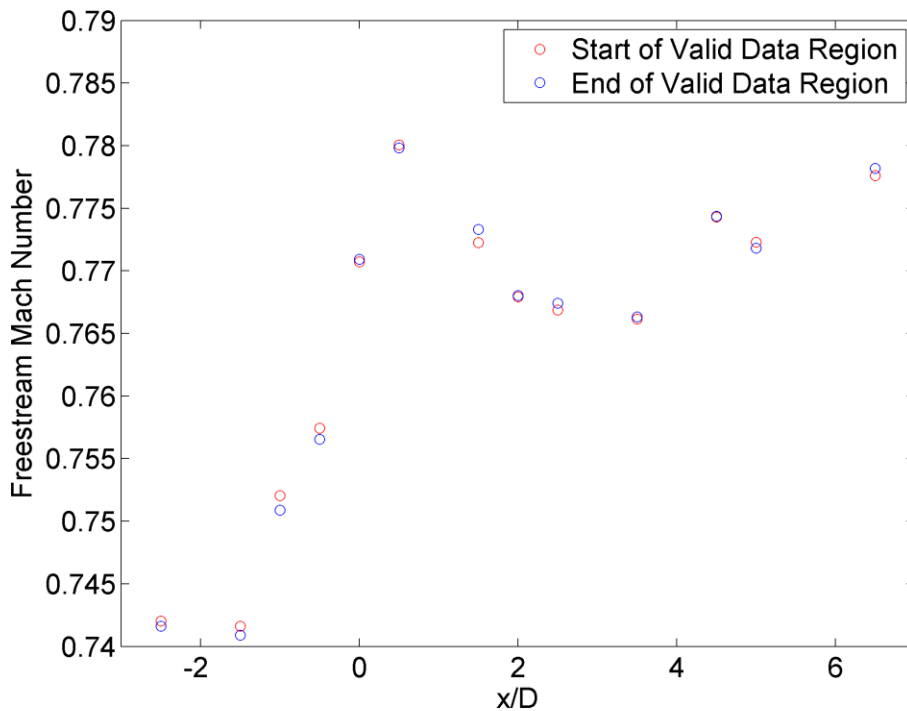


Figure 38: Plot of Freestream Mach Number vs. x/D (With Hemisphere)

Pressure measurements for the three pressure ports downstream of the hemisphere, when the hemisphere was mounted, revealed that the first port (0.5D) experienced the lowest pressure. The second port (1D) experienced the second lowest pressure and the third port (1.5D) experienced the highest pressure of the three ports. The third port actually experienced a slight pressure increase (relative to the freestream static pressure port at the same x/D downstream location).

B. Pressure Measurements During Acetone PLIF Experiments

During acetone PLIF experiments, the large 12" x 5" x 0.5" delrin plate with the array of pressure ports was not needed for pressure measurements. The

typical transonic wind tunnel test section configuration was needed with the two rectangular side windows and the bottom stepped window. One set of the small delrin insert plates, upstream and downstream of one of the rectangular side windows, was outfitted with pressure ports (the same set of delrin insert plates used in the pressure measurement experiments explained in Section VI.A). Each delrin insert plate had three vertically oriented pressure ports, as seen in Figure 28 and Figure 29 (the delrin insert plates on the opposite side of the test section did not have pressure ports). The static pressure ports for the upstream delrin insert plate were approximately $2.75D$ upstream of the centerpoint of the hemisphere and the static pressure ports for the downstream delrin insert plate were approximately $6.25D$ downstream of the centerpoint of the hemisphere. Static pressure was measured for the upstream and downstream delrin insert plate (only the top port for each delrin insert plate, $1.5D$ measured vertically from the centerpoint of the hemisphere). Storage pressure and stagnation pressure were also simultaneously measured. Note that during PLIF experiments the small delrin insert plates with the pressure ports were mounted on the side of the test section where the $12'' \times 5'' \times 0.5''$ delrin plate (with the array of pressure ports) was mounted during the pressure measurement experiments. The small delrin insert plates with the pressure ports were flipped upside down and mounted on the opposite side of the test section during the pressure measurement experiments.

It was confirmed that the freestream static pressure data obtained at these port locations during single-shot acetone PLIF with the hemisphere mounted was consistent with the freestream static pressure data at the corresponding port locations on the $12'' \times 5'' \times 0.5''$ delrin plate obtained during the pressure measurement experiments with the hemisphere mounted (Section VI.A.). Therefore, the freestream static pressure data obtained with the $12'' \times 5'' \times 0.5''$

delrin plate at the port location $0.5D$ downstream of the centerpoint of the hemisphere was assumed with confidence to be approximately the same as the freestream static pressure data for the acetone PLIF experiments at this same location (Note that a window is located at this $0.5D$ port location during acetone PLIF experiments, thus direct pressure measurements at this location are not possible during acetone PLIF experiments). The freestream static pressure at $0.5D$ was taken as the freestream static pressure for the acetone PLIF images with the hemisphere mounted. The freestream static pressure for the acetone PLIF images without the hemisphere mounted was assumed to be equal to the freestream static pressure measured at $0D$ (on the $12'' \times 5'' \times 0.5''$ delrin plate) during the pressure measurement experiments without the hemisphere mounted.

Note that the three pressure ports behind/downstream of the hemisphere on the top wall of the wind tunnel test section were installed after the acetone PLIF single-shot experiments were conducted. During the pressure measurement experiments (Section VI.A.), static pressure data was collected for these three pressure ports behind/downstream of the hemisphere (with and without the hemisphere mounted), while the freestream static pressure data was simultaneously measured at different x/D locations along the centerline of the $12'' \times 5'' \times 0.5''$ delrin plate. The freestream static pressure data in these experiments was found to be consistent with the freestream static pressure data from the acetone PLIF experiments at the corresponding upstream and downstream port locations. Thus, it was assumed that the pressure values obtained at these three port locations behind/downstream of the hemisphere during the pressure measurement experiments (with and without the hemisphere mounted) were approximately the same as if they had actually been measured during the acetone PLIF experiments.

C. Experimental Conditions in Test Section

The data presented in this section is the temperature, pressure, and density data that was used when converting each set of acetone PLIF images (with the hemisphere mounted) to density images. Data without the hemisphere mounted is not presented. Pressure measurement experiments proved that the conditions in the test section are consistent from test run to test run and therefore the pressure data from one specific wind tunnel run was used when converting the acetone PLIF images to density field images (for the mounted hemisphere case; a different set of pressure data was used for the case when the hemisphere was not mounted). The static pressure data, that was used for PLIF images with the hemisphere mounted, was acquired at 0.5D for freestream static pressure and wake static pressure. Freestream static pressure measurements at 0D and 1.5D yielded slightly higher values (portions of the separation region images are at 0D and portions of the wake region images are at 1.5D) than at 0.5D, but the differences in pressures were assumed to not significantly change final density image results. The static pressure data, that was used for the PLIF images without the hemisphere mounted, was acquired at 0D for freestream static pressure (the freestream static pressure port at 0.5D was damaged at this time) and 0.5D for wake static pressure.

The freestream conditions were estimated using the pressure data and isentropic relations. A value of $\gamma=1.4$ and the universal gas constant R for air were assumed for these calculations because the freestream flow was almost entirely air and only a small percentage was acetone. Starting storage temperature ($T_{storage,start}$) was approximately known and set to 300 K. Pressures obtained were first converted to absolute pressures. Then the starting storage pressure ($P_{storage,start}$) and the estimated starting storage temperature were used in

conjunction with the storage pressure data ($P_{storage}$) throughout the test run to estimate the storage temperature ($T_{storage}$) throughout the test run using isentropic relations (explained in Anderson (2007)⁸⁹), as seen in Equation 11. The conditions in the storage tanks and compressed air supply line pipe were assumed to be isentropic. Storage pressure throughout the test run is shown in Figure 39.

$$T_{storage} = \frac{T_{storage\ start}}{\left(\frac{P_{storage\ start}}{P_{storage}}\right)^{\frac{\gamma-1}{\gamma}}} \quad 11$$

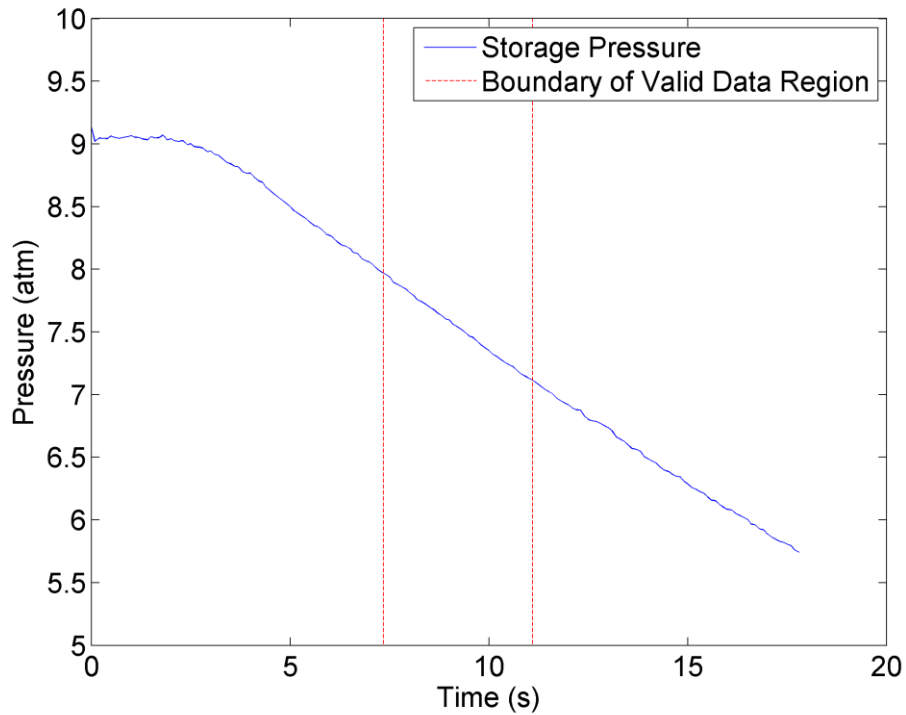


Figure 39: Plot of $P_{storage}$ for Wind Tunnel Test Run (hemisphere mounted)

Stagnation temperature (T_0) throughout the test run was assumed to be equal to the storage temperature throughout the test run and is shown in Figure 40. However, the stagnation pressure (P_0) throughout the test run was not

assumed to be equal to the storage pressure throughout the test run. A valve in the stagnation/settling chamber regulated the stagnation pressure and decreased it greatly from the incoming storage pressure, as seen in Figure 41.

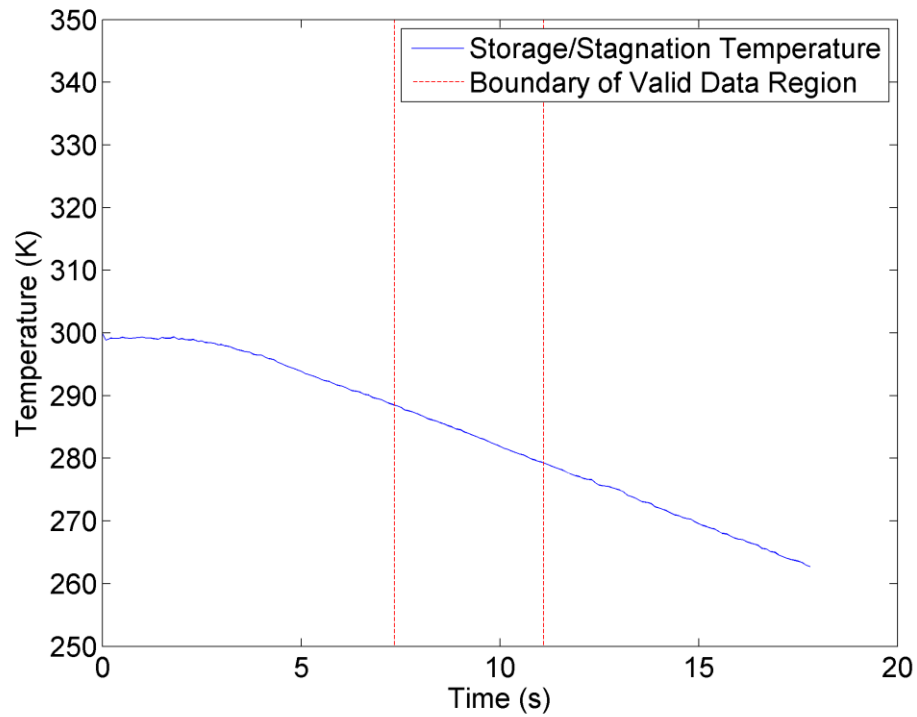


Figure 40: Plot of $T_{storage}=T_0$ for Wind Tunnel Test Run (hemisphere mounted)

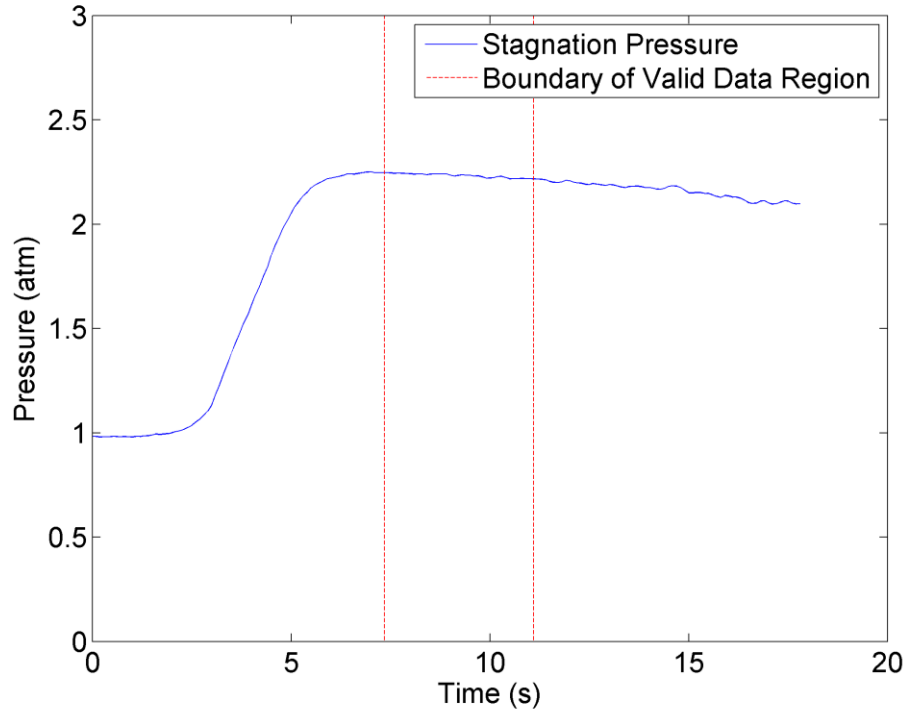


Figure 41: Plot of P_0 for Wind Tunnel Test Run (hemisphere mounted)

Stagnation temperature, stagnation pressure, and freestream static pressure (P_∞) throughout the test run were used to estimate the freestream static temperature (T_∞) throughout the test run using isentropic relations (explained in Anderson (2007)⁸⁹), as seen in Equation 12. Conditions in the test section were assumed to be isentropic.

$$T_{\infty,t} = \frac{T_{0,t}}{\left(\frac{P_{0,t}}{P_{\infty,t}}\right)^{\frac{\gamma-1}{\gamma}}} \quad 12$$

After estimating the freestream static temperature throughout the test run, shown in Figure 42, and knowing the freestream static pressure throughout the test run, shown in Figure 43, the freestream density (ρ_∞) throughout the test run, shown in Figure 44, was estimated through the ideal gas law.

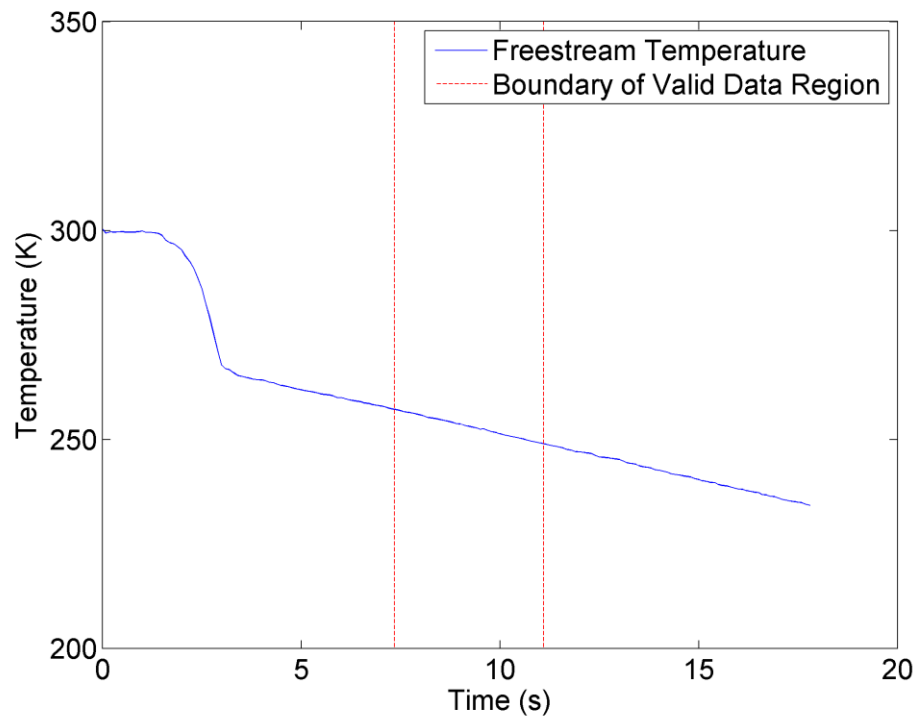


Figure 42: Plot of T_∞ for a Wind Tunnel Test Run (hemisphere mounted)

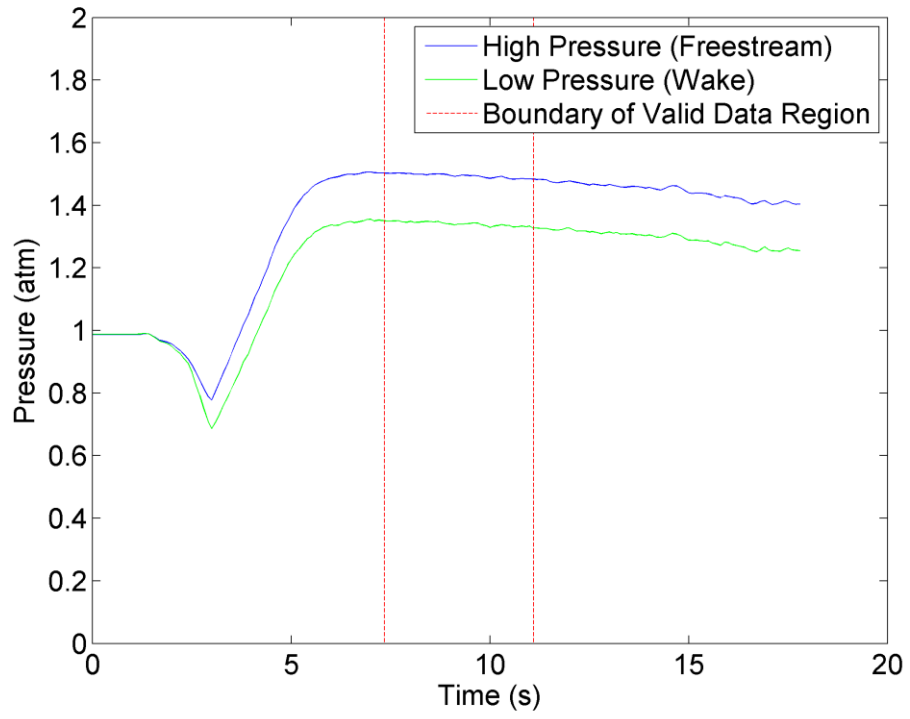


Figure 43: Plot of P_∞ and P_{wake} for Wind Tunnel Test Run (hemisphere mounted)

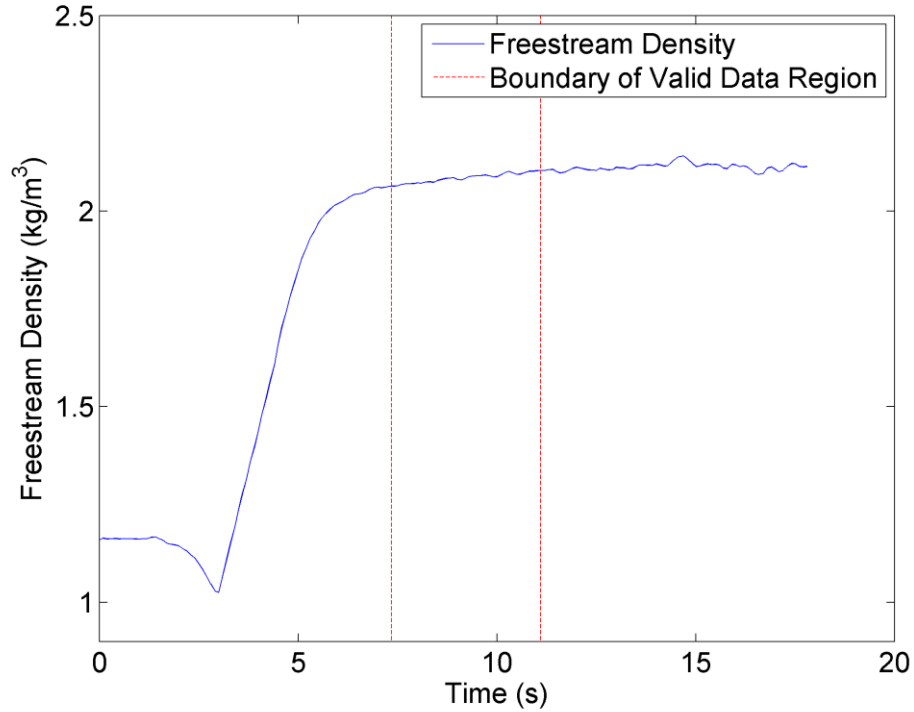


Figure 44: Plot of ρ_∞ for Wind Tunnel Test Run (hemisphere mounted)

Freestream velocity, V_∞ , throughout the test run was approximated using the stagnation temperature throughout the test run and the freestream temperature throughout the test run in conjunction with Equation 13 (the general form of this equation is explained in Anderson (2007)⁸⁹), which leads to Equation 14. Freestream velocity throughout the test run is shown in Figure 45. This freestream velocity is close in value to the freestream velocity values measured in the PIV experiments (Section VIII.), even though the PIV experiments were conducted at a slightly lower stagnation and freestream static pressure.

$$\frac{T_{0,t}}{T_{\infty,t}} = 1 + \frac{(\gamma - 1)}{2} M_{\infty,t}^2 = 1 + \frac{(\gamma - 1)}{2} \left(\frac{V_{\infty,t}}{\sqrt{\gamma R T_{\infty,t}}} \right)^2 \quad 13$$

$$V_{\infty,t} = \sqrt{\frac{2\gamma R(T_{0,t} - T_{\infty,t})}{\gamma - 1}}$$

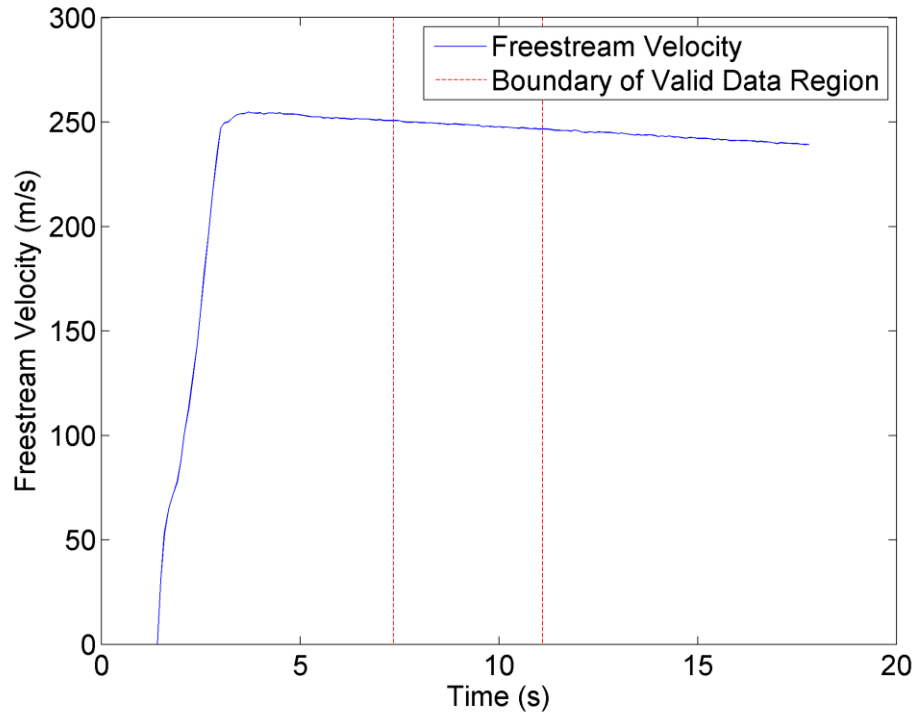


Figure 45: Plot of V_{∞} for Wind Tunnel Test Run (hemisphere mounted)

D. Schlieren and Shadowgraph Imaging

Schlieren images were obtained for the flow field with the hemisphere mounted. Pressure data was not acquired throughout these test runs. However, it should be noted that these experiments were conducted at a slightly lower freestream pressure ($P_{\infty} \approx 1.33 \text{ atm} \approx 19.5 \text{ psia}$) than in the single-shot acetone PLIF experiments (features were expected to be qualitatively similar). Schlieren images were obtained with the knife-edge oriented in a vertical manner and a horizontal manner. The knife edge was oriented both ways because the density gradients in the shear layer were the most intense in the vertical direction and

the density gradients due to the shocks were the most intense in the horizontal direction. These images were qualitative in nature and revealed a horseshoe/necklace vortex, a separated shear layer, and a turbulent wake, as seen in Figure 46. Shocks and lambda shocks⁹⁰ were also present in the images and were located approximately 90° from horizontal, although location was not constant.

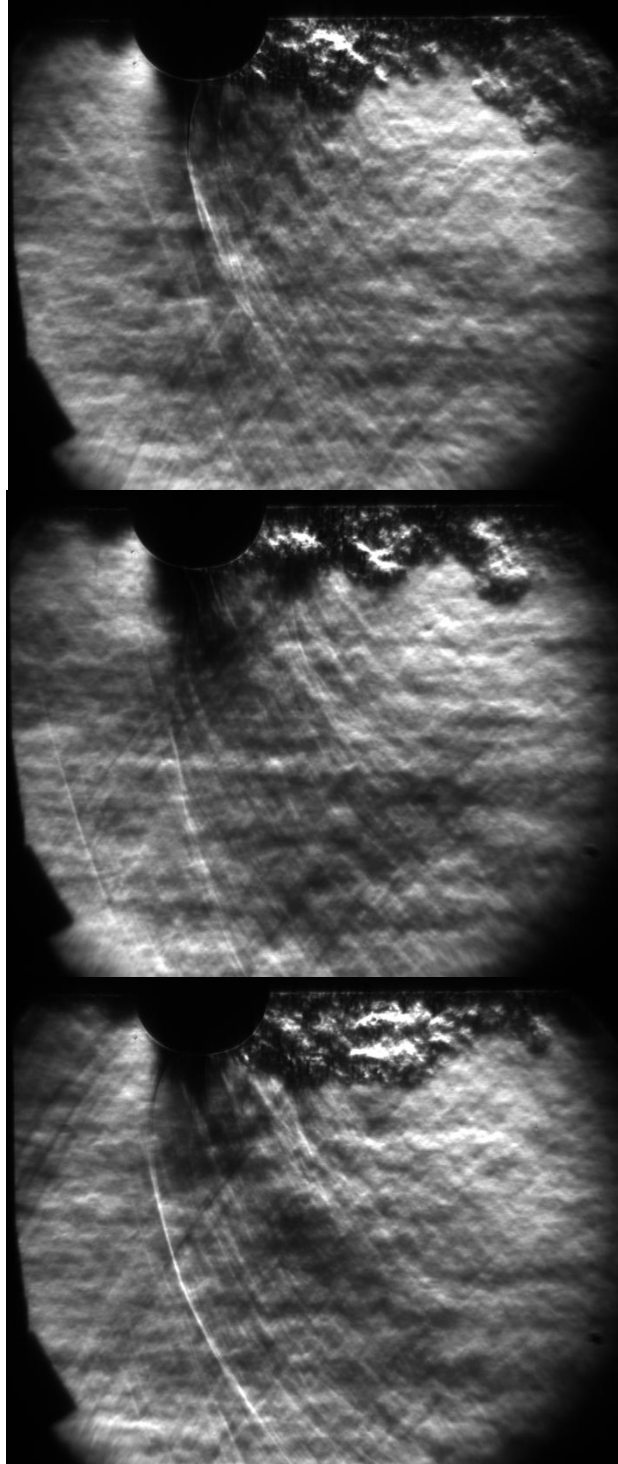


Figure 46: Schlieren Images of Hemisphere ($P_\infty \approx 1.33 \text{ atm} \approx 19.5 \text{ psia}$) – Knife Edge Horizontal

Shadowgraph images were also obtained with the hemisphere mounted (also at a slightly different freestream pressure from the single-shot acetone PLIF experiments). Pressure data was not acquired throughout these test runs either. These images were qualitative in nature and revealed a shear layer, a turbulent wake, and shocks at approximately 90° from the horizontal (the horseshoe/necklace vortex appeared to be very weak, if at all present, in these images). These shocks somewhat dissipated as the distance downward in the test section from the surface of the hemisphere was increased. From this realization, it was concluded that porous walls, a characteristic of most transonic wind tunnel test sections and used to limit shock reflections, were not necessary. Lambda shocks⁹⁰ were also present in a few of these images at the same approximate location as in the Schlieren images.

These Schlieren and shadowgraph images proved that the expected flow features for the flow over a small scale hemisphere were present. This meant that acetone PLIF images should yield differences in fluorescence in the shear layer and wake region corresponding to density fluctuations in the same approximate locations. Note that in some of these Schlieren and shadowgraph experiments, an older hemisphere model was used that was not perfectly hemispherical in shape. Schlieren images in Figure 46 were obtained with the modified model which was hemispherical in shape. This modified model was additionally anodized black for the final single-shot PLIF experiments.

VII. Test Facility Part II: Liquid Acetone/Alumina Particle Seeding

A. Seeding System Design and Operation

The wind tunnel facility is outfitted with a means of uniformly seeding the flow field with acetone molecules for acetone PLIF and acetone molecules/alumina particles for PIV. Liquid acetone is injected far upstream of the test section, it disperses and mixes with pressurized dry air, and it evaporates by the time it reaches the test section. The process for acetone seeding in this work is as follows. A small pressure vessel is filled with liquid acetone and pressurized using a nitrogen tank. An EPDM hose, attached to an exit pipe, is submerged in the liquid acetone, as seen in Figure 47. This exit pipe is attached to a Jefferson 1335 series⁹¹ solenoid valve, which is attached to the outside of the pressure vessel. When the solenoid valve is triggered to open, the liquid acetone is pushed upward through the EPDM hose, out of the pressure vessel, and ultimately through a wall fitting.

The wall fitting is connected through the wall of the cylindrical, compressed air supply line pipe (the same compressed air supply line pipe that receives pressurized air from the storage tanks when the wind tunnel is operational and leads to the stagnation/settling chamber) and extends to the center of this cylindrical pipe. A spray nozzle is attached to the end of the wall fitting and is oriented to spray in the upstream direction. This helps to break up the liquid acetone and make sure it disperses quickly and mixes with dry air, so it can evaporate before entering the test section. This ensures that the acetone is in molecular form and not particle form, so only dry air and acetone vapor are in

the test section when acetone PLIF images are obtained (for PIV experiments, alumina particles are also present).

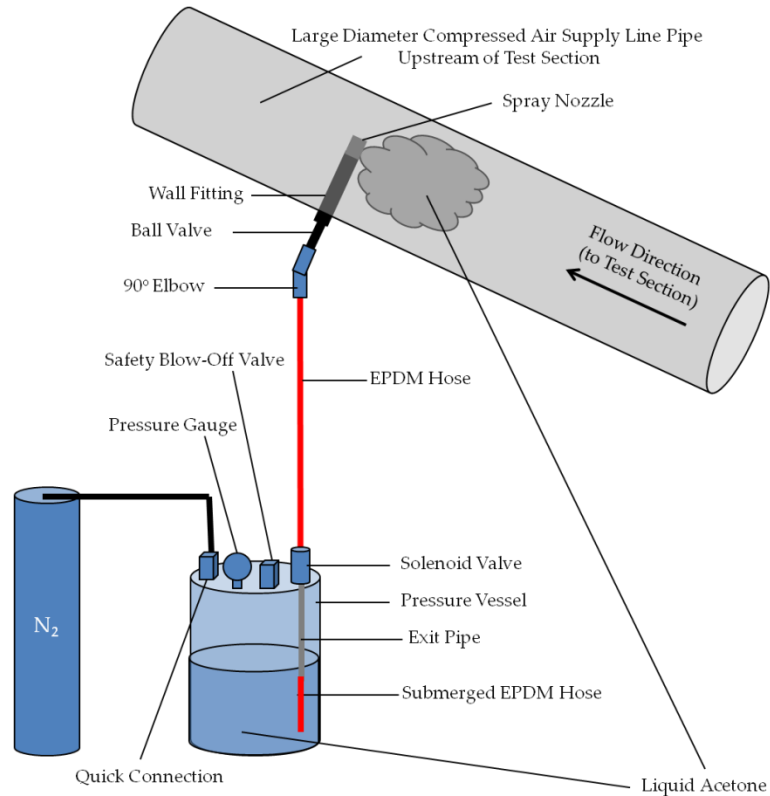


Figure 47: Schematic of Seeder

There is a slight leak at the connection of the wall fitting and the compressed air supply line pipe. It is believed that this does not affect the estimate of acetone mole fraction because the mass flow rate in the wind tunnel test section is so much greater than the mass flow rate of the leak (the mass flow rate of the leak was not actually quantified). Several attempts were made to try and control the leak, including a combination of pipe dope, two o-rings, a nylon spacer, and JB Weld. In the end, even using all four together did not prevent the leak.

B. Acetone Mole Fraction

The amount of liquid acetone injected into the flow is controlled by the pressure difference, Δp , between the pressure in the small pressure vessel containing the liquid acetone and the storage pressure in the compressed air supply line pipe/storage tanks. For each acetone PLIF test run in this work, the compressed air supply line pipe/storage tanks started at a storage pressure of approximately 120 psig and decreased throughout the test run to 70 psig. The nitrogen tank uses a pressure regulator to deliver a constant pressure to the small pressure vessel. A maximum nitrogen pressure of approximately 150 psig was used for acetone PLIF experiments and approximately 135 psig was used for PIV experiments. Therefore, Δp increased throughout the test run and in turn so did the flow rate of liquid acetone into the compressed air supply line pipe and the acetone mole fraction.

An average acetone mole fraction value was estimated (for the time period over which valid acetone PLIF images were acquired during the test run) and used in the fluorescence quantum yield model. Accuracy of the acetone mole fraction, as long as the acetone mole fraction is small, is not that important when using the current fluorescence quantum yield model, as explained in Section III.F.a. Note that in this work the acetone mole fraction was assumed to be constant and to be the average acetone mole fraction value.

The simplest way to obtain the acetone mole fraction is to first obtain the mass flow rate of the liquid acetone injected into the flow. The instantaneous mass flow rate of acetone can be found using a flowmeter (this flowmeter must be compatible with acetone, however). A less accurate method to obtain the mass flow rate is to use a mass scale to measure the mass of acetone injected into the flow during a test run and divide the mass by the run time to obtain an average

acetone mass flow rate. The least accurate method for quantifying the mass flow rate of acetone, the method that was used in this work, is to measure the volume of liquid acetone injected into the flow during a test run. Average acetone mass flow rate can be estimated by using the measured volume of liquid acetone, the density of acetone, and the elapsed time of the test run. This volume is found by measuring the drop in height of the liquid acetone in the small pressure vessel and multiplying it by the cross-sectional area of the pressure vessel. The pressure vessel is a hollow cylinder with a diameter of approximately 9 inches.

During the acetone PLIF experiments, the wind tunnel was automated to begin running when the storage pressure reached 120 psig and stop running when the storage pressure reached 70 psig, keeping the elapsed test run time and drop in liquid acetone level relatively constant from run to run. The liquid acetone level, over the approximately 18 second run time (i.e. the amount of time for the storage pressure to drop from 120 psig to 70 psig during a test run), dropped approximately 5 inches. Thus, the volume of acetone injected into the flow during the 18 second time period was approximately 0.0052 m^3 . The density of acetone is 790 kg/m^3 at 20°C (slightly less than room temperature, but close enough for this calculation).^{58,92-93} Thus, the mass of acetone injected into the flow during the 18 second run time was approximately 4.118 kg. This gave an average mass flow rate of acetone of approximately 0.23 kg/s. This mass flow rate of acetone was then divided by the molar mass of acetone, 0.05808 kg/mol ^{58,92}, to obtain the average molar flow rate of acetone of approximately 3.939 mol/s.

The mass flow rate of the dry air/acetone vapor in the test section was assumed to be equal to the sum of the mass flow rate of dry air in the compressed air supply line pipe and the mass flow rate of acetone injected into the compressed air supply line pipe, as seen in Equation 15.

$$\dot{m}_{\text{DryAir/AcetoneVaporTestSection}} = \dot{m}_{\text{DryAirUpstream}} + \dot{m}_{\text{LiquidAcetoneInjectedUpstream}} \quad 15$$

The equation $\dot{m} = \rho_{\infty}AV_{\infty}$, where ρ_{∞} is the density of the freestream, A is the cross-sectional area of the test section (4" x 4", which is 16 square inches or 0.0103 m²), and V_{∞} is the freestream velocity, was used to estimate the mass flow rate of the dry air/acetone vapor in the test section. Freestream velocity values throughout the test run were estimated with Equation 14 (Section VI.C.) and were verified from PIV experiments (Section VII.). The mass flow rate of dry air/acetone vapor in the test section throughout the test run was estimated and the average mass flow rate of acetone (injected into the compressed air supply line pipe) was subtracted. This yielded the mass flow rate of dry air in the compressed air supply line pipe throughout the test run, which was then divided by the molar mass of dry air, 0.02897 kg/mol⁷⁷, to yield the molar flow rate of dry air throughout the test run.

The acetone mole fraction throughout the test run was then estimated by dividing the average molar flow rate of acetone by the sum of the average molar flow rate of acetone and the molar flow rate of dry air throughout the test run. An approximate average acetone mole fraction value was estimated for the time period over which valid acetone PLIF images were obtained during the test run. The average acetone mole fraction value was rounded up to approximately 3% and assumed constant. In actuality, this is not really the case as the freestream velocity varies throughout the test run, which changes the mass flow rate of air/acetone vapor in the test section. In addition, Δp increases during the test run, so the mass flow rate of acetone injected into the compressed air supply line pipe increases.

To improve the accuracy of the estimated acetone mole fraction, instantaneous acetone mass flow rate data is needed for the liquid acetone

injected into the compressed air supply line pipe. This could be accomplished with a proper flow meter. In addition, thermocouples in the stagnation/settling chamber or the compressed air supply line pipe/storage tanks would enable more accurate estimates of freestream conditions (i.e. P_∞ , T_∞ , ρ_∞ , V_∞). This would in turn enable more accurate estimates of the mass flow rate of dry air/acetone vapor in the test section during the test run.

C. Spray Nozzle Selection

Several spray nozzles were attempted to find a spray nozzle that gave a high enough flow rate of liquid acetone at the specific Δp , while also somewhat breaking up the flow to enable evaporation of the liquid acetone before entering the test section. The spray nozzle that was chosen was a Bete IS8⁹⁴, 1/4" spray nozzle constructed of stainless steel with a rectangular spray pattern. Literature establishes that a pair of these nozzles operating together can generate a flow rate of 13 gpm at 20 psi.⁹⁴ However, the solenoid valve and ball valve before the spray nozzle potentially could have limited this maximum flow rate somewhat. This spray nozzle internally bends the flow, similar to a 90° elbow, and the flow sprays out of the side of the nozzle. The nozzle somewhat breaks up the flow as the nozzle creates a rectangular spray pattern, so this nozzle is somewhat better than using no spray nozzle at all and simply using a 90° elbow. Also, a positive value of Δp is needed to inject liquid acetone and (i.e. the flow rate of acetone at p yields and if a 90° elbow were simply used, too much acetone might have been seeded into the flow field at the necessary Δp .

D. Acetone Vapor Pressure Curve

There is a limit to the amount of liquid acetone that can be evaporated in the flow (i.e. there is a limit to the acetone mole fraction). This is regulated by the vapor pressure curve for acetone. If the acetone mole fraction is too high (for specific conditions of T and P), then the acetone vapor may condense in the test section and/or the liquid acetone (injected into the compressed air supply line pipe) may not fully evaporate before entering the test section. This is because the acetone partial pressure at a particular temperature is too high. Understanding where this limit to acetone mole fraction exists is very important because the fluorescence quantum yield model in this work is for acetone vapor. Until more photophysical information for liquid acetone fluorescence is obtained, it remains imperative that PLIF images are obtained during the test run when condensation is minimal.

Condensation can also cause the windows and hemisphere model to become dirty as liquid acetone dries on their wetted surfaces. A yellowish-brown residue had to be cleaned from the windows and hemisphere model with a mixture of acetone and methanol after each test run. This residue is attributed to the slight condensation of acetone vapor and small amounts of rust on the inner walls of the compressed air supply line pipe, which may have been picked up as the flow traveled to the stagnation/settling chamber and test section. If this residue is not cleaned from the windows after each test run, then imaging through the rectangular side windows is affected. Also, the 266 nm laser sheet cannot pass as easily through the bottom stepped window if it is dirty, affecting the amount of available 266 nm laser energy that can be absorbed by the acetone molecules (subsequently affecting fluorescence signal levels). Note that when no

acetone was seeded into the flow during a test run, the windows and hemisphere model did not need to be cleaned.

The Antoine equation⁹², seen in Equation 16, is a basic equation that comprises three coefficients (A, B, and C) that differ depending on the type of chemical. When this equation is simplified, as seen in Equation 17, it can be used to obtain the vapor pressure curve (vapor pressure, p , is in mm Hg and temperature, t , is in Celsius). For acetone, these coefficients have the following values: A=7.11714, B=1210.595, C=229.664.⁹²

$$\log p = A - \frac{B}{t + C} = 7.11714 - \frac{1210.595}{t + 229.664} \quad 16$$

$$p = 10^{\frac{A - B}{t + C}} = 10^{7.11714 - \frac{1210.595}{t + 229.664}} \quad 17$$

The vapor pressure curve for acetone was plotted, as seen in Figure 48, for a wide range of temperatures, i.e. the full range of freestream temperatures experienced during a wind tunnel test run (plotted in Figure 42). Also in Figure 48, partial pressure of acetone for several acetone mole fraction values was plotted versus temperature at the freestream conditions experienced during a test run in the valid acetone PLIF data region (i.e. when condensation was minimal; this time frame was established through 532 nm scattering tests for condensation explained in Section VII.E.). In this work, an average acetone mole fraction of approximately 3% was used, which creates a partial pressure versus temperature curve that is slightly to the left of the acetone vapor pressure curve, as seen in Figure 48. To the left of the acetone vapor pressure curve is where acetone is in liquid form and to the right of the acetone vapor pressure curve is where acetone is in vapor form. Thus, one would expect condensation to occur in the flow field for all images in the valid acetone PLIF data region. However, it

should be noted that the average acetone mole fraction estimation was a rough calculation and a smaller acetone mole fraction may actually be present. Also, the range of freestream temperatures during a test run was estimated using isentropic relations and storage, stagnation, and freestream static pressure data, so there may be some inaccuracies in these estimates. Regardless, no conclusions about condensation in the flow can be made until a comparison is made with results of actual condensation tests (i.e. 532 nm scattering tests). These experiments are discussed in Section VII.E.

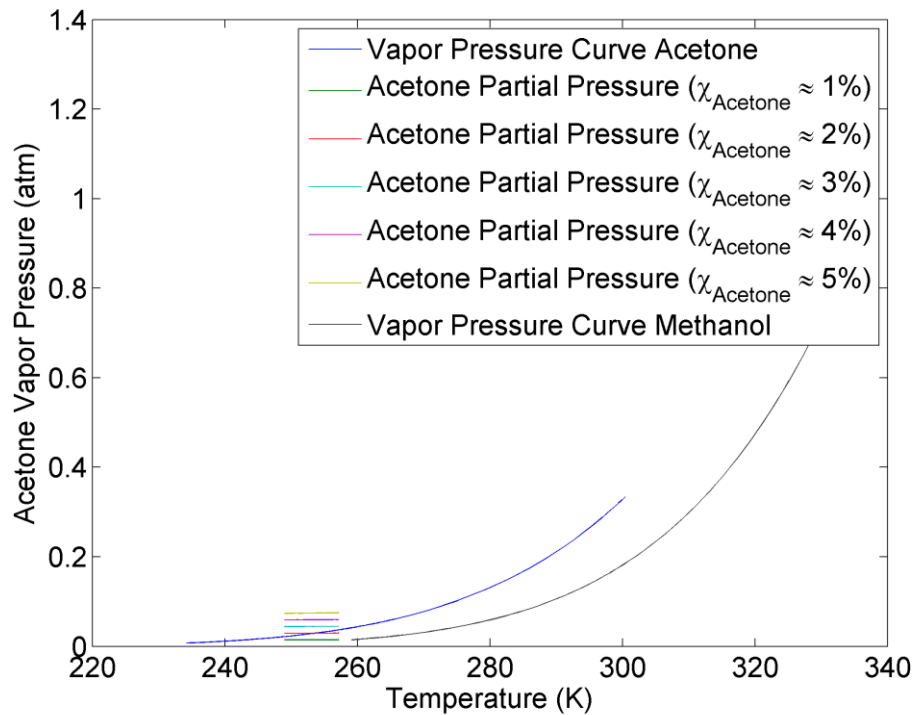


Figure 48: Plot of Acetone Vapor Pressure Curve (partial pressure curves created using freestream pressure and temperature values for valid data region)

The vapor pressure curve for methanol was also plotted in Figure 48 over a range of temperatures for which the curve is valid (approximately 259-338K⁹²). Methanol is a liquid chemical that can possibly be used for PIV seeding instead of acetone because it also evaporates quickly in air. If alumina particles are mixed with methanol, the mixture is injected into the flow far upstream, and methanol evaporates by the time the mixture reaches the test section, then only the alumina particles remain to scatter 532 nm light. The Antoine equation coefficients for methanol are $A=7.8975$, $B=1474.08$, $C=229.13$.⁹² It is clearly seen in Figure 48 that the methanol vapor pressure curve is much more restrictive than the acetone vapor pressure curve because a higher temperature is needed for the same partial pressure in order for methanol to remain in vapor form. Thus, a smaller methanol mole fraction must be used under these conditions to remain in vapor form.

E. Acetone Condensation Tests

Acetone condensation tests (532 nm scattering) were performed to assess whether or not the acetone vapor was condensing in the test section during a typical test run. The injected liquid acetone was assumed to evaporate before entering the test section. However, the storage/stagnation temperature dropped during each test run (causing a drop in freestream temperature) and the accelerated flow over the hemisphere experienced the coldest temperatures in the flow field. In addition, the acetone mole fraction was slightly increasing throughout each test run (even though it was assumed for calculation purposes to be constant).

A New Wave Solo III PIV Laser⁹⁵ (Nd:YAG), with reported capabilities of 50 mJ/pulse at 532 nm, was used for illumination purposes in the condensation

experiments. An $f=-100\text{mm}$ spherical lens, an $f=+150\text{ mm}$ spherical lens, and an $f=-30\text{ mm}$ plano-concave cylindrical lens were used to create a 532 nm laser sheet approximately 1mm thick. This laser sheet passed through the test section in an angled orientation to illuminate the shear layer and wake region of the flow field. Laser light scattering was collected by the CCD of a Cooke Corporation Sensicam QE high-resolution, unintensified camera (specifications explained in Section VIII. and IX.).

As a baseline case, no acetone was seeded into the flow for a typical test run. It was apparent that a small amount of dust particles were present in the flow field because small amounts of particles (low particle density) scattered laser light. After the baseline case was established, the compressor was turned off, the storage tanks were emptied, and the system was not used for approximately 4 hours.

It was important to investigate the extent to which condensation was affected by having the storage tanks pressurized and then sitting for prolonged periods of time before each test run was performed (i.e. it was desired to see if there was any sort of condensation dependency based upon how much time the majority of the pressurized air was contained in the storage tanks). When the storage tanks are initially fully pressurized, the compressed air has a high temperature. However, over time this temperature changes because the storage tanks are steel and are located outside. The storage temperature is high to begin with, so condensation is less likely to occur than if the storage temperature is low to begin with. Five different cases with acetone seeding were investigated after the baseline test was established with no acetone seeding. The compressor was turned on and runs were performed after 20 minutes, then 70 minutes, then 40 minutes, then 50 minutes, and then 70 minutes in order to test time intervals that might have passed between each tunnel run/acetone PLIF experiment.

When the compressor was first turned on, fresh hot air was pressurized in the storage tanks. This air was less likely to condense because it started at a high temperature and was the motivation for the case after 20 minutes, the initial amount of time for the storage tanks to pressurize to 120 psig after turning on the compressor. After this run, it was desired to allow the compressor to operate for a specific amount of time without performing a test run (approximately 70 minutes), other than purging the storage tanks to approximately 75 psig at the 30 minute mark. A test run was performed at the 70 minute mark and then test runs were performed after 40 minutes, after 50 minutes, and after 70 minutes.

During a test run, the storage pressure dropped from 120 psig to 70 psig. After each test run, the tanks were allowed to pressurize and then the residual acetone was blown out of the compressed air supply line pipe by running the tunnel down to a storage pressure of approximately 70 psig with the acetone seeder turned off. Then the tanks would pressurize again, bringing fresh hot air into the storage tanks, but in less quantity than when the compressor was first turned on (i.e. the test after 20 minutes) because the tanks were already at 70 psig at this point. The fresh hot air changed the temperature of the air in the storage tanks. Over time this temperature of the air in the storage tanks also changed due to the fact that the storage tanks are steel and are located outside. Whenever the storage pressure reached approximately 120-125 psig in between test runs, the storage pressure would drop slowly back to 100 psig and then increase back to the maximum storage pressure of approximately 120-125 psig (this cycle was continuous). Immediately before each test run, the storage pressure was purged to approximately 90 psig to cause the storage tanks to pressurize back to a storage pressure of 120 psig, the starting storage pressure for a test run.

All of the condensation tests revealed the fact that acetone was condensing after a specific period of time. The first test run (after 20 minutes) did

show signs of condensation, but not until the end of the test run. All of the other four runs showed condensation at approximately 2/5 of the way through the 18 second test run (at approximately the 5.85-7.2 second mark or image 40-49), then the condensation was minimal for approximately 1/5 of the 18 second test run (at approximately the 7.35-11.1 second mark or image 50-75), and then the condensation strongly reappeared and remained for the rest of the test run. Thus, a small window of time existed where there was a lull in the condensation. The only acetone PLIF images that were processed and converted to density field images were those that were obtained in the time window during the test run when condensation was minimal (i.e. 7.35-11.1 seconds). This is because Thurber's acetone fluorescence quantum yield model is for acetone vapor.

Note that while heavy condensation did occur at certain time intervals during each wind tunnel test run, it was assumed that the liquid acetone particles that formed were very small in size and thus behaved in a similar manner to acetone vapor in terms of fluorescence characteristics. Discussions with other researchers solidified these assumptions. This was further solidified by the fact that fluorescence images when condensation was considered minimal and when condensation was considered to be heavy were very similar in appearance and the flow characteristics that could be seen.

F. PIV Seeding

PIV seeding was achieved the same way as acetone PLIF seeding, except there was one minor change. Alumina particles and liquid acetone were mixed together before being added to the pressure vessel. This alumina particle/liquid acetone mixture was injected into the compressed air supply line pipe. By the time this mixture entered the test section it was only dry air, acetone molecules,

and alumina particles. This ensured that 532 nm laser scattering only occurred off of the alumina particles and not off of acetone particles. This PIV seeding setup is explained in much greater detail in Section VIII. The wind tunnel seeding system is very versatile because it can seed acetone PLIF or PIV experiments. It also provides the ability to perform simultaneous acetone PLIF and PIV experiments should one desire to perform such experiments.

VIII. Particle Image Velocimetry Experiments

A. Background of PIV

Particle image velocimetry is a flow diagnostic technique that is used to obtain velocity vectors for a flow field. A thin 532 nm laser sheet passes through the flow field of interest and the laser light scatters off of particles (either naturally occurring or seeded) in the flow. Image pairs are obtained of this laser scattering with a slight time difference (i.e. interpulse timing), Δt , in between image A and image B.

The PIV image pairs are processed with PIV software (in the case of this work, PIVPROC⁹⁶ was used) and the displacement vectors of the flow field are calculated. Essentially, the x and y pixel displacements of the particles from image A to their new position in image B are calculated. True physical displacement distances are given to the pixel displacements based upon a dot card/ruler image taken of the field of view prior to a test run, which establishes the spatial resolution ($\mu\text{m}/\text{pixel}$). These true physical displacement distances are then divided by Δt between image A and image B to calculate velocity values in the x and y direction, as velocity equals distance divided by time. The velocity vectors can then be used to calculate flow parameters, such as vorticity. If enough image pairs are obtained, then mean values of these parameters can be calculated, along with Reynolds stresses and turbulent kinetic energy. For a more complete explanation of the PIV technique see Raffel et al. (2007)⁹⁷ and Adrian and Westerweel (2011)⁹⁸.

B. Details of Experimental Arrangement

A small set of single-shot PIV image pairs was obtained along the centerline of the hemisphere (imaging plane parallel to flow direction) in order to better characterize the flow field. From these PIV images, the instantaneous values of velocity magnitude and vorticity were calculated and analyzed. This enabled comparison with acetone PLIF data to better understand density field behavior.

a. Illumination and Optical Arrangement

A New Wave Solo III PIV Laser (Nd:YAG), capable of 50 mJ/pulse⁹⁵, was used for illumination purposes for single-shot PIV experiments. The 532 nm laser beam exited the PIV laser head and reflected off of multiple 532 mirrors and passed through an $f=-100$ mm spherical lens and then through an $f=+150$ mm spherical lens. The first spherical lens expanded the laser beam and the second spherical lens focused the laser beam. This beam then reflected off of two more 532 nm mirrors and then passed through an $f=-30$ mm plano-concave cylindrical lens to create a thin 532 nm laser sheet. Width of the laser sheet increased as the sheet propagated away from the cylindrical lens. This laser sheet passed through the bottom window of the wind tunnel test section in a fairly normal orientation and illuminated the centerline plane in the flow field (the sheet was aligned with the centerline of the hemisphere). The thickness of the laser sheet was controlled by the distance between the spherical lenses and the sheet was thinnest in the imaging region. Both spherical lenses, the final two 532 nm mirrors (as well as a 532 nm mirror before the spherical lenses), and the cylindrical lens were

mounted to a translating breadboard for fine tuning of the location of the laser sheet to make sure it was located along the centerline of the hemisphere.

b. Seeding for PIV Experiments

Seeding for PIV experiments was accomplished with the same seeding setup as for acetone PLIF experiments, shown in Figure 47, except liquid acetone and alumina particles were mixed together prior to being poured into the small pressure vessel. Two different types of alumina particles, Sumitomo AKP 20 and Sumitomo AKP 30, were attempted for seeding purposes and in several different mixture ratios with acetone. AKP 20 and AKP 30 have particle diameters of 0.4-0.6 μm and 0.3-0.5 μm , respectively.^{99,100}

Initially, each type of alumina particle was simply poured into the pressure vessel that was filled with acetone and then a rod was used to stir the mixture. This did not mix very well and there was a settling problem, so a blender technique was also attempted. Liquid acetone and alumina particles were mixed in a blender for approximately 30 seconds and then this mixture was poured into the pressure vessel. This initially helped to mix the two components of the mixture better, but there was still a significant settling problem as time progressed after the blender was turned off, the mixture was transferred to the pressure vessel, and eventually the test run was carried out.

Settling caused an excessive amount of alumina particles to be near the bottom of the pressure vessel, so when the liquid acetone reached low levels in the pressure vessel, the concentration of alumina particles in the flow increased greatly. This caused excessive signal (eventually a whiteout effect) and caused the test section windows to become dirty, requiring them to be cleaned after each test run. Condensation of acetone vapor may have also contributed to this

whiteout effect. Note that for PIV experiments a smaller pressure difference, Δp , between the nitrogen tank/small pressure vessel and the compressed air supply line pipe/storage tanks was used than for acetone PLIF experiments. This pressure difference was approximately 10-15 psig.

Methanol was also attempted as an alternative to acetone for mixing purposes with the alumina particles. This is because methanol also evaporates quickly in air (similar to acetone) and is less expensive than acetone. However, for a single partial pressure value, methanol evaporates/condenses at a higher temperature than acetone, as shown in Figure 48. As a result, only small sets of PIV data can be obtained with the methanol/alumina particle mixture (compared to the acetone/alumina particle mixture) before condensation becomes a serious problem. The methanol/alumina particle mixture produced decent results early in test runs, but the fact that condensation limited data set size caused methanol to no longer be considered a viable option for PIV experiments. However, methanol by itself could prove to be a good seeding chemical for 2-D or 3-D flow visualization experiments if it condenses in the region of interest. Methanol created some nice flow visualization images of the flow field when PIV experiments were being conducted.

Overall, there was great difficulty in obtaining a reasonable particle density for 532 nm scattering in this flow field. This was difficult because of the high speed and flow rate of the flow field and the fact that the alumina particles had a settling problem in the liquid acetone they were mixed with. For these reasons, a large PIV data set was not able to be obtained in the current experimental facility. However, possible upgrades and improvements to the PIV experiments, explained in Section XII.B., should help in acquiring large sets of quality PIV data.

c. Camera, Image Acquisition, and PIV Processing

Laser sheet scattering off of the alumina particles was captured using a Cooke Corporation Sensicam QE¹⁰¹ high-resolution, unintensified camera. Further specifications for the Sensicam QE camera are explained in Section IX.A.c. Images were obtained in pairs with a small difference in time (interpulse timing) between image A and image B, as is necessary for PIV experiments. Interpulse timing was selected with a specific constraint in mind. The maximum pixel displacement from image A to image B was set to approximately 8 pixels. This constraint was chosen based upon the PIV software settings.

A program called PIVPROC⁹⁶ was used to calculate pixel displacement for these image pairs. Cross-correlation was applied for the image pairs using a 64 px x 64 px window size on the first pass with a 50% overlap and a 32 px x 32 px window size on each subsequent pass with a 50% overlap (for each image pair in this work, two subsequent passes were performed after the first pass). For PIV experiments, it is desired to have a maximum pixel displacement of approximately 25% of the window size.^{97,98} Thus, for a 32 px x 32 px window size, a maximum pixel displacement of approximately 8 pixels would be used. By applying this constraint of approximately 8 pixels, approximating the freestream velocity (keeping in mind the shear layer velocity is faster) by using Equation 14, and knowing the field of view, the interpulse timing necessary for a max pixel displacement of 8 pixels was approximated for this flow field. This interpulse timing can be tweaked and adjusted during the data acquisition process by processing a single image pair with PIVPROC and analyzing the resulting pixel displacements. Then the interpulse timing can be adjusted and this process can be repeated until a max pixel displacement of approximately 8 pixels throughout the entire imaging region is achieved. In these PIV experiments, the field of view

was 92.95 mm x 49.72 mm and Δt was 2 μs (3 μs was used for one of the data sets, but this data is not presented in this thesis).

Laser pulses and the camera were triggered by two Quantum Composers 9514+ pulse generators¹⁰² at specific time delays, shown in Table 2. The camera, explained in Section IX.A.c., was set to double-shutter mode. The time between the Q-Switch Delay for Laser 1 and the Q-Switch Delay for Laser 2 was the effective Δt between image A and image B.

Table 2: Laser Settings for PIV Experiment

	<u>Pulse Width</u>	<u>Fire Delay</u>	<u>Q-Switch Delay</u>
<u>Laser 1</u>	120 μs	100 μs	280 μs
<u>Laser 2</u>	120 μs	102 μs	282 μs

During image acquisition, only part of the CCD was used (1376 x 736 pixels were used when the CCD is actually 1376 x 1040 pixels). The wake thickness for the wall-attached hemisphere was observed in the Schlieren images to be approximately half of the diameter of the hemisphere. It was desired to view up to approximately 2-2.5 diameters downstream in the PIV images. Therefore, in order to achieve a large field of view to capture this distance downstream, all of the pixels in the horizontal direction on the CCD needed to be used. However, if all the vertical pixels were also used on the CCD, then a lot of the image would have been freestream data. A lot of the freestream area data was unnecessary because the freestream data was spatially changing by a negligible amount throughout each image (temporally, i.e. throughout the test run, the freestream data was slightly changing). Therefore, only part of the freestream data was necessary and the rest was essentially “cropped” and not

acquired by effectively turning off a portion of the pixels in this region. By using fewer pixels on the CCD, images pairs were acquired at a faster rate. This was important as quality/optimum seeding could only be achieved for a short period of time in this flow field.

Once the camera settings were applied, image acquisition proceeded. A ruler image with no flow was first obtained (spatial resolution was found to be 376 pixels/inch) and then PIV image pairs with flow and PIV seeding were obtained. The camera was setup on the opposite side of the test section from the camera setup in the single-shot acetone PLIF experiments (Section IX.), giving the PIV images a natural left to right flow convention. These image pairs were processed with PIVPROC with the settings explained previously in this subsection and with the additional settings of subregion distortion and grid smoothing. Once pixel displacements were calculated for all image pairs, the data file for each image pair was read into MATLAB using the function `piv_vec2mtx()` created by Kyle Lynch. The pixel displacements were converted to velocity vectors using the interpulse timing and the spatial resolution (pixels/inch) from the ruler image. In the end, velocity vectors for this flow field resulted, from which instantaneous velocity magnitude and vorticity were calculated. Instantaneous vorticity was calculated using Equation 18.

$$\bar{\omega} = \left(\frac{dv}{dx} - \frac{du}{dy} \right) \hat{k} \quad 18$$

C. Expectations for PIV Experiments

PIV experiments were expected to yield instantaneous flow properties, such as instantaneous velocity, for the flow field with the hemisphere mounted. This information could then be used to obtain instantaneous vorticity for the

flow field and the instantaneous velocity magnitude. It was expected that the velocity field would clearly define the wake region and the vorticity field would display locations of vortices. It was expected that the flow field would be characterized more thoroughly and after comparison to acetone PLIF data, the flow characteristics causing the density to fluctuate in a particular manner and to what extent would be better understood.

D. Results of PIV Experiments

PIV experiments, although single-shot and very small in number of quality image pairs, revealed interesting and useful information about the flow field. With the hemisphere mounted, the freestream velocity was found to be approximately 250 m/s, which is in relatively good agreement with the freestream velocity calculated from Equation 14. The velocity magnitude greatly decreased in the wake region and was a maximum in the separated shear layer region (approximately 290 m/s), as seen in Figure 49. There was a stagnation point on the front (upstream) and the back (downstream) of the hemisphere where the velocity magnitude dropped to approximately zero. The plot of instantaneous vorticity, seen in Figure 50, revealed regions of large vorticity, particularly in the upper wake and separated shear layer region. In general, regions of large vorticity experience significant pressure drops (and in turn significant density drops). The sign convention for vorticity in the shear layer makes sense because positive vorticity in this frame of reference means vorticity is counterclockwise. No large vorticity values were present on the upstream half of the hemisphere before separation.

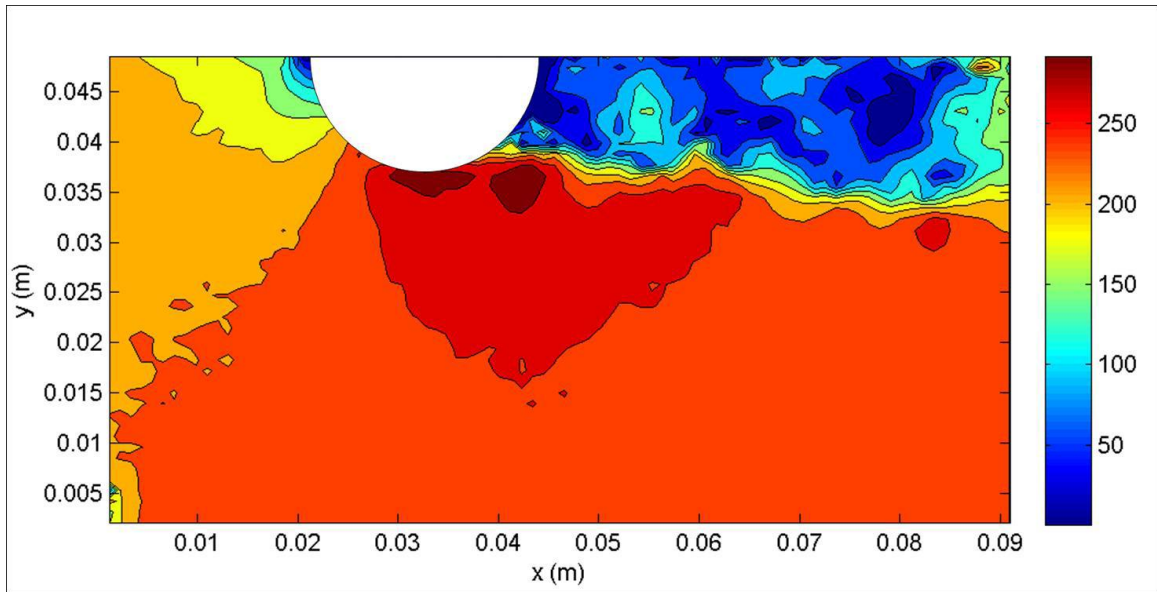


Figure 49: Instantaneous Velocity Magnitude Field (m/s) - Centerline [Reid et al. (2010)¹⁰³]

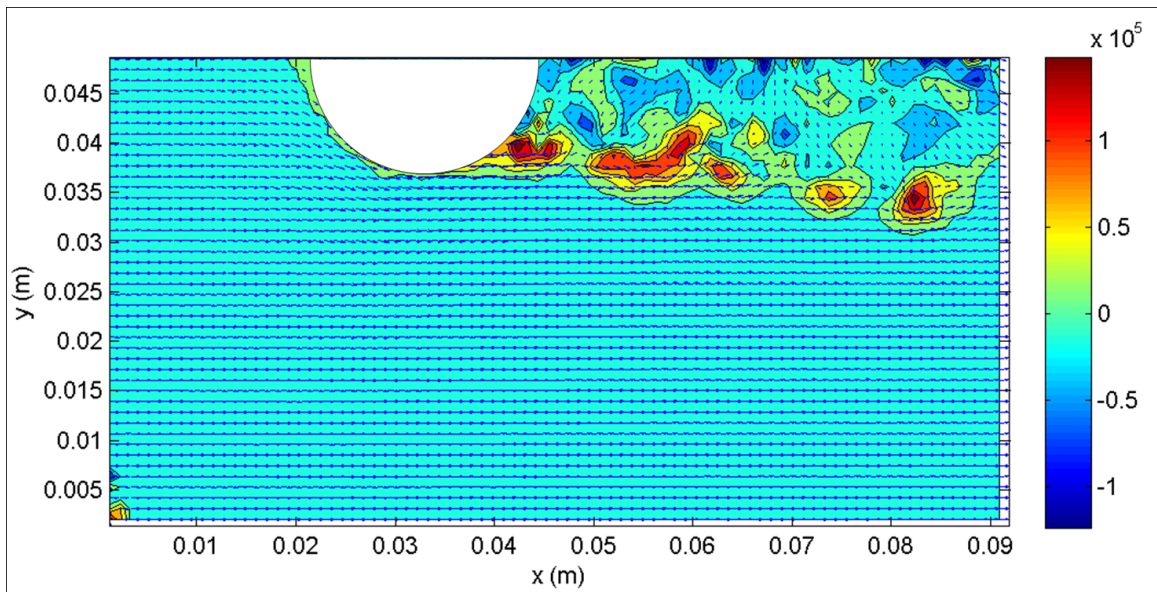


Figure 50: Instantaneous Vorticity Field (rad/s) – Centerline [Reid et al. (2010)¹⁰³]

Note that these PIV experiments were conducted at a slightly lower stagnation pressure and thus freestream pressure than the single-shot acetone

PLIF experiments explained in Section IX. The freestream pressure in the PIV experiments was approximately 1.33 atm or 19.5 psia (pressure data was not acquired throughout the test run). Qualitatively the flow features and flow behavior are expected to be similar in the PIV and single-shot acetone PLIF experiments.

Time-resolved PIV imaging was also attempted with no success. The setup for time-resolved PIV in terms of camera and pulse burst laser system was similar to the time-resolved acetone PLIF experiments presented in Section XI., except the laser wavelength was 532 nm instead of 266 nm. All of the optics were for 532 nm light only and the half waveplate and BBO crystal, necessary for the time-resolved acetone PLIF experiments to convert 532 nm light to 266 nm, were not necessary for time-resolved PIV. Seeding was the same as for single-shot PIV imaging. No conclusive/quality time-resolved PIV data could be obtained, but it should be possible with a better PIV seeding technique and high-speed camera.

IX. Single-Plane, Single-Shot Acetone PLIF Experiments

A. Details of Experimental Arrangement

Single-shot, high-resolution acetone PLIF images were obtained along multiple parallel planes of the flow field. A large set of images (approximately 130 images over five wind tunnel runs, although some of these images were discarded due to image processing difficulties, resulting in only 98 quality images) was obtained in the wake region for the plane that was coincident with the centerline of the hemisphere and smaller sets of images (approximately 26 images per set) were obtained in the wake region for planes that were off-centerline (equally spaced 1/8 inches apart, starting at the centerline and ending at 5/8 inches from the centerline, just past the hemisphere outer edge). The flow field was assumed to be symmetric about the hemisphere's x-axis (x-axis being parallel to the flow direction, passing through the centerline of the hemisphere, and increasing in value as the distance downstream increases). Therefore, images were only obtained for parallel planes on one side of the hemisphere. In addition, a set (approximately 26 acetone PLIF images) with a slightly smaller FOV was acquired along the centerline and focused on the separation region/shear layer. Note that the parallel plane images and the large centerline data set (as well as the separation region images) were obtained on different days.

In these experiments, liquid acetone was seeded into the compressed air supply line pipe far upstream of the test section. The liquid acetone mixed with the dry air in the compressed air supply line pipe and evaporated by the time it reached the test section. A 266 nm laser sheet was passed through the bottom window of the test section and was oriented at an angle of approximately 45-50°

with respect to the horizontal, so that it passed through the shear layer/wake region and centerpoint of the hemisphere (it was discovered late in the image acquisition process for the large set of wake region centerline images that the laser sheet was close to the centerline, but slightly yawed off axis). For separation region acetone PLIF images, the laser sheet angle was slightly adjusted so the most intense portion of the laser sheet was near the separation region on the hemisphere. A fraction of the acetone vapor molecules seeded into the flow field fluoresced and this fluorescence was captured on the CCD of a camera. The fluorescence intensity values in the images were then converted to density by using the image processing and in-situ calibration process and then curves of $S_f/S_{f\infty}$ vs. ρ/ρ_∞ , as explained in Section IV.B.-E.

a. Laser Excitation and Optical Arrangement

A New Wave Solo 200XT PIV Laser⁹⁵ (Nd:YAG) was used in the acetone PLIF experiments (the 532 nm output was converted to 266 nm for excitation purposes). Acetone PLIF experiments were first conducted with a New Wave Solo III PIV Laser⁹⁵ (Nd:YAG), but final acetone PLIF experiments were only conducted with the Solo 200XT. The Solo 200XT and Solo III are dual-head designs that create a 532 nm beam output using frequency doubling crystals. This 532 nm beam output was converted to 266 nm by using a KDP frequency doubling crystal (efficiency approximately 20-30%). In both designs, the second laser was set to fire slightly after the first laser in the dual-head because it was found that more energy output at 266 nm was achieved with this method, as opposed to firing both lasers simultaneously. The second laser in the Solo 200XT dual head was set to fire 10 ns after the first laser. Triggering/timing of the Solo 200XT PIV Laser is explained later in Section IX.A.c.

The Solo III has a reported beam diameter of 3.5 mm and initial 532 nm energy output of 50 mJ/pulse⁹⁵, but these parameters were not confirmed. A measured 266 nm energy output of approximately 22 mJ/pulse, with both lasers firing in the high setting, was achieved with the Solo III. This enabled adequate signal levels in PLIF images, but 2 x 2 binning during image acquisition, which reduces resolution, was necessary to achieve these desired SNR values. The Solo 200XT has a reported beam diameter of 5.5 mm and initial 532 nm energy output of 200 mJ/pulse.⁹⁵ However, the actual measured 532 nm energy output was much less than this reported value. The Solo 200XT, with both lasers firing in the high setting (with a slight time delay of 10 ns between them), was able to nearly double the 266 nm energy output that could be achieved with the Solo III (Solo 200XT yielded 38 mJ/pulse at 266 nm before passing through final optics compared to 22 mJ/pulse for the Solo III). Also, binning was not required to achieve desired SNR values with the Solo 200XT. Therefore, the Solo 200XT was used for excitation purposes to obtain all of the acetone PLIF data presented in this thesis.

The Solo 200XT was mounted to a large laser table that was placed next to the transonic wind tunnel. The 532 nm laser beam exited the PIV laser head, entered a half waveplate to adjust the polarization of the beam, and then entered a KDP conversion crystal to convert the 532 nm light to 266 nm light (the 4th harmonic of Nd:YAG), as seen in Figure 51. After the 532 nm light was converted to 266 nm light, several additional optics were used to filter out residual 532 nm light, steer the beam, expand/focus the beam, and form a thin laser sheet. Filtering out the majority of the residual 532 nm light was achieved by reflecting the beam off of three 266 nm mirrors. The first 266 nm mirror was mounted to the laser table and the other two 266 nm mirrors were mounted to a large stationary breadboard located beneath the wind tunnel.

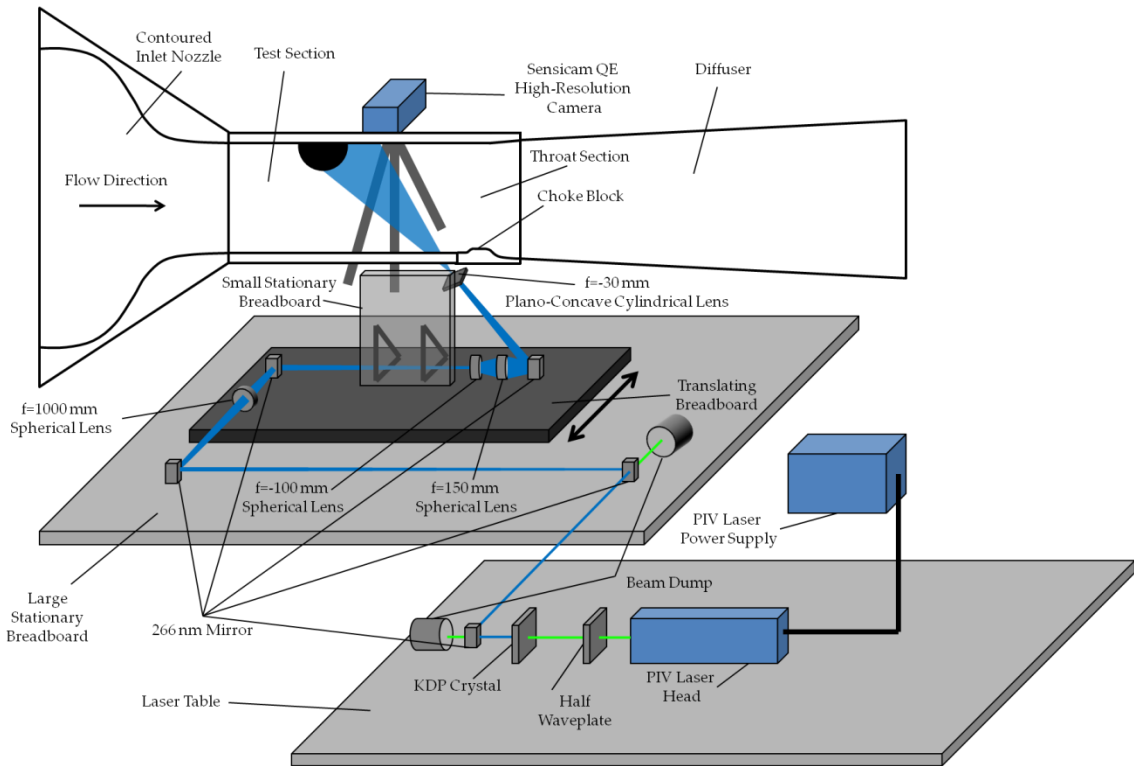


Figure 51: Schematic of Acetone PLIF Experimental Setup

Note that cardboard boxes were used to cover the half waveplate, the KDP crystal, and the first two 266 nm mirrors, as seen in Figure 52. This was done in effort to block ambient 532 nm light, mainly created by the laser beam at each 266 nm mirror and beam dump, from reaching the camera CCD. Small holes were cut in the boxes for the beam to pass through.



Figure 52: Cardboard Boxes to Block Ambient 532 nm Light

The 266 nm beam then passed through an $f=+1000$ mm spherical lens (to counteract the divergence of the beam), reflected off of another 266 nm mirror, and then passed through an $f=-100$ mm spherical lens (to expand the beam) and an $f=+150$ mm spherical lens (to focus the beam), as seen in Figure 51. All four optics were mounted to a small breadboard that could be translated perpendicularly to the freestream flow direction. The 266 nm beam then reflected off of one final 266 nm mirror and passed through an $f=-30$ mm plano-concave cylindrical lens. This cylindrical lens was mounted to a small stationary breadboard (attached to the translating breadboard) that was oriented vertically beneath the test section, as seen in Figure 53. The cylindrical lens formed the focusing beam into a thin laser sheet by spreading the beam in a single direction. Separation distance between the $f=-100$ mm and $f=+150$ mm spherical lenses regulated the thickness of the laser sheet in the imaging region in the test section. The goal was to have a sheet that was as thin as possible, effectively finding the beam waist. In the imaging region the width and thickness of the laser sheet were approximately 25mm and 1mm, respectively.

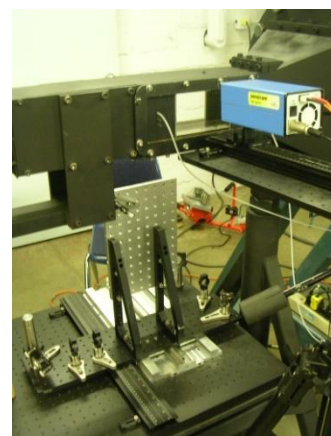
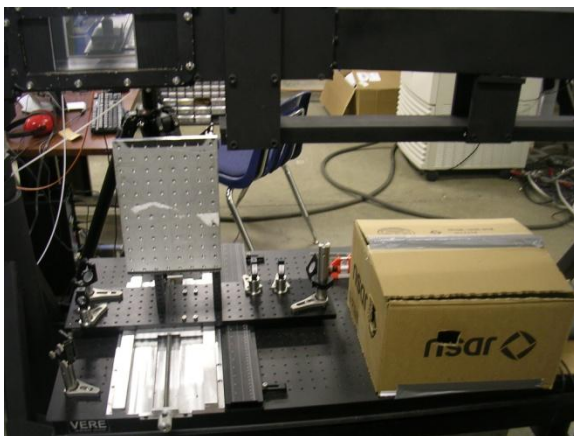


Figure 53: Optical Setup Below Wind Tunnel Test Section

The laser sheet passed through the bottom stepped window of the test section in an angled orientation, so a larger portion of the shear layer could be excited by the most intense portion of the laser sheet whose intensity profile was roughly Gaussian. This increased signal levels over a large portion of the shear layer, yielding higher quality images. Physical and geometric constraints of the transonic wind tunnel prevented the laser sheet from having its most intense portion directly aligned along the shear layer. In early acetone PLIF experiments, the laser sheet was passed through the bottom stepped window of the test section in a normal orientation. However, it was concluded that this did not position enough of the most intense portion of the laser sheet on the most relevant flow features.

In between test runs, the PIV laser was fired at a continuous repetition rate, even when the camera was not acquiring images. This was because the 266 nm energy output increased and leveled-off when the KDP crystal was heated by laser pulses passing through it as a thermal equilibrium state was reached. The half waveplate and KDP crystal were periodically adjusted to obtain/maintain maximum 266 nm energy output. Laser energy of approximately 38 mJ/pulse at 266 nm was achieved (measured after the $f=+1000$ mm spherical lens). It was assumed that the optical transmission efficiency of each of the lenses was approximately 95% and that the optical transmission efficiency of the bottom stepped window was approximately 95%. The 266 nm energy output was measured after the first spherical lens, so the measured 266 nm light (38 mJ/pulse) traveled through two spherical lenses, the cylindrical lens, and the bottom stepped window. This resulted in an overall optical transmission efficiency of approximately 81% ($95\% \times 95\% \times 95\% \times 95\%$). In the end, this resulted in approximately 31 mJ/pulse of 266 nm light in the test section.

It was noticed via laser burn paper (toward the end of image acquisition for the large set of wake region centerline images) that the laser sheet was yawed slightly off axis. The sheet passed through the centerpoint of the hemisphere, but angled slightly to the left with downstream distance (from a bird's eye perspective facing downstream). Over the length of the field of view, the laser sheet was off the centerline axis by approximately 2.5 degrees (approximately 2 mm over FOV of 45.51 mm x 34.40 mm and approximately 1.4 mm over FOV of 32.12 mm x 24.28 mm). It was concluded that this was a relatively small error when compared to the size of the wake at the farthest downstream location (over 45mm) in the imaging region. It is simply noted for completeness.

It was also noticed that the bottom stepped window showed slight traces of green light (532 nm) when the PIV laser was firing (i.e. when the 266 nm laser sheet was passing into the test section). It was thought that this was residual 532 nm light in the laser sheet. The beam passed through five 266 nm mirrors after conversion from 532 nm to 266 nm and before entering the test section, so residual 532 nm light was or was almost completely dropped out. If any residual 532 nm light exists in the laser sheet, then it is eliminated from raw PLIF images when the average background/dark image with the laser firing is subtracted from each single-shot acetone PLIF raw image.

b. Seeding for Single-Shot Acetone PLIF Experiments

As explained in Section VII., liquid acetone was seeded into the compressed air supply line pipe far upstream of the test section. The liquid acetone evaporated by the time it reached the test section. A larger pressure difference (than for PIV experiments) between the small pressure vessel and the compressed air supply line pipe/storage tanks had to be used in the PLIF

experiments because large amounts of acetone were necessary to generate enough fluorescence signal to be collected by the CCD. The average acetone mole fraction was approximately 3%. The wind tunnel was run without acetone seeding for several seconds after each test run with acetone seeding in order to clear out any residual acetone, so the results of the next test were not tainted with extra acetone. Windows and the hemisphere model were also cleaned after each test run with acetone seeding. For more information on seeding for acetone PLIF, see Section VII.

c. Camera and Image Acquisition

Acetone PLIF images were captured with a Cooke Corporation Sensicam QE¹⁰¹ high-resolution (1376 x 1040 pixels), unintensified camera. The pixel size for the CCD is 6.45 μm x 6.45 μm and the quantum efficiency is approximately zero at 266 nm. Acetone fluoresces with a spectrum of 350-550 nm, with peaks at 435 nm and 480 nm.^{48,49} Based upon these facts and the quantum efficiency curve of the Sensicam QE CCD, the quantum efficiency was taken as 58% for the experiments in this work (this is the quantum efficiency at the approximate wavelength between the two peak fluorescence wavelengths). The analog to digital converter is 12-bit, thus the maximum digital count for this CCD is 4095. The analog to digital conversion factor is 4 photoelectrons per count for low gain and 2 photoelectrons per count for high gain. Thus, the maximum photoelectrons that can be captured per pixel for high gain is 8,190 and for low gain is 16,380. The full well capacity for this CCD is 18,000 electrons.¹⁰¹

The Sensicam QE was mounted to a tripod (through the use of a breadboard) and was oriented to image through one of the rectangular side windows. Pitching the camera downward slightly (approximately 4° for

centerline wake region and centerline multiple parallel plane data sets and approximately 2° for centerline separation region data set) blocked some of the noise on the surface of the top wall of the test section and the surface of the hemisphere, as seen in Figure 54. The top wall of the test section does not transmit light and the 266 nm laser sheet was reflecting off of this surface and causing the wall to fluoresce a low visible wavelength. This was a slight problem in early experiments that was improved by tilting the camera downward. Tilting effects were not accounted for in image processing as the tilt angle was so small. The effects on solid collection angle, changes in magnification, and changes in spatial resolution were assumed to be negligible from this tilt angle.



Figure 54: Camera Setup

A 25 mm lens was used with an aperture setting of $f/1.6$. A small extension tube was also used (height approximately 5mm). The spatial resolution and field of view for the planes in the flow field are shown in Table 3. In the raw images the flow convention was right to left (this was corrected in image processing and in-situ calibration so final density images have left to right flow convention, the

more traditional convention for flow field imaging). No binning was used for the images obtained and a normal (i.e. low) gain setting was used.

Table 3: Spatial Resolution and Field of View for Planes Investigated

	Spatial Resolution ($\mu\text{m}/\text{pixel}$)	Field of View (mm x mm)
Wake Region Centerline (All Sets)	33.07	45.51 x 34.40
D/8	32.56	44.81 x 33.87
D/4	31.44	43.26 x 32.69
3D/8	31.05	42.73 x 32.29
D/2	30.24	41.61 x 31.45
5D/8	29.13	40.08 x 30.29
Separation Region Centerline	23.35	32.12 x 24.28

Laser and camera were triggered by the same Quantum Composers 9514+ pulse generators¹⁰² used in the PIV experiments, except different settings were used as seen in Table 4. The camera was triggered slightly before the 532 nm laser beam left the laser head, so that the electronic shutter could be fully open when the 266 nm sheet reached the test section and the acetone molecules fluoresced. The rate for the triggers was set to a period of 0.15 sec, thus the timing between each image was 0.15 seconds.

Table 4: Laser and Camera Settings for Acetone PLIF Experiments

	<u>Pulse Width</u>	<u>Fire Delay</u>	<u>Q-Switch Delay</u>	<u>Delay</u>
<u>Laser 1</u>	120 μs	100 μs	290 μs	
<u>Laser 2</u>	120 μs	100.2 μs	290.1 μs	
<u>Camera</u>	20 μs			280.5 μs

A ruler image was acquired before each plane was imaged. Then a set of approximately 50 dark images without the laser firing was acquired (laser remained on, but its path to the test section was blocked after the first 266 nm mirror), so the readout noise of the CCD could be obtained. Approximately 50 dark images with the laser sheet firing into the test section were also acquired, so the background noise could be obtained. Finally, acetone PLIF images were acquired for the centerline and multiple parallel planes in the wake region and for the centerline near the separation region.

B. Expectations for Single-Shot Acetone PLIF Experiments

There were several expectations for the single-shot acetone PLIF experiments. It was expected that high-quality fluorescence images of the shear layer and wake region would be obtained and the density data for these regions would be quantified. It was expected that the strongest density fluctuations would occur in the shear layer and upper wake region because PIV data revealed that the strongest positive vorticity values exist in these regions. The strongest negative vorticity values were observed to occur sporadically near the wall, so strong density drops should be observed here as well. Schlieren and shadowgraph imaging also revealed strong density gradients in the shear layer and wake regions. Density was predicted to drop a maximum of 30% from the

freestream density in the shear layer and wake region. The centerline separation region acetone PLIF images were also expected to reveal vortex cores, i.e. regions of large density drop, in the separated shear layer.

C. Analysis of Density Images

The single-shot acetone PLIF experiments yielded quality density images. To obtain density data from the raw PLIF images, an image processing and in-situ calibration procedure, explained in Section IV.B., was performed for each raw image and then curves of $S_f/S_{f\infty}$ vs. ρ/ρ_∞ , explained in Section IV.E., were used to quantify the normalized density field for each $S_f/S_{f\infty}$ image. Note that all PLIF images acquired during a test run can be compared to each other once they are in normalized density form, even though the freestream conditions, acetone mole fraction, and laser intensity profile/energy in reality are slightly different for each image.

All of the images were non-dimensioned in terms of hemisphere diameters from the origin (centerpoint of the hemisphere). It should be noted that non-dimensioning was fairly simple for the centerline images as the laser sheet clearly illuminated the boundaries of the hemisphere (although camera tilt caused some clipping of the bottom boundary of the hemisphere; in particular this made the bottom of the hemisphere in the separation region images appear to not exactly be located at $y/D=0.5D$). An arc was drawn in the images based upon the centerpoint location and the radius of the hemisphere. The centerpoint location was iteratively moved in the x and y direction until the arc fell as best as possible along the boundaries of the hemisphere in the image. However, this proved more difficult for the off-centerline parallel plane images of the wake region as the FOV slightly changed for these planes and the boundaries of the

hemisphere were not as clearly illuminated. The test run with no hemisphere mounted relied upon a centerline wake region data set with the hemisphere mounted (acquired earlier that same day) to figure out where the centerpoint was located. Therefore, the accuracy of non-dimensioning for all images is not perfect. The normalized density image (centerline wake region) for Example Image Z (i.e. the example acetone PLIF raw image used to explain the image processing and in-situ calibration procedure in Section IV.B.) is shown in Figure 55.

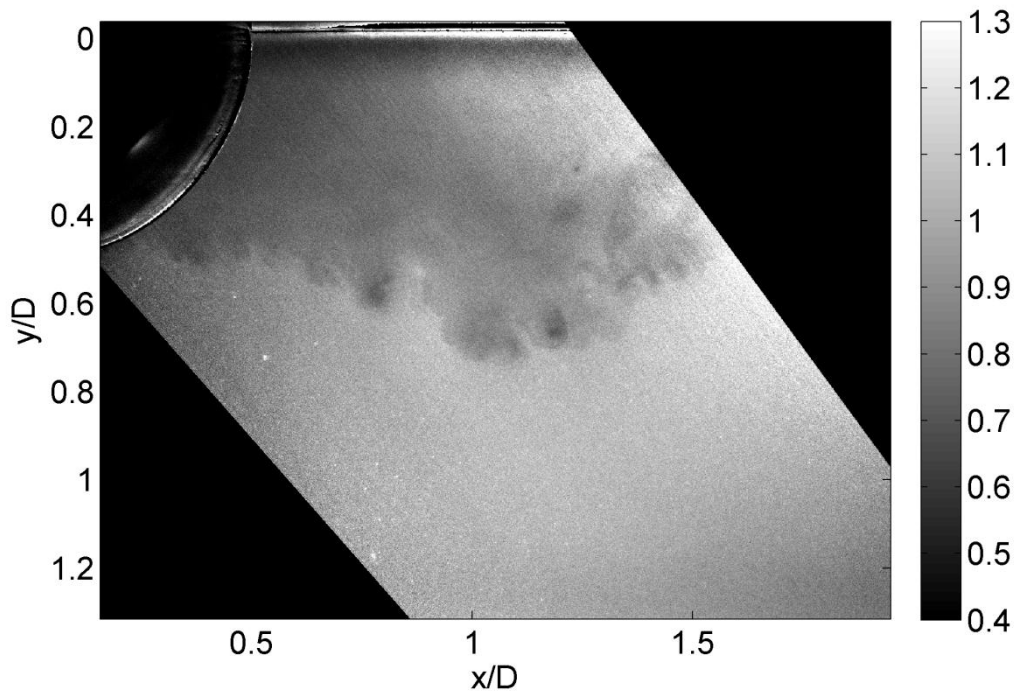


Figure 55: Example Single-Shot Acetone PLIF Density Image (values normalized to freestream) – Centerline – Wake Region

a. Centerline Wake Region Images

A representative set of normalized density images for the centerline wake region is presented and additional images are shown in Appendix A. In these images the wake region was clearly seen on the downstream side of the hemisphere. In the wake, the density was seen to drop 20-40% of the freestream density. The wake thickness was typically approximately half of the diameter of the hemisphere, as seen in Figure 56.

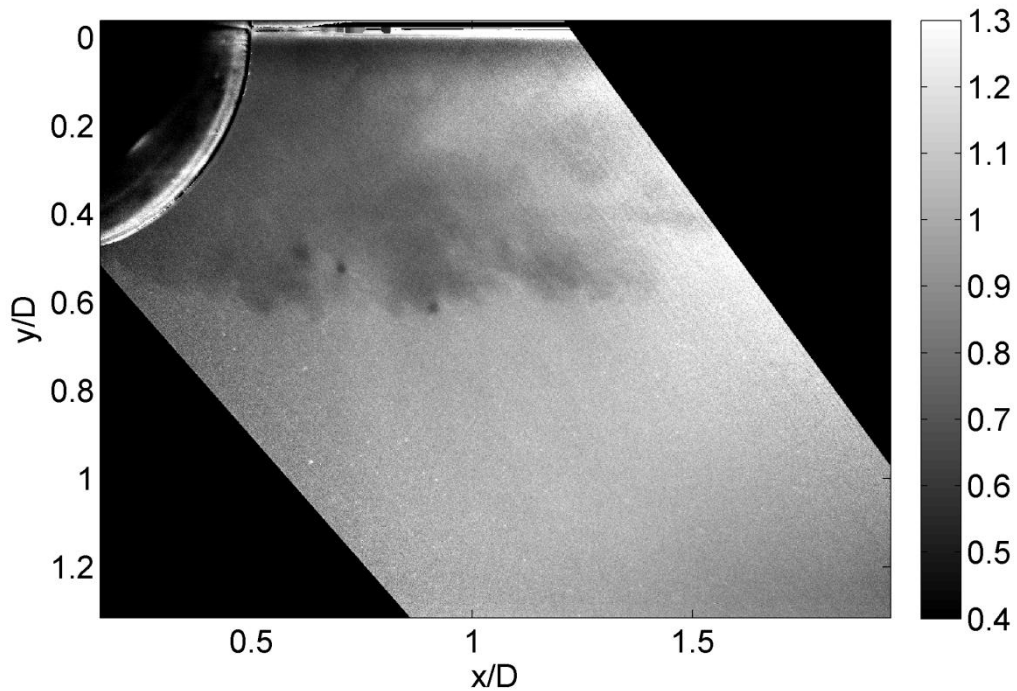


Figure 56: Wake Thickness of Single-Shot Acetone PLIF Density Image (values normalized to freestream) – Centerline – Wake Region

However, this varied some throughout a test run. A large flapping/sweeping motion was present in some images where the wake thickness would drop and a little bit farther downstream would grow back to normal thickness, or sometimes even thicker than half the diameter of the hemisphere. This behavior is clearly

seen in Figure 57. Sometimes the wake thickness would just abruptly drop, as seen in Figure 58.

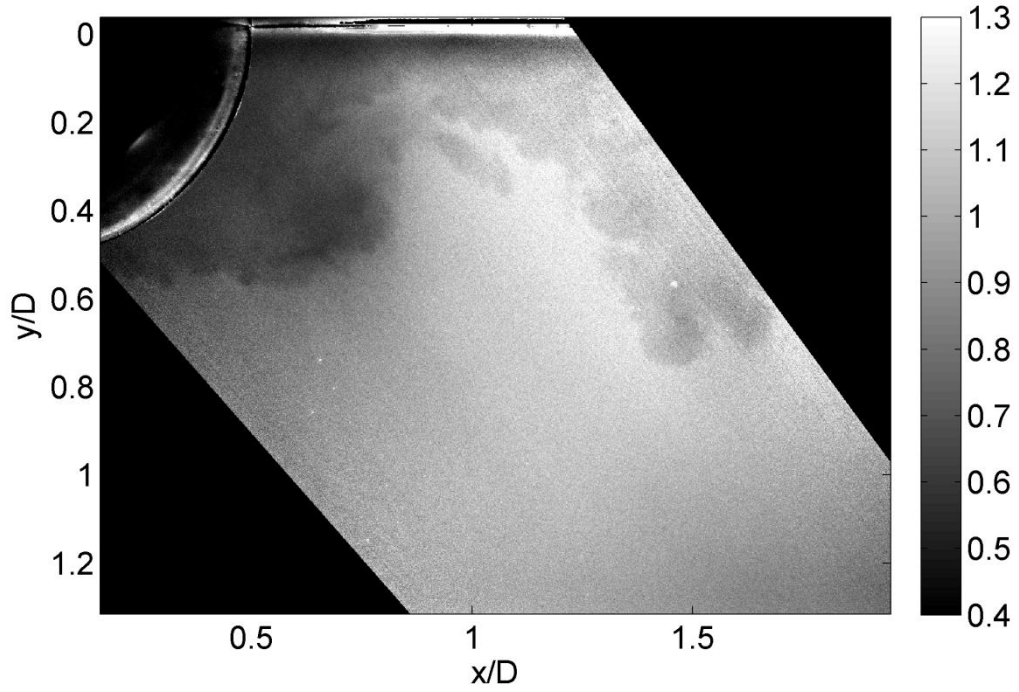


Figure 57: Flapping Motion in Single-Shot Acetone PLIF Density Image (values normalized to freestream) – Centerline – Wake Region

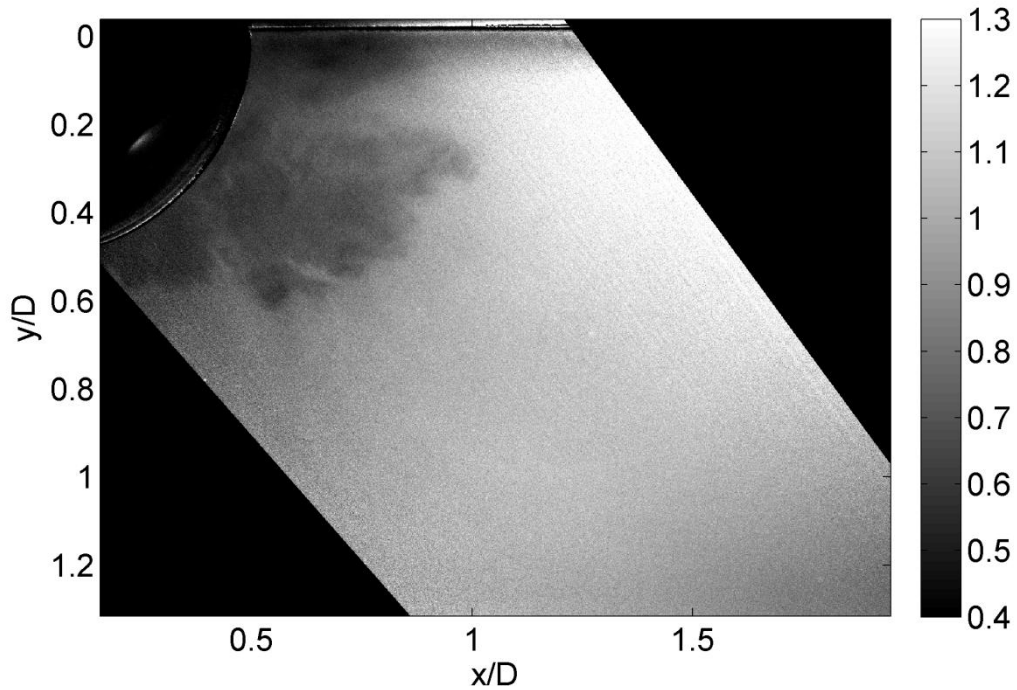


Figure 58: Abrupt Drop in Wake Thickness in Single-Shot Acetone PLIF Density Image (values normalized to freestream) – Centerline – Wake Region

The shear layer and upper wake region also exhibited many interesting features such as distinct vortex cores, as seen in Figure 56 and Figure 59 (this image also exhibits flapping motion similar to that present in Figure 57). Throughout all of the images acquired for the centerline wake region, the density was measured to drop by up to 45-50% of the freestream density in the vortex cores.

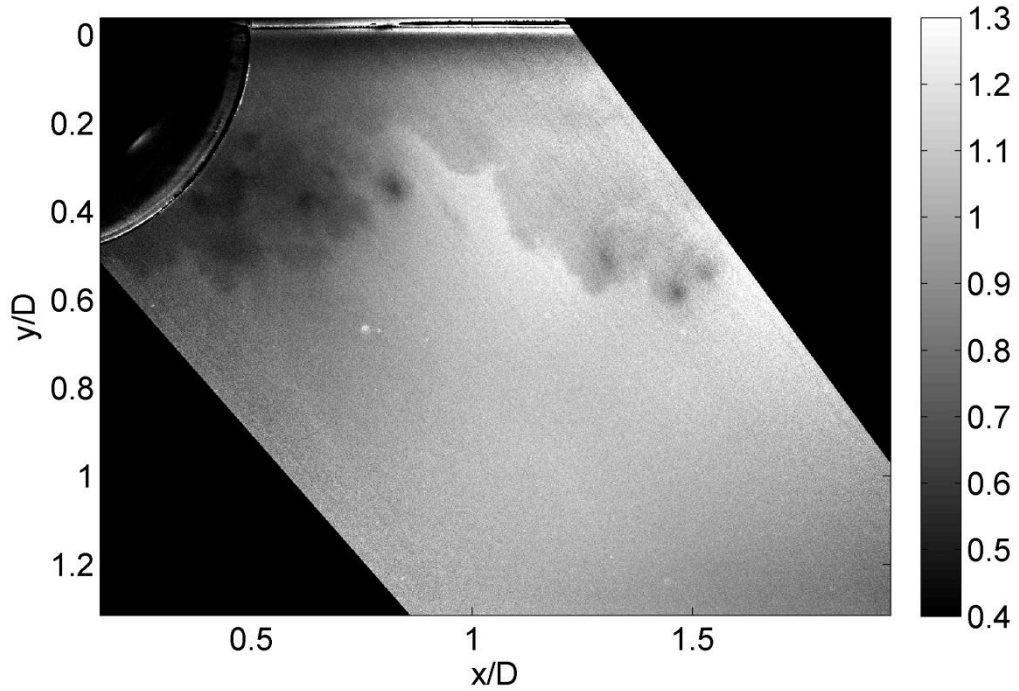


Figure 59: Vortex Cores in Single-Shot Acetone PLIF Density Image (values normalized to freestream) – Centerline – Wake Region

Near the vortex cores, a swirling motion could usually be seen where the higher density flow was being folded, swirled, and mixed into the lower density flow because of the presence of these vortex cores. This folding and swirling behavior can be clearly seen in Figure 60.

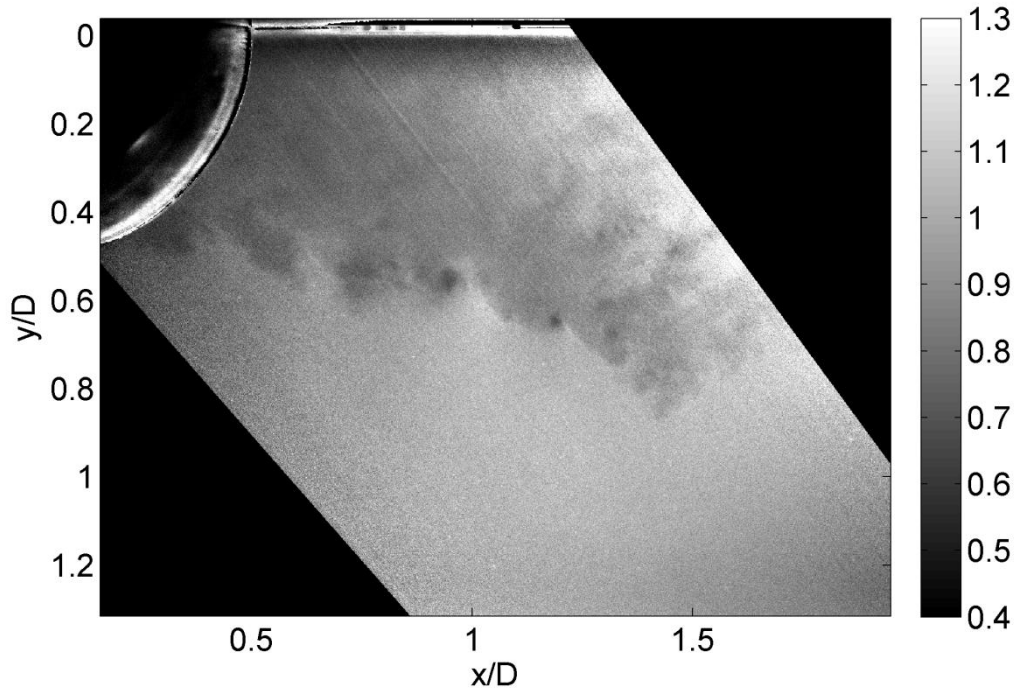


Figure 60: Swirling/Folding Near Vortex Cores in Single-Shot Acetone PLIF Density Image (values normalized to freestream) – Centerline – Wake Region

The shear layer and upper wake region not only possessed vortex cores, but also possessed large protruding structures. Density drops in these structures were less than in the vortex cores, but the size of these structures was larger than the vortex cores, as seen in Figure 61. The wake did not always possess very strong structures with a lot of movement. As seen in Figure 62, the shear layer and wake region sometimes appeared fairly calm, although this was infrequent.

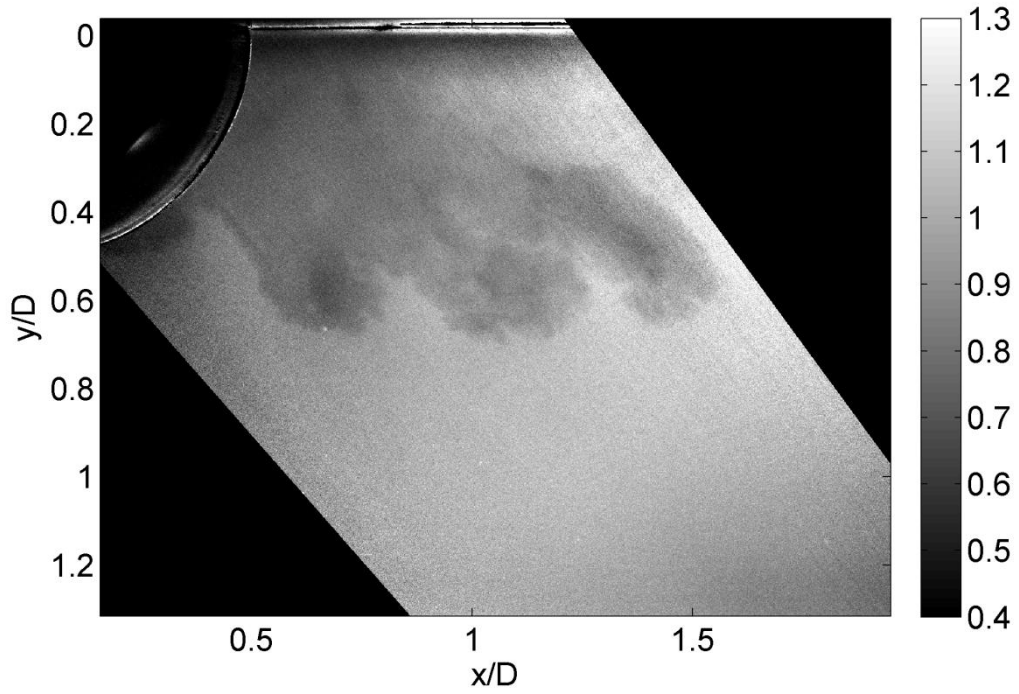


Figure 61: Large Protruding Structures in Single-Shot Acetone PLIF Density Image (values normalized to freestream) – Centerline – Wake Region

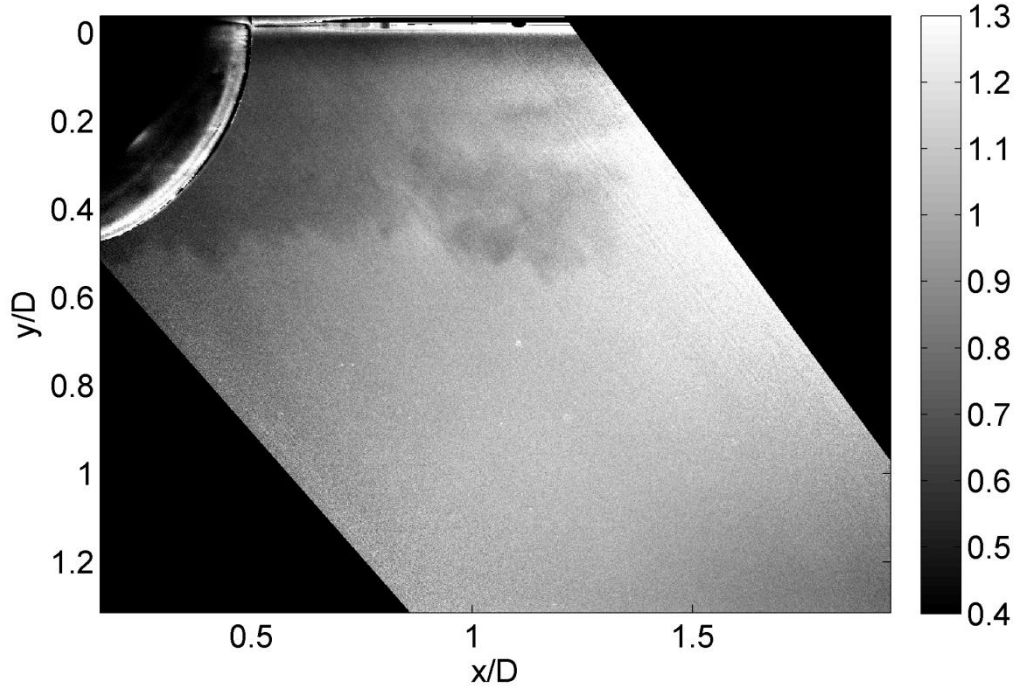


Figure 62: Fairly Calm Shear Layer and Wake in Single-Shot Acetone PLIF Density Image (values normalized to freestream) – Centerline – Wake Region

Ensemble average and standard deviation of the centerline wake region images also revealed important information. The ensemble average of the normalized density images (an average of 98 images, even though 130 were actually obtained; 32 images were discarded because of streakiness in the images due to high intensity freestream particles and/or the fact that flow features extended into the freestream region where correction coefficients were calculated), seen in Figure 63, reveals that the maximum density drops from the freestream occurred in the near wake and shear layer region. The density drops from the freestream became less intense as the downstream distance increased.

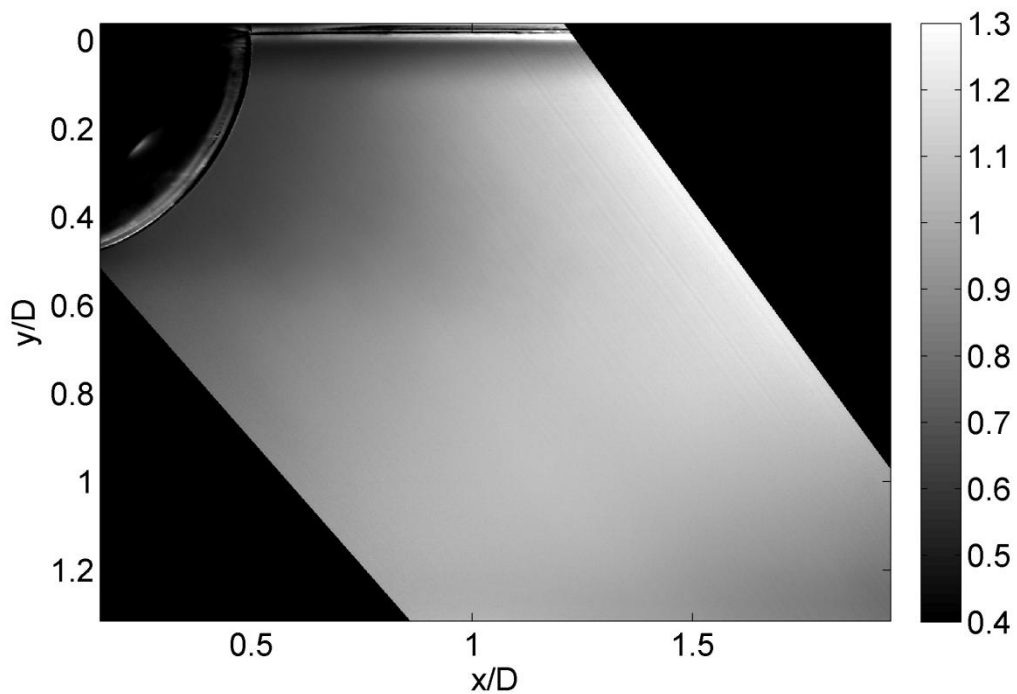


Figure 63: Ensemble Average of Single-Shot Acetone PLIF Normalized Density Images – Centerline – Wake Region

Vortex cores were not visible in the ensemble average image, while they were visible in the instantaneous, single-shot images previously presented. This

ensemble average image clearly shows that image processing has room for improvement because the freestream density values on the edges/corners of the image are slightly less than the rest of the freestream density values and a somewhat bright band extends from the upper middle portion of the image to the middle right portion of the image (brighter means higher density). The standard deviation of the normalized density images (the same 98 images used for the ensemble average calculation of normalized density), seen in Figure 64, reveals that the maximum normalized density fluctuations from image to image were located in the shear layer and upper wake region. These fluctuation values were seen to be $\rho/\rho_\infty \approx 0.12-0.14$.

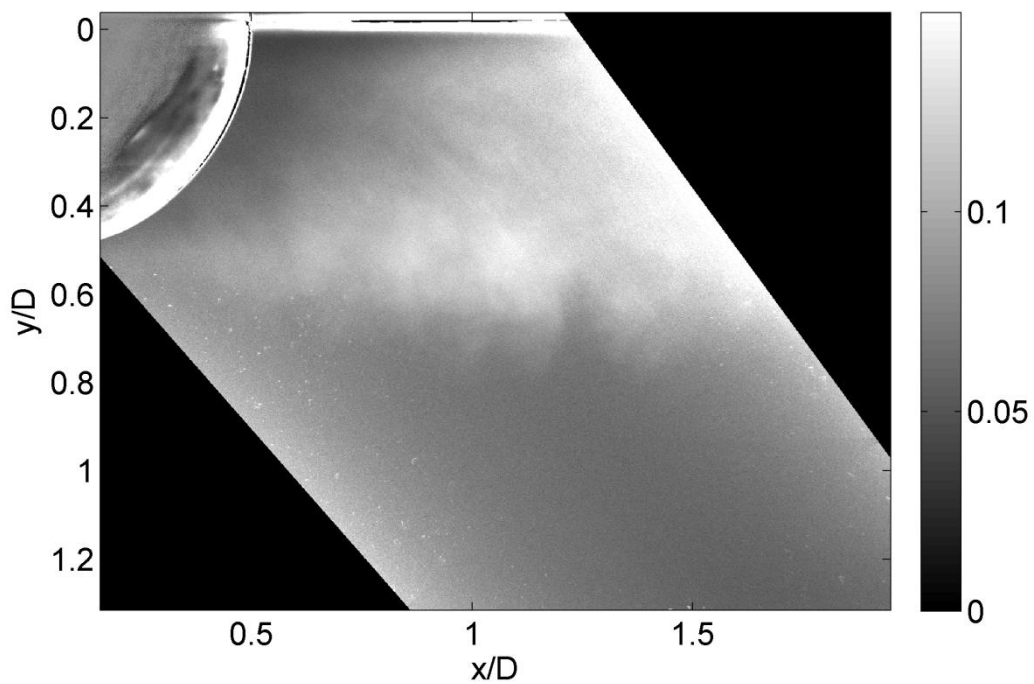


Figure 64: Standard Deviation of Single-Shot Acetone PLIF Normalized Density Images – Centerline – Wake Region

b. Parallel Plane Wake Region Images

Acetone PLIF density images obtained along parallel planes in the wake region also revealed many interesting characteristics. A representative image from each set is presented, as well as an explanation of the general flow behavior observed for the set of images acquired for each plane. Additional images for each plane are shown in Appendix B. Images from the $D/8$ plane revealed characteristics similar to the centerline wake region images, as expected due to proximity. The wake was still clearly present in each image. Flapping motions in the wake were still present in some images, as well as tight, dark vortex cores and folding motions in some images. Density drops from the freestream were fairly comparable to the centerline wake region data. A representative image from the $D/8$ plane is shown in Figure 65.

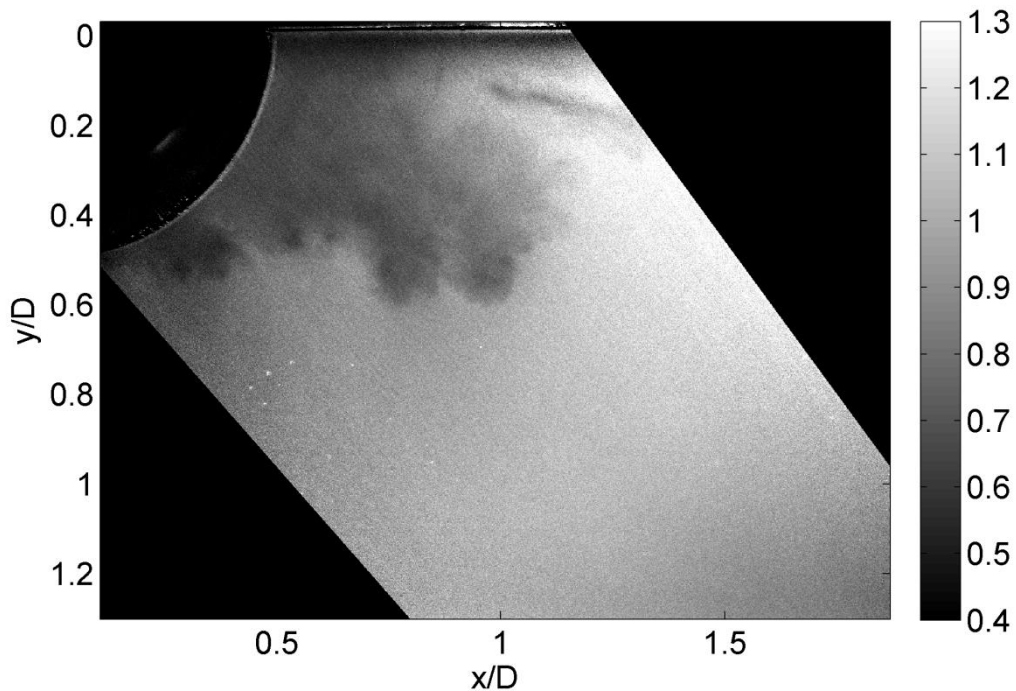


Figure 65: $D/8$ Plane Single-Shot Acetone PLIF Density Image (values normalized to freestream)

Images from the D/4 plane still revealed the wake region, however some images showed a wake that quickly dropped out. Dark vortex cores could still be seen in some of the images, as well as flapping motions. Density drops from the freestream were comparable to the centerline wake region images. A representative image from the D/4 plane is shown in Figure 66.

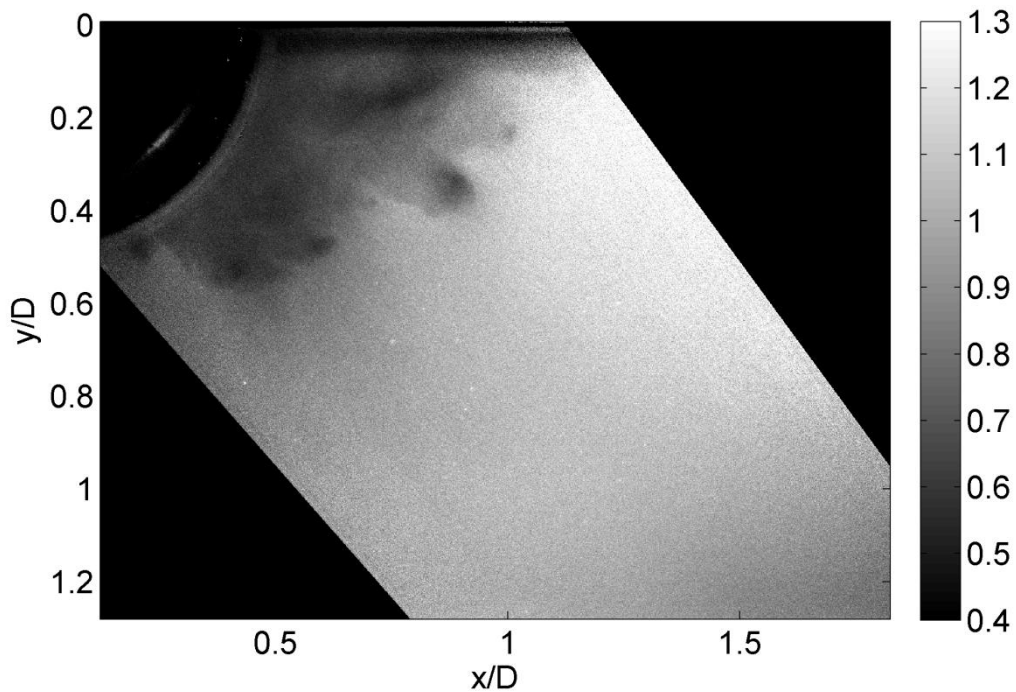


Figure 66: D/4 Plane Single-Shot Acetone PLIF Density Image (values normalized to freestream)

Images from the 3D/8 plane revealed fairly tight and strong vortex cores in the shear layer and upper wake region. Also, the flapping motion could be seen in some of the images. Thickness of the wake in several images tended to bend down/decrease at an angle as downstream distance increased (from the centerpoint of the hemisphere) and then the thickness dropped out. Density drops in the shear layer and wake region were comparable to the density drops

in the centerline wake region images. A representative image from the 3D/8 plane is shown in Figure 67.

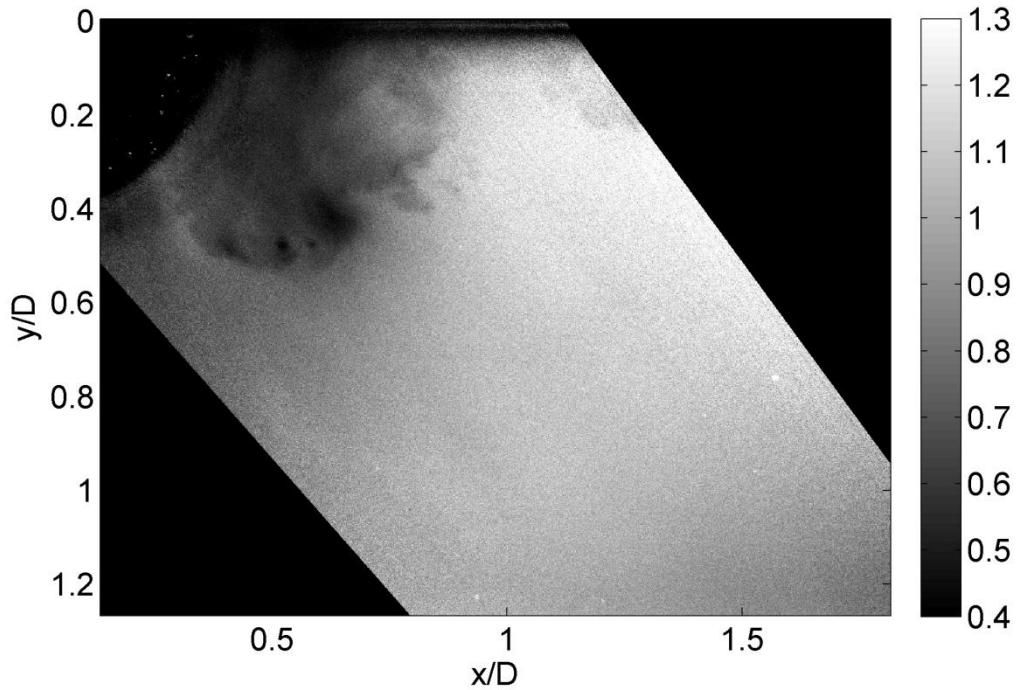


Figure 67: 3D/8 Plane Single-Shot Acetone PLIF Density Image (values normalized to freestream)

The D/2 plane images revealed a much more sporadic and random wake region. In some images the bottom portions of the wake could be seen, but the thickness was frequently less than half of the diameter of the hemisphere. In some images no wake could be seen at all. Tight vortex cores were no longer present in these images. Most of the low density features were dark puffs, signifying structures that protruded outwardly from the inner region of the wake. The density drops in these puffs were comparable to the density drops experienced in the centerline wake region images. A representative image from the D/2 plane is shown in Figure 68.

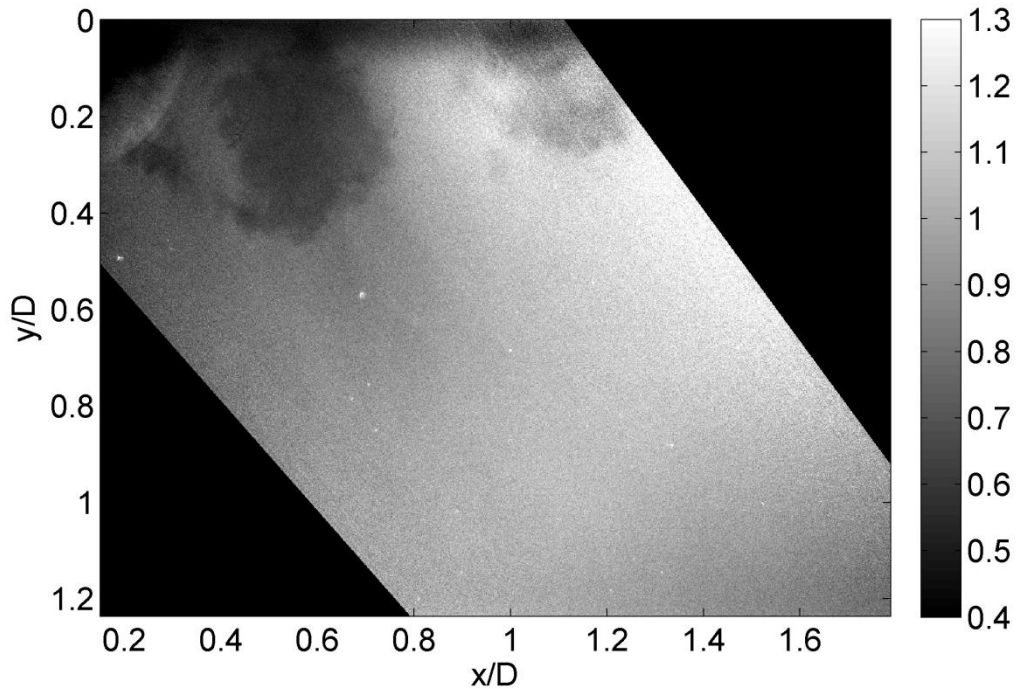


Figure 68: D/2 Plane Single-Shot Acetone PLIF Density Image (values normalized to freestream)

The 5D/8 plane images did not show much detail at all. Only a few images showed any relative changes in the density downstream of the hemisphere. Again these changes in density were characterized by infrequent dark puffs that appeared in the middle to lower portion of the wake region. A representative image from the 5D/8 plane is shown in Figure 69.

One would expect to see the horseshoe/necklace vortex at this plane location, but imaging of this flow feature was not possible. This is because all of the images from each plane, including this plane, had a dark region near the top edge of the image. This was most likely due to vignetting and the fact that the camera was slightly tilted downward, both of which affect signal levels. For the 5D/8 plane images the horseshoe/necklace vortex would have been located in this region. Additionally, if part or all of the horseshoe/necklace vortex had been

located outside of this dark region, then the density drops in the horseshoe/necklace vortex might not have been large enough to be detected by this density measurement technique.

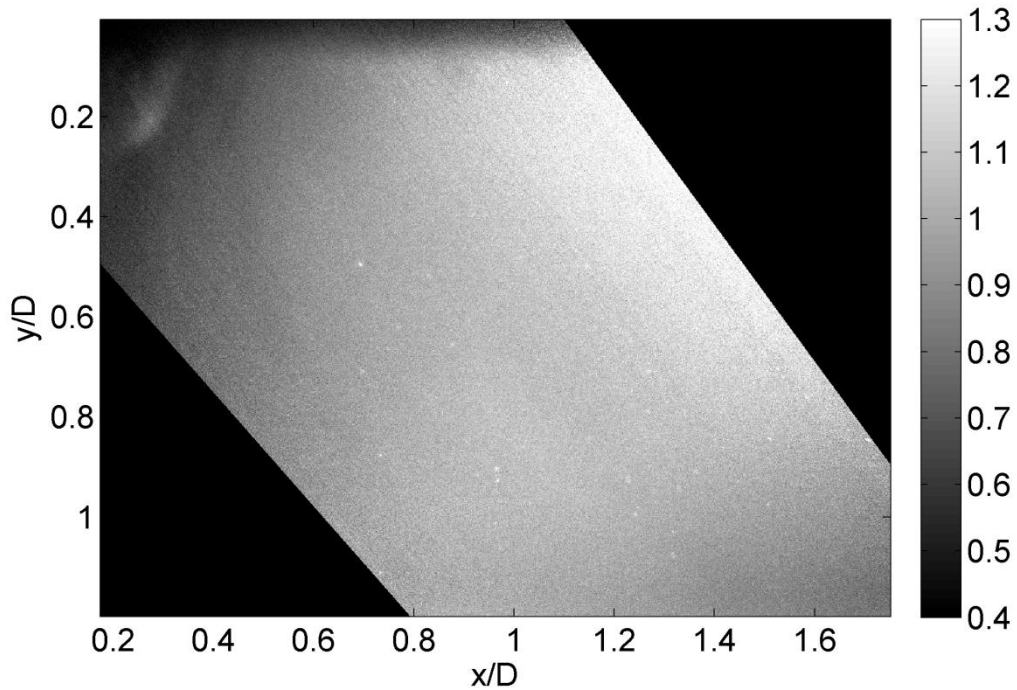


Figure 69: 5D/8 Plane Single-Shot Acetone PLIF Density Image (values normalized to freestream)

c. Centerline Separation Region Images

Two representative centerline separation region images are presented and additional centerline separation region images are shown in Appendix C. These images revealed a separated shear layer and shocks. The separation point was typically located at approximately 80° - 90° from horizontal (there was some variation in this location from image to image). Some of the shocks that formed near the separation point were weak shocks, as seen in Figure 70. However, some

of the shocks that formed near the separation point were stronger shocks, in particular lambda shocks⁹⁰, as seen in Figure 71. As expected, the density increased across all the shocks.

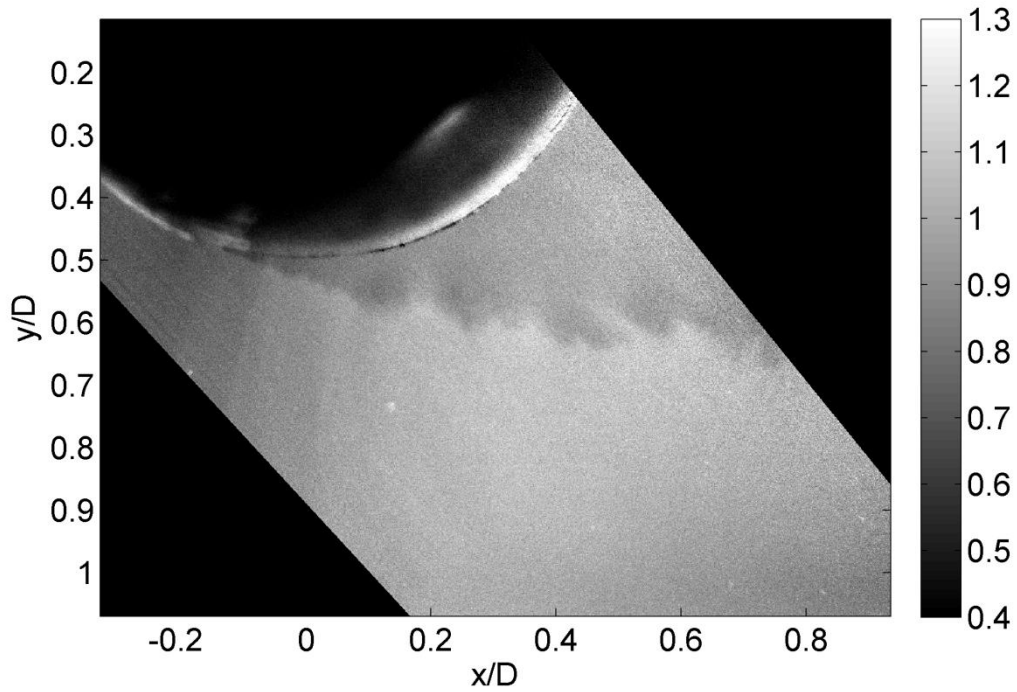


Figure 70: Weak Shocks for Single-Shot Acetone PLIF Density Image (values normalized to freestream) – Centerline – Separation Region

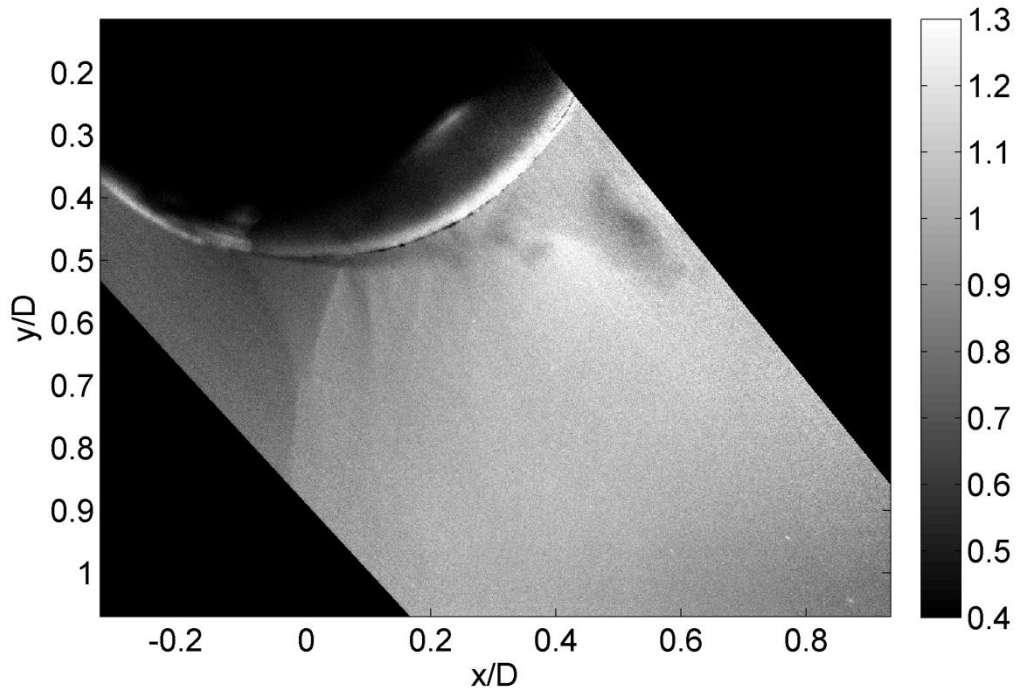


Figure 71: Lambda Shocks for Single-Shot Acetone PLIF Density Image (values normalized to freestream) – Centerline – Separation Region

d. What Causes Flow Separation on the Hemisphere?

The separation of a boundary layer on the surface of a hemisphere is similar to the separation of a boundary layer on the surface of a sphere/cylinder. When the flow is incompressible and the Reynolds number is relatively low ($Re < 3 \times 10^5$), the boundary layer on the surface is laminar and separation typically occurs at approximately $80-90^\circ$ from the horizontal when an adverse pressure gradient is reached. However, at higher Reynolds numbers ($Re > 3 \times 10^5$), this laminar boundary layer separates and reattaches, transitioning to a turbulent boundary layer. When the boundary layer on the surface of the sphere is turbulent, separation is delayed and instead occurs at a higher angle relative to the horizontal. This causes a significant decrease in drag as the wake thickness decreases. For more information on the flow over a sphere/cylinder, transition

from laminar to turbulent flow over a sphere/cylinder, and flow separation over a sphere/cylinder, see Anderson (2007)⁸⁹, Houghton and Carpenter (1993)⁹⁰, and Munson et al. (2002)¹⁰⁴.

With the above information in mind, one must question the cause of the early separation in Figure 70 and Figure 71. In these images the separation occurs at approximately 80-90°, which suggests laminar boundary layer separation. However, $Re_D \approx 840,000-890,000$, which by the above explanation means that the boundary layer should be fully transitioned to turbulent and remained attached and not fully separate until a higher angle relative to the horizontal is reached. The answer to this question is the Mach number was greater in this flow field (the flow was compressible), whereas the explanation of boundary layer separation in the previous paragraph applies to incompressible flow over a sphere/cylinder.

Separation was driven more by Mach number than Reynolds number in this work because the Mach number was higher, approximately 0.78 in the freestream. A plot of drag coefficient versus Mach number and Reynolds number for a sphere is shown in Figure 72. There is a significant drop in drag coefficient when transition occurs from a laminar to a turbulent boundary layer on the surface of a sphere. For Mach 0.78, it can be assumed from Figure 72 that the drag coefficient does not drop significantly at $Re_D \approx 840,000-900,000$. Thus, in this work the boundary layer was not transitioning to a turbulent boundary layer and detaching at a higher angle relative to the horizontal. Flow separation was actually occurring sooner and was not strongly influenced by Reynolds number. Separation in this case was affected more by Mach number.

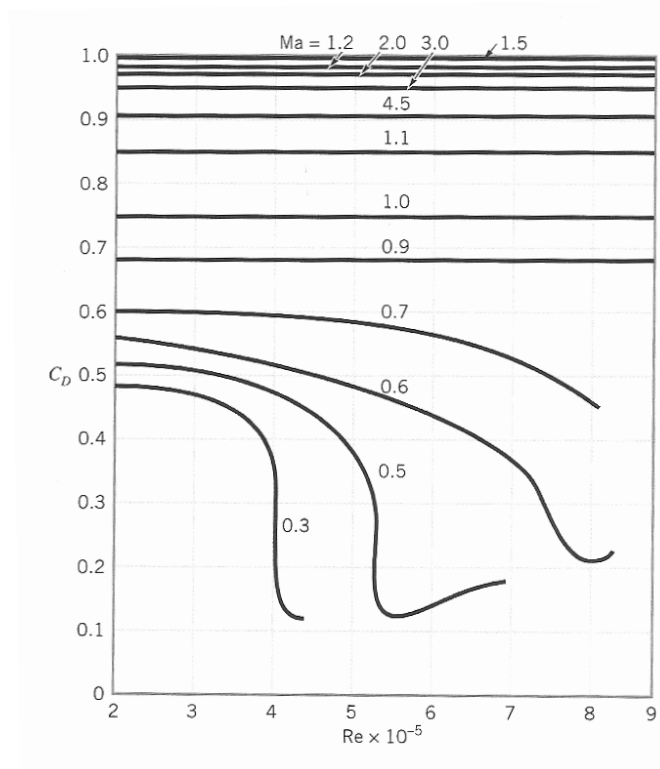


Figure 72: Plot of Drag Coefficient (C_D) vs. Reynolds Number (Re) and Mach Number (Ma) for a Sphere [Munson et al. (2002)¹⁰⁴]

Most likely, the separation in Figure 70 and Figure 71 is shock-induced separation. When a shock forms on the surface, as seen in Figure 70 and Figure 71, there is an increase in pressure which can cause full detachment of the laminar boundary layer. This type of separation is shown in Figure 73 (this type of shock is known as a lambda shock⁹⁰). However, in other cases at slightly lower Mach numbers, shocks can form on the surface and the laminar boundary layer can detach and reattach and transition to a turbulent boundary layer (or it can remain attached and remain laminar).⁹⁰

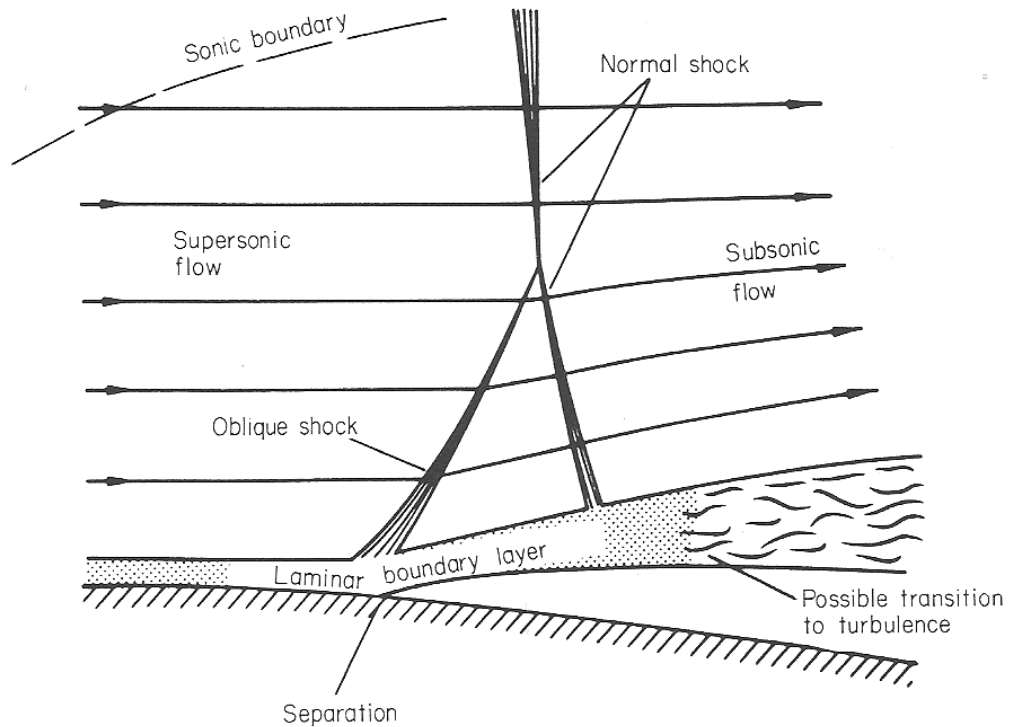


Figure 73: Lambda Shock and Laminar Boundary Layer Separation [Houghton and Carpenter (1993)⁹⁰]

D. Overall Error in Density Measurement

Overall error in the measurement of flow density can be characterized by two forms of error: random error and bias error. Overall random error in the density measurement was caused by uncertainty in local pressure and random error in measured fluorescence signal. Uncertainty in local pressure caused a maximum random error of +/- 2.5% in the measured density, as explained in Section IV.F. Random error in measured fluorescence signal was quantified by dividing the standard deviation of the normalized density images by the ensemble average of the normalized density images, essentially dividing Figure 64 by Figure 63. The freestream region has constant conditions of T_∞ , P_∞ , and ρ_∞ .

and thus should have a constant normalized density value in the freestream region of approximately 1 and a standard deviation of normalized density of approximately 0 in the freestream region. However, it was calculated that the normalized density fluctuates by up to 6-7% of the local average normalized density in the freestream region, thus 6-7% random error. Signal levels are less on the edges of the laser sheet and therefore shot noise increases causing the random error to increase in these regions. Pixel binning could have been used to decrease the random pixel-to-pixel error, but this would have decreased the resolution of the images. Overall random error was found by taking the square root of the sum of the squares of each component of random error. For the current experiments this overall random error in the density measurement was found to be at most approximately +/- 8%. Note that cameras with greater sensitivity and/or lasers with greater energy output can reduce this random error significantly.

Overall bias error was not quantified for this work, although its existence in this work is explained. Bias error was caused by error in the fluorescence quantum yield model, error from interpolation/extrapolation of absorption cross-section data, and error caused by imperfect image processing and in-situ calibration. Fluorescence quantum yield and absorption cross-section bias error can be improved by performing static/flow cell measurements of acetone vapor at different temperatures and pressures close to experimental conditions (these proposed experiments are explained in Section XII.B.c.). This enables direct interpolation of absorption cross-section data (no extrapolation) and enables the fluorescence quantum yield model to be optimized. Also, updates to Thurber's model, suggested by other researchers^{51,62-63}, can be implemented to increase accuracy. Bias error from imperfect image processing and in-situ calibration can be improved with more laser energy, a more sensitive camera, and flat field

correction images (these proposed improvements and others are explained in Section XII.B.b.).

Imperfect image processing can leave dark or light regions in the image where intensity should be constant, such as the freestream. When density is quantified for these normalized signal images, these differences in intensity become differences in density in regions where density should be constant. For example, acetone PLIF images were acquired along the centerline without the hemisphere mounted. It can clearly be seen in these density images, such as Figure 74, that the top left and bottom right corners of the images exhibit dark regions, signifying density drops up to 15-20%, even though there should not be density drops in these regions. This is most likely due to COS^4 vignetting (and vignetting that prevents rays on the edges of the object from reaching the CCD) and would be improved by applying an average flat field correction image to the PLIF images (after average dark image subtraction). These flat field correction images would be PLIF images with no hemisphere mounted.

Note that density drops purely from vignetting effects need to be given proper consideration when analyzing the density drops in density images with the hemisphere mounted. The off-centerline images with the hemisphere mounted (and the centerline images without the hemisphere mounted) were obtained on different days from the large centerline wake region data set with the hemisphere mounted. However, it was assumed that the dark regions just explained were present in all data sets. Even with this bias error, the density fluctuations in the shear layer and wake region could still be visualized adequately.

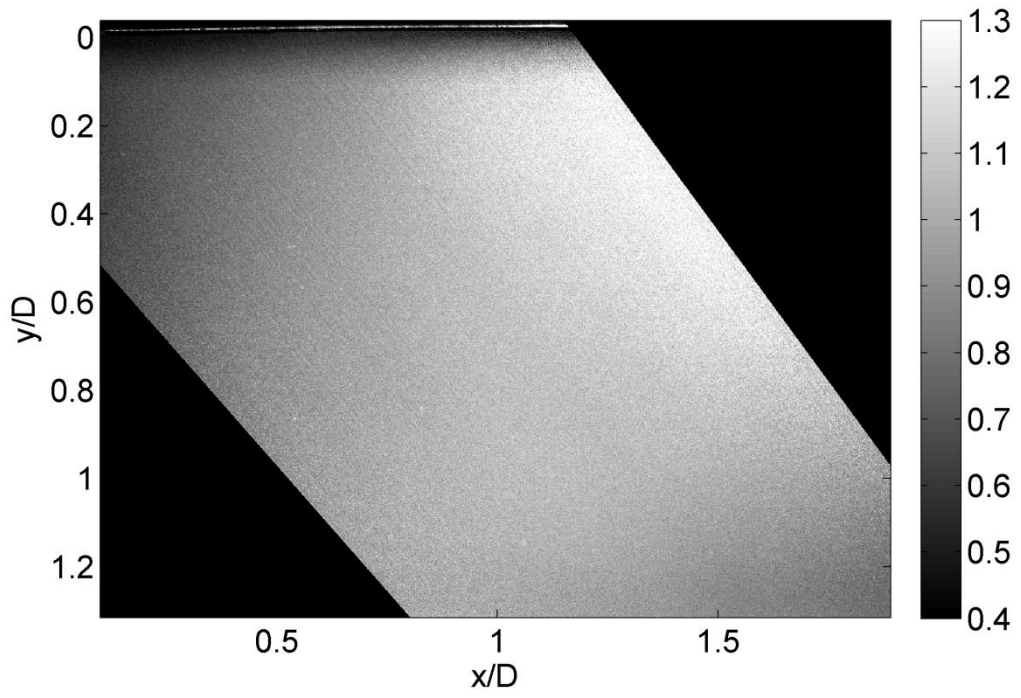


Figure 74: No Hemisphere Single-Shot Acetone PLIF Density Image (values normalized to freestream)

X. Calculating Aero-Optic Distortion from Density Values

A. Overview of Aero-Optic Distortion Calculations and Characteristics of Wavefront

Aero-optic distortion values were calculated for the centerline wake region density images obtained in Section IX. For each image, the density field was converted to index of refraction data and an optical wavefront was propagated through the index of refraction field virtually. The optical wavefront comprised numerous parallel rays that initially propagated from an imaginary plane (width equal to the beam diameter and perpendicular to the rays themselves and thus the wavefront propagation angle) that passed through the centerpoint of the hemisphere. These rays propagated from this imaginary plane to the freestream region. Beam type (planar, pre-distorted, etc.), wavefront angle of propagation, propagation length, beam diameter and number of rays, and wavefront wavelength were specified for the wavefront. The optical path length was calculated for each ray that made up the wavefront by integrating the index of refraction values along each ray over the length of each ray. Then optical path difference values were calculated for each ray. This procedure is presented in detail in the following paragraphs.

Note that aero-optic distortion was only calculated for the centerline wake region images and not the centerline separation region or off-centerline plane images. Also, only the centerline wake region images that were used for calculating ensemble average and standard deviation of the normalized density images were used in calculations of aero-optic distortion. Also, note that particles that are not adequately filtered during the image processing and in-situ

calibration procedure can affect the aero-optic distortion calculation. This is because these particles appear as high index of refraction values in the index of refraction images (high density values in the density images). Thus, when a ray propagates through one of these high index of refraction values, *OPL* increases much more than it normally would if the particle (i.e. high index values) was not in the image.

The first step in the process of calculating aero-optic distortion was calculating the indices of refraction of each density field image using Equation 1. The value of $K(\lambda_{wf})$ varies slightly depending on the wavelength of the wavefront (For 532 nm, the wavefront wavelength used in this work, $K(\lambda_{wf}) \approx 2.27 \times 10^{-4} \text{ m}^3/\text{kg}^{17-18,39-40,105}$). An index of refraction value of 1, which is the index of refraction for air in a vacuum, was assigned to all points/pixels inside of the hemisphere using a masking procedure. To make sure that fluorescence on the surface of the hemisphere was not interfering with the wavefront distortion calculations, this masking procedure extended slightly beyond the actual surface of the hemisphere. In essence, a slightly larger diameter hemisphere, with all index of refraction values equal to 1, was placed over the actual hemisphere in the image.

The beam/wavefront characteristics were specified next. In this work, the only wavefront type that was investigated was the planar wavefront and it comprised 100 rays equally spaced apart, physically/geometrically equal in length, and parallel to one another. Beam diameter was set to be 1/3 of the diameter of the hemisphere, which is consistent with other aero-optic investigations of turrets.^{7,17} This selection of beam diameter also emulated a possible real-world application. The wavefront propagated from the starting plane at the centerpoint of the hemisphere to the freestream at a wavefront

propagation angle of 0.60 radians (approximately 34.4 degrees). This beam did not extend all the way to the bottom right corner of each image because of the dark region in the bottom right corner that could not be eliminated during the image processing and in-situ calibration procedure (however, this dark region would not have affected aero-optic distortion results if the beam had extended into this region because this dark region is essentially the same in each image and is thus bias error). The index of refraction image for Example Image Z is shown in Figure 75 (with the propagating wavefront displayed) and in Figure 76 (with only the outline of the propagating wavefront displayed). Additional example wavefronts and their associated distortion values are presented in Appendix D.

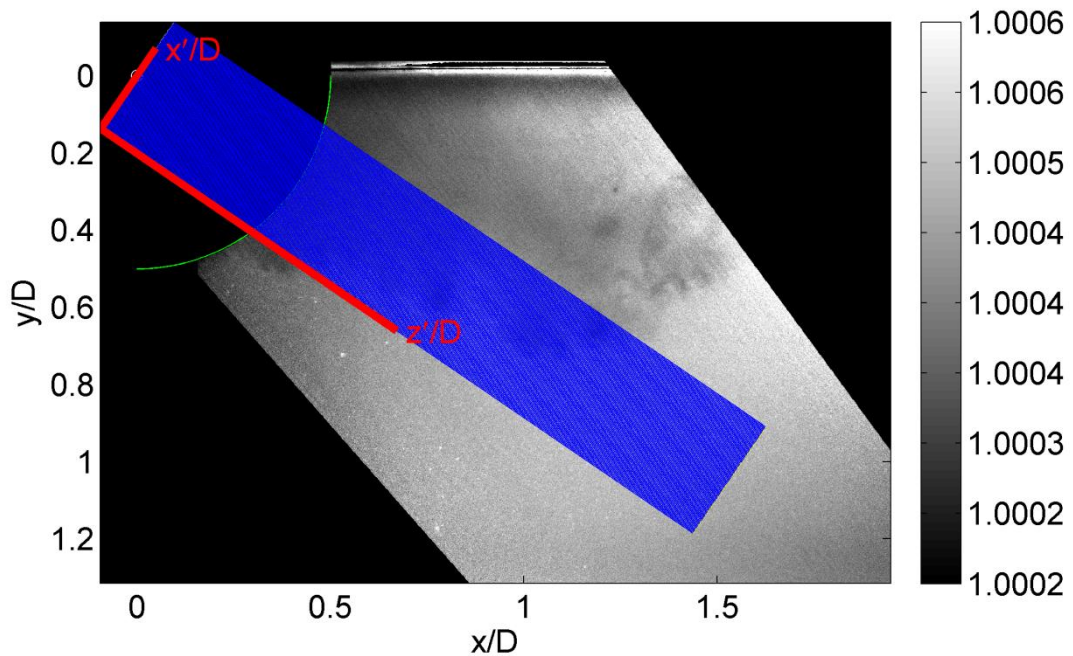


Figure 75: Example Index of Refraction Image with Wavefront Geometry Drawn

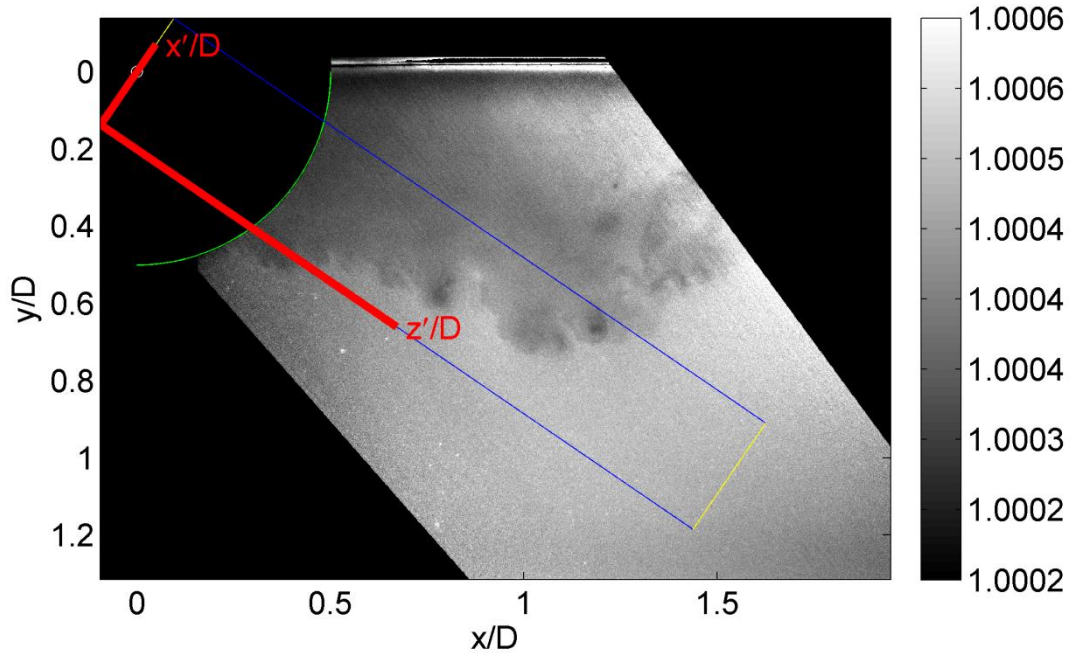


Figure 76: Example Index of Refraction Image with Outline of Wavefront Geometry Drawn

B. Calculation of *OPL* and *OPD*

Once the wavefront characteristics were established, calculations of *OPL* and *OPD* were performed. For a single index of refraction image, *OPL* was calculated for each ray. This was done by integrating the index of refraction values for each ray from the starting plane (that passes through the centerpoint of the hemisphere) to the freestream region using Equation 3. It was assumed that the amount of refraction through each pixel was small compared to the size of each pixel. Thus, it was assumed that the pixels along each physical/geometric ray were the correct pixels to integrate over to calculate *OPL* (i.e. the optical path remained within the pixels that lied along the physical/geometric ray). \overline{OPL} , the mean spatial *OPL* across the aperture/beam, was calculated and subtracted from the *OPL* value for each ray to yield an *OPD* value for each ray. This entire

process was repeated for all instantaneous images to yield a set of *OPD* values for each image for the specific wavefront characteristics.

A plot of *OPD* for the example index of refraction image in Figure 75 and Figure 76 is shown in Figure 77. It physically made sense that *OPD* values were high for $x'/D \approx 0-0.075$ because this portion of the wavefront propagated through a large region of the higher density freestream. Thus, *OPL* values were higher for this portion of the wavefront as a result. *OPD* values decreased in the middle portion of the wavefront, $x'/D \approx 0.075-0.21$, because low density structures were present (these low density structures extended across this portion of the wavefront with a slightly more shallow angle than the wavefront propagation angle). *OPL* values were lower for this portion of the wavefront as a result. At $x'/D \approx 0.21-0.24$ there was a slight jump in the values of *OPD*. This resulted from a small pocket of high density freestream fluid that entered the shear layer and wake region and caused the values of *OPL* for this portion of the wavefront to be higher as a result. For the remainder of the diameter of the wavefront, $x'/D \approx 0.24-0.33$, the *OPD* values decreased again due to low density structures, such as a vortex core, and then increased slightly. This caused the values of *OPL* for this portion of the wavefront to initially be higher and to later be lower. A spatial rms value was calculated for the set of *OPD* values for each image and a scatter plot of this data, spatial *OPD_{rms}*, is shown in Figure 78. A histogram of spatial *OPD_{rms}* data is also presented in Figure 79.

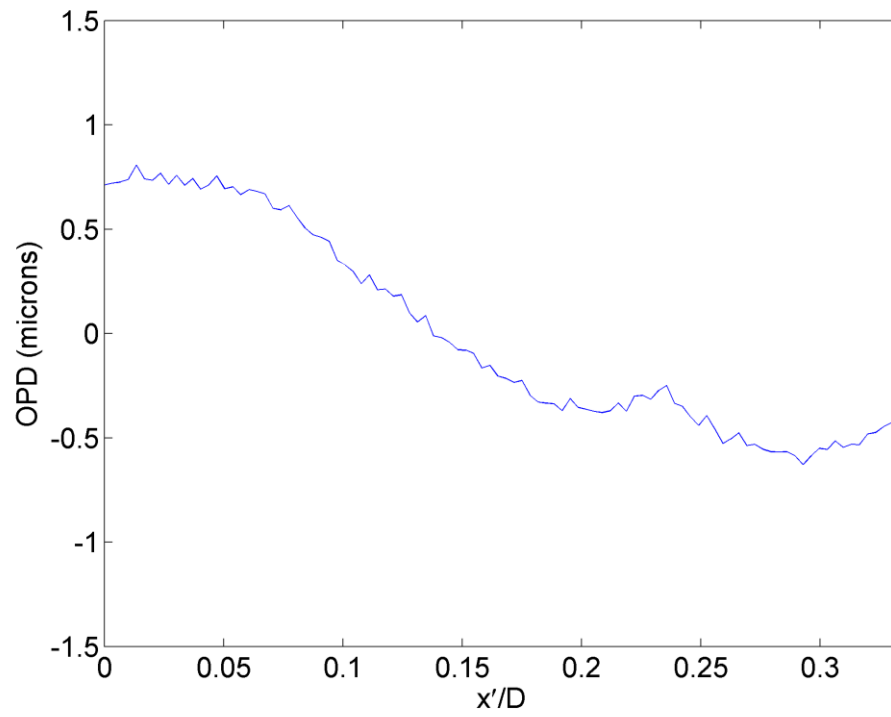


Figure 77: Plot of OPD vs. x'/D for Example Index of Refraction Image

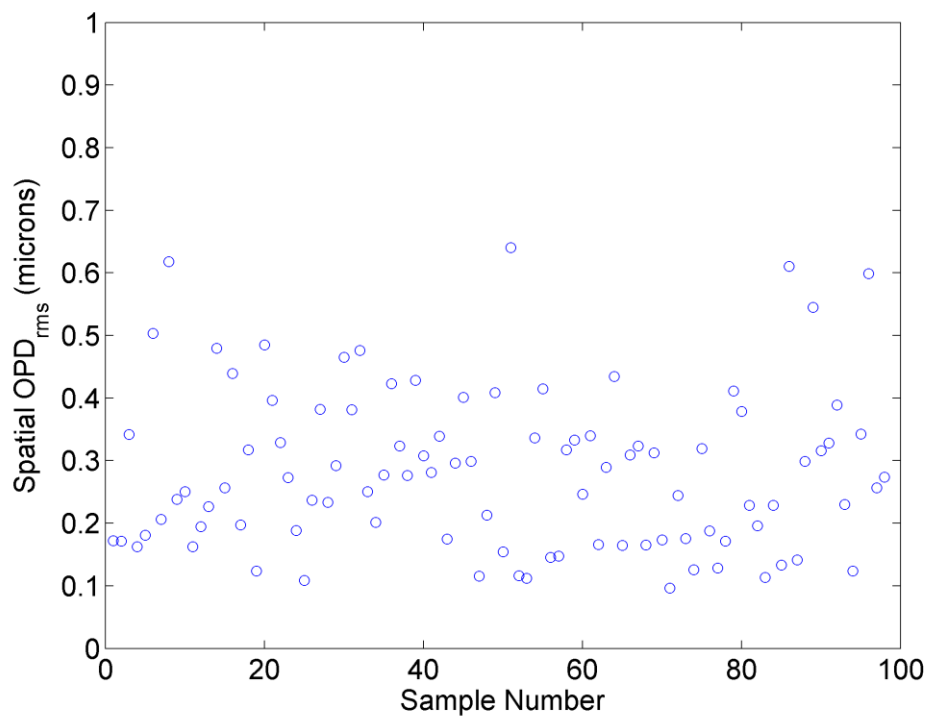


Figure 78: Scatter Plot of Spatial OPD_{rms} Values for Images

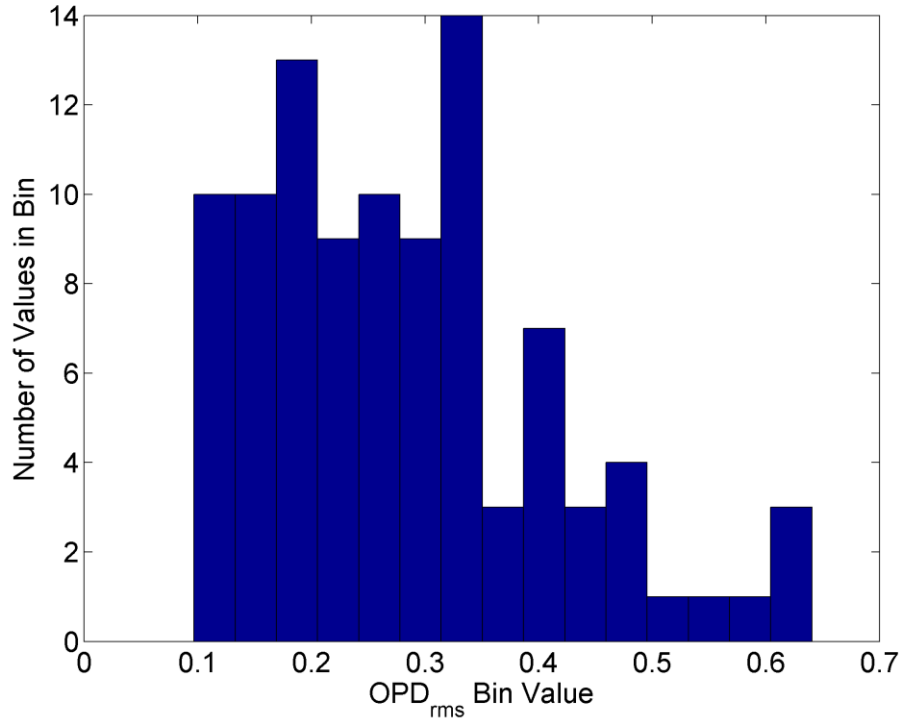


Figure 79: Histogram of OPD_{rms} Values for Images (15 bins)

C. Calculation of Steady and Unsteady Wavefront Distortion

The steady component of the wavefront distortion was found by calculating $\langle OPD \rangle$, the ensemble average of OPD , and is shown in Figure 80. The shape of this plot can be mainly attributed to the geometry of the hemisphere (i.e. the curved surface of the hemisphere). As explained in Section X.A., all pixels within the hemisphere were assigned index of refraction values of 1. Thus, before reaching the hemisphere surface, rays at the middle portion of the wavefront had to travel longer distances through index of refraction values of 1 and rays at the outer portions of the wavefront had to travel shorter distances through index of refraction values of 1. All rays that made up the wavefront were physically/geometrically equal in length. Therefore, rays at the outer portions of

the wavefront had to travel longer distances through higher index of refraction regions (outside the surface of the hemisphere) as a result. This caused the *OPL* values at the outer portions of the wavefront to be higher than the middle portion of the wavefront and was the main reason the plot of $\langle OPD \rangle$ was a smooth curve with its minimum at the approximate middle of the wavefront. There was an additional contributing factor as well. The density field (or index of refraction field) throughout time also played a role. Upon inspection of the ensemble average of normalized density images in Figure 63, it was seen that lower normalized density values radiated outwardly from the hemisphere and increased as radial distance increased. The density pattern was an arc shape, which was similar in shape to the $\langle OPD \rangle$ plot.

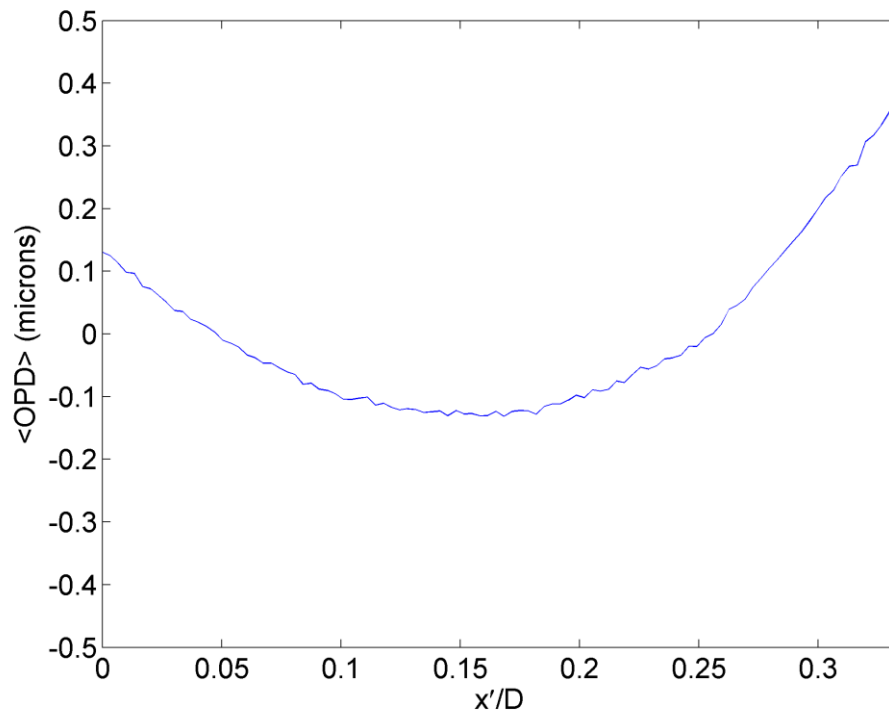


Figure 80: Plot of $\langle OPD \rangle$ vs. x'/D

The unsteady component of the wavefront distortion, which is the true indication of the extent of the aero-optic distortion due to the turbulent flow, is $OPD' = OPD - \langle OPD \rangle$. A plot of OPD' vs. x'/D for the example index of refraction image in Figure 75 and Figure 76 is shown in Figure 81.

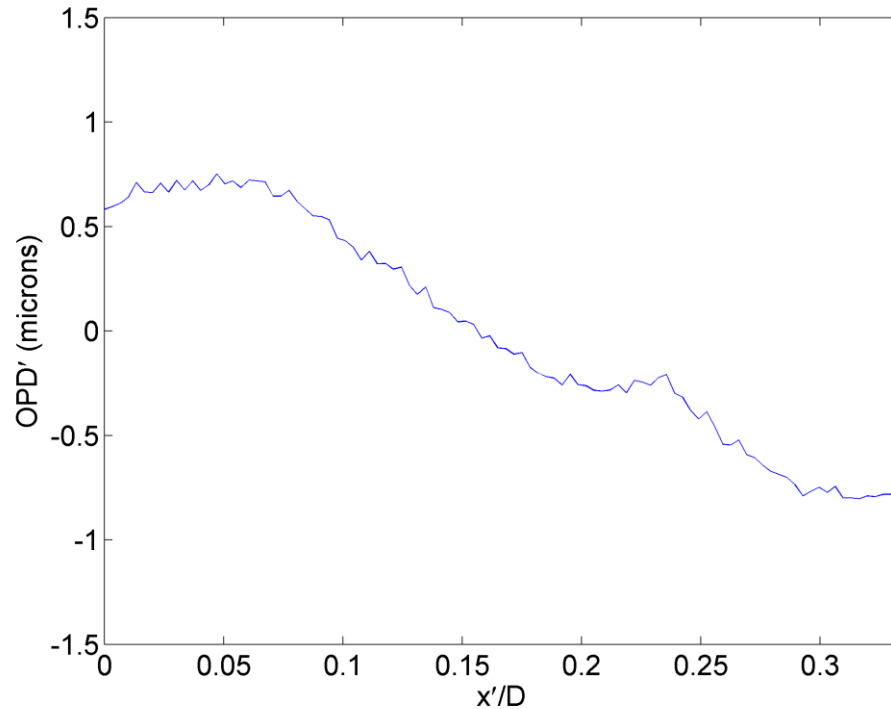


Figure 81: Plot of OPD' vs. x'/D for Example Index of Refraction Image

Finding conditions (i.e. wavefront propagation angle) where the unsteady component of wavefront distortion is minimal is critical. This can be achieved by calculating a set of temporal OPD'_{rms} values at several different wavefront propagation angles. Essentially, this is a calculation of the standard deviation of OPD for the entire set of images for the same wavefront, just at different wavefront propagation angles. In this work, only one wavefront propagation angle was investigated, but this procedure could be repeated for several

wavefront propagation angles. A plot of temporal OPD'_{rms} vs. x'/D is shown in Figure 82. It can be seen that for this particular wavefront propagation angle, OPD fluctuated the least in the middle portion of the wavefront and fluctuated the most at the outer portions of the wavefront.

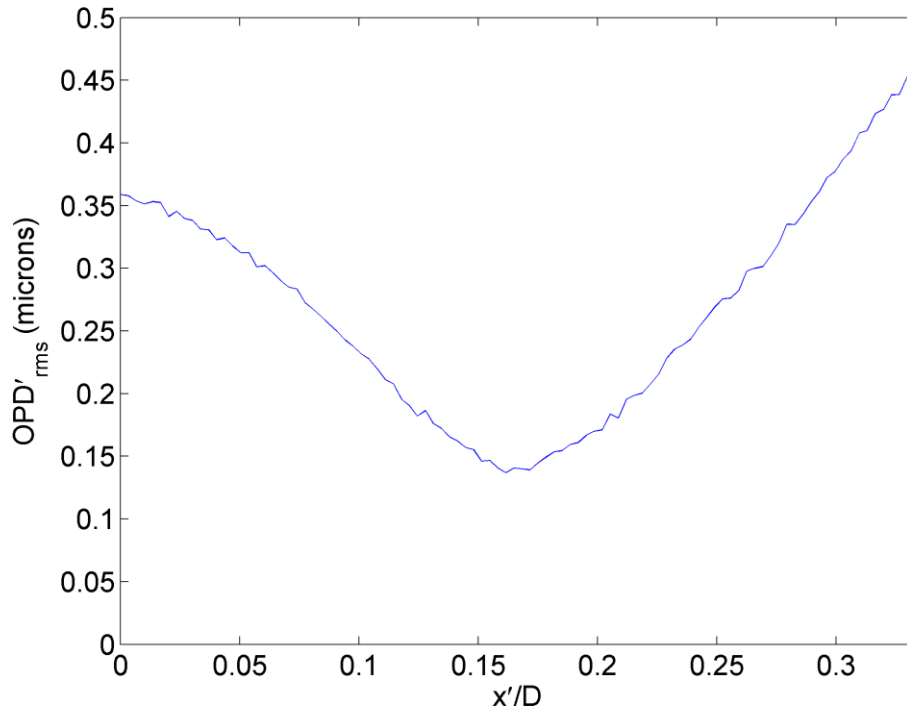


Figure 82: Plot of Temporal OPD'_{rms} vs. x'/D

XI. Time-Resolved Acetone PLIF Experiments

In addition to high-resolution, single-shot acetone PLIF images of the flow field, attempts were made to obtain time-resolved acetone PLIF images of the flow field. The goal of these experiments was to see if quality acetone PLIF images could be obtained at very fast image acquisition speed with the current laboratory equipment. It was assumed that if acetone PLIF images, with conclusive data/adequate SNR, could be obtained under these conditions along a single plane, then movement to 3-D measurements in the future would be straightforward. The only major change needed would be to use a galvanometric scanning mirror (266 nm) instead of a stationary 266 nm mirror. However, if quality acetone PLIF images could not be obtained at very fast image acquisition speed with the current laboratory equipment, then proper diagnoses would need to be made in order to remedy this problem. In the future, there would be no use incorporating a scanning mirror to try and obtain 3-D density data if the high-speed camera itself cannot pick up the necessary fluorescence signal or if the pulse burst laser cannot provide enough energy per pulse at 266 nm for excitation. Thus, time-resolved experiments were deemed necessary in order to make potential problems much more manageable.

A. Details of Experimental Arrangement

a. Laser Excitation and Optical Arrangement

Excitation for time-resolved acetone PLIF was provided by a megahertz rate pulse burst laser system.^{15-16,103,106} This laser was capable of creating

approximately 20 mJ/pulse of 532 nm light at 500 kHz.¹⁰³ In this optical setup, the 532 nm light was converted to 266 nm (resulting in an energy output of approximately 4 mJ/pulse) using a BBO crystal instead of a KDP crystal. The laser sheet was passed through the bottom window of the test section in a normal orientation (not angled as was done in the single-shot PLIF experiments because time-resolved tests were performed prior to the single-shot experiments). The laser sheet was located along the centerline of the hemisphere and did not move position. An $f=-100$ mm spherical lens, an $f=+150$ mm spherical lens, and an $f=-30$ mm plano-concave cylindrical lens were used to create the approximately 200 μm thick and 3.5 inches wide laser sheet. As in the single-shot acetone PLIF experiments, the first spherical lens expanded the beam, the second spherical lens focused the beam, and the cylindrical lens formed the thin laser sheet when the focusing beam passed through it. This optical setup was slightly different from the single-shot acetone PLIF experiments in terms of where the specific optical components were placed. In this setup, all of the optical components were placed on a laser table and a long breadboard was attached to the laser table. This table was positioned next to the wind tunnel test section and the breadboard extended beneath the wind tunnel test section. A stationary 266 nm mirror on this breadboard reflected the expanding 266 nm laser sheet upward through the bottom window of the test section.

b. Seeding for Time-Resolved Acetone PLIF Experiments

Seeding for the time-resolved acetone PLIF experiments was performed in the same manner as for the single-shot acetone PLIF experiments. However, there were a few slight differences. Slightly greater nitrogen tank pressure was used in these experiments (the pressure ranged from approximately 160-170

psig) than in the single-shot acetone PLIF experiments to pressurize the small pressure vessel filled with liquid acetone. The starting storage pressure approximately ranged from 115-125 psig. Thus, Δp was greater than in the single-shot acetone PLIF experiments. Also, time-resolved PLIF experiments were attempted with a Bex YH hollow cone stainless steel spray nozzle, as well as the Bete IS8 spray nozzle, explained in Section VII.C. The YH spray nozzle was $\frac{1}{4}$ " , had a 90° spray pattern, and was reported in literature to spray 0.99 gpm at 20 psig, 1.21 gpm at 30 psig, and 1.71 gpm at 40 psig.¹⁰⁷

c. Camera and Image Acquisition

For the first attempt at time-resolved acetone PLIF, a DRS Hadland Ultra 68^{15-16,103} camera was used. This camera has a resolution of 220×220 pixels and can operate at up to 500,000 frames per second in bursts of 68 images.^{15-16,103} A 50 mm focal length lens was used with no extension tube.

For the second attempt at time-resolved acetone PLIF, a Specialised Imaging SIM02 – Multi-Channel Framing Camera¹⁰⁸ was used. This camera has a much greater resolution than the Ultra 68 camera, having a resolution of 1360×1024 pixels.¹⁰⁸ This setup was actually not time-resolved per se, but the goal of this particular attempt was to see if this camera could obtain quality acetone PLIF images at single-shot speed (the New Wave Solo III PIV Laser⁹⁵, half-waveplate, and KDP crystal were used for excitation; the Solo 200XT PIV Laser⁹⁵ was no longer on loan at the time). The idea was that if this camera could obtain quality single-shot acetone PLIF images (at low image acquisition speed), then it could easily obtain time-resolved PLIF images (at a high image acquisition speed) when coupled with the pulse burst laser.

Note that the cameras used in the time-resolved PLIF experiments were positioned on the opposite side of the wind tunnel from where the Sensicam QE camera was positioned for the single-shot acetone PLIF experiments. In this location, the cameras naturally imaged the flow in a left to right orientation. Also, note that the laser setup and seeding, explained in Section X.A.a.-b., only applied to the experiments conducted using the DRS Hadland ULTRA 68 camera. Laser excitation for attempts with the Specialized Imaging SIM02 camera was achieved with the New Wave Solo III PIV Laser, half-waveplate, and KDP crystal. These experiments with the SIM02 camera were performed after the single-shot acetone PLIF experiments and were similar in terms of setup (location of optical components on the large breadboard beneath the wind tunnel test section and propagation of the laser sheet through the test section at an angle), but used the Solo III PIV Laser instead of the Solo 200XT. Seeding conditions (i.e. Δp) for the experiments with the SIM02 were the same as for the single-shot acetone PLIF experiments, with only the Bete IS8 spray nozzle being utilized. Starting and ending storage pressures for the experiments with the SIM02 were also the same as for the single-shot acetone PLIF experiments (started at 120 psig and ended at 70 psig).

B. Expectations for Time-Resolved Acetone PLIF Experiments

The main expectation for the time-resolved acetone PLIF experiments was that either conclusive, quality acetone PLIF data would be obtained with the pulse-burst laser system and high-speed camera along the centerline plane or hurdles preventing this would be properly diagnosed and remedies would be proposed. If these images could be obtained, then movement to 3-D density measurements through laser sheet scanning acetone PLIF in the future would be

straightforward and would just involve the addition of a galvanometric scanning mirror that is compatible with 266 nm light.

C. Results of Time-Resolved Acetone PLIF Experiments

Time-resolved acetone PLIF experiments did not yield any quality data. The Ultra-68 camera was unable to acquire adequate signal time-resolved acetone PLIF images, so it was no longer a viable option for time-resolved measurements. The SIM02 also could not obtain adequate signal acetone PLIF images, even at low (i.e. single-shot) image acquisition speed, so it was no longer a viable option for time-resolved measurements.

There were distinct reasons why the time-resolved acetone PLIF experiments did not yield quality data. The most obvious reason was the pulse burst laser system only provided 266 nm excitation energy of approximately 4 mJ/pulse, whereas the Solo III PIV Laser and Solo 200XT PIV Laser provided approximately 18-22 mJ/pulse (slightly less excitation energy achieved in these experiments compared to the initial single-shot experiments with the Solo III) and 38 mJ/pulse, respectively, before passing through final optical components. This in principle should have caused the laser fluence and thus the signal to drop by an order of magnitude when using the pulse burst laser system versus the Solo 200XT PIV Laser (less than an order of magnitude drop when using the Solo III versus the Solo 200XT). Also, the laser sheet was wider during time-resolved PLIF experiments with the pulse burst laser (Ultra 68 camera), than single-shot PLIF experiments with the Solo 200XT PIV Laser. This should have caused an additional decrease in laser fluence and thus signal (the width of the laser sheet was not assumed to additionally affect laser fluence and thus signal when using

the Solo III PIV Laser (SIM02 camera) because the laser sheet was not as wide as the laser sheet when using the pulse burst laser).

Also, the Sensicam QE camera, used for single-shot acetone PLIF, does not have a beam splitter in its design, while the Ultra 68 and the SIM02 high-speed cameras, both intensified, utilize multiple beam splitters. Beam splitters decrease the intensity of the light that comes into the camera and thus the Ultra 68 and SIM02, by having beam splitters, naturally decrease the signal before the intensifier is reached. Additionally, signal collection is decreased because the maximum aperture size (minimum $f/\#$) for each camera is limited by beamsplitter optical arrangement. The SIM02 also could not collect signal below 395 nm (due to the design of the beam splitter), which affected the overall amount of collected signal. Acetone fluoresces over a wavelength range of 350-550 nm and the fluorescence peaks at 435 nm and 480 nm.^{48,49} Thus, a significant portion of signal is lost from 350-395 nm when using the SIM02 camera. Beamsplitter information and characteristics for the Hadland Ultra 68 camera were not available. The beam splitters and their effect on $f/\#$ were estimated to cause a decrease in collected signal of at least one order of magnitude. Overall, the pulse burst laser system and camera technology currently in use for the time-resolved acetone PLIF experiments were estimated to cause a decrease in collected signal, compared to the single-shot acetone PLIF experiments, of two orders of magnitude.

Despite the current failure of the time-resolved acetone PLIF experiments, the success of the single-shot acetone PLIF experiments proved that quality signal acetone PLIF images could be obtained for this flow field and density data could be obtained for single planes. In terms of time-resolved acetone PLIF and moving to 3-D density measurements through laser sheet scanning acetone PLIF in the future, it is just a matter of having the proper equipment to create and

collect this signal. The only components missing are greater 266 nm intensity/energy from the pulse burst laser system, a proper high-speed camera, and for future 3-D experiments, a proper galvanometric scanning mirror that can handle 266 nm light.

Another amplifier is currently being added to the pulse burst laser system, bringing the total number of amplifiers to six. This should increase the 532 nm laser energy output to approximately 30 mJ/pulse at 500 kHz. In turn, this will increase the 266 nm laser energy output, yielding greater signal and higher quality acetone PLIF data.

Several high-speed camera technologies are also available, or are in production, and have promising characteristics. These include technology from Shimadzu, MIT's Lincoln Laboratories (in development), and Princeton Scientific Instruments. These camera designs do not have beam splitters and have CCDs with large pixels, both of which increase signal levels (the benefit of large pixels is demonstrated in the next paragraph). The pulse burst laser delivering greater 266 nm laser energy to the acetone molecules and high-speed cameras with no beam splitters and larger pixels on the CCD should enable quality time-resolved acetone PLIF data to be obtained.

A Princeton Scientific Instruments, Inc. PSI-4 Ultra Fast Framing Camera¹⁰⁹ is currently on loan from The Ohio State University and it is believed that this camera has favorable enough characteristics to obtain quality time-resolved acetone PLIF images. The camera has a resolution of 80 x 160 pixels and can operate at up to 3,000,000 frames per second in bursts of 28 images.¹⁰⁹ Quantum efficiency of the PSI-4 camera CCD is 35% at 256 nm and 313 nm and is 55% at 660 nm.¹⁰⁹ It is assumed that for the fluorescence spectrum of acetone, the quantum efficiency would be approximately 45%. The size of each pixel on the PSI-4 camera CCD is 115 μm x 115 μm (area of CCD is 18.4 mm x 9.2 mm).¹⁰⁹ This

means that the physical area of each pixel on the PSI-4 CCD is approximately 318 times larger than the physical area of each pixel on the Sensicam QE CCD (the Sensicam QE camera was used for single-shot acetone PLIF and yielded quality PLIF images). After taking into account optical fill factor for each CCD (optical fill factor for PSI-4 CCD is 48%¹⁰⁹ and optical fill factor for Sensicam QE CCD is approximately 80-81%¹⁰¹), it is found that each pixel on the PSI-4 CCD has an optically active area that is approximately 190 times larger than the optically active area for each pixel on the Sensicam QE CCD. When the quantum efficiency values for each CCD are additionally taken into account (the Sensicam QE CCD quantum efficiency was assumed to be 58% for this work, as explained in Section IX.A.c.), it is found that a single pixel on the PSI-4 CCD collects approximately 147 times more photons than a single pixel collects on the Sensicam QE CCD (assuming both CCDs are exposed to the same amount and wavelength of light). This is an increase of two orders of magnitude in signal collected when using the PSI-4 camera versus the Sensicam QE camera. Time constraints prevented the implementation of the PSI-4 camera to obtain time-resolved acetone PLIF data.

A compatible galvanometric scanning mirror is a necessity for future 3-D laser sheet scanning acetone PLIF experiments. It reflects the beam through the plano-concave cylindrical lens and into the test section, while also deflecting throughout time. This causes the laser sheet to scan across the flow field. A company named SCANLAB¹¹⁰ manufactures 266 nm galvanometric scanning mirrors that are large enough for the diameter of the 266 nm beam output from the pulse burst laser system and should be compatible for this work. However, the mirror alone would not just be purchased. The SCANLAB galvanometer would also need to be purchased. This is because the SCANLAB 266 nm mirror itself would probably not interface correctly with the current GSI Lumonics VM500+¹¹¹ galvanometer (Cambridge Technology is part of GSI) here at Auburn

University. Budget and time constraints prevented the implementation of this galvanometric scanning mirror from SCANLAB.

XII. Conclusions and Future Work

A. Conclusions

The work presented in this thesis demonstrated that acetone planar laser induced fluorescence is a viable technique for density measurements in a high-velocity, compressible flow field. A transonic wind tunnel was designed and fabricated in order to investigate the shear layer and wake region of a wall-mounted hemisphere in a freestream flow ($M_\infty \approx 0.78$). Single-shot acetone PLIF images were obtained along multiple parallel planes of this flow field and the density field was found for these images. Final density images were high-quality and revealed a shear layer and turbulent wake region. The wake region exhibited a flapping/sweeping motion that caused the wake thickness to vary (typically the wake thickness was $\frac{1}{2}$ of the diameter of the hemisphere). Density images also revealed distinct vortex cores in the shear layer and upper wake region where the density greatly dropped, sometimes up to 45-50% of the freestream density. Also, the centerline separation region images revealed shocks near the boundary layer separation point (the location of the separation point was not constant).

Once density field data was obtained for the single-shot acetone PLIF images, aero-optic distortion values were calculated for a planar wavefront propagating through the centerline wake region images (converted from density images to index of refraction images) at a single propagation angle. The steady and unsteady wavefront distortion was calculated for this wavefront propagation angle. This proved that this density measurement technique can be applied to aero-optics in a straightforward manner.

Time-resolved acetone PLIF imaging was attempted along the centerline of the hemisphere without success. However, it is believed with confidence that quality time-resolved acetone PLIF images can be obtained after upgrades are made to the pulse-burst laser system and a high-speed camera with more favorable characteristics is utilized. Once it is proven that time-resolved acetone PLIF images can be acquired and a capable galvanometric scanning mirror (for 266 nm light) is obtained, 3-D laser sheet scanning acetone PLIF should be easily carried out in the future.

PIV images were also obtained along the centerline of the hemisphere. It was apparent in these images, although they were very small in number, that large vorticity values existed in the shear layer and upper wake region. This was consistent with the density data because the shear layer and upper wake region revealed low density vortex cores in these regions. PIV results also showed that the maximum velocity magnitude was located in the shear layer and a stagnation point existed on the front (upstream) and the back (downstream) of the hemisphere.

Overall, this work provides a great base for future work that includes improvements to the experimental facility/setup and density measurement technique itself, as well as investigation of other high-velocity, compressible flow fields. This work provides density data for comparison with other models, such as the WCM and CFD. It also provides wavefront distortion data for comparison with other wavefront measurement techniques that can be used to study the optical environment of this flow field. Finally, the success of this work is a springboard for future 3-D density measurements using laser sheet scanning acetone PLIF.

B. Future Work

Even with the success of the acetone PLIF density measurement technique in this work, there are many improvements that could and should be made in order to increase the accuracy and quality of the results for this flow field and other flow fields. This technique will likely be implemented to study the density field of other compressible flows in the future, so increasing quality and accuracy of results is very important. If there were no budget or time constraints, improvements would be made to the wind tunnel, the optical setup/image processing/camera/excitation laser, fluorescence quantum yield model and absorption cross-section data, and particle image velocimetry experiments. Validation experiments would also be conducted to verify the density measurement technique itself and the aero-optic distortion calculations.

a. Improvements to the Wind Tunnel

The main improvement to the wind tunnel would come in the form of an AR-coated UV fused silica window for the top wall of the test section. During acetone PLIF experiments, the 266 nm laser sheet caused the top wall of the test section to fluoresce, creating large amounts of noise on and near the wall and preventing quality fluorescence signal data for the flow from being obtained very close to the wall. The Sensicam QE was tilted downward to improve this problem. The downside to this tilting method was the collected signal decreased near the wall. The tilt also added an extra wrinkle to COS^4 vignetting (not accounted for during the COS^4 vignetting correction). Also, because the laser sheet was not parallel to the CCD, the spatial resolution from point to point (pixel to pixel) in the images slightly changed in the vertical direction (not

accounted for during the image processing and in-situ calibration procedure). During PIV experiments there were also intense reflections of 532 nm light off of the top wall of the wind tunnel. If a stepped window with the same dimensions, glass type, and AR coating as the bottom stepped window were installed on the top wall of the test section, this problem would be greatly improved. There would need to be one slight modification to the window design however.

In order to mount the hemisphere securely with no aluminum exposed, except for the hemisphere itself, the window would need to be counter-bored. The counter-bored hole would comprise a $\frac{1}{2}$ " diameter for the top $\frac{1}{2}$ " of the thickness of the step window (non-wetted face of window) and then a $\frac{1}{4}$ " diameter for the bottom $\frac{1}{2}$ " of the thickness of the step window (wetted face of window). Then an aluminum (or delrin or some other material) plug that fits the dimensions of the counter-bored hole would be machined and placed in this counter-bored hole. This plug would have a through hole that a bolt could pass through and the hemisphere could then be mounted to this plug with a bolt, as seen in Figure 83. As the bolt is tightened, the hemisphere and plug would pull tighter together and butt up against the glass because the $\frac{1}{4}$ " portion of the counter-bored hole is smaller than the 1" diameter hemisphere and the $\frac{1}{2}$ " diameter top portion of the plug. It is important that the top portion of the counter-bored hole is smaller in diameter than the hemisphere diameter to minimize the possibility of light reflecting off of the plug and/or causing the plug to fluoresce, creating ambient light/noise. The top window itself would be held in place using an aluminum bracket that bolts to the wind tunnel, as is done to secure the bottom stepped window and the rectangular side windows. Budget and time constraints prevented this change to the wind tunnel from becoming a reality before this thesis was completed, but it is an easy fix and the most practical fix if one has the means to pay for the modification.

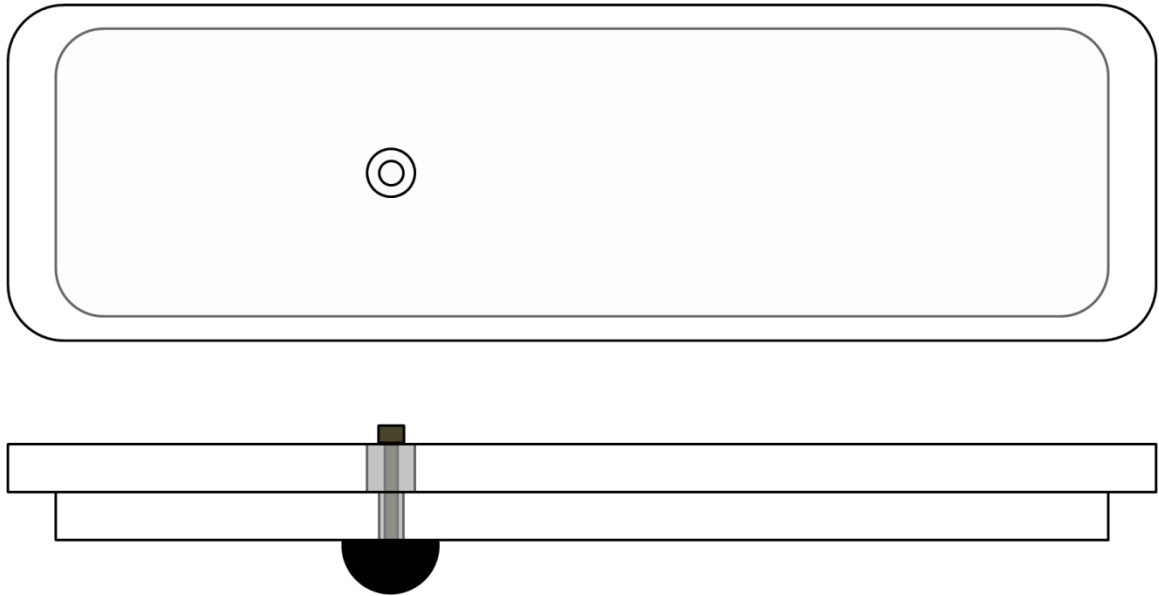


Figure 83: Design for Top Wall Stepped-Window (not drawn exactly to scale)

In addition, more pressure ports would be installed in the test section. Pressure ports are currently installed on the top wall of the test section just behind/downstream of the hemisphere. If the new window idea above were used, then pressure ports would still be installed for the top wall as follows. Currently, there is an aluminum insert available that is the same size and nearly the same shape as the bottom stepped window. It is used in place of the bottom window when the bottom window is not needed. A through hole and a bolt would be used to mount the hemisphere to the aluminum insert. Then pressure ports would be installed in this aluminum insert, directly behind/downstream of the hemisphere. Delrin could also be used instead of an aluminum insert and would be easier to machine. Pressure ports would also be installed on the hemisphere itself to give a better idea of what kind of experimental pressure bounds to place on the $S_f/S_{f\infty}$ vs. ρ/ρ_∞ curves. This would potentially decrease error in the density measurement technique.

Thermocouples would also be installed in the storage tanks and the stagnation/settling chamber. This would enable very accurate measurements of storage temperature and stagnation temperature, which should be (and in this work were assumed to be) approximately equal to each other throughout the test run. In turn this would enable more accurate estimates of the freestream static temperature, which is currently estimated using storage pressure, stagnation pressure, static pressure, the isentropic relations, and an estimate of the starting storage temperature. The freestream static temperature could also be confirmed by obtaining velocity field data through PIV and coupling the freestream velocity with the stagnation temperature (or storage temperature) and Equation 19⁸⁹.

$$c_p T + \frac{u^2}{2} = c_p T_0 \quad 19$$

Leaks in the wind tunnel would also be better sealed. This is in regard to leaks where the test section and diffuser are joined, leaks where the diffuser, 90° elbow, and ceiling pipe are joined (currently wrapped in heavy-duty Saran wrap), slight leaks in the test section itself, and slight leaks where the wall pipe fitting for the seeding system is inserted into the compressed air supply line pipe. The wall pipe fitting would actually be welded to the compressed air supply line pipe to stop leaks instead of the current method of using pipe dope, two o-rings, a nylon spacer, and JB Weld which only decreases the severity of the leaks.

Finally, access to the inside of the test section would be improved. Currently, to obtain access to the inside of the test section, either the bottom stepped window or one of the rectangular side windows has to be completely removed. This involves loosening many bolts which is not only tedious, but also degrades the integrity of the wind tunnel because the test section is made of aluminum. Several of the tapped holes have to be re-tapped as threads on the bolts tear away the fresh inner threads of each tapped hole. The best solution

would be to somehow make the transonic wind tunnel test section more like the supersonic wind tunnel test section at Auburn University. The supersonic wind tunnel has a section just downstream of the test section that slides into the farther downstream diffuser when the tunnel is not in use, allowing easy access to the test section, as seen in Figure 84. When experiments are ready to be conducted, this section is slid back into place and a large bolt on each side of the wind tunnel test section holds this sliding section in place. This would probably mean that an overhaul of the downstream portion of the test section and the entire diffuser would be necessary if this was pursued. Although this is not necessary to obtain high-quality data, this would save significant time during experiments. The windows and hemisphere model had to be cleaned after each acetone PLIF test run (requiring test section access) and this would greatly shorten the time for that process.



Figure 84: Easy Access to Supersonic Wind Tunnel Test Section

b. Improvements to Optical Setup, Image Processing, and Camera/Excitation Laser

Image quality would be increased through improvements to the optical setup, image processing, and the camera/excitation laser. This is because image processing would be less complex and SNR values in the images would be greater. The optical setup and image processing for acetone PLIF experiments would be improved by obtaining a positive focal length, large aperture convex cylindrical lens with a width greater than or equal to the desired width of the laser sheet. This convex cylindrical lens would be placed after the plano-concave cylindrical lens in the optical setup and would collimate the trapezoidal laser sheet. The laser sheet intensity profile (roughly Gaussian) would remain constant throughout the flow field, making laser sheet non-uniformity correction much simpler. The relationship $I_{Laser,ij} \propto \frac{1}{R_{ij}}$ would not need to be implemented because there would be no beam spreading where drops in laser sheet intensity occur along lines of constant θ_j . Also, regions/lines of constant laser sheet intensity would all be parallel to each other as opposed to being angled regions/lines that fan outwardly and are not parallel to each other (as is the case for the current acetone PLIF images after the correction for drops in laser sheet intensity along lines of constant θ_j is applied). Thus, a theoretical origin would not need to be found. The particle filtering procedure would also be improved and maybe even performed after the correction for drops in laser sheet intensity along lines of constant θ_j , but before the correction for the Gaussian laser sheet intensity profile. Image processing and in-situ calibration would additionally be improved by obtaining and using flat field correction images, as explained in Section IX.D.

A dot card image would be obtained instead of a ruler image in order to calculate the spatial resolution of the image. This would provide a more accurate spatial resolution measurement throughout a larger portion of the image and make barrel or pin cushion distortion clearly visible if it exists. Also, aligning the laser sheet along the imaging plane and then focusing the camera would be simpler.

For time-resolved and future 3-D acetone PLIF experiments, capable high-speed cameras are being researched and upgrades are currently being made to the pulse burst laser system. As explained in Section XI.C., the PSI-4 camera is a very strong candidate as it possesses qualities that on paper suggest that it can obtain quality acetone PLIF images at high image acquisition speed. Combining this type of camera with the upgraded pulse burst laser system, also explained in Section XI.C., should allow quality time-resolved acetone PLIF images to be obtained. This may even enable a smaller acetone mole fraction to be used during these experiments, which should increase the window of time over which images can be obtained without condensation. The same concept can be applied to the single-shot acetone PLIF experiments. If a more powerful PIV laser is acquired and the 532 nm output is converted to 266 nm, then the SNR values in the acetone PLIF images will increase. This should enable a smaller acetone mole fraction to possibly be used while still achieving adequate SNR values.

c. Improvements to Fluorescence Quantum Yield Model and Absorption Cross-Section Data

Extraction of density from the acetone PLIF images depended upon absorption cross-section data and fluorescence quantum yield data established by a researcher (Thurber (1999)⁴⁸) outside of Auburn University. The fluorescence

quantum yield model was optimized for this experimental data and data from literature. This data was collected at conditions that were somewhat different than those experienced in the work presented in this thesis. However, the absorption cross-section data and fluorescence quantum yield data (calculated from fluorescence signal and absorption cross-section) were expected to be fairly accurate when applied to the work presented in this thesis because this work relied upon normalized values of absorption cross-section and fluorescence quantum yield. Thus, relatively speaking, large errors in either variable should have scaled together and cancelled out as the variables were normalized. Also, the experimental conditions at which the data were obtained were not extremely different from this work. However, a lot of data was still extrapolated and accuracy in all the data can still be improved, so obtaining laboratory data for the conditions in this hemisphere flow field would be very beneficial. To improve the accuracy of ϕ and σ results, flow cell and static gas cell measurements would be made for the experimental conditions experienced during a typical test run.

The proposed experiments would be similar to those performed by Thurber, explained in Section III.F.a., except a flow/static cell would be filled with acetone vapor and dry air and set to the pressure boundaries established in the acetone PLIF test runs conducted in the transonic wind tunnel. Density would be increased from zero to the stagnation density by adjusting the temperature accordingly. Fluorescence signal data would be obtained by exciting the acetone molecules with 266 nm light and simultaneously absorption cross-section data would be obtained. The average acetone mole fraction for a wind tunnel test run is known and would be incorporated into this experiment and monitored to make sure each case accurately reflects this acetone mole fraction. This collected data would be used to test the accuracy of the fluorescence quantum yield model (the normalized fluorescence quantum yield can be found

from the normalized fluorescence signal and the normalized absorption cross-section by using Equation 8). If modifications to specific parameters in the fluorescence quantum yield model need to be made, then these changes would be made. Additionally, the experimentally found values of σ vs. T would be used for calculation of σ for a specific T input. Much more accurate curves of $S_f/S_{f\infty}$ vs. ρ/ρ_∞ would be created, resulting in more accurate density field calculations. If one did not want to use the model and wanted to purely rely upon the experimental data, then that would be acceptable too. In essence, because the fluorescence signal would be found, the $S_f/S_{f\infty}$ vs. ρ/ρ_∞ curves could be created by normalizing the fluorescence signal to the approximate freestream fluorescence signal case.

The collision aspects of the model would also be updated. These updates would take into account the polarity of acetone, so collisions between acetone molecules would be modeled more accurately to take into account the dipole moment.⁴⁸ This would be achieved by using the Stockmayer potential instead of the Lennard-Jones potential, as suggested by Thurber.⁴⁸ Also, the terms for molecule collision diameter and collision potential energy for collisions between non-polar molecules and polar acetone molecules would be correctly input into the model to take into account dipole moment, as suggested by Thurber.⁴⁸ These modifications will result in a more accurate collision frequency and collision rate term, k_{coll} . Suggested updates to the overall model from other researchers^{51,62-63} will also be considered and those concluded to be reasonable updates/improvements to the model will be implemented into the model.

Finally, the photophysics of liquid acetone would be studied more in-depth so if condensation did still occur, its effect on fluorescence signal would be better understood. Liquid acetone photophysics are explained in Tran (2008)⁵⁰.

d. Improvements to Particle Image Velocimetry Experiments

Several improvements would also be made to the PIV experiments. First and foremost, the PIV seeding would be greatly improved. For high-speed wind tunnels, a cyclone seeder^{97,112-115} or a Laskin nozzle^{97,98} (with injection into the compressed air supply line pipe or into the stagnation/settling chamber) is the best solution for seeding purposes. However, the facility at Auburn University is currently limited where this is not a possibility. Therefore, this facility needs to be upgraded to house a functional cyclone seeder or Laskin nozzle or some other improvement needs to be made to the current seeder. Currently, the particles are settling on the bottom of the pressure vessel and sticking together, so this needs to be remedied somehow. An improved seeder would enable large sets of single-shot data to be obtained, as well as time-resolved PIV data.

The second improvement, after improving seeding, would be obtaining a large set of single-shot PIV data for the centerline separation region and wake region with which turbulent properties such as Reynolds stresses, turbulent kinetic energy, and average vorticity could be calculated. The final improvement would be obtaining a set of time-resolved PIV data for the centerline separation region and wake region (a new high-speed camera, a Cordin Model 222-4G Camera¹¹⁶, that is currently being acquired by the Advanced Laser Diagnostics Laboratory at Auburn University would be used). This time-resolved PIV data could be coupled with the Weakly Compressible Model to estimate pressure, temperature, and density fields. These estimated density fields could then be compared to the density fields measured from acetone PLIF experiments. In addition, the estimated pressure fields could be compared to the experimental bounds currently placed on pressure (for the $S_f/S_{f\infty}$ vs. ρ/ρ_∞ curves) to improve the accuracy of these bounds. This would result in more accurate density field data.

e. Validation of Density Measurement Technique and Wavefront Distortion Calculations

In the future, a more basic compressible flow field, whose density field and characteristics are well-characterized and established in literature, will be investigated with the acetone PLIF density measurement technique. This will enable validation of the density measurement technique and enable better understanding of the effects of error on the density measurement technique.

Also in the future, wavefront/aero-optic distortion measurements would be made for the hemisphere flow field using a Shack-Hartmann wavefront sensor or some other wavefront measurement technique. This would enable direct comparison between measured wavefront/aero-optic distortion results and calculated wavefront/aero-optic distortion results obtained from density field images (acquired using the acetone PLIF density measurement technique). A background oriented Schlieren (BOS) technique for aero-optics¹¹⁷ is also being developed by Abhishek Bichal, a PhD candidate for Dr. Brian Thurow in the Advanced Laser Diagnostics Laboratory at Auburn University, and it should be able to make wavefront/aero-optic distortion measurements of this flow field in the future.

Works Cited

- ¹Gordeyev, S., Jumper, E., Vukasinovic, B., Glezer, A., and Kibens, V., "Fluidic Control of a Turret Wake, Part II: Aero-Optical Effects," 47th AIAA Aerospace Sciences Meeting and Exhibit, Orlando, Florida, 5-8 January 2009, AIAA-2009-0817.
- ²Mani, A., Wang, M., and Moin, P., "Computational study of aero-optical distortions by a turbulent wake," Center for Turbulence Research Annual Research Briefs 2006, Notre Dame, Indiana, 2006.
- ³Laufer, G., *Introduction to Optics and Lasers in Engineering*. New York, New York: Cambridge University Press, 1996.
- ⁴Allaby, M., *Encyclopedia of Weather and Climate*. Revised Edition. New York, New York: Facts on File, Inc., 2002.
- ⁵Zhao, Y., Han, Y., Fan, Z., Qiu, F., Kuo, Y., Kaufman, A., and Mueller, K., "Visual Simulation of Heat Shimmering and Mirage," To appear at IEEE Transactions on Visualization and Computer Graphics, Kent State University, Kent, Ohio.
- ⁶Jumper, E.J. and Fitzgerald, E.J., "Recent advances in aero-optics," *Progress in Aerospace Sciences*, Notre Dame, Indiana, 2001, Volume 37, pp. 299-339.
- ⁷Gordeyev, S., Hayden, T.E., and Jumper, E.J., "Aero-Optical and Flow Measurements Over a Flat-Windowed Turret," *AIAA Journal*, Notre Dame, Indiana. February 2007, Volume 45, Number 2, pp. 347-357.
- ⁸Gordeyev, S., Post, M.L., McLaughlin, T., Cenicerros, J., and Jumper, E.J., "Aero-Optical Environment Around a Conformal-Window Turret," *AIAA Journal*, Notre Dame, Indiana, July 2007, Volume 45, Number 7, pp. 1514-1524.
- ⁹Platt, B.C. and Shack, R., "History and Principles of Shack-Hartmann Wavefront Sensing," *Journal of Refractive Surgery*, Pasadena, California, September/October 2001, Volume 17, pp. S573-S577.

- ¹⁰Schwiegerling, J. and Neal, D.R., "Historical Development of the Shack-Hartmann Wavefront Sensor," University of Arizona, Tucson, Arizona.
- ¹¹Rennie, M., Ponder, Z., Gordeyev, S., Nightingale, A., and Jumper, E., "Numerical Investigation of Two-Dimensional Compressible Shear Layer and Comparison to Weakly Compressible Model," Directed Energy Professional Society Beam Control Conference, Monterey, California, 3-7 March 2008.
- ¹²Fitzgerald, E.J. and Jumper, E.J., "The optical distortion mechanism in a nearly incompressible free shear layer," *Journal of Fluid Mechanics*, Houston, Texas, 2004, Volume 512, pp 153-189.
- ¹³Jumper, E.J., "Adaptive Optics for Turbulent Shear Layers," Final Report, Air Force Office of Scientific Research, AFRL-SR-AR-TR-07-0218, University of Notre Dame, Notre Dame, Indiana, 20 December 2006.
- ¹⁴Ponder, Z.B., Rennie, R. M., Abado, S., and Jumper, E.J., "Span-wise Wavefront Measurements Through a Two-Dimensional Weakly-Compressible Shear Layer," 41st Plasmadynamics and Lasers Conference, Chicago, Illinois, 28 June – 1 July 2010, AIAA 2010-4495.
- ¹⁵Thurrow, B.S. and Lynch, K.P., "Development of a High-Speed Three-Dimensional Flow Visualization Technique," *AIAA Journal*, Auburn, Alabama, December 2009, Volume 47, Number 12, pp. 2857-2865.
- ¹⁶Williams, S. T., Melnick, M.B., "3-D Visualization of a Turbulent Boundary Layer," 40th Fluid Dynamics Conference and Exhibit, Chicago, Illinois, 28 June – 1 July 2010, AIAA 2010-4277.
- ¹⁷Gordeyev, S. and Jumper, E., "Fluid dynamics and aero-optics of turrets," *Progress in Aerospace Sciences*, Notre Dame, Indiana, 2010, Volume 46, pp. 388-400.
- ¹⁸Gordeyev, S. and Jumper, E., "Fluid Dynamics and Aero-Optical Environment Around Turrets," AIAA, Notre Dame, Indiana, 2009, AIAA 2009-4224.

- ¹⁹Gordeyev, S., Post, M.L., McLaughlin, T., Cenicerros, J., and Jumper, E.J., "Survey of Optical Environment over Hemisphere-on-Cylinder Turret Using Suite of Wavefront Sensors," 37th AIAA Plasmadynamics and Lasers Conference, San Francisco, California, 5-8 June 2006, AIAA-2006-3074.
- ²⁰Siegenthaler, J.P., Jumper, E.J., and Gordeyev, S., "Atmospheric Propagation Vs. Aero-Optics," 46th AIAA Aerospace Sciences Meeting and Exhibit, Reno, Nevada, 7-10 January 2008, AIAA 2008-1076.
- ²¹Cain, A.B., Ng, T.T., Jumper, E.J., Wittich, D.J., Cavalieri, D., and Kerschen, E.J., "An Optical Propagation Improvement System and the Importance of Aeroacoustics," 39th Plasmadynamics and Lasers Conference, Seattle, Washington, 23-26 June 2008, AIAA 2008-4212.
- ²²Rennie, R. M., Crahan, G., and Jumper, E.J., "Aerodynamic Design of an Aircraft-Mounted Pod for Improved Aero-Optic Performance," 48th AIAA Aerospace Sciences Meeting Including the New Horizons Forum and Aerospace Exposition, Orlando, Florida, 4-7 January 2010, AIAA 2010-437.
- ²³Vukasinovic, B., Glezer, A., Gordeyev, S., Jumper, E., and Kibens, V., "Hybrid Control of a Turret Wake, Part I: Aerodynamic Effects," 48th AIAA Aerospace Sciences Meeting Including the New Horizons Forum and Aerospace Exposition, Orlando, Florida, 4-7 January 2010, AIAA 2010-86.
- ²⁴Vukasinovic, B. and Glezer, A., "Control of a Separating Flow over a Turret," AIAA, Atlanta, Georgia, 2007, AIAA 2007-4506.
- ²⁵Vukasinovic, B., Glezer, A., Gordeyev, S., Jumper, E., and Kibens, V., "Active Control and Optical Diagnostics of the Flow over a Hemispherical Turret," AIAA, Atlanta, Georgia, 2008, AIAA 2008-598.
- ²⁶Vukasinovic, B., Glezer, A., Gordeyev, S., Jumper, E., and Kibens, V., "Fluidic Control of a Turret Wake: Aerodynamic and Aero-Optical Effects," Georgia Institute of Technology, Atlanta, Georgia.
- ²⁷Vukasinovic, B., Glezer, A., Gordeyev, S., Jumper, E., and Kibens, V., "Fluidic Control of a Turret Wake, Part I: Aerodynamic Effects," 47th AIAA Aerospace Sciences Meeting Including The New Horizons Forum and Aerospace Exposition, Orlando, Florida, 5-8 January 2009, AIAA 2009-816.

- ²⁸Wang, K., Wang, M., Gordeyev, S., and Jumper, E., "Computation of Aero-Optical Distortions over a Cylindrical Turret with Passive Flow Control," University of Notre Dame, Notre Dame, Indiana.
- ²⁹Savory, E. and Toy N., "The flow regime in the turbulent near wake of a hemisphere," *Experiments in Fluids*, Guildford, Surrey, United Kingdom, 1986, Volume 4, pp. 181-188.
- ³⁰Bakić, V. and Perić, M., "Visualization of Flow Around Sphere for Reynolds Numbers Between 22 000 and 400 000," *Thermophysics and Aeromechanics*. Belgrade, Serbia and Montenegro, 2005, Volume 12, Number 3, pp. 307-315.
- ³¹Jang, Y.I. and Lee, S.J., "PIV analysis of near-wake behind a sphere at a subcritical Reynolds number," *Experiments in Fluids*, Hyoja Dong, Pohang, Republic of Korea, 2008, Volume 44, Number 6, pp. 905-914.
- ³²Sedighi, K. and Farhadi, M., "Three-Dimensional Study of Vortical Structure Around a Cubic Bluff Body in a Channel," *Facta Universitatis Series Mechanical Engineering*, Babol, Mazandaran, Iran, 2006, Volume 4, Number 1, pp. 1-16.
- ³³Tufo, H.M., Fischer, P.F., Papka, M.E., and Szymanski, M., "Hairpin Vortex Formation, a Case Study for Unsteady Visualization," University of Chicago, Chicago, Illinois, 28 July 1999.
- ³⁴Tsutsui, T., "Flow around a sphere in a plane turbulent boundary layer," *Journal of Wind Engineering and Industrial Aerodynamics*, Yokosuka, Kanagawa, Japan, 2008, Volume 96, pp. 779-792.
- ³⁵Stewart, B.E., Leweke, T., Hourigan, K., and Thompson, M.C., "Wake formation behind a rolling sphere," *Physics of Fluids*, Victoria, Australia and Marseille, France, 2008, Volume 20, pp. 071704-1 – 071704-4.
- ³⁶Sarioglu, M. and Yavuz, T., "Vortex Shedding From Circular and Rectangular Cylinders Placed Horizontally in a Turbulent Flow," *Turkish Journal of Engineering and Environmental Sciences*, Trabzon, Turkey, 2000, Volume 24, pp. 217-228.

- ³⁷Kim, D. and Choi, H., "Laminar flow past a hemisphere," *Physics of Fluids*, Yuseong, Daejeon, Korea, August 2003, Volume 15, Number 8, pp. 2457-2460.
- ³⁸Krajnović, S. and Davidson, L., "Flow Around a Three-Dimensional Bluff Body," 9th International Symposium on Flow Visualization, Göteborg, Sweden, 2000.
- ³⁹Merzkirch, W., *Flow Visualization*. New York, New York: Academic Press, Inc., 1974.
- ⁴⁰Merzkirch, W., *Flow Visualization*. Second Edition. Orlando, Florida: Academic Press, Inc., 1987.
- ⁴¹Adams, E., "Advanced Tactical Laser A laser cannon that blasts from the air," *Popular Science*, 1 June 2004, Accessed 18 April 2011 <<http://www.popsci.com/scitech/article/2004-06/advanced-tactical-laser>>.
- ⁴²"Advanced Tactical Laser (ATL)," *GlobalSecurity.org*, Accessed 18 April 2011 <<http://www.globalsecurity.org/military/systems/aircraft/systems/atl.htm>>.
- ⁴³"Advanced tactical laser aircraft fires high-power laser in flight," *The official web site of the U.S. Air Force*, 19 June 2009, Accessed 18 April 2011 <<http://www.af.mil/news/story.asp?id=123154924>>.
- ⁴⁴Catrakis, H.J., Garcia, P.J., and Nathman, J.C., "Cumulative Aero-Optical Interactions Along Laser Beam Propagation Paths: Experiments and Computations," 44th AIAA Aerospace Sciences Meeting and Exhibit, Reno, Nevada, 9-12 January 2006, AIAA 2006-1495.
- ⁴⁵Catrakis, H.J., "Aero-Optical Wavefront Propagation and Refractive Fluid Interfaces in Large-Reynolds-Number Compressible Turbulent Flows," Final Report to the Air Force Office of Scientific Research, AFRL-SR-AR-TR06-0229, University of California (UC)-Irvine, Irvine, California, 31 March 2006.
- ⁴⁶Catrakis, H.J., "Equipment for Aero-Optical Flow Imaging," Final Report, Air Force Office of Scientific Research, AFRL-SR-AR-TR-04-0146, University of California (UC)-Irvine, Irvine, California, 29 February 2004.

- ⁴⁷Wyckham, C.M., Zaidi, S.H., Miles, R.B., and Smits, A.J., "Characterization of Optical Wavefront Distortions Due to a Boundary Layer at Hypersonic Speeds," 34th Plasmadynamics and Lasers Conference, Orlando, Florida, 23-26 June 2003, AIAA 2003-4308.
- ⁴⁸Thurber, M.C., "Acetone Laser-Induced Fluorescence for Temperature and Multiparameter Imaging in Gaseous Flows," Topical Report TSD-120, Stanford University, Stanford, California, March 1999.
- ⁴⁹Lozano, A., "Laser-Excited Luminescent Tracers For Planar Concentration Measurements in Gaseous Jets," Dissertation, Stanford University, Stanford, California, August 1992.
- ⁵⁰Tran, T.T., "Acetone Planar Laser-Induced Fluorescence and Phosphorescence for Mixing Studies of Multiphase Flows at High Pressure and Temperature," Dissertation, Georgia Institute of Technology, Atlanta, Georgia, August 2008.
- ⁵¹Hartwig, J.W., "Acetone-LIF at Elevated Pressure and Temperature for 282 nm Excitation: Experiments and Modeling," Thesis, Case Western Reserve University, Cleveland, Ohio, January 2010.
- ⁵²Bryant, R.A., Donbar, J.M., and Driscoll, J.F., "Acetone laser induced fluorescence for low pressure/low temperature flow visualization," *Experiments in Fluids*, Ann Arbor, Michigan, 2000, Volume 28, pp. 471-476.
- ⁵³Kohse-Höinghaus, K. and Jeffries, J.B., *Applied Combustion Diagnostics*. New York, New York: Taylor & Francis, 2002.
- ⁵⁴Tran, T., Kochar, Y., and Seitzman, J., "Measurements of Acetone Fluorescence and Phosphorescence at High Pressures and Temperatures," AIAA. Atlanta, Georgia, 2006.
- ⁵⁵"Chem-Guide Chemical Resistance Information For Plastic and Metal Valves and Fittings," *NIBCO Inc. Catalog C-CRG-0710*, 2010, Accessed 2011 <<http://www.nibco.com/assets/ChemGuide.pdf>>.

- ⁵⁶Danehy, P.M., Wilkes, J.A., Alderfer, D.W., Jones, S.B., Robbins, A.W., Patry, D.P., and Schwartz, R.J., "Planar laser-induced fluorescence (PLIF) investigation of hypersonic flowfields in a Mach 10 wind tunnel (invited)," 25th AIAA Aerodynamic Measurement Technology and Ground Testing Conference, San Francisco, California, 5-8 June 2006, AIAA 2006-3442.
- ⁵⁷Hirschfelder, J.O., Curtiss, C.F., Bird, R. B., *Molecular Theory of Gases and Liquids*. New York, New York: John Wiley & Sons, Inc., 1954.
- ⁵⁸Reid, R.C., Prausnitz, J.M., and Sherwood, T.K., *The Properties of Gases and Liquids*. Third Edition. New York, New York: McGraw-Hill, Inc., 1977.
- ⁵⁹Brokaw, R.S., "Predicting Transport Properties of Dilute Gases," *Industrial and Engineering Chemistry Process Design and Development*, Cleveland, Ohio, April 1969, Volume 8, Number 2, pp. 240-253.
- ⁶⁰Mourits, F.M. and Rummens, F.H.A., "A critical evaluation of Lennard-Jones and Stockmayer potential parameters and of some correlation methods," *Canadian Journal of Chemistry*, Regina, Saskatchewan, Canada, 1977, Volume 55, pp. 3007-3020.
- ⁶¹Troe, J., "Theory of thermal unimolecular reactions at low pressures. II. Strong collision rate constants. Applications," *The Journal of Chemical Physics*, Göttingen, West Germany, Volume 66, Number 11, pp. 4758-4775.
- ⁶²Braeuer, A., Beyrau, F., and Leipertz, A., "Laser-induced fluorescence of ketones at elevated temperatures for pressures up to 20 bars by using a 248 nm excitation laser wavelength: experiments and model improvements," *Applied Optics*, Erlangen, Germany, 10 July 2006, Volume 45, Number 20, pp. 4982-4989.
- ⁶³Koch, J.D., Hanson, R.K., Koban, W., and Schulz, C., "Rayleigh-calibrated fluorescence quantum yield measurements of acetone and 3-pentanone," *Applied Optics*, Stanford, California, 1 November 2004, Volume 43, Number 31, pp. 5901-5910.

- ⁶⁴Kearney, S.P. and Reyes, F.V., "Quantitative temperature imaging in gas-phase turbulent thermal convection by laser-induced fluorescence of acetone," *Experiments in Fluids*, Albuquerque, New Mexico, 2003, Volume 34, pp. 87-97.
- ⁶⁵Nygren, J., Hult, J., Richter, M., Aldén, M., Christensen, M., Hultqvist, A., and Johansson, B., "Three-Dimensional Laser Induced Fluorescence of Fuel Distributions in an HCCI Engine," *Proceedings of the Combustion Institute*, Lund, Sweden, 2002, Volume 29, pp. 679-685.
- ⁶⁶Choi, H.J., Ko, Y.S., and Chung, S.H., "Visualization of Concentration Field in a Vortex Ring Using Acetone PLIF," *Journal of Visualization*, Seoul, Korea, 2002, Volume 5, Number 2, pp. 145-152.
- ⁶⁷Murakami, E. and Papamoschou, D., "Eddy Convection in Coaxial Supersonic Jets," *AIAA Journal*, Irvine, California, April 2000, Volume 38, Number 4, pp. 628-635.
- ⁶⁸Catrakis, H.J., Aguirre, R.C., Ruiz-Plancarte, J., Thayne, R.D., McDonald, B.A., and Hearn, J.W., "Large-scale dynamics in turbulent mixing and the three-dimensional space-time behavior of outer fluid interfaces," *Journal of Fluid Mechanics*, Irvine, California, 2002, Volume 471, pp. 381-408.
- ⁶⁹Dimotakis, P.E., Catrakis, H.J., and Fourquette, D.C., "Flow structure and optical beam propagation in high-Reynolds-number gas-phase shear layers and jets," *Journal of Fluid Mechanics*, Pasadena, California, 2001, Volume 433, pp. 105-134.
- ⁷⁰Kingslake, R., *Optics in Photography*. Bellingham, Washington: SPIE Optical Engineering Press, 1992.
- ⁷¹Clemens, N.T., "Flow Imaging," *Encyclopedia of Imaging Science and Technology*. New York, New York: John Wiley and Sons, Inc., 2002.
- ⁷²Van Walree, P., "Vignetting," *Toothwalker.org*, 2010, Accessed 2010 <<http://toothwalker.org/optics/vignetting.html>>.
- ⁷³Laskaris, N., "Vignetting," University of Edinburgh, Edinburgh, Scotland.

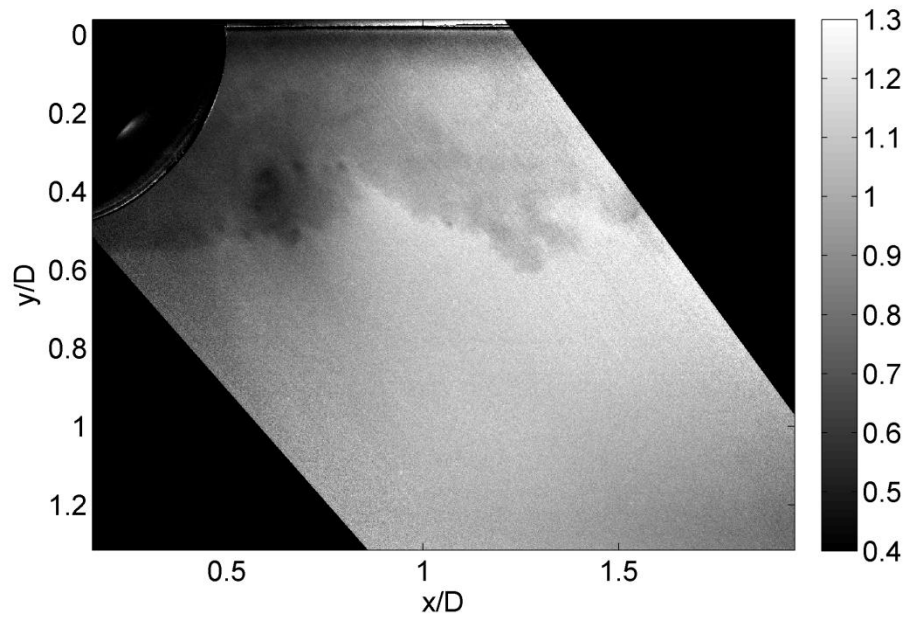
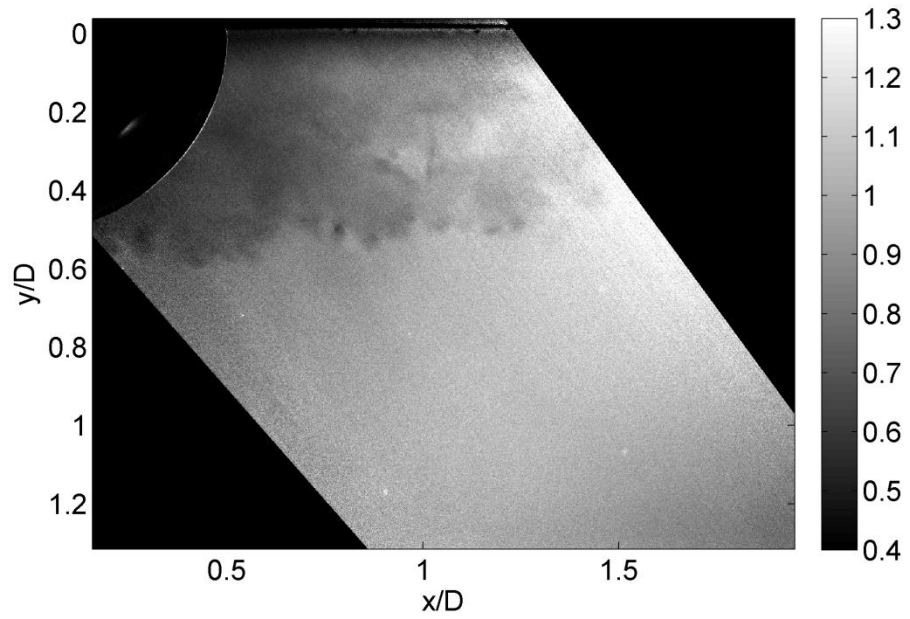
- ⁷⁴Zheng, Y., Lin, S., and Kang, S.B., "Single-Image Vignetting Correction," Shanghai Jiaotong University, Microsoft Research Asia.
- ⁷⁵Aggarwal, M., Hua, H., and Ahuja, N., "On Cosine-fourth and Vignetting Effects in Real Lenses," *IEEE*, Urbana, Illinois, 2001.
- ⁷⁶"What is a CCD?" *Spectral Instruments*. 2008. Accessed 2010 <http://www.specinst.com/What_Is_A_CCD.html>.
- ⁷⁷"Molecular Mass of Air," *The Engineering Toolbox*, Accessed 18 October 2010. <http://www.engineeringtoolbox.com/molecular-mass-air-d_679.html>.
- ⁷⁸"Air: Its Composition and Properties," *Universal Industrial Gases, Inc.*, 2009, Accessed 2011 <<http://www.uigi.com/air.html>>.
- ⁷⁹Hanson, R.K., "Laser Diagnostics for Reacting Flows," Final Technical, Air Force Office of Scientific Research, Stanford University, Stanford, California, 1 November 2010.
- ⁸⁰Gierczak, T., Burkholder, J.B., Bauerle, S., and Ravishankara, A.R., "Photochemistry of acetone under tropospheric conditions," *Chemical Physics*, Boulder, Colorado, 1998, Volume 231, pp. 229-244.
- ⁸¹Wall, David, "Design of a Solid Wall Transonic Wind Tunnel," AIAA Region II Student Conference, Huntsville, Alabama, 2-3 April 2009.
- ⁸²Bell, J.H. and Mehta, R.D., "Contraction Design for Small Low-Speed Wind Tunnels," Joint Institute for Aeronautics and Acoustics, NASA, Ames Research Center, JIAA TR – 84, Stanford University, Stanford, California, April 1988.
- ⁸³Brassard, D., "Transformation of a Polynomial for a Contraction Wall Profile," Lakehead University, Ontario, Canada, 24 February 2003.
- ⁸⁴"S1-UV Fused Silica," *ESCO Products*, Accessed 2010 <http://www.escoproducts.com/html/s1-uv_fused_silica.html>.
- ⁸⁵"BK-7 Optical Glass," *ESCO Products*, Accessed 2010 <http://www.escoproducts.com/html/bk-7_optical_glass.html>.

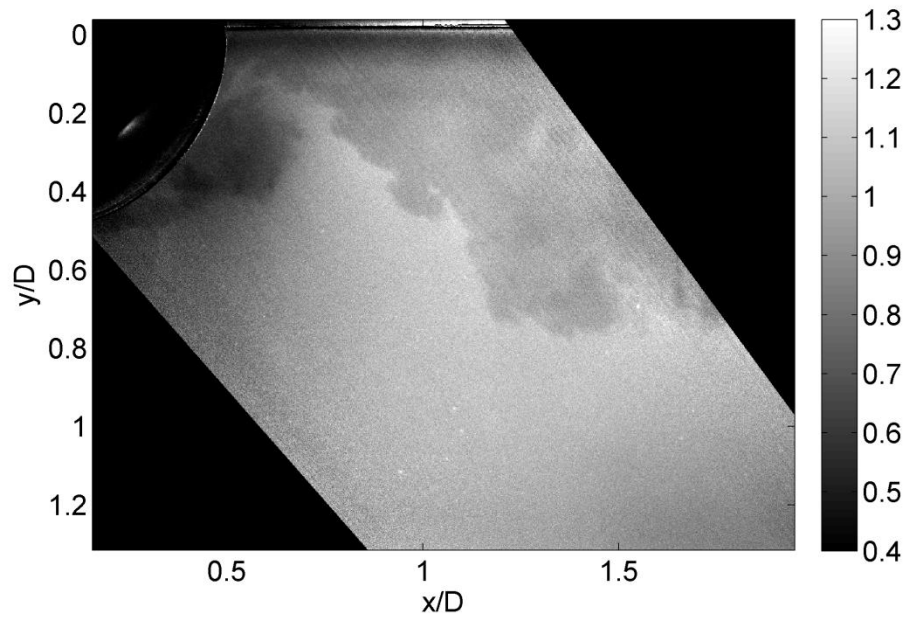
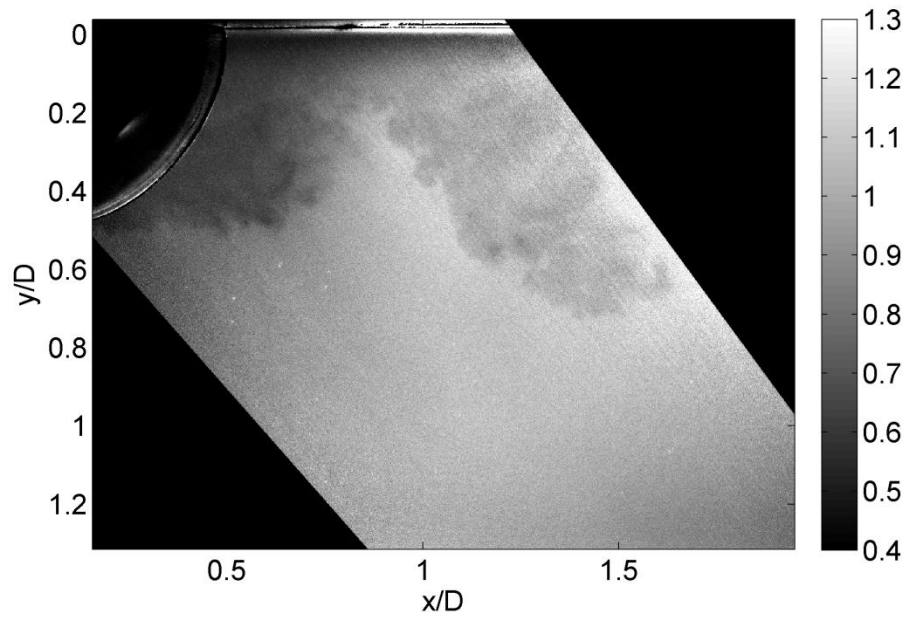
- ⁸⁶"NI USB-6259 BNC," *National Instruments*, 2011, Accessed 2011
<<http://sine.ni.com/nips/cds/view/p/lang/en/nid/209150>>.
- ⁸⁷"Rhodamine 590*," *Exciton*, Accessed 2011
<<http://www.exciton.com/pdfs/RH590.pdf>>.
- ⁸⁸"PX209 and PX219 Series," *Omega Engineering, Inc.*, 2010, Accessed 23
November 2010
<http://www.omega.com/ppt/pptsc.asp?ref=PX209_PX219&Nav=preb00>.
- ⁸⁹Anderson, John D., Jr., *Fundamentals of Aerodynamics*. Fourth Edition. New York,
New York: The McGraw-Hill Companies, Inc., 2007.
- ⁹⁰Houghton, E.L. and Carpenter, P.W., *Aerodynamics For Engineering Students*.
Fourth Edition. New York, New York: John Wiley & Sons, Inc., 1993.
- ⁹¹"General Catalog/2a Product Data and Specifications Solenoid Valves Magnetic
Level Switches," *Jefferson Solenoid Valves USA, Inc.*, 2005, Accessed 18 April
2011 <<http://www.jeffersonvalves.com/repositorio/pdfs-ingles/general-catalog.pdf>>.
- ⁹²Dean, J.A., *Lange's Handbook of Chemistry*. Fifteenth Edition. New York, New
York: McGraw-Hill, Inc., 1999.
- ⁹³"Density," *The Physics Hypertextbook*, 2010 Glenn Elert, Accessed 18 November
2010 <<http://physics.info/density/>>.
- ⁹⁴"IS," *BETE Fog Nozzle, Inc.*, 2011, Accessed 2010
<http://www.bete.com/pdfs/BETE_IS.pdf>.
- ⁹⁵"Solo PIV Nd:YAG Laser System Operator's Manual," New Wave Research
Inc., April 2006.
- ⁹⁶Wernet, M.P., "Particle Image Velocimetry Processing: PIVPROC Version 6.60,"
National Aeronautics and Space Administration Glenn Research Center, 5
May 2007.
- ⁹⁷Raffel, M., Willert, C.E., Wereley, S.T., and Kompenhans, J., *Particle Image
Velocimetry A Practical Guide*. Second Edition. New York, New York:
Springer-Verlag Berlin Heidelberg, 2007.

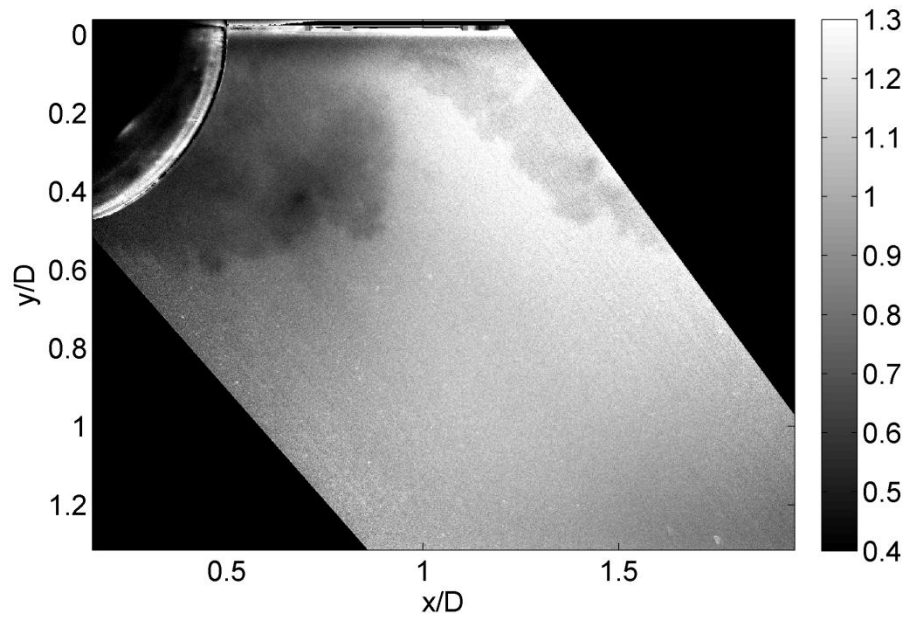
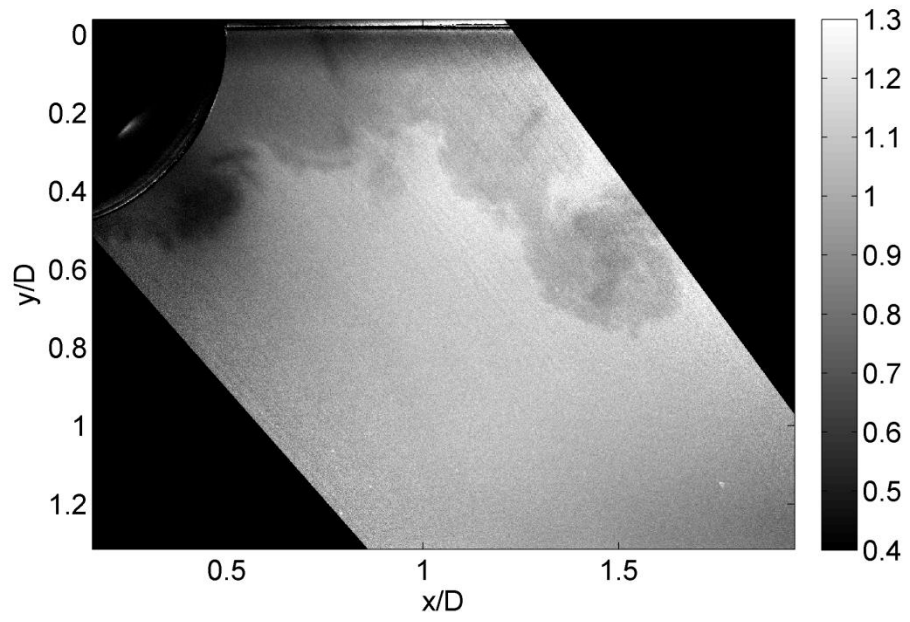
- ⁹⁸Adrian, R.J. and Westerweel, J., *Particle Image Velocimetry*. New York, New York: Cambridge University Press, 2011.
- ⁹⁹Fujiwara, S., Tamura, Y., Maki, H., Azuma, N., and Takeuchi, Y., "Development of New High-Purity Alumina," Sumitomo Chemical Co., Ltd. Basic Chemicals Research Laboratory, 2007.
- ¹⁰⁰Hackley, V.A., Somasundaran, P., and Lewis, J.A., *Particles in Particulate Systems Properties and Applications*. Surfactant Science Series Volume 104. New York, New York: Marcel Dekker, Inc., 2002.
- ¹⁰¹"sensicam sensicam qe sensicam em Operating Instructions," *Cooke Corporation*, 2004, Accessed 2010
<http://www.cookecorp.com/fileadmin/user_upload/db/download/MA_SCOPIE_0411.pdf>.
- ¹⁰²"9500+ Series Pulse Generator," *Quantum Composers, Inc.*, 2010, Accessed 2010
<<http://www.quantumcomposers.com/9500-plus-main>>.
- ¹⁰³Reid, J.Z., Lynch, K.P., and Thurow, B.S., "Further Development of a High-Speed 3-D Density Measurement Technique for Aero-Optics," 40th Fluid Dynamics Conference and Exhibit, Chicago, Illinois, 28 June – 1 July 2010, AIAA 2010-4844.
- ¹⁰⁴Munson, B.R., Young, D.F., and Okiishi, T.H., *Fundamentals of Fluid Mechanics*. 4th Edition. New York, New York: John Wiley & Sons, Inc., 2002.
- ¹⁰⁵Gordeyev, S., Jumper, E.J., Ng, T.T., and Cain, A.B., "Aero-Optical Characteristics of Compressible, Subsonic Turbulent Boundary Layers," 34th AIAA Plasmadynamics and Lasers Conference, Orlando, Florida, 23-26 June 2003, AIAA-2003-3606.
- ¹⁰⁶Thurow, B.S., Satija, A., and Lynch, K., "Third-generation megahertz-rate pulse burst laser system," *Applied Optics*, Auburn, Alabama, 10 April 2009, Volume 48, Number 11, pp. 2086-2093.
- ¹⁰⁷"Bex Spray Nozzles Catalog No. 56a," *BEX Spray Nozzles*, 2009, Accessed 4 October 2010 <<http://www.bex.com/literatr/images/catalog.pdf>>.

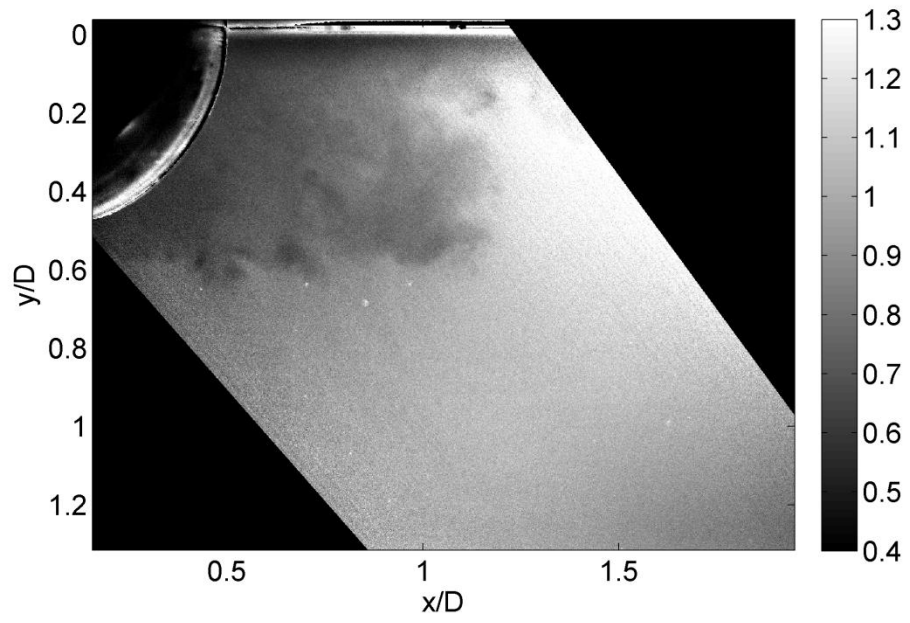
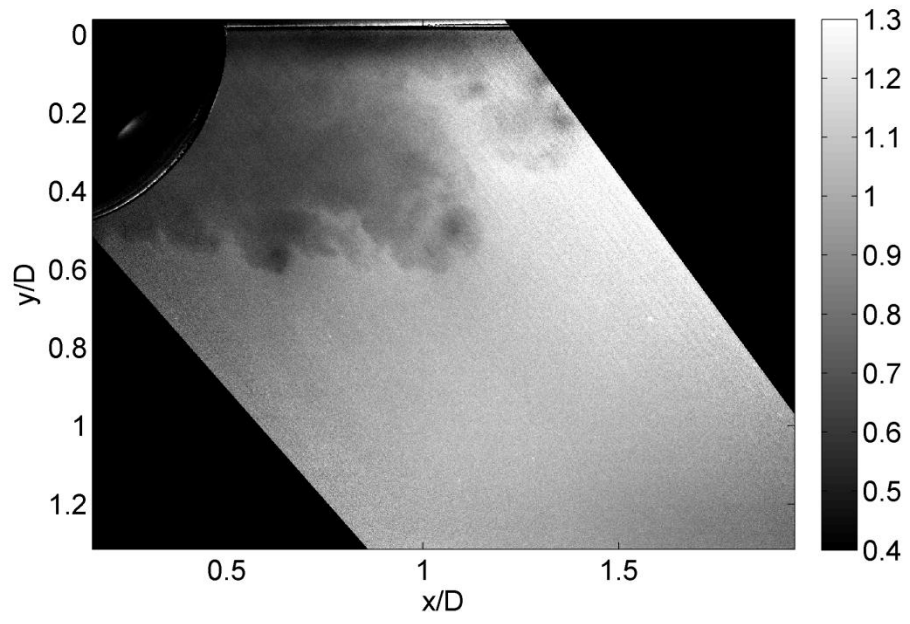
- ¹⁰⁸“SIM02 – Multi-Channel Framing Camera,” *Specialised Imaging Limited*, 2010, Accessed 2010 <http://www.specialised-imaging.com/sim02_multi_channel_framing_camera.php>.
- ¹⁰⁹“Ultra Fast Framing Camera,” *Princeton Scientific Instruments, Inc.*, 2001, Accessed 2010 <<http://www.prinsci.com/ffcam.htm>>.
- ¹¹⁰“Galvanometer Scanners,” *SCANLAB AG*, Accessed 2010 <<http://www.scanlab.de/en/-/products/dynAXIS>>.
- ¹¹¹“Model VM500plus Moving Magnet Closed Loop Galvo,” *Cambridge Technology*, 2009, Accessed 2010 <<http://camtech.com/products/Legacy/VM500+.html>>.
- ¹¹²Schrijer, F.F.J., Scarano, F., and van Oudheusden, B.W., “Application of PIV in a Mach 7 double-ramp flow,” *Experiments in Fluids*, Delft, The Netherlands, 2006, Volume 41, pp. 353-363.
- ¹¹³Urban, W.D. and Mungal, M.G., “Planar Velocity Measurements in Compressible Mixing Layers,” AIAA - 35th Aerospace Sciences Meeting, Reno, Nevada, 1997, AIAA 97-0757.
- ¹¹⁴Ghaemi, S., Schmidt-Ott, A., and Scarano, F., “Nanostructured tracers for laser-based diagnostics in high-speed flows,” *Measurement Science and Technology*, Delft, The Netherlands, 2010, Volume 21.
- ¹¹⁵Ragni, D., Schrijer, F., van Oudheusden, B.W., and Scarano, F., “Particle tracer response across shocks measured by PIV,” *Experiments in Fluids*, Delft, The Netherlands, 2010.
- ¹¹⁶“Gated Intensified Cameras,” *Cordin Company*, Accessed 18 April 2011 <<http://www.cordin.com/prodgifr.html>>.
- ¹¹⁷Bichal, A. and Thurow, B., “Development of a Background Oriented Schlieren Based Wavefront Sensor for Aero-Optics,” AIAA – 40th Fluid Dynamics Conference and Exhibit, Chicago, Illinois, 28 June – 1 July 2010, AIAA 2010-4842.

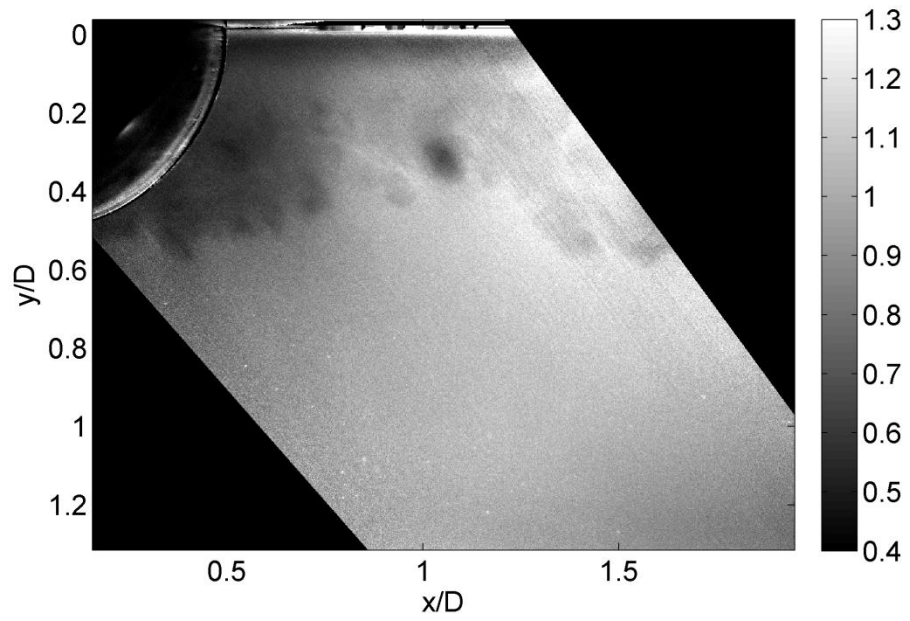
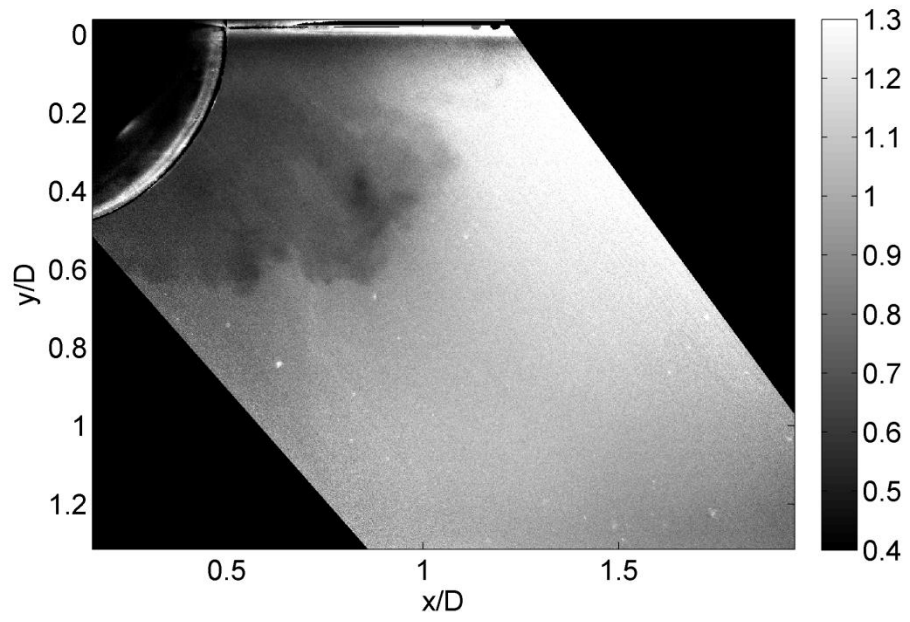
Appendix A: Single-Shot Acetone PLIF Density Images (values normalized to freestream) - Centerline – Wake Region

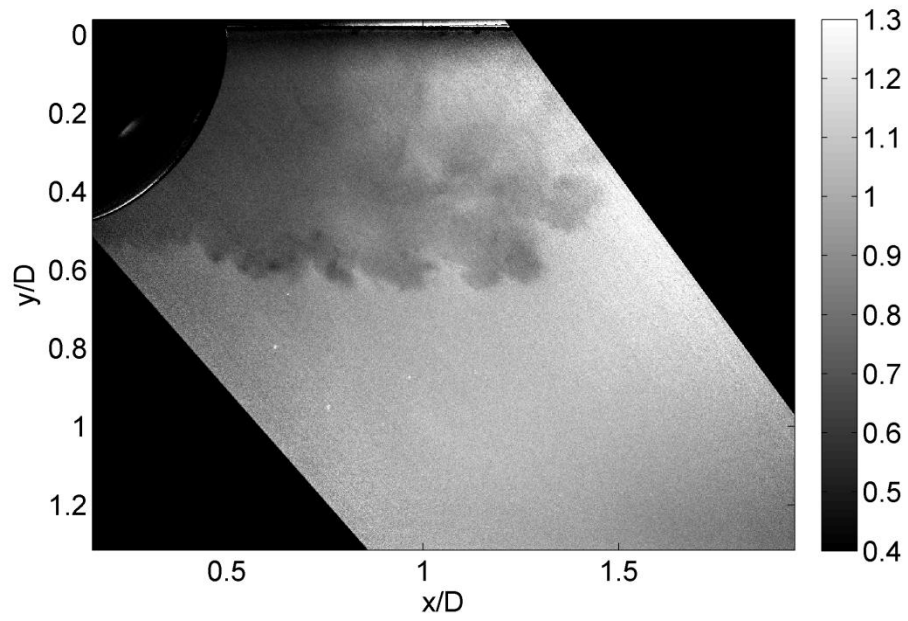
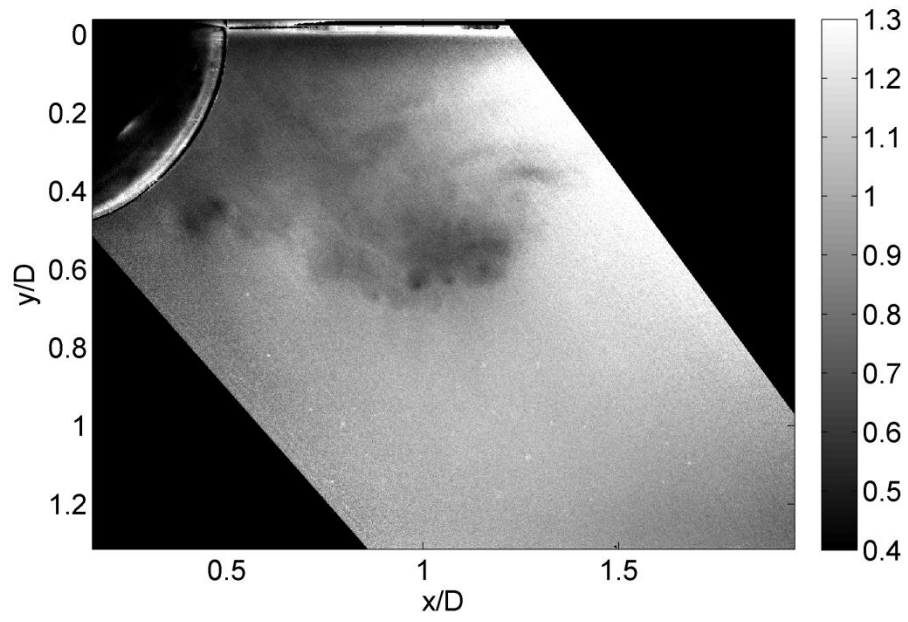


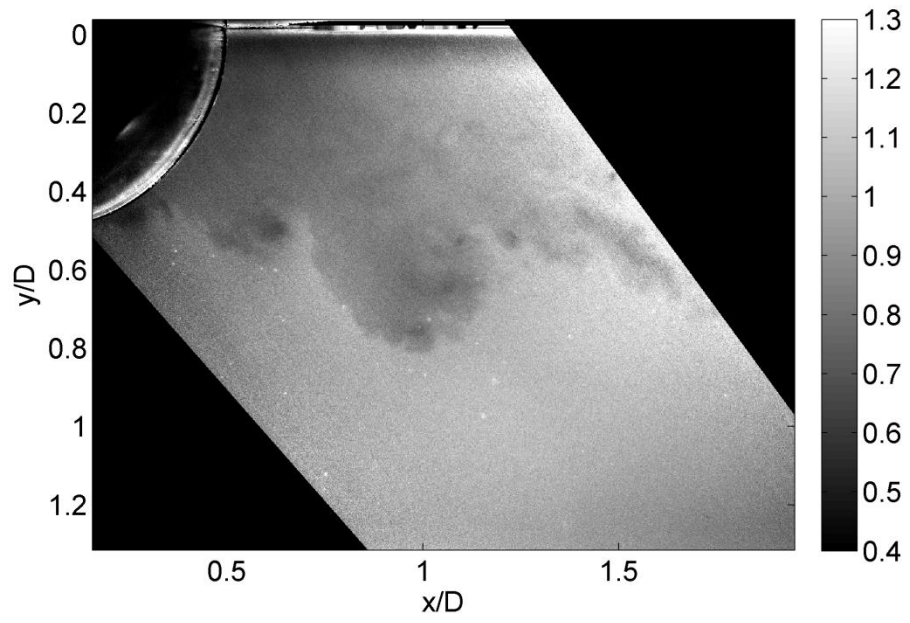
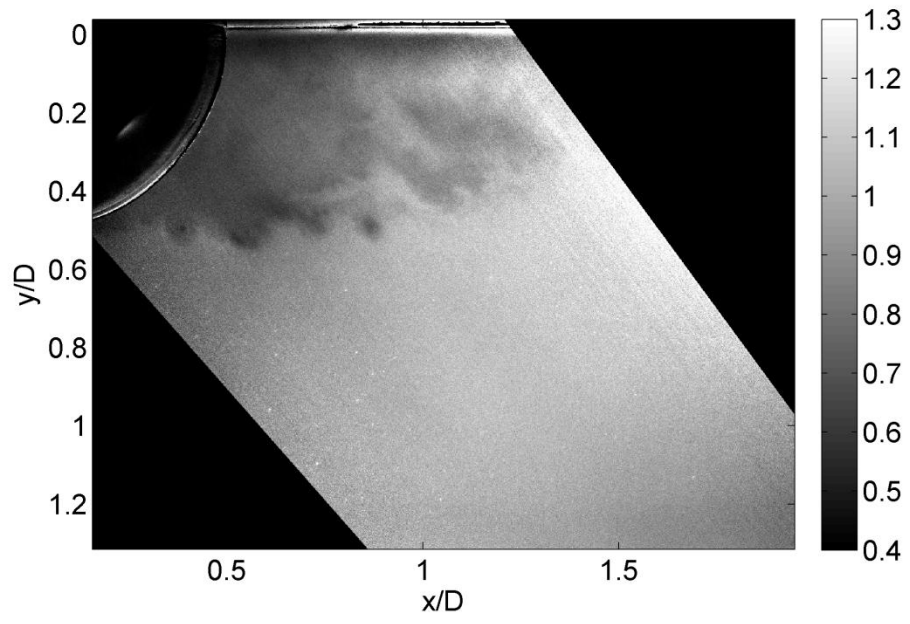


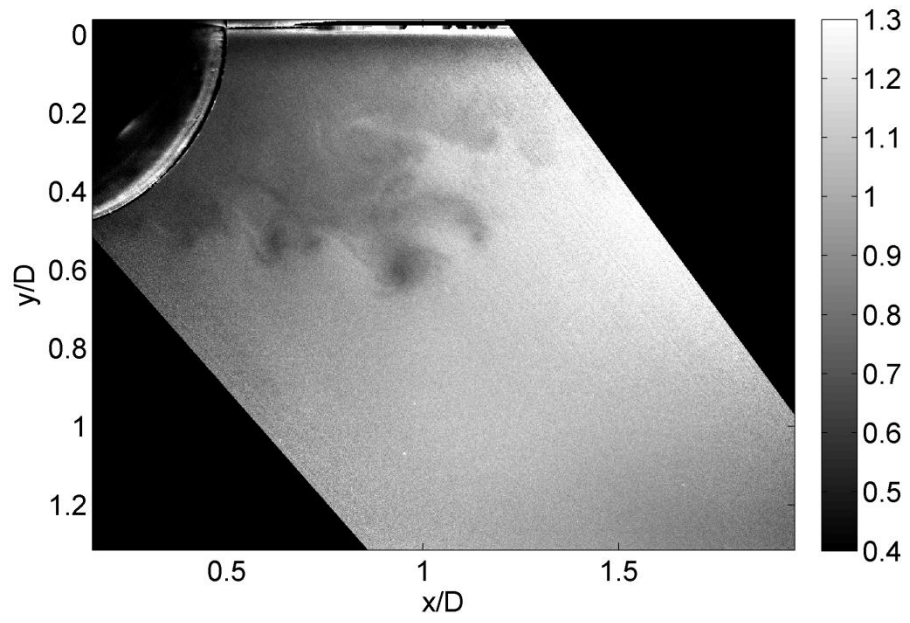
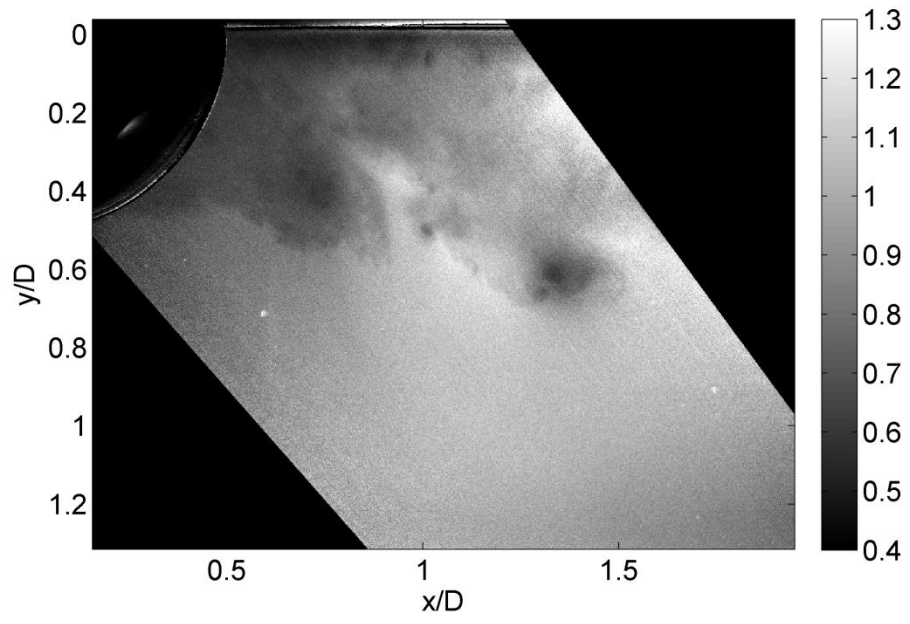


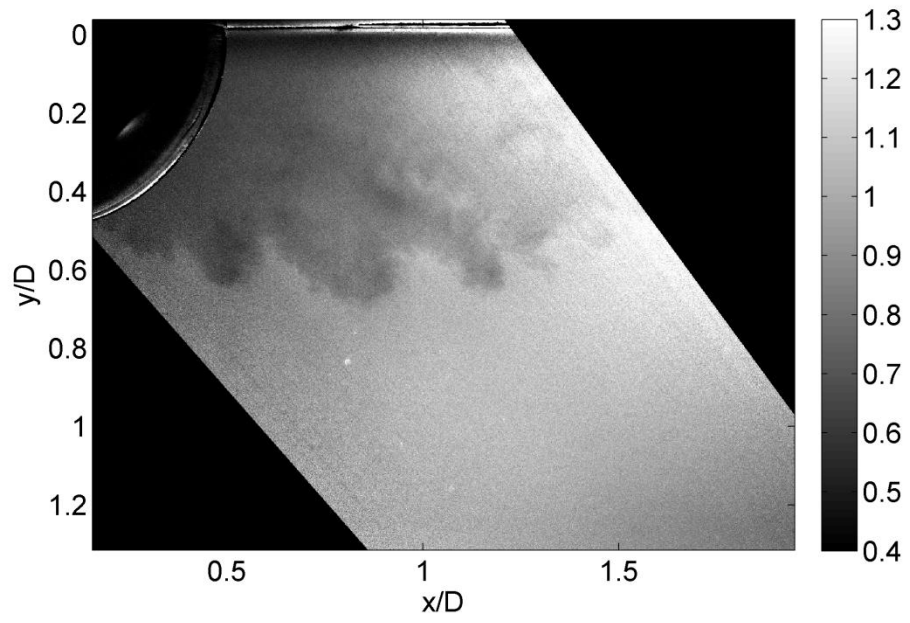
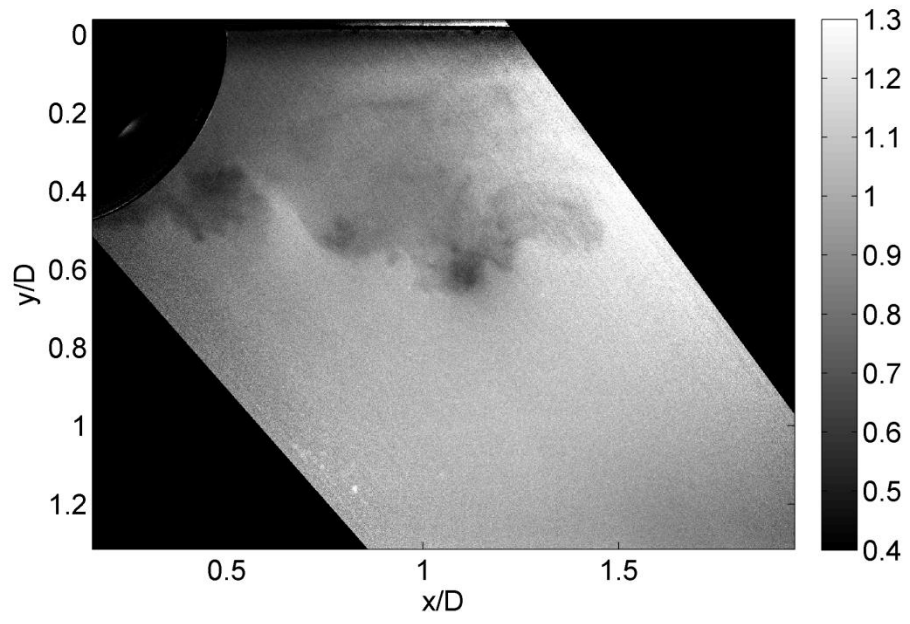


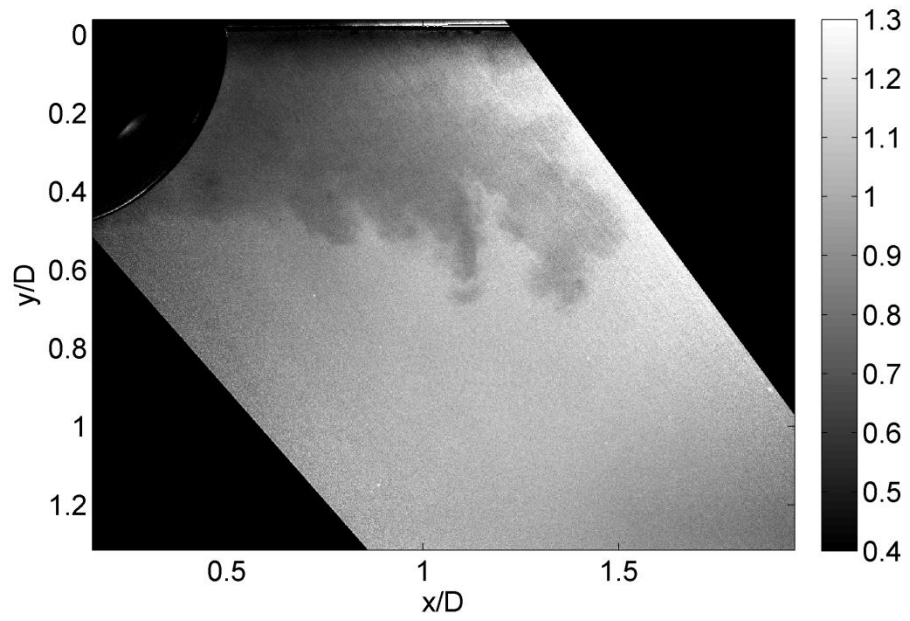
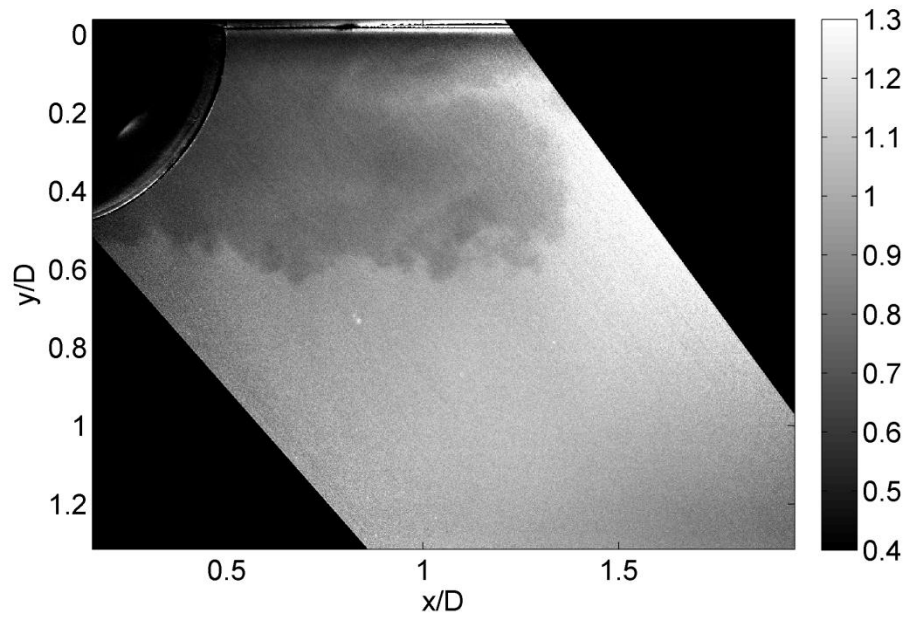






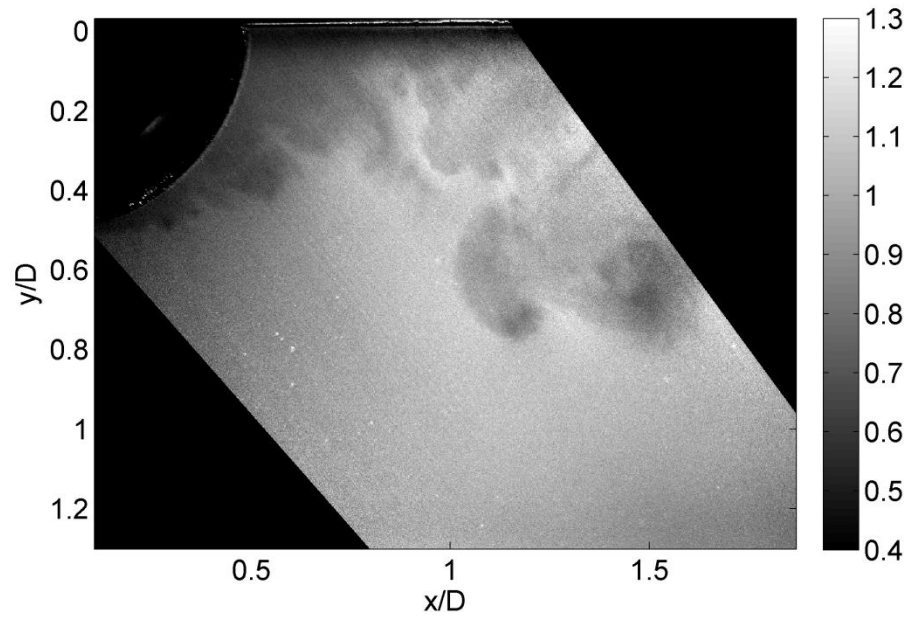




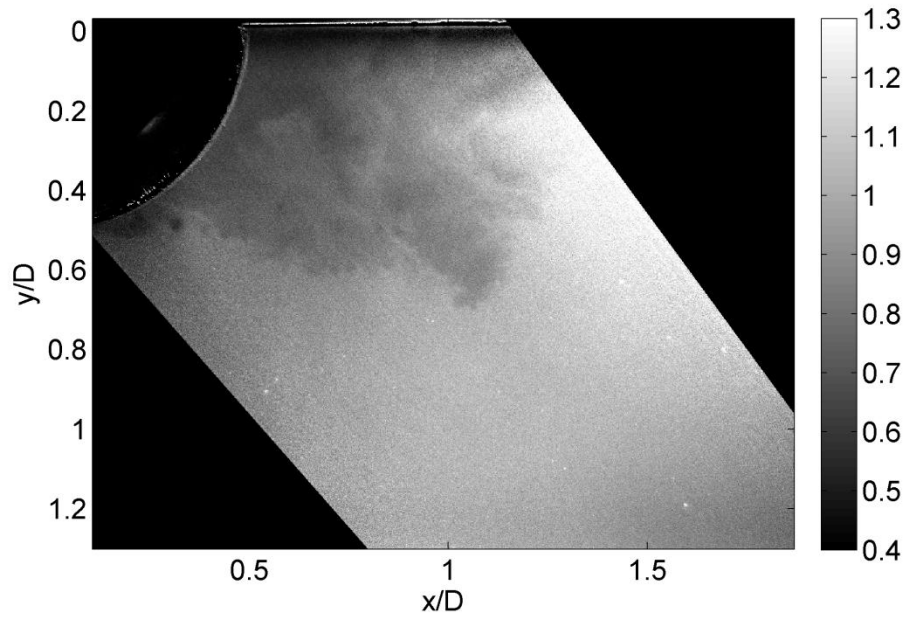
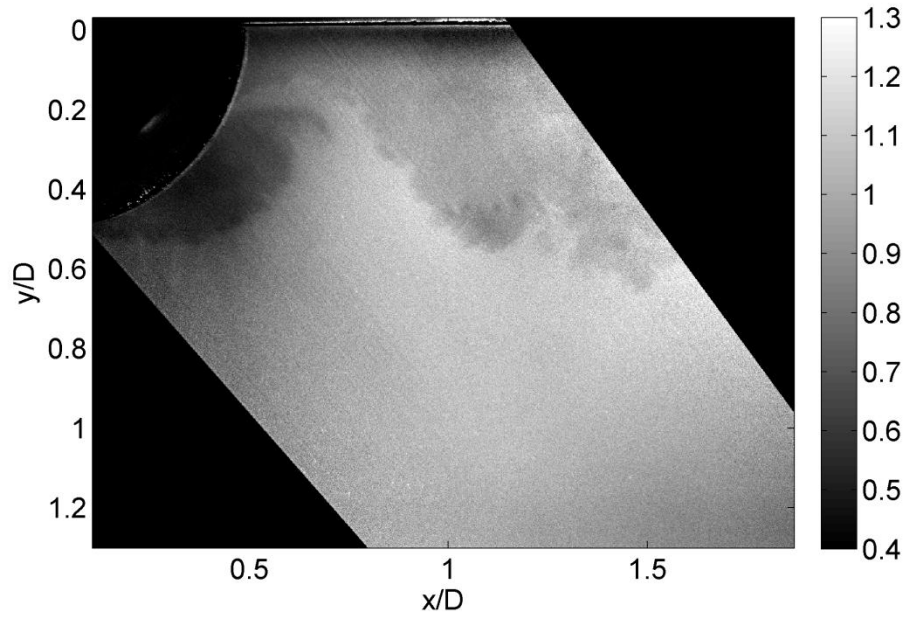


**Appendix B: Off-Centerline Plane, Single-Shot Acetone PLIF Density Images
(values normalized to freestream) – Wake Region**

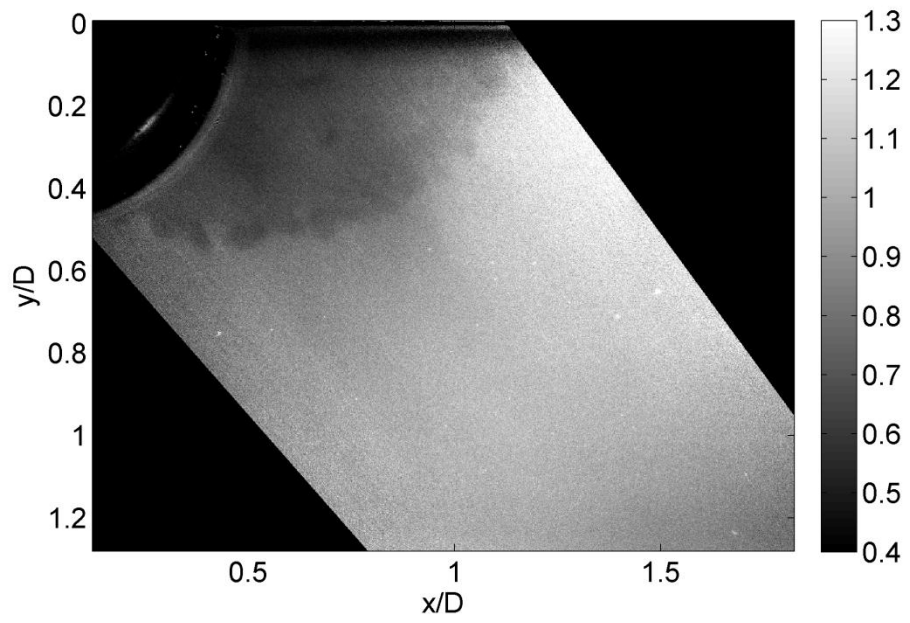
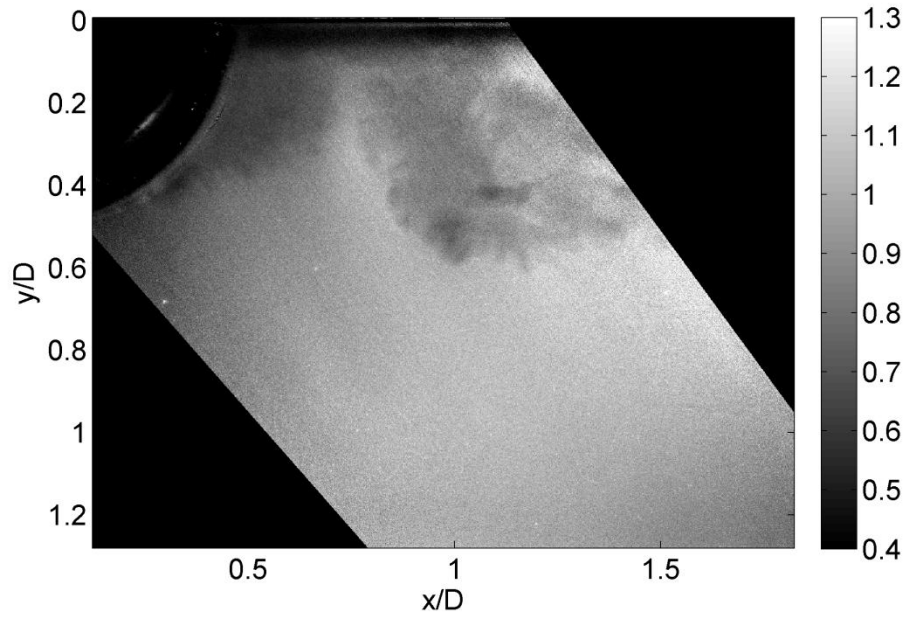
D/8 Plane



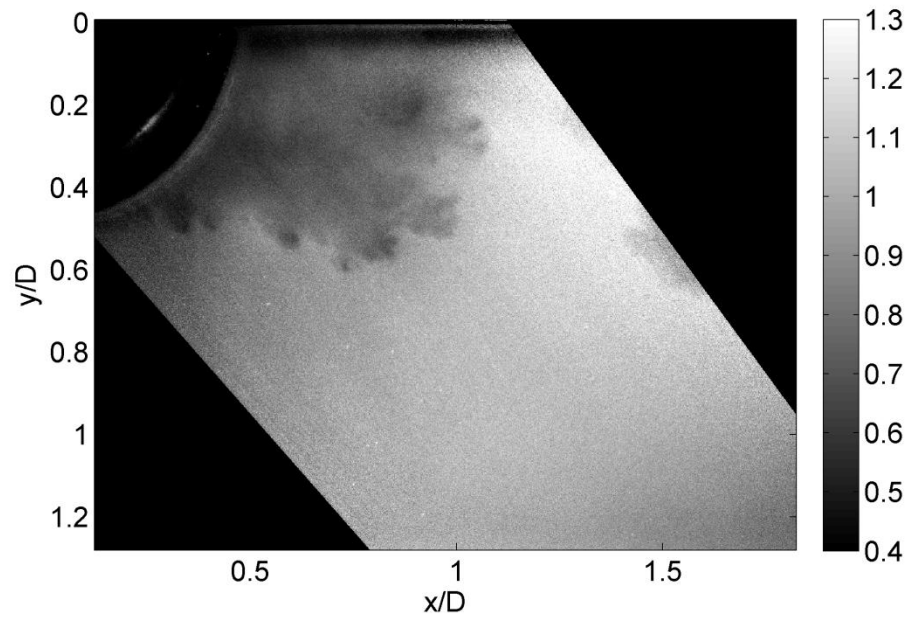
D/8 Plane



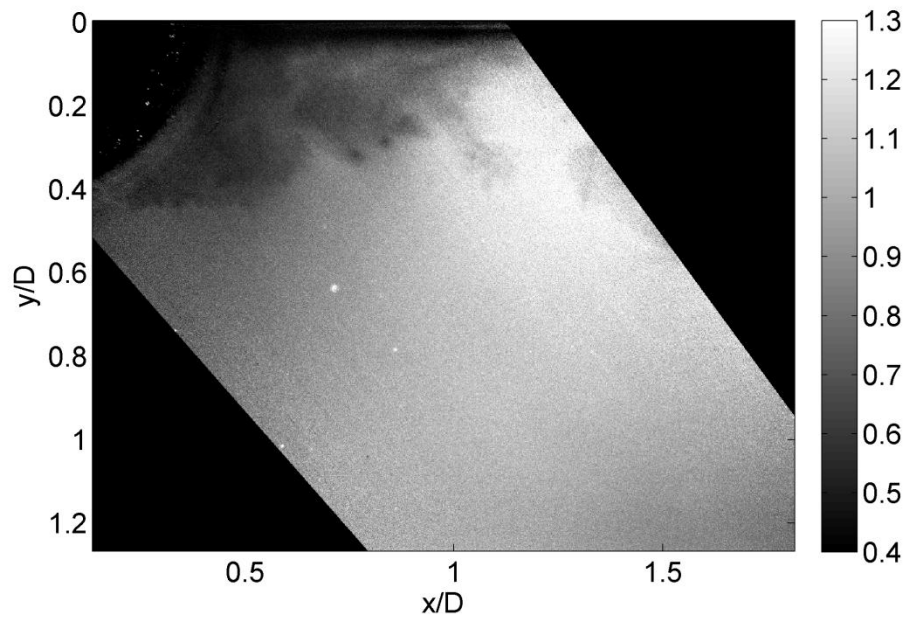
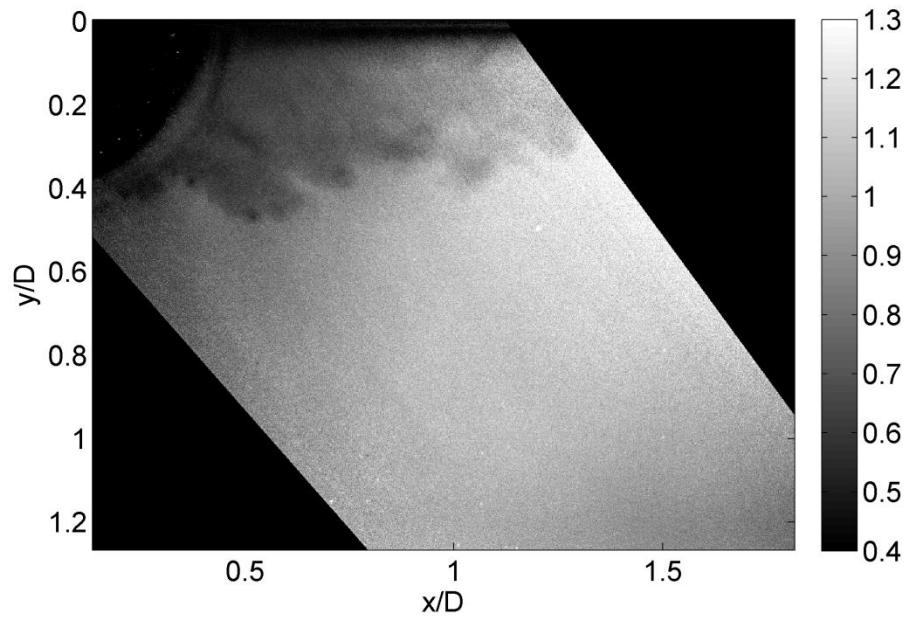
D/4 Plane



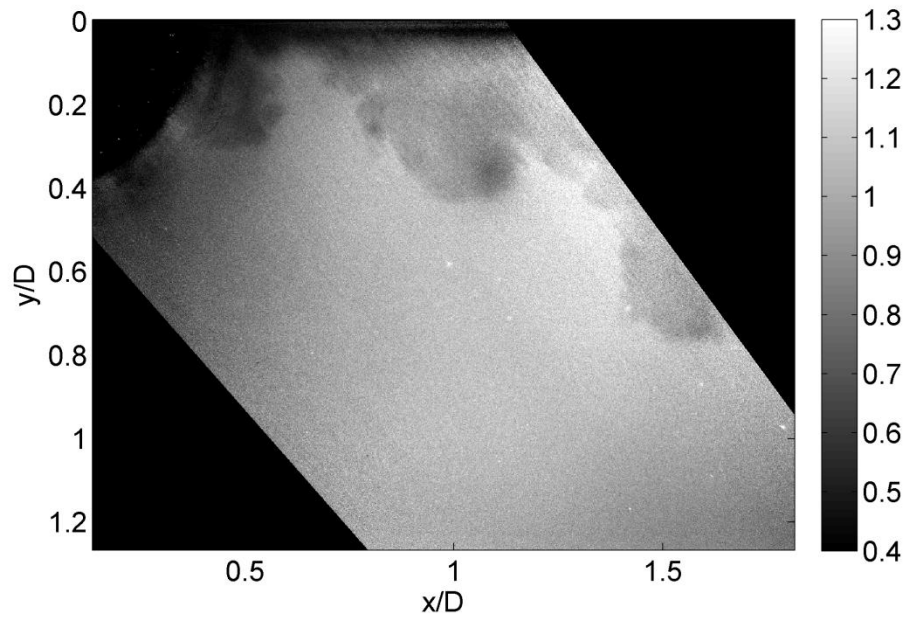
D/4 Plane



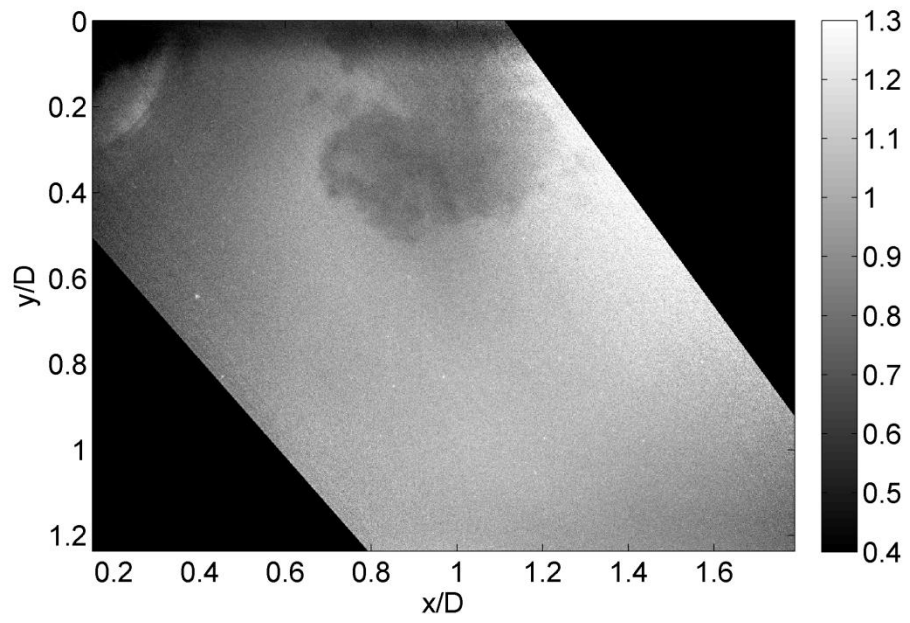
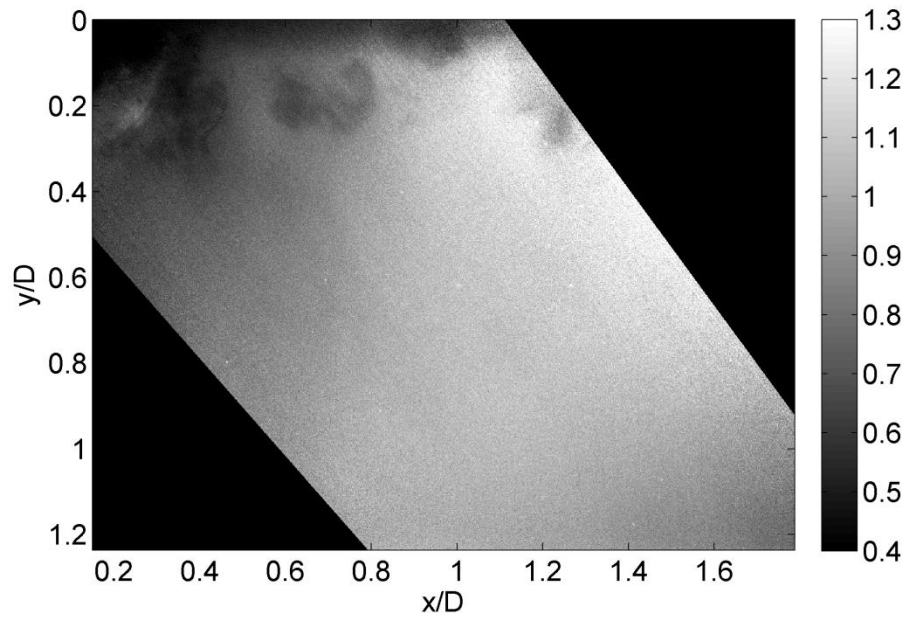
3D/8 Plane



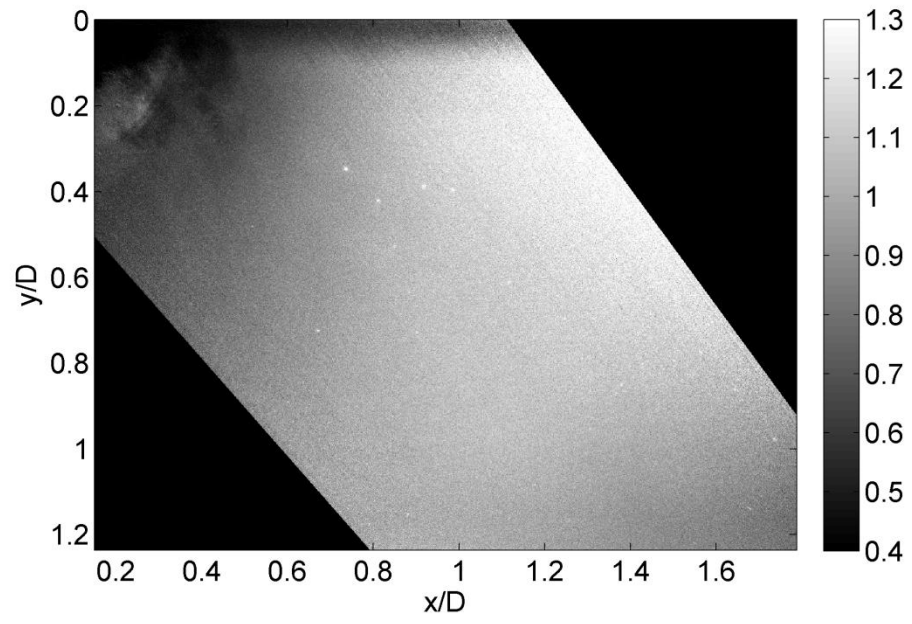
3D/8 Plane



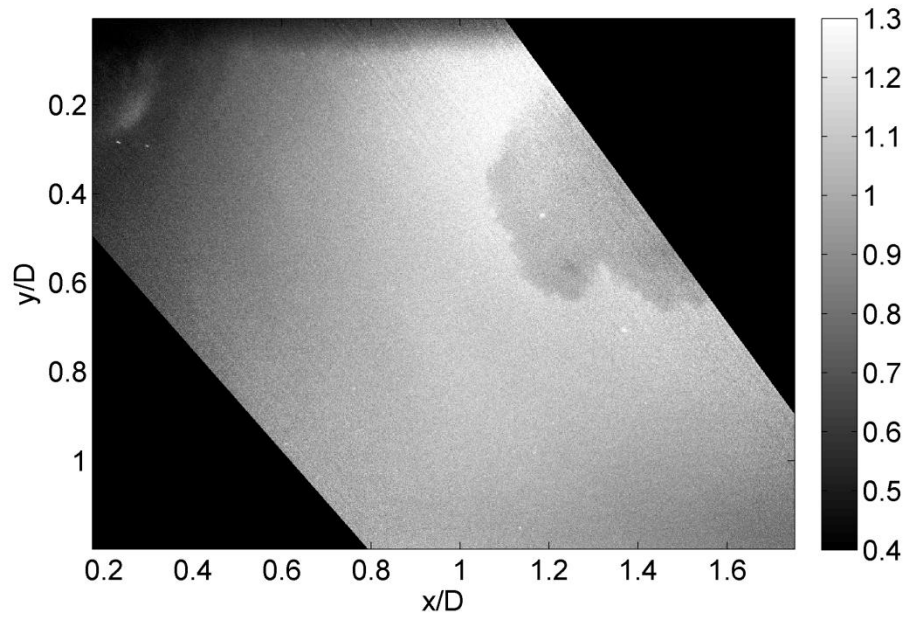
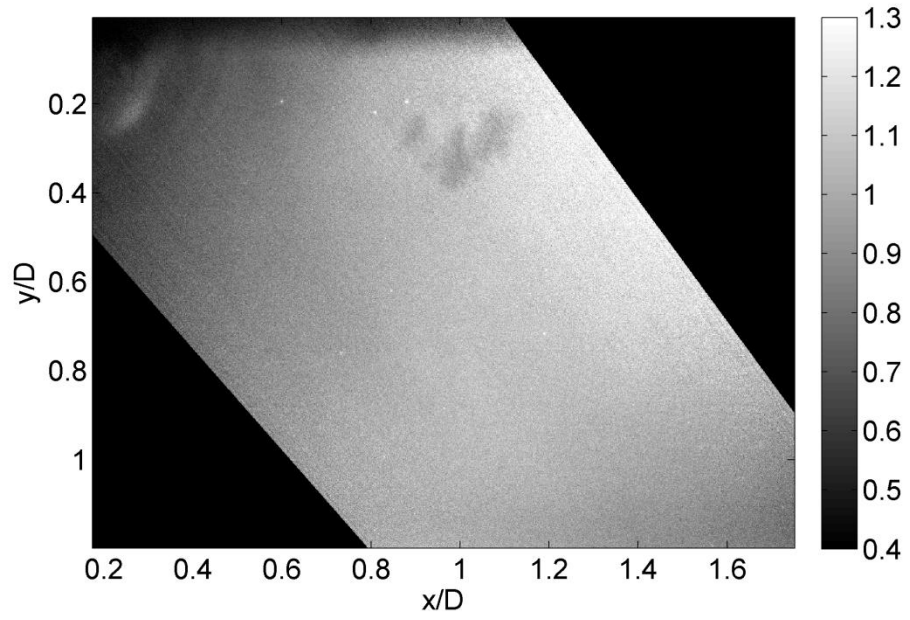
D/2 Plane



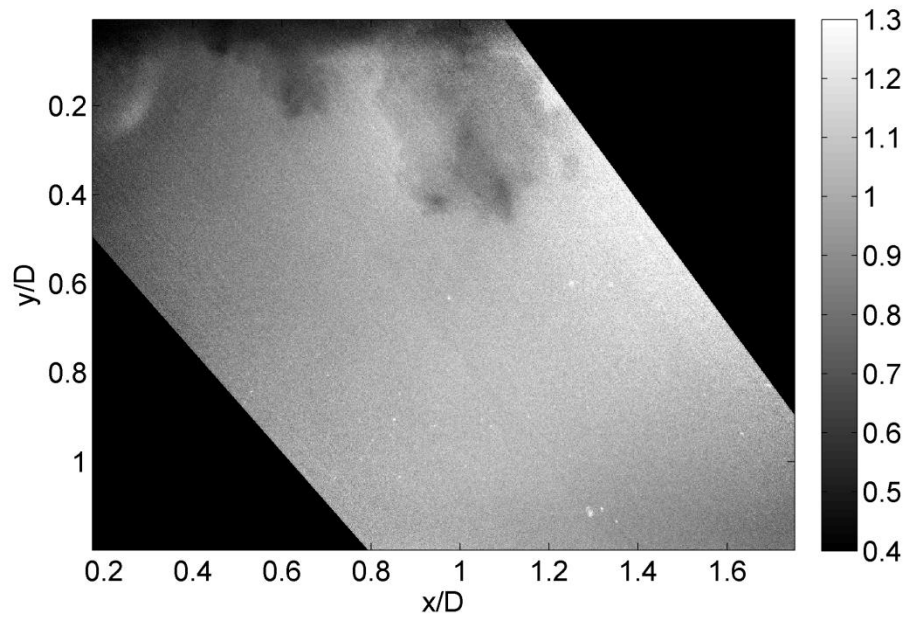
D/2 Plane



5D/8 Plane

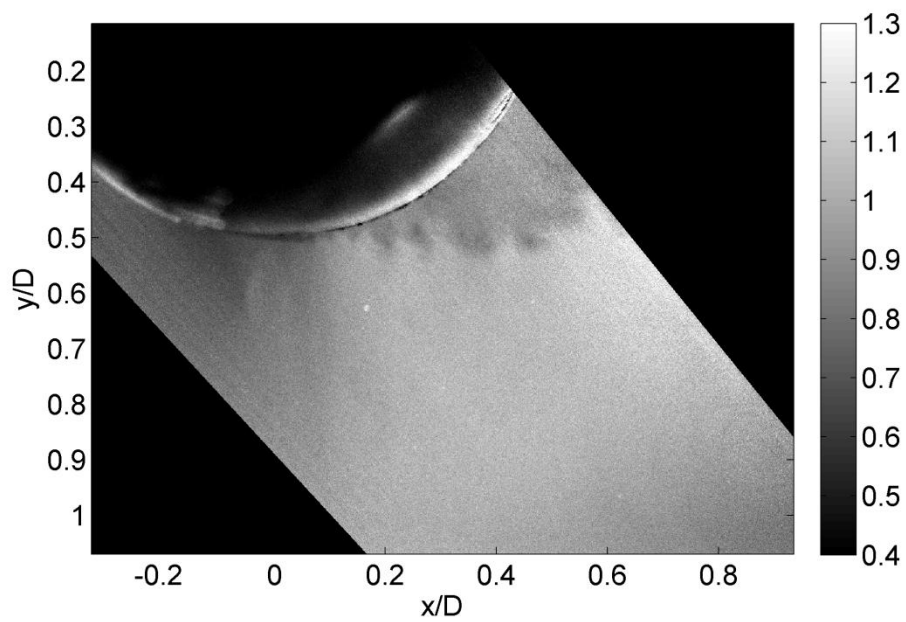
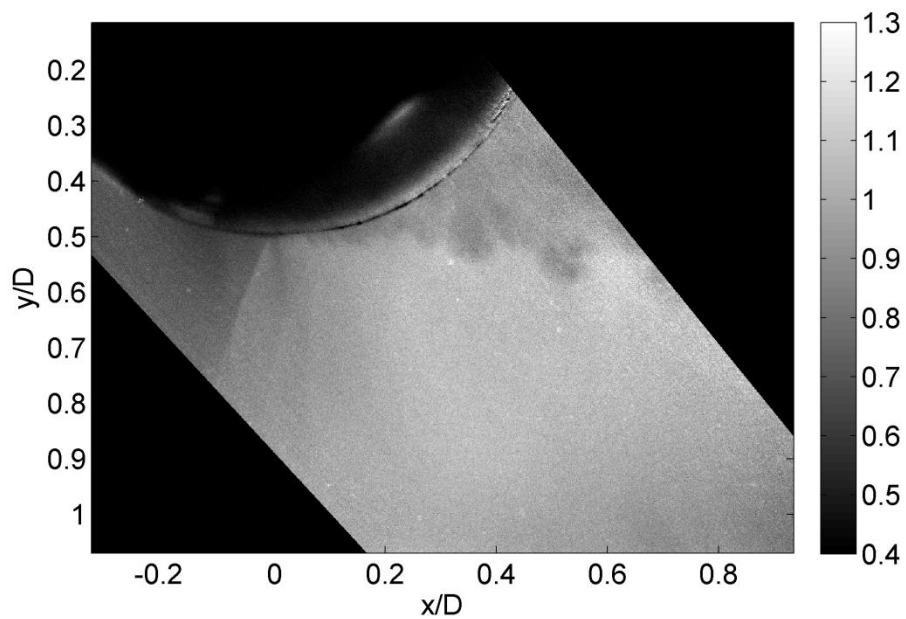


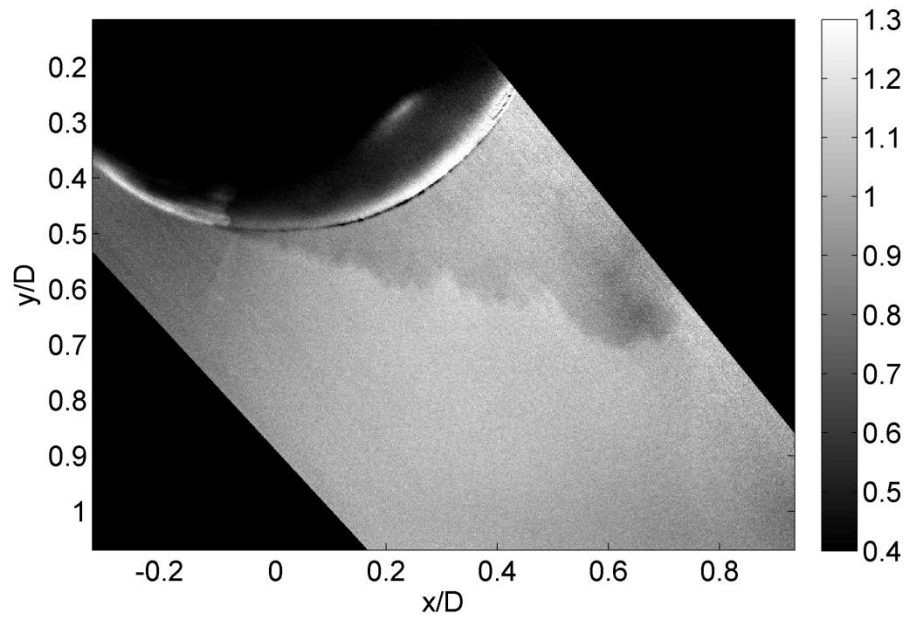
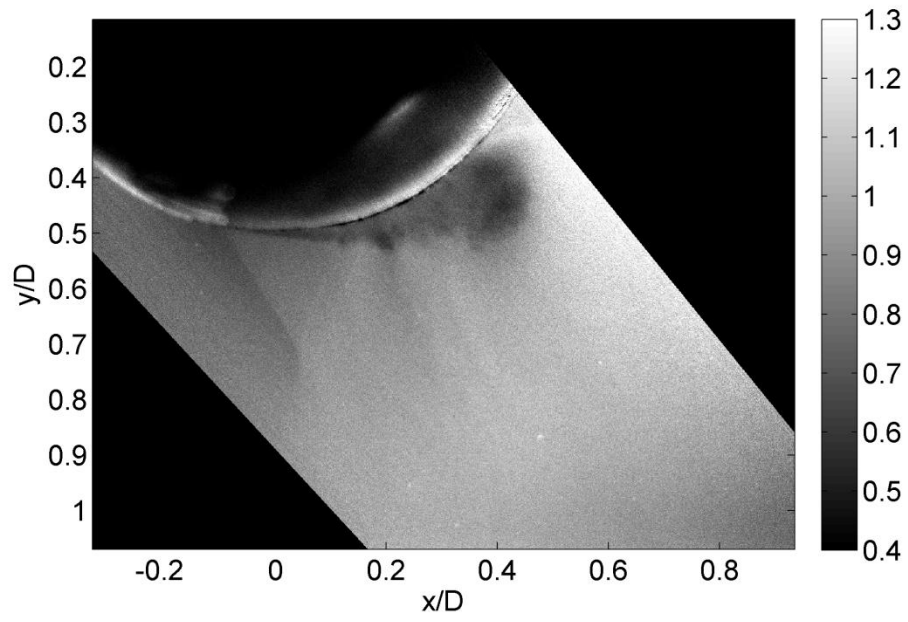
5D/8 Plane



*Typically in this work when images had streaks caused by particles in the freestream, the image was discarded. However, this image was one of the very few images in this particular image set (5D/8 plane) that showed significant density fluctuations and thus was not discarded.

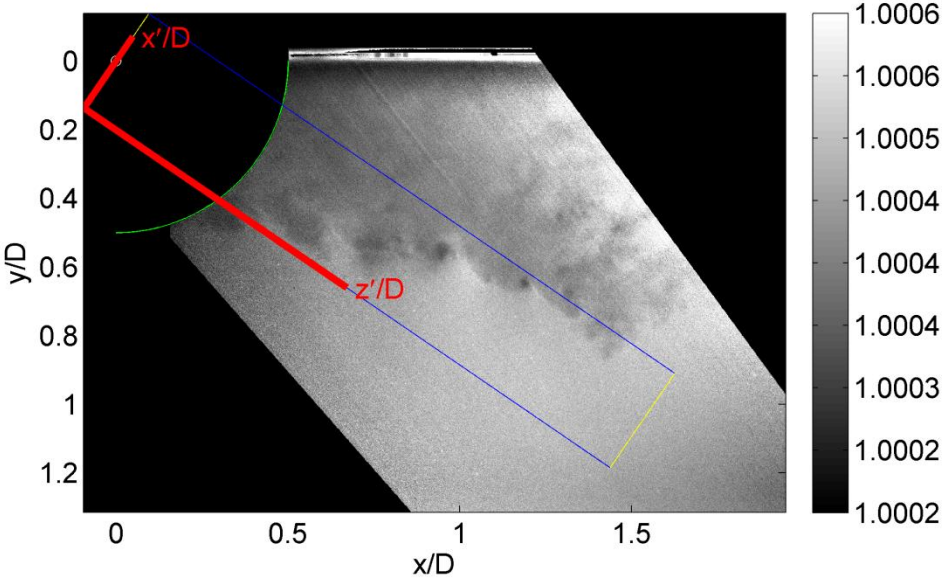
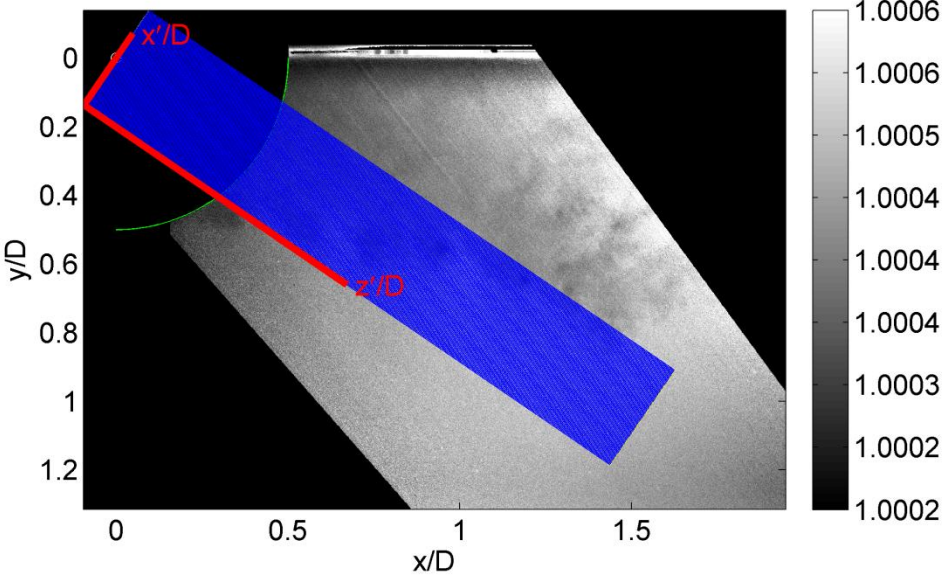
Appendix C: Single-Shot Acetone PLIF Density Images (values normalized to freestream) – Centerline – Separation Region



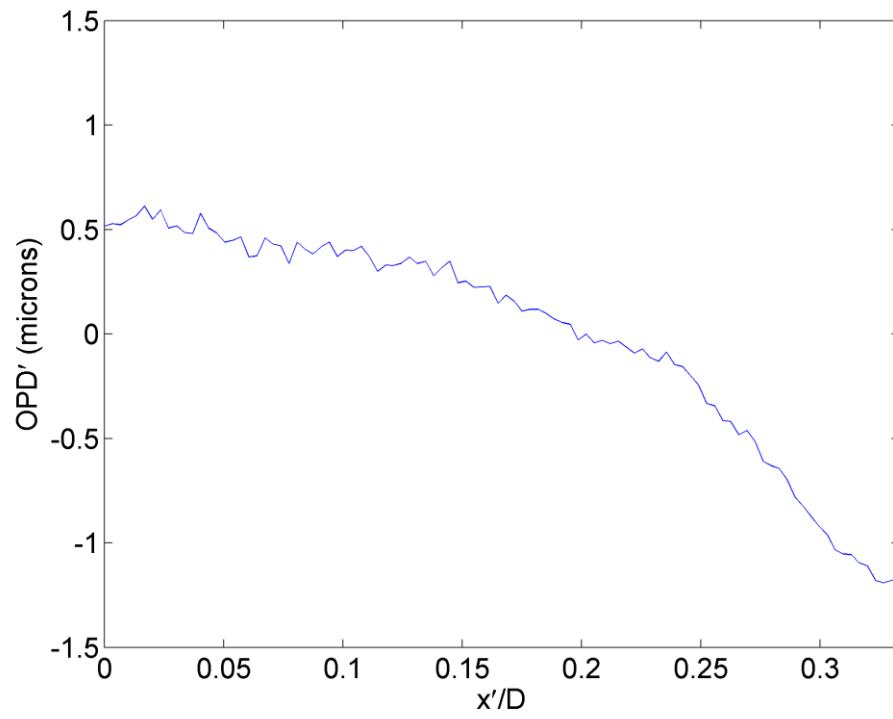
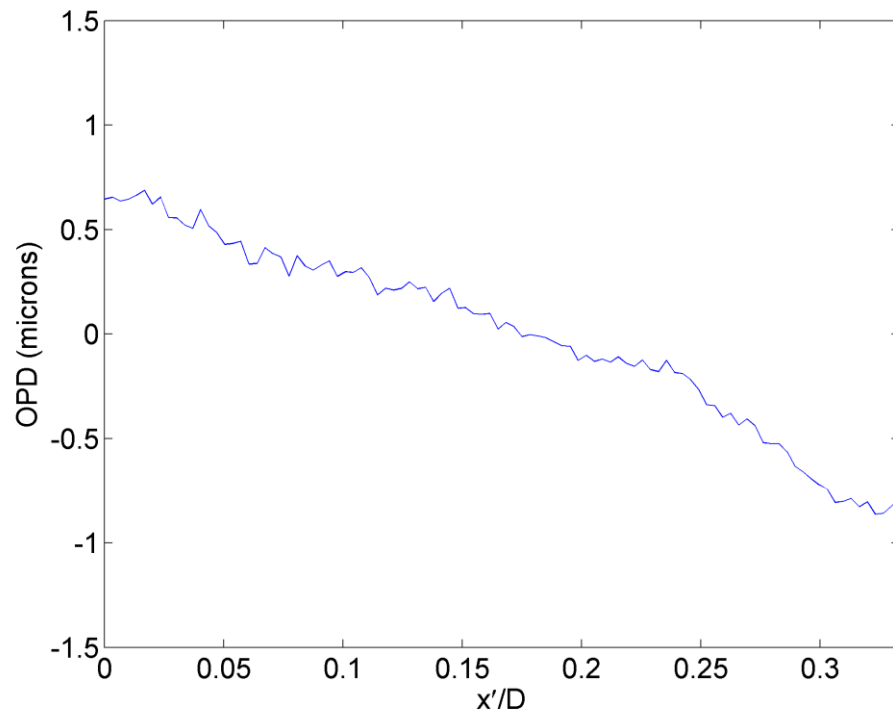


Appendix D: Example Wavefronts

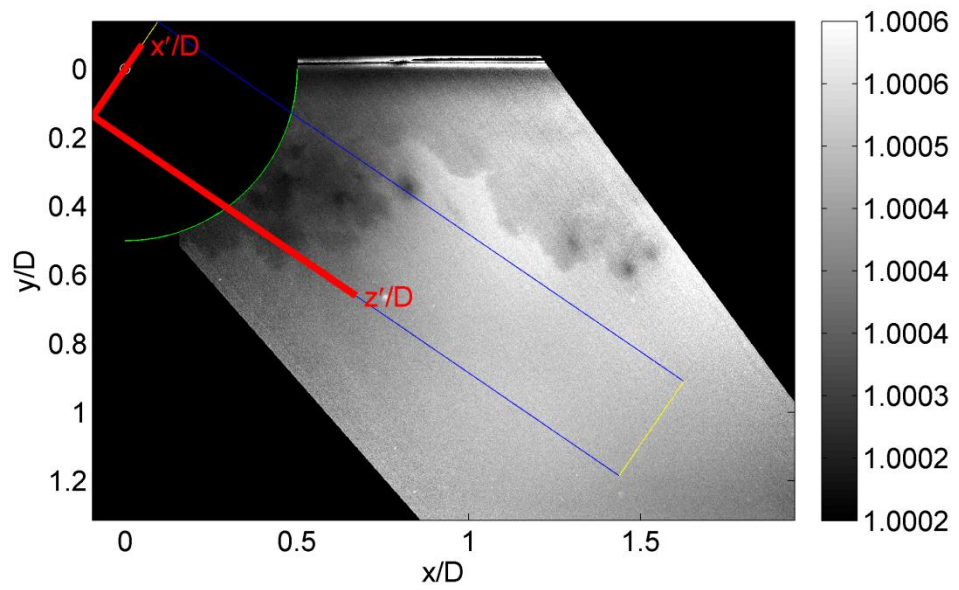
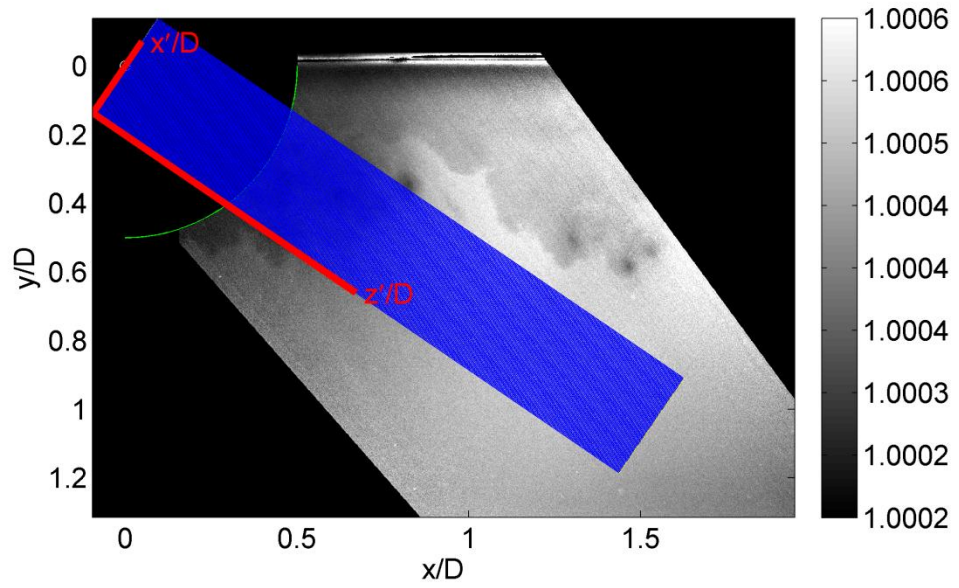
Example Wavefront #1



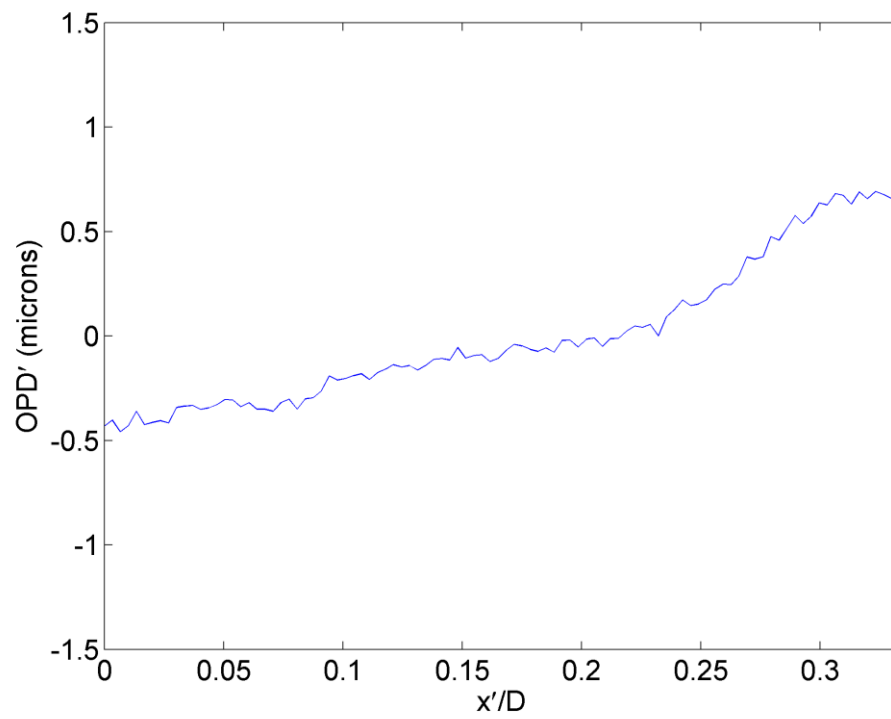
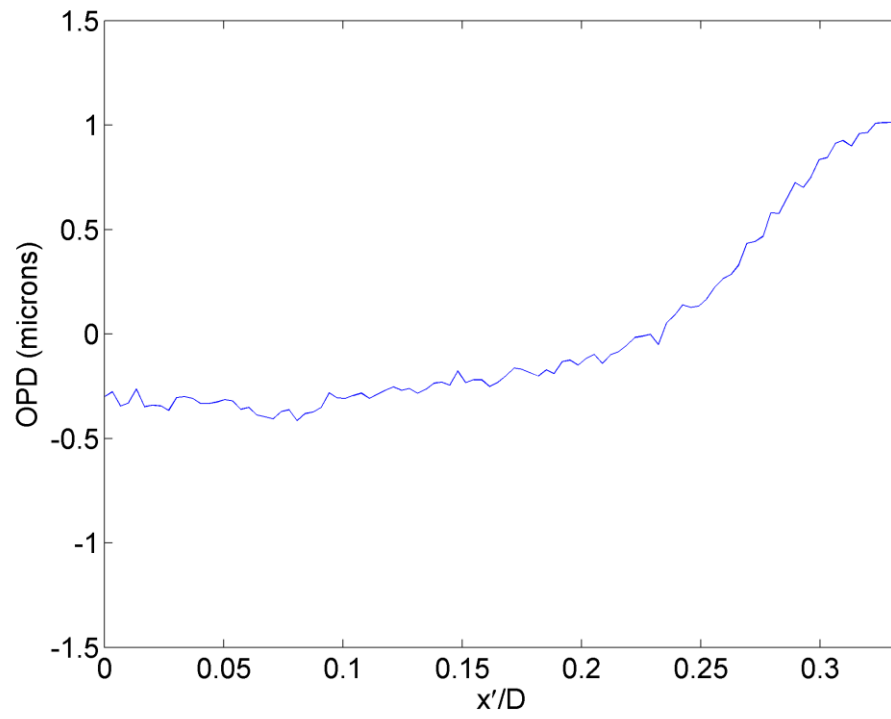
Example Wavefront #1



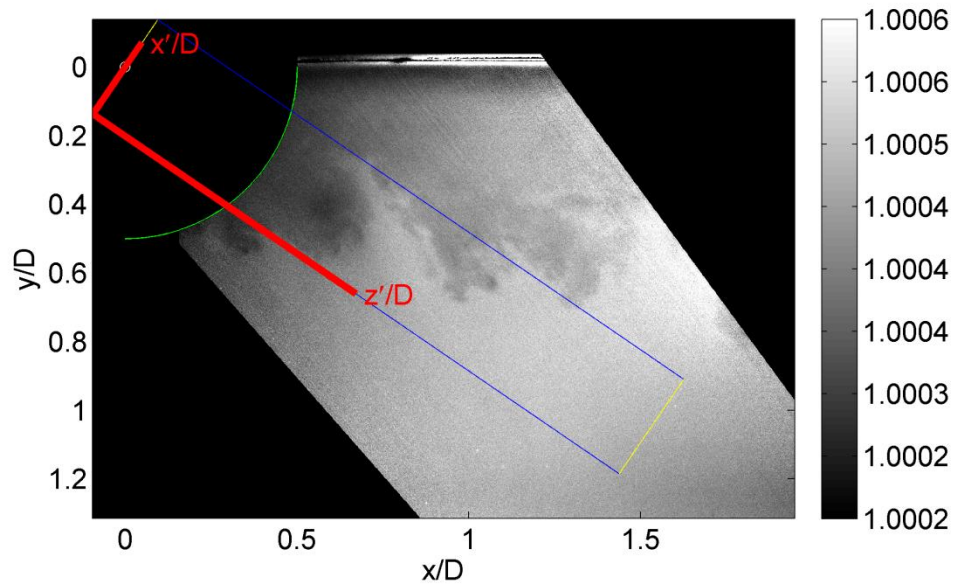
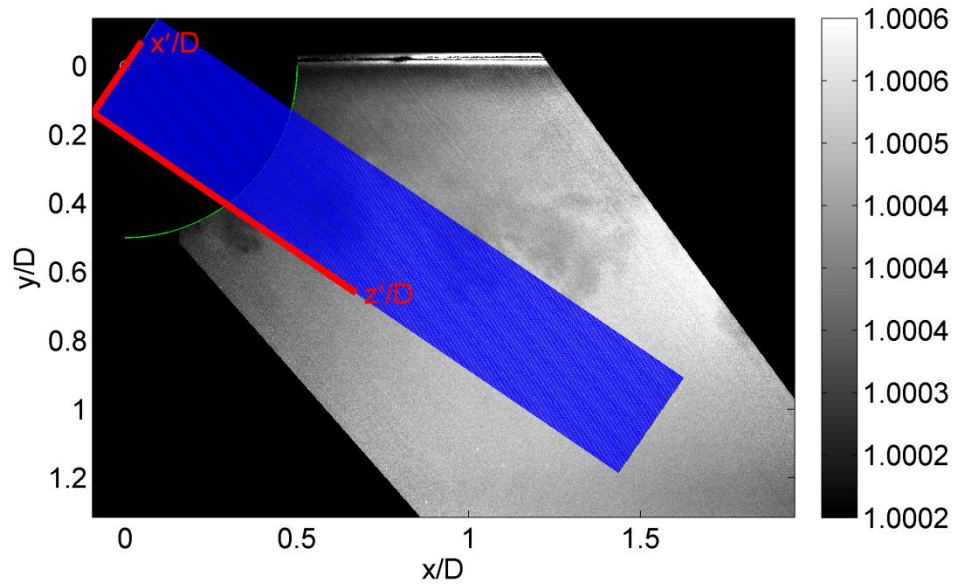
Example Wavefront #2



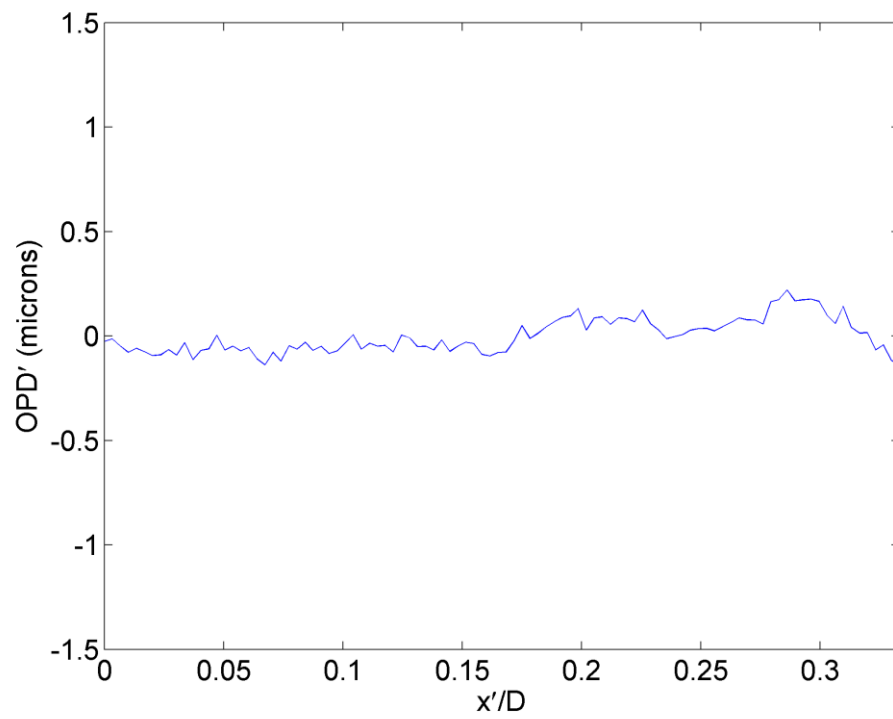
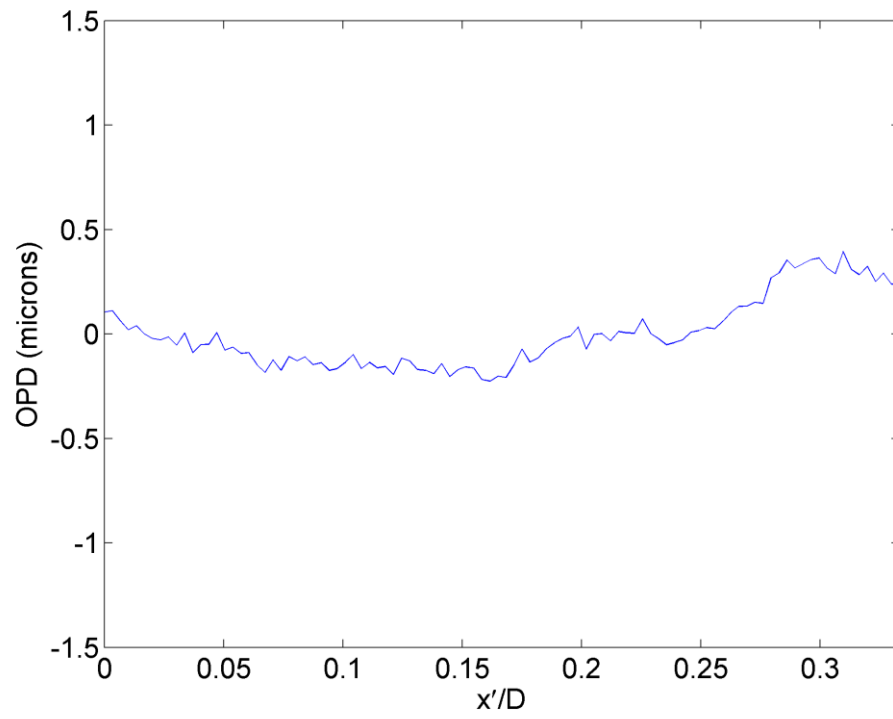
Example Wavefront #2



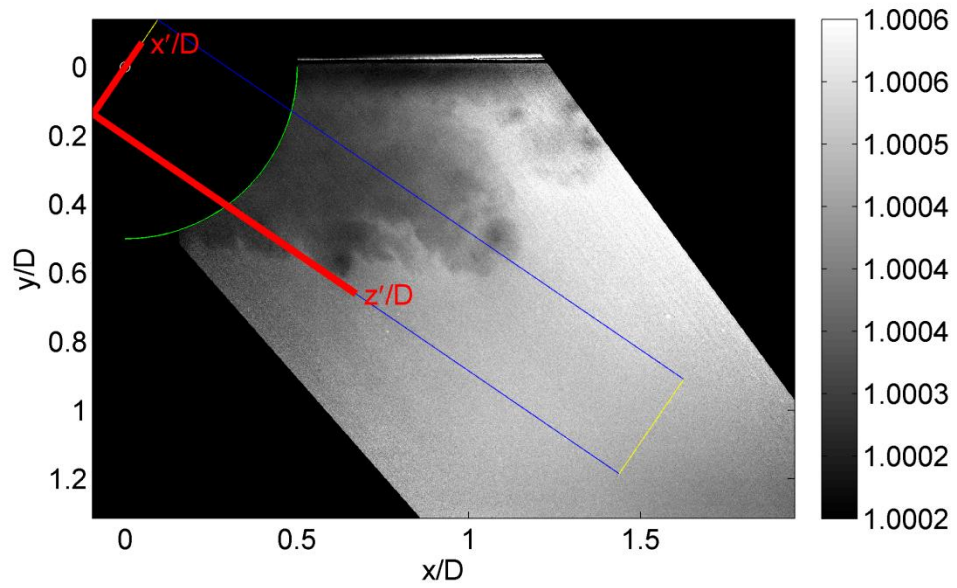
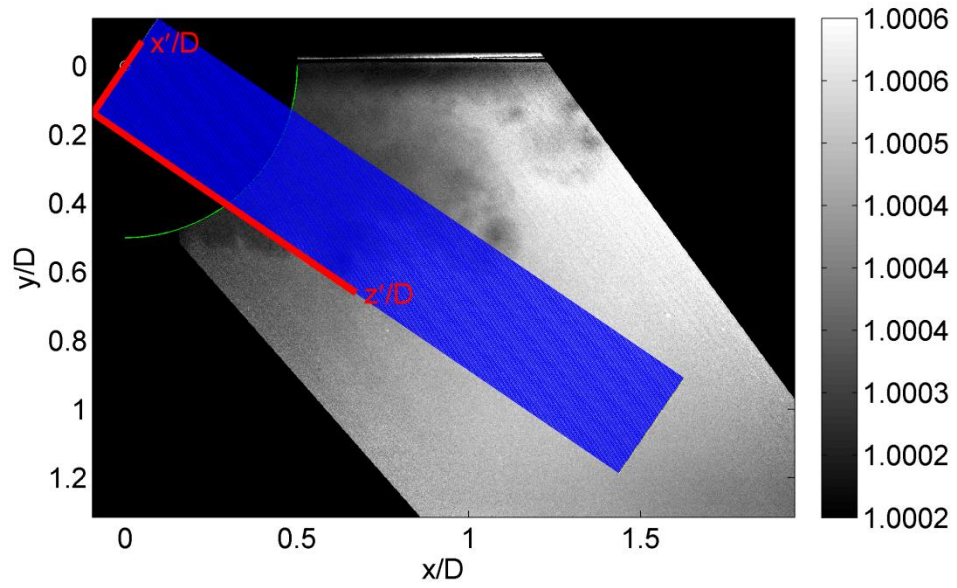
Example Wavefront #3



Example Wavefront #3



Example Wavefront #4



Example Wavefront #4

